

**BODY-FIXED, THREE-AXIS  
REFERENCE SYSTEM STUDY**

**Phase I Final Report**

FACILITY FORM 402	<b>66. 3.8.8.68.</b>	
	(ACCESSION NUMBER)	(THRU)
	<i>372</i>	<i>1</i>
	(PAGES)	(CODE)
	<i>CR-78669</i>	<i>21</i>
	(TASK OR OR TRM OR AD NUMBER)	(CATEGORY)

TRW No. 4499-6007-R0000

2 MAY 1966

Prepared by  
D. D. Otten

Prepared for  
NATIONAL AERONAUTICS AND SPACE ADMINISTRATION  
GEORGE C. MARSHALL SPACE FLIGHT CENTER  
Huntsville, Alabama

Under  
Contract No. NAS8-20209

GPO PRICE \$ \_\_\_\_\_

CFSTI PRICE(S) \$ \_\_\_\_\_

Hard copy (HC) 7.00

Microfiche (MF) 1.75

**TRW SYSTEMS**

ff 653 July 65

*807-40798*

---

**BODY-FIXED, THREE-AXIS  
REFERENCE SYSTEM STUDY**

---

**Phase I Final Report**

---

TRW No. 4499-6007-R0000

2 MAY 1966

Prepared by  
D. D. Otten

Prepared for  
NATIONAL AERONAUTICS AND SPACE ADMINISTRATION  
GEORGE C. MARSHALL SPACE FLIGHT CENTER  
Huntsville, Alabama

Under  
Contract No. NAS8-20209

**TRW** SYSTEMS

BODY-FIXED, THREE-AXIS  
REFERENCE SYSTEM STUDY

PHASE I FINAL REPORT

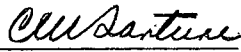
2 May 1966

TRW No. 4499-6007-R0000

Prepared by:

  
D. D. Otten

Approved:

  
C. W. Sarture  
Director, Guidance and  
Navigation Laboratory

## ACKNOWLEDGEMENT

The data contained in this report represent the combined efforts of members of the technical staff at TRW Systems and at the NASA Marshall Space Flight Center. It is appropriate, therefore, to acknowledge the valuable assistance of the major contributors to the document, with reference to their responsibilities:

### TRW Systems

K. L. Baker - Computer Equations, Alignment Studies, Software Error Analysis; M. J. Laubenstein - Performance Analysis; W. H. Musser - DDA and GP Mechanization Studies; D. D. Otten - Study Direction, Technical Contributions to portions of the studies, and final editing of the report; R. C. Rountree - SAP and PIGA analyses; R. W. Richardson and T. A. Fuhrman - Instrument Studies; W. J. Tallon - Electrically Rebalanced OA Systems Studies; G. R. Wilde - GP Memory and Timing Estimates; R. L. Turner - certain aspects of Algorithm Studies; and G. J. Zaremba - Encoder Studies. Important study review contributions were also made by E. I. Ergin, J. A. Vanderlaan, and E. C. Wirth of TRW Systems.

### NASA/MFSC

Of considerable importance to the study was the help rendered by Marshall Space Flight Center personnel. Particularly helpful was the Contracting Officer's representative, F. P. Daniel. In addition, the assistance of G. Doane, H. Kennel, and C. D. Carlisle is greatly appreciated.

## CONTENTS

1.	INTRODUCTION	1-1
1.1	STUDY INERTIAL INSTRUMENTS	1-3
1.2	ANGULAR ENCODER SURVEY	1-3
1.3	STUDY ATTITUDE REFERENCE AND NAVIGATION EQUATIONS	1-4
1.4	STUDY ALIGNMENT TECHNIQUES	1-4
1.5	SYSTEM PRELIMINARY DESIGN	1-4
1.6	ERROR MODELING	1-4
1.7	COMPUTER STUDIES	1-4
1.8	PERFORMANCE ANALYSIS	1-4
1.9	COMPARISON OF SYSTEMS	1-4
2.	SUMMARY	2-1
2.1	FEASIBILITY OF THE SELECTED CONFIGURATION	2-2
2.1.1	System Description	2-2
2.1.2	System Error Model and Performance	2-4
2.1.3	System Parameters	2-4
2.2	COMPARISON OF SYSTEMS	2-5
2.2.1	Alternate Strapped-Down System Description	2-5
2.2.2	Comparison of Systems	2-7
2.3	KINEMATICAL REPRESENTATION STUDIES	2-9
2.4	COMPUTER EQUATIONS AND PERFORMANCE	2-13
2.4.1	Direction Cosine Computation Errors	2-13
2.4.2	Alignment Study	2-17
2.4.3	Acceleration Integration	2-17
2.5	COMPUTER STUDIES	2-18
2.6	RATE-SENSITIVE ERROR TERMS	2-20
2.7	ENCODER STUDIES	2-23
2.7.1	Background	2-23
2.7.2	Shaft Readout Devices	2-23
2.7.3	Inductosyn and Theodosyn Systems	2-25
2.8	ELECTRICALLY REBALANCED OUTPUT AXES SYSTEM CONSIDERATIONS	2-27
2.9	INSTRUMENT STUDIES	2-27

## CONTENTS (Continued)

3.	PERFORMANCE ANALYSIS	3-1
3.1	TRAJECTORY DEFINITIONS	3-2
3.2	SELECTED SYSTEM PERFORMANCE	3-5
3.2.1	Error Model	3-5
3.2.2	SIRA Errors	3-6
3.2.3	Instrument Orientation	3-9
3.2.4	Results	3-15
3.3	ALTERNATE SYSTEM	3-16
3.3.1	Error Model	3-16
3.3.2	Instrument Orientation	3-19
4.	KINEMATICAL REPRESENTATIONS	4-1
4.1	DESCRIPTION OF THE KINEMATICAL REPRESENTATIONS	4-1
4.1.1	Direction Cosines	4-1
4.1.2	Euler Symmetrical Parameters and Rodriguez Parameters	4-2
4.1.3	Quaternions	4-4
4.1.4	Cayley-Klein Parameters	4-5
4.1.5	Four-Parameter Euler Angle Representation	4-8
4.1.6	Three-Parameter Euler Angle Representation	4-10
4.1.7	Rodriguez-Cayley, Gibbs Vector, and Vector Presentations	4-10
4.2	TAYLOR'S SERIES EXPANSIONS OF EULER'S SYMMETRICAL PARAMETERS AND THE FOUR GIMBAL EULER ANGLES	4-11
4.2.1	Euler Symmetrical Parameters - Second-Order Taylor's Series Expansion	4-12
4.2.2	Four-Gimbal Euler Angle - Second-Order Taylor's Series Expansion	4-13
4.3	COMPUTER REQUIREMENTS	4-15
4.3.1	General Purpose Mechanization	4-15
4.3.2	DDA Mechanization	4-16
	REFERENCES	4-18

## CONTENTS (Continued)

5.	COMPUTER EQUATIONS AND PERFORMANCE	5-1
5.1	EQUATION DESCRIPTION	5-2
5.1.1	Attitude Reference Equations	5-7
5.1.2	Acceleration Integration Equations	5-11
5.1.3	Compensation Equations	5-13
5.1.4	Body Rate Computation	5-15
5.1.5	Linear Interpolation of Guidance Commands	5-16
5.1.6	Attitude Error Signals	5-17
5.1.7	Prelaunch Alignment	5-20
5.2	ATTITUDE REFERENCE EQUATION ANALYSIS	5-26
5.2.1	Taylor's Series Constant Slew Error Analysis	5-26
5.2.2	Scientific Simulation Test Results	5-35
5.2.3	Direction Cosines Coning Studies	5-42
5.2.4	The Attitude Reference Integration Rate	5-58
5.2.5	Attitude Reference Equation Quantization	5-61
5.3	ALIGNMENT STUDY	5-63
5.3.1	Scientific Simulation Description	5-63
5.3.2	Simulation Results	5-68
5.4	ACCELERATION INTEGRATION ANALYSIS	5-74
5.4.1	Acceleration Integration Errors	5-75
5.4.2	Error Analysis for Single Axis Slews and Constant Accelerations	5-76
5.4.3	Estimated Computer Word Length	5-80
	REFERENCES	5-82
6.	COMPUTER STUDIES	6-1
6.1	DDA CONCEPT	6-1
6.1.1	Preliminary Considerations	6-1
6.1.2	DDA Computational Elements	6-4
6.1.3	System Description	6-5
6.1.4	DDA Operation	6-7
6.1.5	Input/Output	6-9
6.1.6	DDA Memory System	6-10
6.1.7	DDA Signal Flow	6-13
6.1.8	DDA Computational and Component Requirements	6-24

## CONTENTS (Continued)

6.2	GP COMPUTER CONCEPT	6-25
6.2.1	Hardware Considerations	6-25
6.2.2	Sizing Results	6-27
7.	SAP AND PIGA ANALYSIS	7-1
7.1	DERIVATION OF EQUATIONS OF MOTION	7-1
7.1.1	Model	7-1
7.1.2	Preliminary Equations	7-2
7.1.3	Angular Velocities	7-3
7.1.4	Output Axis Equation	7-5
7.1.5	Input Axis Equation	7-9
7.2	SAP ERROR TERMS	7-16
7.2.1	Derivation of SAP Error Terms	7-16
7.2.2	Error Term $\epsilon_1$ (Fixed Torque, G-Sensitive)	7-19
7.2.3	Error Term $\epsilon_2$ (Ramp Input of $\omega_2$ )	7-20
7.2.4	Error Terms $\epsilon_3$ to $\epsilon_9$ (Rectification)	7-21
7.3	PIGA ERROR TERMS	7-32
7.3.1	Derivation of PIGA Error Terms	7-34
7.4	VIBRATION ENVIRONMENT	7-35
7.4.1	Angular Vibration	7-36
7.4.2	Linear Vibration	7-38
7.5	ERROR SOURCE MAGNITUDES	7-39
7.5.1	Angular Transients	7-39
7.5.2	Sinusoidal Errors	7-41
7.5.3	Random Errors	7-56
	REFERENCES	7-64
8.	ENCODER STUDIES	8-1
8.1	DESCRIPTION OF ENCODERS AND SURVEY RESULTS	8-1
8.1.1	Optical Concept	8-2
8.1.2	Variable Reluctance Concept	8-2
8.1.3	Variable Capacitance Concept	8-4
8.1.4	Magnetic Concept	8-5
8.1.5	Induction Concept	8-5
8.1.6	Mechanical Concept	8-7

## CONTENTS (Continued)

8.2	INDUCTOSYN SYSTEM	8-7
8.2.1	Principle of Operation	8-7
8.2.2	Accuracy	8-8
8.2.3	Inductosyn Readout	8-10
8.3	THEODOSYN SYSTEM	8-15
8.3.1	Description	8-15
8.3.2	Theodosyn Errors	8-17
	REFERENCES	8-18
9.	ELECTRICALLY REBALANCED OUTPUT AXIS SYSTEM	9-1
9.1	PULSE TORQUING, SDF, RATE INTEGRATING GYROS	9-1
9.2	CATEGORIES OF PULSE TORQUING LOGIC	9-17
9.2.1	Synchronized Pulse Rate (Period $T_s$ ): Fixed Pulse	9-17
9.2.2	Synchronized Pulse Rate Period ( $T_s$ ): Variable Pulse	9-22
9.2.3	Nonsynchronous Pulses	9-23
9.3	PULSE TORQUING ELECTRONIC CIRCUITRY	9-24
9.3.1	Logic and Power Switching Circuitry	9-24
9.3.2	Constant Current Generator	9-27
10.	NEW CONCEPTS	10-1

## ILLUSTRATIONS

1-1	Study Block Diagram	1-3
2-1	Selected Configuration, Functional Block Diagram	2-3
2-2	Alternate Strapped-Down Configuration, Functional Block Diagram	2-6
2-3	Coning Study Results	2-15
2-4	Classification of Electrically Rebalanced Output Axis Systems	2-28
3-1	Inertial Velocity as a Function of Flight Time	3-3
3-2	Altitude as a Function of Flight Time	3-4
3-3	Flight Path Angle as a Function of Flight Time	3-4
3-4	Comparison of Cutoff Times of Various Stages of Powered Flight	3-5
3-5	Gyro Model Coordinate	3-7
3-6	Frequency Function for a Uniform Distribution	*
3-7	Instrument Orientation	3-9
3-8	Two Orientations of Yaw Gyro at Launch	3-11
3-9	Two Orientations of Pitch Gyro at Launch	3-12
5-1	Software Mechanization	5-3
5-2	Alignment Equations	5-4
5-3	Flight Equations	5-5
5-4	Gimbal Angle Orientation	5-18
5-5	Alignment Equations Flow Diagram	5-22
5-6	Alignment Equations Flow Diagram	5-24
5-7	Angular Acceleration Profile	5-36
5-8	Resulting Rotation Rate Profile	5-37
5-9	Resulting Attitude Rotation Angle	5-37
5-10	Coning Study Results	5-43
5-11	Typical Coning Study Results	5-49
5-12	Typical Coning Study Results	5-52
5-13	Typical Coning Study Results	5-53
5-14	Saturn C-5 LOR (Suborbital Start) Vehicle on the Launcher/Umbilical Tower	5-64
5-15	Saturn V LOR Vehicle on the Launcher/Umbilical Tower	5-64
5-16	Saturn V Deflection on Launcher/Umbilical Tower	5-65
5-17	Alignment Gain Plot	5-70

\* This Figure will be found on Page 6 of the Classified Annex, TRW Document No. 4499-7200.13-001.

## ILLUSTRATIONS (Continued)

6-1	In and Out of Memory Data Sequence	6-8
6-2	DDA Block Diagram	6-14
6-3	DDA Signal Flow Block Diagram	6-15
6-4	Special Input/Output Equipment	6-26
6-5	Program Linkage Flow Required for Strapped-Down System	6-28
7-1	SAP Model	7-1
7-2	SAP Block Diagram	7-15
7-3	Simplified SAP Block Diagram	7-22
7-4	Angular Vibration Spectrum	7-36
7-5	Summary of Visual Inspection of Recordings	7-37
7-6	Line Diagram of SAP Control System	7-44
7-7	Reproduction of Root Locus Printout	7-46
7-8	Root Locus Traces (Upper Half Plane Only)	7-47
7-9	Amplitude of $\frac{\theta}{\omega_2}$ (j $\omega$ )	7-48
7-10	Phase Angle of $\frac{\theta}{\omega_2}$ (j $\omega$ )	7-48
7-11	Normalized Drift Rate $\frac{\epsilon_3}{\Omega_2 \Omega_3}$	7-51
7-12	Normalized Drift Rate $\frac{\epsilon_4}{ L_{e'}  \Omega_3}$	7-51
7-13	Normalized Drift Rate $\frac{\epsilon_5}{ L_{pe'}  \Omega_3}$	7-52
7-14	Normalized Drift Rate $\frac{\epsilon_6}{\Omega_2 \Omega_3}$	7-52
7-15	Normalized Drift Rate $\frac{\epsilon_7}{ L_{e'}  \Omega_3}$	7-53
7-16	Normalized Drift Rate $\frac{\epsilon_8}{ L_{pe'}  \Omega_3}$	7-53
8-1	Incremental Reluctance Encoder Block Diagram (4N System)	8-3
8-2	Microgyn Configuration	8-4
8-3	Magnetic Transducer	8-6

## ILLUSTRATIONS (Continued)

8-4	Inductosyn Transducer Discs	8-7
8-5	Incremental Angle Encoder Block Diagram	8-13
8-6	Waveforms – Incremental Angle Encoder	8-14
8-7	Theodosyn Configuration	8-16
9-1	The Generic Pulse Rebalance Loop	9-4
9-2	Constant Power Pulse Torque Representation	9-6
9-3	Pulse-on-Demand Pulse Torque Representation	9-9
9-4	Torque Generator Tuning	9-15
9-5	Classification of Output Axis Rebalance Techniques	9-18
9-6	Synchronized Pulse Rate, Fixed Pulse Width, Two Charge State System ( $f_m > f_c$ )	9-19
9-7	Synchronized Pulse Rate, Fixed Pulse Width, Two Charge State System ( $f_c > f_m$ )	9-20
9-8	Four Charge State System	9-21
9-9	Pulse Width Modulated, Two Current Level System	9-23
9-10	Pulse Torquing Channel	9-25
9-11	Precision Reference Voltage Generator	9-28

TABLES

2-I	Strapped-Down IMU Characteristics	2-5
2-II	Summary of Performance Analysis Typical Electrically Rebalanced Output Axis System	2-8
2-III	Comparison of Selected and Alternate Systems	2-9
2-IV	Estimates for Parameter Updating and Forming the Direction Cosine Matrix	2-12
2-V	Direction Cosine Slewing Errors	2-15
2-VI	Results of Attitude Reference Error Studies	2-16
2-VII	Comparison of GP and DDA Approach	2-18
2-VIII	Approximate Drift Rate Errors and Causes	2-22
2-IX	Acceleration Measurement Errors and Causes	2-23
2-X	Shaft Angle Readout Devices	2-24
2-XI	Gyro Characteristics	*
2-XII	Accelerometer Characteristics	*
3-I	Error Model Used for MSFC Study	*
3-II	Comparison of Injection Errors (LV) for Two Yaw Gyro Orientations	3-13
3-III	Comparison of Injection Errors (LV) for Two Pitch Gyro Orientations	3-14
3-IV	Injection Errors (Local Vertical) for MSFC Body Fixed 3-Axis Reference System	*
3-V	Summary of Performance Analysis Typical Electrically Rebalanced Output Axis System	3-17
4-I	General Purpose Computer Requirements	4-17
5-I	Summary of Attitude Reference Equation Analysis	5-35
5-II	Slewing Performance Results, Second-Order Taylor's Series	5-38
5-III	Taylor's Series Error in True Vehicle Coning Rate	5-48
5-IV	Algorithm Coning Rate Error in Degress Per Hour	5-50
5-V	Taylor's Series Error	5-51
5-VI	Algorithm Coning Rate Error in Percent	5-54
5-VII	Algorithm Coning Rate Error	5-55
5-VIII	Coning Error for Taylor's Series Algorithm	5-56
5-IX	Coning Errors for Backward Differencing Algorithm	5-57
5-X	Coning Errors for Algorithm A	5-58
5-XI	First- and Second-Order Taylor's Series Slewing Errors	5-59
5-XII	Acceleration-Integration Errors for a Constant 5 Deg/Sec Slew About the $X_b$ Axis and a Constant 3-g Acceleration Along the Y Body Axis	5-81

\*These tabulations will be found on Pages 3, 4, 9, 10, respectively, of the Classified Annex, TRW Document No. 449-7200.13-001.

TABLES (Continued)

5-XIII	Summary of Velocity Transformation Equation Errors with No Vehicle Limit Cycling	5-81
6-I	Sequence of Operations During Integration Cycle Consecutive Integrations Followed by ADD Cycle	6-7
6-II	DDA Element Count	6-24
6-III	Summary of MSFC Strapped-Down System Memory and Timing Requirements	6-29
7-I	Neglected Output Axis Torques	7-7
7-II	Neglected Input Axis Torques	7-13
7-III	Drift Rate Errors and Causes	7-18
7-IV	Equivalent Sinusoidal Angular Oscillations	7-38
7-V	$\epsilon_3/\Omega_2\Omega_3$ Calculations	7-50
7-VI	Drift Rectification Error Magnitudes (Sinusoidal)	7-54
7-VII	Drift Rectification Error Magnitudes (Sinusoidal) for Extended Environment	7-55
7-VIII	Drift Rectification Error Magnitudes (Random)	7-58
7-IX	Drift Rectification Error Magnitudes (Random) for Extended Environment	7-59
8-I	Estimated Inductosyn System Characteristics	8-11
8-II	Inductosyn Preliminary MTBF Calculations	8-11

## 1. INTRODUCTION

In June 1965, under Contract No. NAS8-20209, the Marshall Space Flight Center (MSFC) awarded TRW Systems (formerly STL) a feasibility study designated as "Body-Fixed 3-Axis Inertial Reference System or Application of an Analytic Platform to Future Missions." The background to this study as provided by MSFC is as follows:

"In recent years, inertial guidance hardware technology has advanced to a state where an analytic platform system may provide an inertial reference which is superior to present systems in which inertial sensors are mounted together on a gimbaled platform. In such an analytic platform system, the inertial sensors are mounted directly to the carrier vehicle, having provision in a digital computer for the function which gimbals provide in present systems.

"The problems in implementing such a system fall into the following three categories:

- (a) The inertial sensors are body mounted rather than being on a stabilized platform. This environment is more severe because the instruments are subjected to all of the vehicle motions with the results that the inertial sensors measure quantities in an entirely different regime.
- (b) The data rates necessary to characterize vehicle motions for ultimate use in vehicle navigation are very high. These quantities which are fundamentally analog in nature must be converted to digital signals at a very high rate.
- (c) Vehicle attitude rate data will be used to derive vehicle attitude in space. The computations for providing this may be very complicated and require very high accuracy and speed.

"Surveys of the progress of the industry in solving these problems were conducted in 1964 and 1965. These surveys indicated that indeed progress was being made and that such a system might provide significant benefits for the future space system."

The basic objective of the study was to determine the feasibility of application of an analytic platform system for use on a Saturn boost mission. To accomplish this, it was necessary to (1) study inertial instruments and angular encoders which might be utilized; (2) consider the attitude-reference and navigation equations which would perform the analytic reference; (3) determine computer requirements and perform computer preliminary design; and (4) perform system error modeling, flight simulations, and alignment studies. The results obtained have demonstrated the feasibility of using a given (though not necessarily optimum) analytic platform configuration for the mission.

While the potential advantages of the strapped-down inertial reference system have been often quoted, they will be repeated here to establish the motivation behind the study. Because of the early development status of strapped-down guidance, none of these advantages has yet been conclusively demonstrated. Further, a system optimized for one mission might have relative advantages which differ from those of a system optimized for an alternate mission. Nevertheless, the possible advantages of the strapped-down system in comparison with a gimbaled system are tabulated below:

- Minimum maintenance problems.
- Wideband body rate data can be provided for control system stabilization.
- Minimum size, weight, and power for a reference utilizing well-developed components.
- Minimum mechanical complexity (this may imply higher reliability even though the electronic complexity of the strapped-down system is greater).
- All-attitude operation.
- Compatibility and flexibility of usage with other sensors, such as star trackers, radars, etc.
- Highly amenable to techniques of redundancy.
- Minimum configuration constraints.

The approach studied in detail was defined by MSFC and involved the use of three single-axis platforms (SAP) and three pendulous-integrating-gyroscope-accelerometers (PIGA). Such a system has high accuracy potential. In addition, it can function despite relatively high body angular rates.

To accomplish the study objectives, nine tasks were performed as indicated in the block diagram of Figure 1-1; these tasks are briefly discussed in the following paragraphs.

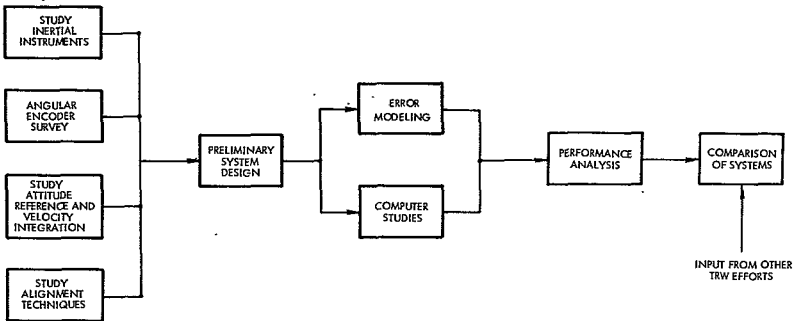


Figure 1-1. Study Block Diagram

### 1.1 STUDY INERTIAL INSTRUMENTS

Various sensors and subsystems with potential use in analytic platforms were investigated relative to their performance, interface requirements, and development status. Only conventional components were considered for this study; that is, "exotic" instruments such as the electrostatic gyro, laser gyro, nuclear spin gyro, etc., were not considered.

### 1.2 ANGULAR ENCODER SURVEY

A survey of angular encoders was made to determine whether the high-accuracy encoder requirements of this system were feasible and desirable from an engineering point of view. The encoders considered during the study included inductance, reluctance, capacitance, magnetic, optical, and mechanical.

### 1.3 STUDY ATTITUDE REFERENCE AND NAVIGATION EQUATIONS

The attitude reference equations considered were Direction Cosines, Euler Symmetrical Parameters, Cayley-Klein Parameters, Quaternions, Euler Angle Systems, and the Gibbs Vector. Two methods of integrating the accelerometer increments were also considered.

### 1.4 STUDY ALIGNMENT TECHNIQUES

Two methods of alignment were developed and simulated on a digital computer.

### 1.5 SYSTEM PRELIMINARY DESIGN

An MSFC concept of an accurate strapped-down system (using three SAP's and three FIGA's) was studied in detail. All the equations required to be mechanized in the computer were written both in digital differential analyzer (DDA) and general purpose (GP) form. These included the equations covering attitude reference, navigation, alignment, compensation, guidance command iteration and resolution, and body rate.

### 1.6 ERROR MODELING

An error model of this system was developed which included contributions from the equations, alignment errors, angular rate effects on the instruments, and the normal (stable platform) instrument errors.

### 1.7 COMPUTER STUDIES

Studies were performed to determine the timing and memory requirements for both GP and DDA computer mechanizations. In addition, estimates were made of the hardware required for this application.

### 1.8 PERFORMANCE ANALYSIS

Finally, the error model was used for a performance analysis.

### 1.9 COMPARISON OF SYSTEMS

Certain parameters of the SAP and FIGA systems are compared with parameters of a strapped-down system using rate-integrating gyros (with pulse rebalanced output axes) and force rebalanced accelerometers.

## 2. SUMMARY

This section summarizes the study results contained in Sections 3 through 9 of the TRW Systems Phase 1 Final Report.

Our study demonstrates the feasibility of using a strapped-down inertial reference assembly (SIRA) and an associated strapped-down digital computer (SDC) to replace the presently used ST-124 gimbaled IMU for guidance of the Saturn booster. The system that was investigated in detail uses three gyros, each mounted on a table with one degree of angular freedom (commonly termed three SAP's) for providing the data required to maintain an attitude reference. In addition, three PIGA's are used to sense acceleration. Our report includes a comparison of certain aspects of this system and an alternate strapped-down system mechanization.\*

Several kinematic representations suitable for the maintenance of the attitude reference in the computer were investigated, and direction cosines were chosen for further study. All computer equations (for both the GP and the DDA usage) were derived. The accuracy of the critical equations was studied.

The sensitivity of the SAP and PIGA to body rate inputs was studied, and the numerical effects were calculated. The accuracy of the instruments was not seriously degraded by the environment expected, provided that the PIGA's are compensated for body rates. Similarly, the study of angular encoders for shaft-angle readout demonstrates that devices with suitable resolution, accuracy, size, weight, and reliability are readily available.

Computational requirements for both the GP and DDA mechanizations were considered. The GP is strongly recommended by virtue of its flexibility.

Some aspects of the alternate strapped-down approach\* (electrical rebalance of the gyro output axis) are presented. In addition, a catalog of instruments suitable for use in a strapped-down system is given. These two efforts provide some generally useful background material.

---

\* Data for the alternate mechanizations were available from prior TRW Systems' efforts.

## 2.1 FEASIBILITY OF THE SELECTED CONFIGURATION

A brief description of the system selected for further study is given below and is followed by a presentation of the system error model and performance, and certain parameters.

### 2.1.1 System Description

The block diagram of Figure 2-1 depicts the selected configuration which uses three SAP's. An angular rate ( $\omega$ ) along a gyro input axis causes a precession of the gyro about the output axis. The gyro gimbal angle pick-off voltage is amplified, demodulated, and filtered to provide an error signal. This signal is shaped and amplified in order to drive the single-axis table in such a direction that the gyro float is torqued back to null. Thus, the single-axis table keeps rates about the table axis (gyro input axis) nulled. As a result, the angle between the table and the body is the integral (in body space) of the body angular rate about that axis. An incremental platform angle pickoff ( $\Delta\alpha$ ) will be used because of inherent simplicity. There would be no net advantage to the use of a whole angle pickoff. Pitch, roll, and yaw systems are identical in construction.

PIGA's are used to sense acceleration ( $a$ ). Note that the block diagrams of the PIGA's and the gyro loop are functionally very nearly identical.

The PIGA is compensated for input axis body rates as well as bias and scale factor.

The computer implemented provides computations necessary to make the system equivalent to a platform system. The incremental angles are used to provide the attitude reference as well as the body attitude rate data. The attitude reference equations along with the compensated velocity pulses are used to integrate the total velocity in inertial space and to provide incremental velocity outputs to the main guidance computer. Equations are also required for initial alignment, and the configuration shown uses the PIGA's for leveling and external information (optical) for the azimuth reference. The attitude reference equations and the commanded attitude are used to provide inputs to the attitude error computations. Attitude error signals are also computed.

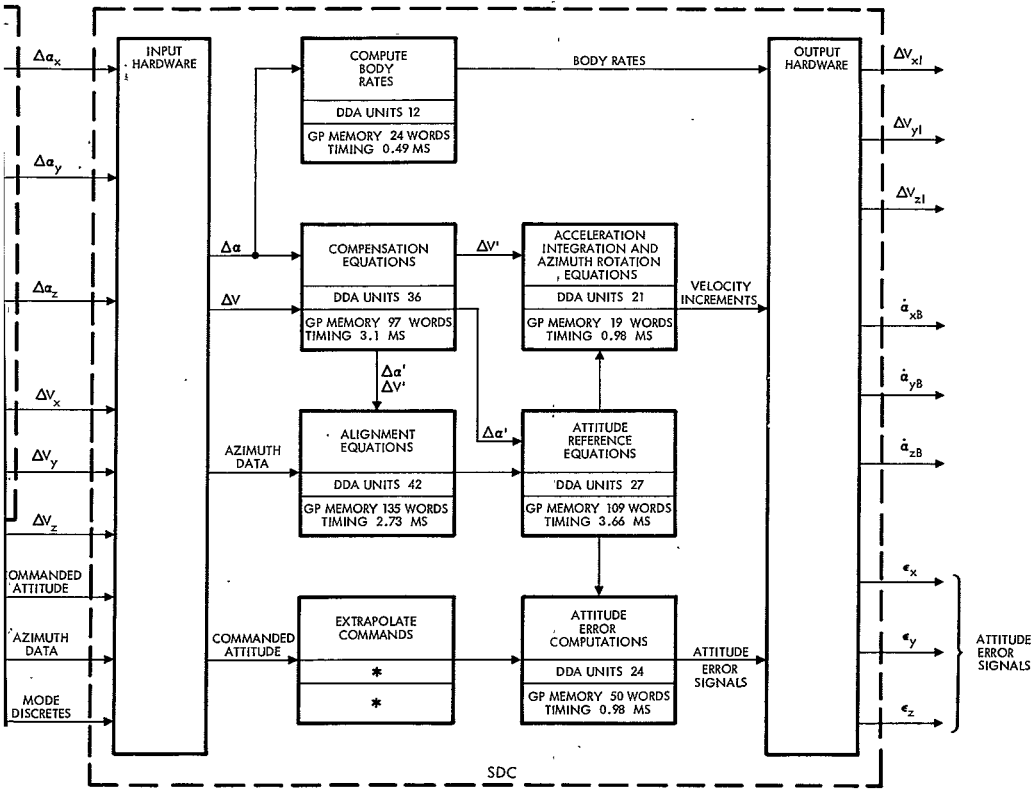
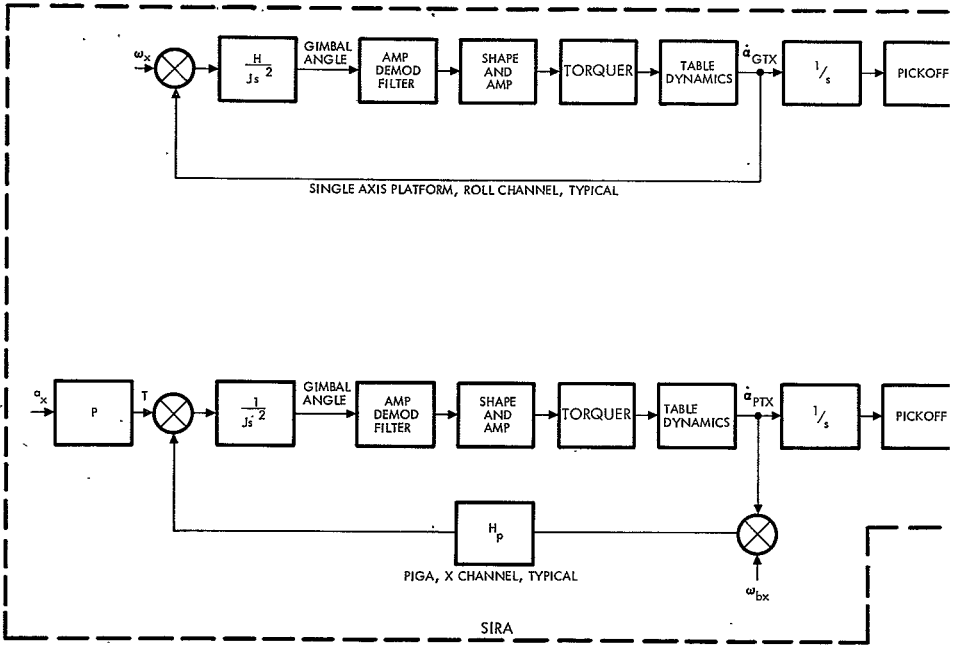


Figure 2-1. Selected Configuration, Functional Block Diagram

2



NOTE: 14 SAMPLERS ALSO REQUIRED FOR DDA (SEE SECTION 6)

\*MINIMUM COMPLEXITY IMPLEMENTATION SHOWN FOR ALL EQUATIONS IN THIS CASE THE FUNCTION IS NOT PERFORMED

2-3 

Certain computer requirements are also indicated on Figure 2-1. The number of units\* required for a DDA is given as well as the memory and timing requirements for a typical, state-of-the-art, airborne computer. (See Section 6 for the groundrules assumed in the computer sizing.) Several sets of equations are possible for some of the functions indicated. These are discussed in detail in Section 5. The simplest equations possible for the two computer mechanizations were used to obtain the requirements noted in Figure 2-1.

### 2.1.2 System Error Model and Performance

The system error model discussed in detail in Section 3 takes into consideration: (1) the usual instrument error terms which would be obtained with the instruments mounted on a stable platform; (2) body angular rate sensitive terms (see Section 7); and (3) computational errors (see Section 5). This error model was "flown" on a Saturn-Centaur (Voyager injection) trajectory with no parking orbit, and the resultant injection errors are presented in the Confidential annex appended to this report. The total inertial velocity at injection is approximately 10,800 m/sec (35,500 ft/sec). Section 3 presents a detailed discussion of the performance analysis. The results ( $3\sigma$  velocity error of 3.0 m/sec and position error of 1.26 km) clearly demonstrate the feasibility of an accurate boost of a spacecraft using the selected strapped-down system configuration in place of a conventional IMU.

### 2.1.3 System Parameters

Table 2-I provides a summary of the characteristics of the strapped-down IMU. Characteristics of the SIRA were obtained from MSFC where certain preliminary design efforts for such a system are underway. The SDC estimates are obtained from Section 6.

---

\* A unit can be an integrator, adder, or sampler as defined in Section 6.

Table 2-1. Strapped-Down IMU Characteristics

	Weight		Average Power (watts)	Size (in.)	MTBF (hr)
	kgm	lb			
Computer Subsystem (SDC)					
DDA	7.0	15.5	64	13 x 7 x 5.5	14,000
GP	8.2	18.0	82	14.5x7x5.5	10,000
Inertial Subsystem (SIRA)	15.9	35.0	26.5*	≈1-ft dia sphere	Not available
Gas Supply (7.5 hr)	12.3	27.0	Negligible	1/2-ft <sup>3</sup> sphere	Not available
Total IMU					
DDA	35.2	77.5	90.5		
GP	36.3	80.0	108.5		
* If a heater is used for temperature control, this number will increase.					

## 2.2 COMPARISON OF SYSTEMS

Information pertinent to the "Alternate System" described herein was obtained from work performed by TRW Systems on other contracts.

### 2.2.1 Alternate Strapped-Down System Description

Figure 2-2 is a functional block diagram of the alternate configuration. The SIRA instruments consist of three single-degree-of-freedom, rate integrating gyros and three pendulous accelerometers, each of which has functionally identical pulse rebalancing electronics.\* Just as with the selected configuration, each gyro pulse represents an increment of angle about the gyro input axis. These pulses are accepted as inputs to the SDC where they are compensated (for gyro input-axis misalignments, scale factor, bias, and mass unbalance terms), and then utilized to compute the attitude of the vehicle with respect to an inertial reference frame.

\* This system is such that torquing (or forcing) current is continuously applied.

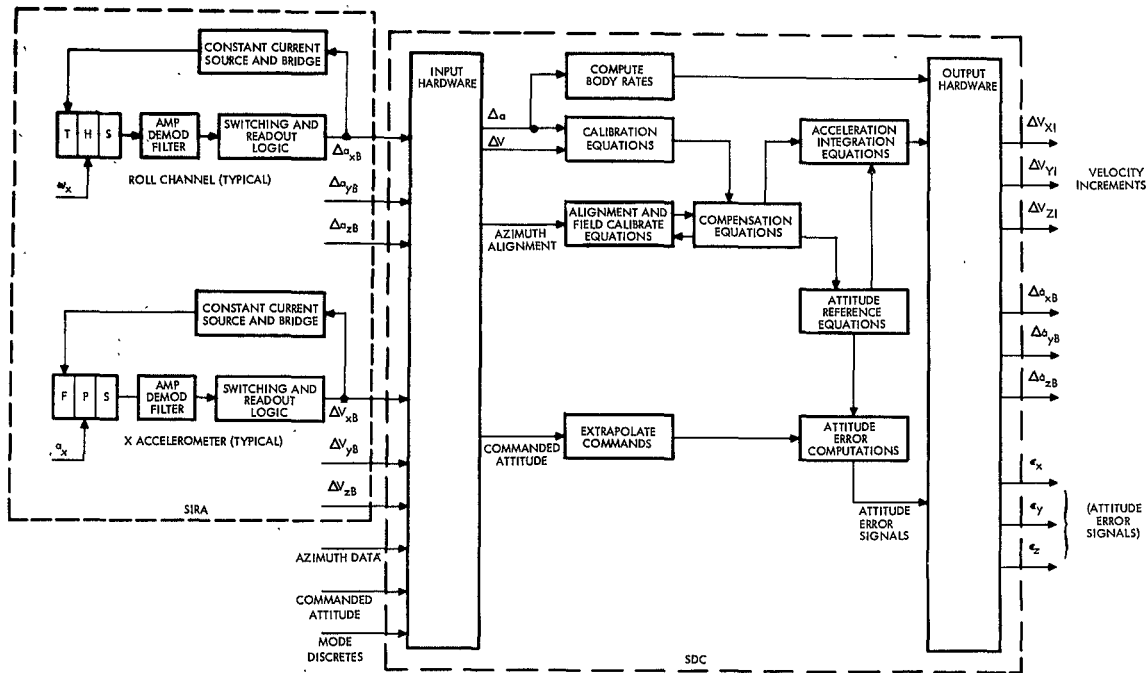


Figure 2-2. Alternate Strapped-Down Configuration, Functional Block Diagram

Each accelerometer pulse represents an increment of velocity along a body axis as was the case with the FIGA's. The pulses are compensated for bias, scale factor, and input-axis misalignment.

The computer interface for both configurations is identical except for the following:

- (1) Higher frequency input pulses are received from the alternate system. This disadvantage stems from the method of processing gyro data in the SIRA, which results in a minor increase in input hardware and no accuracy improvement.
- (2) The alternate system has more calibration requirements. This is a result of the difference in stability of the instruments used. In order to obtain the required accuracy, it is necessary further to calibrate (automatically) gyro biases and thrust axis accelerometer scale factor during the prelaunch countdown (see Subsection 3.3).

The error model discussed in Subsection 3.3 for the alternate system is repeated here as Table 2-II. The performance of this system on the Saturn-Centaur (Voyager injection) trajectory previously discussed is included in that table: The errors are greater by a factor of 3 over the previous system.

### 2.2.2 Comparison of Systems

Table 2-III compares the physical parameters and performance of the selected system and the alternate system. The numbers used for the computers are taken from Section 6, and the alternate system SIRA physical parameters are from MSFC. The computer numbers for both strapped-down systems are considered to be the same. Note that such important aspects as cost, development status, and reliability are not compared.

Table 2-II. Summary of Performance Analysis Typical Electrically Rebalanced Output Axis System

Error Source	Error Magnitude (3σ)	Position Error (ft)			Velocity Error (ft/sec)		
		ΔP	ΔR	ΔN	ΔVE	ΔVR	ΔVN
<b>Accelerometer Chamber Errors</b>							
Bias							
X Accel	80 μg	290	1020	--	1.0	2.2	--
Y Accel	80 μg	--	--	1090	--	--	1.9
Z Accel	80 μg	930	610	--	1.3	2.2	--
Bias Correlated with Inertial Reference Alignment							
Y Axis	190 μg	--	--	1290	--	--	5.1
Z Axis	190 μg	1100	100	--	1.1	0.8	--
Rectification Error							
X Accel	105 μg	540	2070	--	1.8	3.9	--
Y Accel	150 μg	--	--	2070	--	--	3.6
Z Accel	150 μg	1740	1140	--	2.1	-3.9	--
Bias Correlated with Scale Factor							
X Accel	190 μg/g	330	-1470	--	0.3	-2.8	--
Scale Factor							
X Accel	105 μg/g	180	2250	--	1.2	4.5	--
Nonlinearity							
X Accel	90 μg/g	150	1950	--	0.9	3.9	--
<b>Gyro Channel Errors</b>							
Bias							
X Gyro	0.16 deg/hr	--	--	1870	--	--	7.0
Y Gyro	0.16 deg/hr	3490	-3490	--	5.1	-13.9	--
Z Gyro	0.16 deg/hr	--	--	3900	--	--	8.0
Spin Axis Mass Unbalance							
X Gyro	0.12 deg/hr/g	--	--	2490	--	--	8.4
Bias Correlated with Spin Axis Unbalance							
X Gyro	0.60 deg/hr	--	--	5400	--	--	14.0
Vibration Induced Drift Rate							
X Gyro	0.06 deg/hr	--	--	690	--	--	2.7
Y Gyro	0.06 deg/hr	1380	1380	--	1.8	-5.1	--
Z Gyro	0.06 deg/hr	--	--	1290	--	--	3.0
Scale Factor							
Y Gyro	180 X 10 <sup>-6</sup> deg/deg	360	-450	--	0.3	-2.1	--
Nonlinearity							
Y Gyro	90 X 10 <sup>-6</sup> deg/deg	180	-210	--	0.3	-1.2	--
Gyro Alignment							
X Gyro to Y Accel	60 arc sec	--	--	150	--	--	2.1
Inertial Reference Alignment							
Azimuth	60 arc sec	--	--	4290	--	--	7.2
RSS		4460	5710	8900	6.6	17.6	22.5
RSS of ΔPos, ΔVel		11,476 ft			29.3 ft/sec		
		3,498 m			8.9 m/sec		

Table 2-III. Comparison of Selected and Alternate Systems

System	Weight		Steady State Power (watts)	Attitude Rate Limitation	Velocity Error (3 $\sigma$ )	Position Error (3 $\sigma$ )
	(kgm)	(lb)				
Selected System						
With DDA	35.2*	77.5	90.5***	**	[9.9 ft/sec] [(3.0 m/sec)]	[4,100 ft] [1.26 km]
With GP	36.3*	80.0	108.5***	60 deg/sec		
Alternate System						
With DDA	15.7	34.5	142	**	[31.4 ft/sec] [(9.6 m/sec)]	[12,200 ft] [3.66 km]
With GP	16.8	37.0	160	10 deg/sec		
* Includes 7,5-hr gas supply.						
** Will take transients up to rate indicated for GP, but sustained rate limitations are much lower (See Subsection 2.5.)						
*** Does not include heater.						

### 2.3 KINEMATICAL REPRESENTATION STUDIES

This subsection summarizes investigations of various kinematical representations which might be used to provide the mathematical angular reference relating body attitude to a given inertial attitude. The investigations are given a thorough treatment in Section 4.

Numerous kinematical representations such as these have been developed as shown by the tabulation below:

- Three-Parameter Systems

Three-gimbal Euler angle representation (several mechanizations possible)

Gibbs Vector (alternately known as Rodriguez-Cayley parameters or vector presentation)

- Four-Parameter Systems

Euler's symmetrical parameters (alternately known as Rodriguez parameters)

Quaternions

Cayley-Klein parameters

Four-gimbal Euler angle representation (several mechanization possible)

- Four- to Nine-Parameter Systems

Direction cosines

Expansion of this list through the development of new techniques is feasible, although such an effort is beyond the scope and intent of this study. Although ten different names are given above, there are actually only seven different systems.

The three-parameter systems have distinct singularities. For certain attitudes of the vehicle and finite body angular rate inputs, the required parameter rate is infinite, making it impossible to compute fast enough to maintain the attitude reference. For some missions, this might present little or no difficulty, as evidenced by the fact that three-gimbal inertial platforms find wide usage. However, there is no apparent advantage in the use of either of the three-parameter systems, and there is an obvious disadvantage in their inflexibility for a complex mission. Therefore, the three-parameter systems were not considered as candidates for maintenance of the attitude reference. The other techniques have no singularities.

The terminology "four-gimbal Euler angle," although somewhat artificial, will be retained here as the definition of the mathematical equivalent of a four-gimbal, all-attitude, inertial platform configuration.

The three remaining four-parameter systems, Euler symmetrical parameters, Quaternions, and Cayley-Klein parameters can each be derived independently of the others. Of these, the Cayley-Klein parameters and the Quaternions use specially defined complex numbers (sometimes termed hypercomplex) and operations. Section 4 demonstrates that

the four independent parameters of each of these systems are identical. Thus, if one begins either with Cayley-Klein parameters or with Quaternions and derives a matrix defining the functional relationship between a rate of change of the parameter and the body angular rate of change, that particular matrix will be identical for all three systems. The fundamental requirement of the analytic platform is that it be able to transform the vectors from body space to inertial space, and vice-versa. The equations relating the direction cosines to the independent parameters of the Euler symmetrical, Cayley-Klein, and Quaternion representations are also identical. Thus, in this sense all three systems are equivalent.

This equivalence greatly simplifies the problem. It remains only to evaluate the relative merits of direction cosines, Euler symmetrical parameters and the four-gimbal Euler angle system. The evaluation criteria here involve the computer requirements (both memory and timing for both GP and DDA) and accuracy considerations.

While body rates are not directly available in any presently known accurate strapped-down implementation, incremental body angles are available. Therefore, each of the algorithms must be expanded to perform an approximate integration (see Section 4). An obvious choice would be either a first- or second-order Taylor's series. Several other expansions are readily available, but studies of alternate expansions for the direction cosine parameters (see Subsection 4.3) have indicated a clear preference for the Taylor's series expansion. Computer requirements established for these systems are summarized in Table 2-IV.

It is obvious from the table that there is an advantage to the use of direction cosines for the maintenance of the analytic reference from the point of view of computer timing and memory. There appears to be no physical reason why the accuracy of direction cosine reference would be surpassed by the use of either of the other candidates. The proper investigation of accuracy would require a computer simulation, since a solution to this problem is not amenable to a hand analysis.

Table 2-IV. Estimates for Parameter Updating and Forming the Direction Cosine Matrix

Kinematical Representation	GP ESTIMATES				DDA ESTIMATES
	Memory Estimates (Words)		Timing Estimate (msec)		Number of Units Required
	Program	Constant and Variable	General	TRW GP Computer	
Direction Cosines					
First-order Taylor's series	58	21	132A + 18M	2.58	27
Second-order Taylor's series	88	21	156A + 30M	3.66	*
Euler Symmetrical Parameters					
First-order Taylor's series	143	28	154A + 22M	3.08	50
Second-order Taylor's series	163	28	167A + 29M	3.7	*
Four-Gimbal Euler Angle +					
First-order Taylor's series	221	45	320A + 66M	7.82	70
Second-order Taylor's series	397	66	510A + 101M	12.17	*
A = Add times M = Multiply times * Not considered necessary because of high computational rates available for DDA + Assumes that a small angle approximation is valid for the redundant gimbal					

Further, several expansions of each alternate parameter plus numerous inputs would be required. Because of these considerations, direction cosines were selected for further study.

In addition to providing the background for the above discussion, Section 4 contains a description of all the kinematical representations considered, some discussions of their properties, and a presentation of the equations applicable to this study. In addition, the second-order Taylor's series expansion for the Euler-symmetrical parameters and the four-gimbal Euler angle system are presented. Finally, further discussion of the computer requirements for the selected representations is given.

## 2.4 COMPUTER EQUATIONS AND PERFORMANCE

This subsection provides a brief summary of the work presented in Section 5, which includes all computer equations as well as software error analysis.

As implied in Subsection 2.1, discussions with MSFC early in the study phase established that the following operations be performed by an SDC:

- (1) Inertial instrument error compensation
- (2) Attitude reference equations
- (3) Acceleration integration in inertial coordinates
- (4) Prelaunch alignment
- (5) Linear interpolation of guidance commands
- (6) Generation of attitude error signals
- (7) Computation of the vehicle body rates as measured by the gyros.

All equations required for the above and derived in forms suitable for both DDA and GP mechanization are presented in Section 5. In several cases, more than one set of equations was considered.

The accuracy of only three sets of the above equations is critical to the proper performance of the strapped-down system. That is, if the computer errors for the attitude reference, velocity integration, and alignment equations are made sufficiently small by the selection of the proper equations word size and iteration rate, it will follow that the errors made by the same computer on the other computations are completely negligible. Thus, accuracy analyses were limited to those areas.

### 2.4.1 Direction Cosine Computation Errors

The direction cosine equations used for the attitude reference were expanded with a Taylor's series to provide an algorithm suitable for use in a spacecraft digital computer. Two other expansions, Backwards Differencing and Algorithm A (a Runge-Kutta technique modified to improve accuracy) were compared with a first- and second-order Taylor's series

expansion for accuracy when subjected to coning motion of the vehicle. The results are summarized in the graph of Figure 2-3, which is an empirically obtained normalized curve from which the error resulting from an input of two orthogonal sinusoidal rates of equal amplitude and 90-degree phase shift can be calculated. The error of any of the four algorithms for any limit cycle amplitude, frequency, and computer sampling interval may be found as follows:

- (1) Normalize the computer sampling interval with respect to the limit cycle period. For example, the normalized sampling interval for a 0.5-cps signal and a 20-msec sampling interval is  $0.02T/2.0 = 0.01T$ .
- (2) Obtain the percent error from the normalized graph. For instance, the percent error for the Taylor's series is 0.1% for the 0.5 cps signal and a 20-msec sampling interval.
- (3) Calculate the correct vehicle coning rate in the desired units. For a 0.5-cps signal with an amplitude of 0.1 rad, the vehicle coning rate is

$$\omega' = (0.01)^2 (\pi) (0.5) = 1.5708 \times 10^{-4} \text{ rad/sec}$$

$$\omega' = 0.5655 \text{ rad/hr} = 32.403 \text{ deg/hr}$$

- (4) The coning error is 0.1% of 32.4 deg/hr or an equivalent drift of 0.034 deg/hr.

The results of Figure 2-3 and the relative complexity of the computer equations led to a clear choice of the Taylor's series expansion for maintenance of the attitude reference.

An analysis of the errors made when the vehicle turns at a constant rate about one axis (termed slewing) was also made, and analytical error terms were derived. The results of that analysis are summarized in Table 2-V. The incremental angle is designated  $\Delta$ . The second-order Taylor's series' primary advantage is the reduction of the scale factor error. The choice of first or second order is a tradeoff between the available computer space, maximum available computation rate, and the required accuracy.

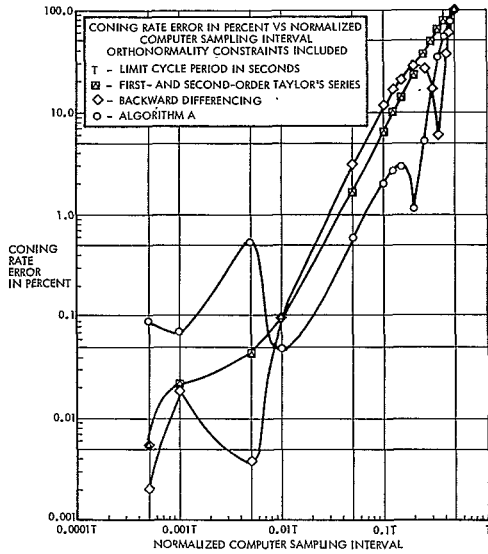


Figure 2-3. Coning Study Results

Table 2-V. Direction Cosine Slewing Errors

	Single Axis Slew		Three Axis Slew	
	Scale Factor Error	Per Cycle Angle Error	Scale Factor Error	Per Cycle Angle Error
First-order Taylor's series	$\sqrt{1 + \Delta^2}$	$-\frac{\Delta^3}{3}$	$\sqrt{1 + 3\Delta^2}$	$-\Delta^3$
Second-order Taylor's series	$\sqrt{1 + \Delta^4/4}$	$-\Delta^3/6$	$\sqrt{1 + 9\Delta^4/4}$	$-\frac{\Delta^3}{2}$

In Table 2-VI below, the errors for both algorithms are tabulated for four different sampling rates. From the table, it appears that the first-order Taylor's series meets a drift criterion of 0.01 deg/hr if sampled faster than every 6.4 msec, and the second-order Taylor's series meets that drift criterion if sampled faster than every 8.5 msec. In the error analysis of Section 3, it has been conservatively assumed that a 10-msec computation time will be available and a second-order expansion used, resulting in an error of 0.015 deg/hr ( $3\sigma$ ).

Table 2-VI. Results of Attitude Reference Error Studies

Computer Sampling Rate in msec	Drift Errors of the First-Order Taylor's Series ( $10^{-2}$ deg/hr)					Drift Errors of the Second-Order Taylor's Series ( $10^{-2}$ deg/hr)				
	15	10	7.5	5	2	15	10	7.5	5	2
Slewing Errors (maximum rate = 6 deg/sec)	5.37	2.3	1.34	0.6	0.0956	2.69	1.15	0.67	0.3	0.033
Coning Errors (0.05 deg at 3 cps)	2.07	1.0	0.044	0.028	0.0081	2.07	1.0	0.044	0.028	0.0081
RSS $3\sigma$	5.76	2.51	1.34	0.6	0.096	3.39	1.52	0.67	0.3	0.033

During a 1000-sec flight, the second-order Taylor's series would update the direction cosines 100,000 times. Suppose it is desired to keep the roundoff error less than 13 arc sec. An unjustifiably conservative approach would assume roundoff additive and yield a requirement of

$$\frac{13 \text{ arc sec} \times 4.85 \times 10^{-6}}{\times 10^5} \text{ rad/arc sec} = 6.31 \times 10^{-10} \text{ rad}$$

which would require 31 bits.

A much more realistic approach is to divide the attitude error at injection by the  $\sqrt{n}$ , i. e.,

$$\Delta\theta = \frac{13 \times 4.85 \times 10^{-6}}{\sqrt{10^5}} = \frac{10^{-8} \times 4.85 \times 13}{3.16} = 2 \times 10^{-7}$$

which is equivalent to a word length of 23 bits.

Thus the required word length for the attitude reference equations is estimated to be between 23 and 31 bits. The actual word length required will be obtained from the next phase of the study by performing hypocomp simulations of typical trajectories, and is likely to be near 23 bits.

If a DDA is used, the roundoff errors are likely to be negligible as a result of the nature of the DDA operation.

#### 2.4.2 Alignment Study

Two methods of alignment were simulated. Quantization of the input was not simulated. The results show that the constant-gain filter methods may be used for the alignment but will require almost an hour to reduce an initial error of 1 deg to less than 20 arc sec. Also, both alignment methods presented in Section 5 may be used although the first method, a servoing technique, is preferable.

Since the constant gain filters require a long calibration time, it is recommended that a variable gain filter be used (such as a Kalman filter). Since it is desirable to align up to launch time, it is also suggested that the variable gains be changed to constant gains of  $10^{-5}$  when the alignment has attained an accuracy of about 10 arc sec.

#### 2.4.3 Acceleration Integration

A preliminary examination of the acceleration integration equations accuracy is presented in Subsection 5.4.

The software errors of these equations are examined in that section, with consideration given neither to computer quantization errors nor to errors associated with the fact that the accelerometers are not all located at the same point. These errors will be analyzed in Phase 2 of the MSFC study.

Furthermore, the work performed to date is not sufficient to support a specific prediction in the velocity and position errors at the end of a nominal flight. Sufficient work has been accomplished however to indicate the likelihood that these errors can be kept under 0.3 m/sec. (1 ft/sec) per axis.

Since the acceleration-integration errors are nonlinear functions of the vehicle accelerations, vehicle angular motions, and the equation iteration rate, the acceleration integration accuracy must be obtained from simulation. Since the errors are nonlinear, different combinations of vehicle motions and accelerations must also be simulated.

The word length requirements for a general-purpose computer were estimated to be between 18 and 26 bits. These word lengths were arrived at by dividing the desired quantization error by the number of computer cycles during a flight,  $n$  (conservative approach, 26 bits), and by dividing by the  $\sqrt{n}$  (optimistic approach, 18 bits). The actual word length requirement will be verified in Phase 2 of the study with simulations.

## 2.5 COMPUTER STUDIES

Table 2-VII illustrates some of the basic differences between the DDA and GP approach.

Table 2-VII. Comparison of GP and DDA Approach

Characteristic	DDA (Simplest Equation Set)	DDA With Extrapolation	GP Computer
Iteration time (msec)	1.072	1.568	7.5 to 8.6
Integrated circuits	553	636	1,111
Memory size (bits)	9,464	12,428	18,432
Power (watts)	64	68	82
Weight (lb)	15.5	15.5	18.0
Reliability MTBF (hr)	14,000	13,200	10,600
Computer size (in. <sup>3</sup> )	13 x 7 x 5.5	13 x 7 x 5.5	14.6 x 7 x 5.5
Flexibility	Poor	Poor	Good

The response time or iteration time for both systems differs by a factor of 7 for the simplest set of equations considered. The maximum iteration time given for the GP device assumes a much more complicated set of equations than for the DDA but does not differ much from the minimum time. The exact nature of these equations is given in Section 5, and the assumptions inherent in the estimates are given in Section 6.

The GP device is able to track at maximum input angular rates of 60 deg/sec per axis. Consider the DDA using the simplest equation set. Under these conditions, it is possible for the DDA solution to lag behind if the gyro inputs are at their maximum rate. For a full 16-bit accumulator (input time buffer), it would take the DDA  $(2^{16}) (1.072 \text{ msec}) = 7 \text{ sec}$  to countdown and process the data obtained for a 60-deg rotation at maximum rate (10 arc sec or 17-bit SAP encoder assumed). The GP device, on the other hand, does not have this difficulty. Generally, the solution within the GP will have slightly greater errors for 60 deg/sec inputs, but a sustained input rate of this magnitude for the DDA as designed would effectively cause a loss of reference. The GP output solution will lag somewhat, since the output devices are countdown counters and would probably operate at about 512 kpps. Transients of 60 deg/sec can be tolerated with the DDA.

Thus for nominal input data rates (less than 1.4 deg/sec), the DDA can initiate the first increment of the solution within 1.072 msec. The GP computer would require a minimum of 7.5 msec. The DDA will thus have slightly better accuracy for the range of rates likely to occur during a Saturn boost, and can provide the attitude error signals for these rates with much less pure time delay.

The GP device can take advantage of the fact that some calculations are not required every iteration. Thus the computational workload can be shared over many iterations. The DDA cannot use this freedom to any particular advantage.

Of considerable importance is the flexibility involved in using these devices. Certain items such as constants and scale factors may be changed

within the DDA. However, the sequence and type of instructions are essentially wired in, and changes would necessitate the replacement or modification of the core stack.

In summary, then, the GP approach affords more flexibility and the ability to maintain tracking at high turning rates, all at the expense of added hardware and slightly reduced accuracy with a nominal environment.

The DDA involves less hardware, yields a faster solution for moderate turning rates, but loses accuracy when high rates are maintained over any extended period of time. The DDA also lacks the flexibility inherent in a GP approach. It does have slight weight, power, and reliability advantages.

The above considerations have led to the recommendation of a GP design. The addition of guidance equations (prediction and steering equations) to the computational load would strengthen this decision. Other possible requirements, such as automatic self-check and execution of discrete time-dependent commands, would further favor a GP decision.

## 2.6 RATE-SENSITIVE ERROR TERMS

The literature on inertial guidance systems contains extensive analyses of instrument errors. These analyses generally neglect effects of body angular rates because the components are mounted on an inertial platform. Thus it was necessary (see Section 7, summarized briefly here) to derive the equations of motion for a single-degree-of-freedom gyro when mounted on a single-axis platform (used either as a SAP or PIGA). The transfer functions for the drive servos were obtained from MSFC. The error terms obtained are a function of the dynamic environment to which the instruments are exposed, and hence Saturn flight data were analyzed to develop a representative input to the error model.

The angular rate-sensitive error terms are listed in the following two tables. Table 2-VIII presents the SAP drift-rate terms, their causes, and the errors resulting from the assumed environment. Table 2-IX presents similar information pertaining to the PIGA. These terms are

approximations that will be verified by a computer analysis in the second phase of the study. The SAP terms in Table 2-VIII are based on the following assumptions which are discussed in detail in Section 7.

- (1) Platform rotation angle ( $\theta_p$ ) remains essentially constant.
- (2) Forcing functions are generally periodic in nature.
- (3) The float angle ( $\theta$ ) and the platform angle rate ( $\dot{\theta}_p$ ) are not excited by the SAP spin axis component of vehicle angular velocity ( $\omega_3$ ).
- (4) Superposition is used in certain applications where it is not rigorously permissible.
- (5) Product of inertia and anisoinertia terms that appear in the Output Axis Equation are negligible.
- (6) Most of the "cross-product" terms from the derivation of the Input Axis Equation are negligible.

The above assumptions generally apply to the PIGA terms in Table 2-IX with one fundamental difference. Due to the rotation of the PIGA, it was further assumed that drift rectification effects would be negligible as a result of the averaging effects of the table rotation.

The following notation is used in Tables 2-VIII and 2-IX:

- P = Pendulosity of PIGA
- $H_x$  = Magnitude of angular momentum component pertaining to gyro spinning wheel
- $\omega_1, \omega_2, \omega_3$  = Component magnitudes of vehicle angular velocity along the platform axes
- $\Omega_1, \Omega_2, \Omega_3$  = Amplitudes of vibrational forms of  $\omega_1, \omega_2, \omega_3$
- $I_y$  = Moment of inertia of float about its output axis
- $\theta$  = Output axis angle (between float and platform)
- $\theta_p$  = Input axis angle (between platform and vehicle)
- $\psi_1, \psi_2, \psi_3, \psi_4$  = Phase angles of  $\omega_2$  relative to  $\omega_3$ ,  $L_{P_e}'$  relative to  $\omega_3$ ,  $L_{P_e}'$  relative to  $\omega_3$ , and  $\omega_3$  relative to  $\omega_3$ , respectively.

$$\left| \frac{\theta}{\omega_2} \right| = \text{Magnitude of transfer function } \frac{\theta}{\omega_2}$$

$$\angle \frac{\theta}{\omega_2} = \text{Phase shift of transfer function } \frac{\theta}{\omega_2}$$

Table 2-VIII. Approximate Drift Rate Errors and Causes

Error No.	Error Cause	Error Term	Numerical Value, deg/hr, (Worst Case)
$\epsilon_1$	$L_e'$ are fixed torques, mass unbalances, anisoelectricity (MSFC error model)	$\frac{L_e'}{H_r}$	*
$\epsilon_2$	Ramp input of $\omega_2$ (constant angular acceleration during finite time interval)	$-\frac{I_y}{H_r} \dot{\omega}_2$	Negligible
$\epsilon_3$	Rectification due to sinusoidal inputs of $\omega_2$ and $\omega_3$	$\frac{1}{2} \left  \frac{\theta}{\omega_2} \right  \Omega_2 \Omega_3 \cos \left( \frac{\theta}{\omega_2} - \psi_1 \right)$	0.003
$\epsilon_4$	Rectification due to sinusoidal inputs of $L_e'$ and $\omega_3$ ( $L_e'$ are $M_{ubs}$ and $M_{ubi}$ activated by vibration inputs)	$\frac{1}{2} \left  \frac{\theta}{L_e'} \right  \left  L_e' \right  \Omega_3 \cos \left( \frac{\theta}{L_e'} - \psi_2 \right)$	Negligible
$\epsilon_5$	Rectification due to sinusoidal inputs of $L_{pe}'$ and $\omega_3$ ( $L_{pe}'$ are friction torques or mass unbalances excited by vibration)	$\frac{1}{2} \left  \frac{\theta}{L_{pe}'} \right  \left  L_{pe}' \right  \Omega_3 \cos \left( \frac{\theta}{L_{pe}'} - \psi_3 \right)$	0.020
$\epsilon_6$	Rectification due to sinusoidal inputs of $\omega_2$ and $\omega_3$ (different propagation through loop than $\epsilon_3$ )	$\frac{1}{2} \frac{I_y}{H_r} \left  \frac{\dot{\theta}_p}{\omega_2} \right  \Omega_2 \Omega_3 \cos \left( \frac{\dot{\theta}_p}{\omega_2} - \psi_1 \right)$	Negligible
$\epsilon_7$	Rectification due to sinusoidal inputs of $L_e'$ and $\omega_3$ (different propagation through loop than $\epsilon_4$ )	$\frac{1}{2} \frac{I_y}{H_r} \left  \frac{\dot{\theta}_p}{L_e'} \right  \left  L_e' \right  \Omega_3 \cos \left( \frac{\dot{\theta}_p}{L_e'} - \psi_2 \right)$	Negligible
$\epsilon_8$	Rectification due to sinusoidal inputs of $L_{pe}'$ and $\omega_3$ (different propagation through loop than $\epsilon_5$ )	$\frac{1}{2} \frac{I_y}{H_r} \left  \frac{\dot{\theta}_p}{L_{pe}'} \right  \left  L_{pe}' \right  \Omega_3 \cos \left( \frac{\dot{\theta}_p}{L_{pe}'} - \psi_3 \right)$	Negligible
$\epsilon_9$	Rectification due to sinusoidal inputs of $\omega_x$ and $\omega_3$ (maximum value occurs when $\omega_x$ and $\omega_3$ are in phase)	$\frac{1}{2} \frac{I_y}{H_r} \Omega_x \Omega_3 \cos \psi_4$	0.015

\* See MSFC supplied error model of Section 3.

Table 2-IX. Acceleration Measurement Errors and Causes

Errors	Error Cause	Error Term
$\Delta A_1$	$L_e'$ are bias, scale factor errors (MSFC error model)	$\frac{L_e'}{P}$
$\Delta A_2$	Ramp input of $\omega_2$ (constant output axis angular acceleration during finite time interval). Negligible error.	$-\frac{I_y}{P} \dot{\omega}_2$
$\Delta A_3$	Any form of component of vehicle angular velocity along PIGA input axis (compensated for in the computer).	$\frac{H_r}{P} \omega_X$

## 2.7 ENCODER STUDIES

### 2.7.1 Background

This subsection briefly summarizes the survey of digital encoders described in Section 8 in more detail. The survey was concentrated on encoders having a resolution of 10 arc sec (17 bits) or better. Present studies indicate that this resolution is sufficient for the SAP.\* The encoder presently used on the PIGA has adequate resolution (0.05 m/sec).

Two of the encoders considered, namely the theodosyn and inductosyn, are particularly suited for SAP angle readout. Briefly, the theodosyn system consists of a complex electro-optical transducer and the associated digitizing circuits; the inductosyn is in essence a multi-pole air-core resolver.

The results of the study are tabulated in Table 2-X. The following paragraphs are applicable to this table.

### 2.7.2 Shaft Readout Devices

For the most part, Table 2-X is limited to devices whose resolution and accuracy figures meet the requirements of  $2^{17}$  bits or better. Exception to this criterion was taken only when a particular type of encoder was not commercially available with the desired range, resolution, and accuracy. In this case, the closest available resolution is given. Table 2-X is based on information obtained from the references given for Section 8 and on discussions with the manufacturers.

\* These studies will be refined in Phase 2.

Table 2-X. Shaft Angle Readout Devices

Resolution (bits)	Accuracy (arc/sec)	Output	Vendor	Trade Name	Transducer Diameter (Size (in.))	Weight (lb)	Power (w)	Type	Cost (\$)	Reliability	Remarks
18	±5	Incremental	Dynamic Research	Theodolyn	2.3 x 4	1.3 (includes electronics)	1.5 (includes electronics)	Dual-line optical interference	6,000 to 10,000	1 year (MTBF)	Microcircuits used; direction and zero-reference given. No accumulator. Beryllium housing.
18	±5	Absolute	Baldwin	-	4.6 x 9.9	36 (includes electronics)	25 (includes electronics)	Coded optical disc	8620.00 (includes electronics)	-	Discrete circuit components
19	±2.5	Incremental	Wayne George	Digisyn	2.5 x 6	6.5 (includes electronics)	25 (includes electronics)	Photo-electric cell (strobe lamp)	-	-	Discrete circuit components
13	±40	Absolute	Norden	-	3.2 x 1.75	-	1.0	Magnetic	-	-	-
12	±150	Incremental	Data Tech	Incosyn	2 x 4.5	1.1 (includes electronics)	0.9 (includes electronics)	Reluctance	-	-	-
19	±2.5	Incremental	Norden	Microsyn	5.3 x 3.5	4.5 (includes electronics)	150 (includes electronics)	Capacitive	-	-	Discrete circuits components
18	±5	Incremental	Parsons	Inductosyn	0.2 x 1	2.5 (includes electronics)	2.5 (includes electronics)	Inductance	1000.00	Electronic; 157,000 hr	Hybrid circuit components
19	±5	Absolute	Norden	-	4 x 1.75	0.8	0.4	V-brush mechanical	-	-	-
18	10	Absolute	Solvere	High accuracy resolver	1.5 x 5.4	2.3	5.0	Resolver	-	-	-

The explanatory notes given below define the headings of Table 2-X.

- Resolution. The binary exponent of the encoder single turn quantization level. A 7-bit encoder resolves  $2^7 = 128$  elements per turn (360 deg) of the input shaft.
- Accuracy. A measure of the absolute location of resolution elements on the encoder circle.
- Transducer Size. The dimensions of the transducer envelope. Most encoders have a servo type cylindrical package, and the length listed includes the input shaft.
- Weight. Weight of the transducer unit, excluding any external electronics package unless otherwise noted. (The weight of high resolution encoders electronics is typically much higher than that for the transducer.)
- Power. Input power required to operate the transducer assembly. (Power requirements of high resolution encoder electronics are typically much higher than those of the transducer.)
- Type. An indication of the type of system, i. e., optical, magnetic, or mechanical (brushes). The various approaches are outlined in Section 8.
- Cost. Since most encoders are supplied to special order, few vendors maintain standard price lists. Single unit prices are included where possible.
- Reliability. The basis for the noted MTBF (theodosyn) is not known. The reliability calculations for the inductosyn are given in Subsection 5.2, Table 5-III.

### 2.7.3 Inductosyn and Theodosyn Systems

As stated, it appears the inductosyn or theodosyn system is a suitable encoder for the SAP. The reasons for not considering other devices are summarized briefly in the following paragraphs.

Briefly, the magnetic and reluctance devices do not comply with the resolution and accuracy requirements.

The Baldwin Company's coded optical disc and the Wayne George Company's digisyn are too heavy and are not readily adaptable to the envisioned configuration of the SAP. The same is true of the Norden

Company's microgyn device. Additionally, the use of a motor and the fact that capacitive transducers are normally very susceptible to electrical noise are arguments against the choice of the microgyn.

The reliability of Norden's mechanical encoder is suspect because of its brush surface contact.

A single-speed, high-accuracy resolver is normally very sensitive to null shifts caused by thermal or mechanical environments (shock, vibration, etc.). An inductosyn has a weight advantage over a multipole resolver.

The theodosyn and the inductosyn encoding systems have certain inherent desirable characteristics. However, each system has advantages and disadvantages with respect to the other:

- (1) The mechanical simplicity of the inductosyn transducer vs the mechanical complexity of the theodosyn transducer.
- (2) The simplicity of the theodosyn digitizing circuitry vs the relative complexity of the signal processing circuits associated with the inductosyn system.

From the mechanical aspect, the inductosyn transducer is preferred. The inductosyn's mechanical advantages are even more pronounced in view of the fact that the rotor and the stator may be directly printed (in reasonably convenient sizes such as 3, 7, and 12 in. diameters) onto the moving and the stationary components of a customer's rotary device. Special tailoring of the rotor and stator sizes is also available. From the design aspect of a sophisticated rotary instrument, this mechanical simplicity is welcome. On the other hand, the theodosyn offers advantages from the viewpoint of implementing the processing circuitry.

The principal circuit advantages of the theodosyn system compared with the inductosyn system are enumerated below:

- (1) The theodosyn transducer divides one shaft revolution into 9.9 (approximately) arc-sec increments, while the inductosyn zero-crossing output occurs every degree. Hence, the inductosyn must be supplemented by electrical circuits to provide the desired digital resolution.

- (2) The theodosyn provides a quadrature signal. Hence, the directional information need not be supplied by the circuitry as it is in the case of the inductosyn system. Also, the sine-cosine relationship may be used to eliminate logical ambiguities. With the inductosyn system, the ambiguities occurring in the transition region (the end of a given degree increment and start of the successive one) must be considered in the design of the processing circuitry.
- (3) Although both circuits operate on a sinusoidal transducer signal output, the inductosyn system requires waveform tolerances much tighter than those of the theodosyn system.
- (4) Other characteristics of the two systems, such as instrument errors, small signal level output, disc ruling accuracy (theodosyn) and printing accuracy (inductosyn), are approximately equivalent.

## 2.8 ELECTRICALLY REBALANCED OUTPUT AXES SYSTEM CONSIDERATIONS

The major portion of the study was oriented towards the single-axis platform method of the strapped-down system. Section 9 was thus included in order to introduce an alternate technique of electrically rebalancing the output axis of a gyro. It includes a tutorial discussion of the fundamentals of pulse torquing, a classification of systems (see Figure 2-4), and some considerations of the electronic circuitry required for pulse torquing.

## 2.9 INSTRUMENT STUDIES

The purpose of this subsection is to present the major features and performance parameters associated with typical inertial quality gyros and accelerometers suitable for strapped-down guidance applications. While the lists are by no means exhaustive, the items described represent a reasonable cross-section of the instruments presently available.

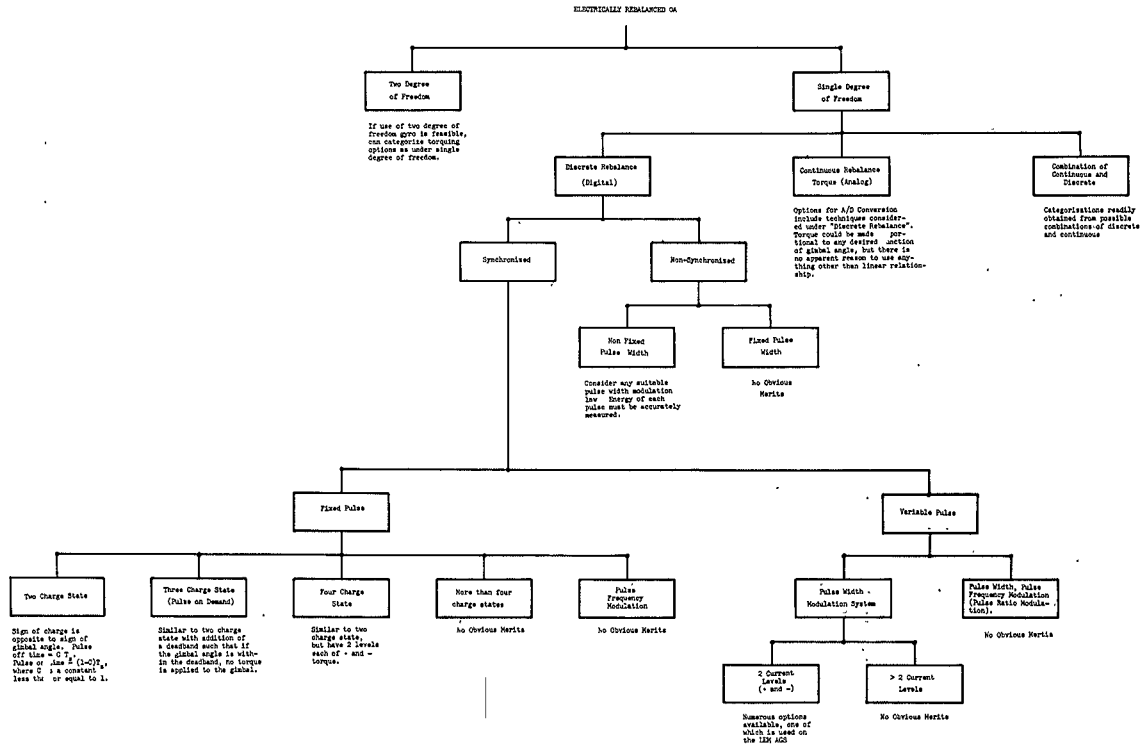


Figure 2-4. Classification of Electrically Rebalanced Output Axis Systems

The various sensors listed below are described in the CONFIDENTIAL annex appended to this report.

<u>Manufacturer</u>	<u>Model</u>
<u>Single-Degree-of-Freedom Gyros</u>	
Honeywell	GG-87
Honeywell	GG-327 (Prototype for GG334)
Kearfott	2590
Kearfott	2566
Kearfott	2542/2543
MIT	25 IRIG
NASA/Bendix	AB-5
Nortronics	GI-M1
Nortronics	GI-K7
Sperry	SYG 1000

Accelerometers

Pendulous Integrating Gyros

Honeywell	GG162/GG226
Kearfott	KAIG
MIT	16 PIGA
NASA/Bendix	AB-3

Magnetic Drag Cup Gyros

Autonetics	VM4A
------------	------

Vibrating String Gyros

Arma	D4E
------	-----

Force Balance Gyros

Bell	Mod VII
Donner	4310
Honeywell	GG177
Honeywell	GG116
Kearfott	2401

The gyro and accelerometer parameters presented in the appended tables were obtained from such sources as test reports, proposal information, and sales brochures. Much of the test data used were based on results obtained from only one or two instruments; and, in some cases, the test specimens were prototypes or early production-lot models. Hence, the results may not represent the performance of the population of instruments currently being produced. These uncertainties were accounted for as the tables were compiled, particularly in the area of performance parameters. An attempt was made to adjust the various estimates to a common level based on engineering judgment so that meaningful comparisons could be made between the various instruments.

Only single-degree-of-freedom units were included. Each of the single-degree-of-freedom gyros listed must be operated with its float near pickoff null. This can be accomplished by using a single-axis stable platform which maintains the gyro near null by means of angular position feedback. Another technique is to attach the gyro case rigidly to the vehicle and servo the float to pickoff null by means of electrically excited rebalance torques. The torque-to-balance loop may be of a pulsed or analog type. In either case, an integration of the rebalance torque current is generally required for angle readout and is usually obtained by counting the torque pulses or the output of a voltage- (torquer current) to-frequency converter, more generally an A/D converter. The characteristics of the rebalance loops are not included in the appended tables.

A variety of accelerometers considered feasible for this application has been included in the tables. The integrating types (PIGA's, velocity meter, and VSA) are body-mounted and require only servo rebalance electronics for operation. Note that the PIGA type sensors are gyroscopic devices and therefore highly sensitive to angular rate, a factor which must be considered in the system design. The force balance accelerometers require a servo loop to maintain the seismic mass at pickoff null. As with the torqued gyros, the rebalance current must be integrated either by means of counting a pulsed rebalance current or, in the analog case, by counting the frequency output of a voltage-to-frequency converter. The characteristics of these electronic assemblies have not been included in the tables in the CONFIDENTIAL annex.

### 3. PERFORMANCE ANALYSIS

A flight error analysis was made for both candidate configurations. The configuration selected for detailed study has the gyros and accelerometers strapped to the body, with each gyro having one degree of freedom about the input axis, i. e. , it is a single-axis platform. The case of the gyro is rotated through the angle required to null the component of angular velocity along the specified body axis. This angle is ideally equal and opposite to the angle through which the missile has rotated about the same axis.

Instrument performance appropriate for use on a stable platform was supplied by MSFC. When used in the strapped-down configuration, additional errors occurred as a result of body angular rates. The magnitudes of these terms are derived in Section 7. Error terms resulting from alignment and computer errors are derived in Section 5. Additional environmental effects from temperature and pressure perturbations are included here. The computational errors are small with respect to the hardware errors.

The trajectory used was generated from an existing TRW Saturn-Centaur (Voyager injection trajectory) by eliminating the parking orbit and terminating the Centaur second burn at the same inertial velocity as the reference trajectory supplied by MSFC. Subsection 3.1 defines this trajectory. A comparison of the trajectories showed that the TRW trajectory could adequately be substituted for the reference trajectory supplied by MSFC.

Two different orientations of the pitch and yaw gyro SAP output axes were considered, with one orientation of the roll gyro and the accelerometers studied. The total error model, which included the pitch and yaw gyro orientations leading to the smallest errors, gives a  $3\sigma$  velocity of 3.0 m/sec.

Subsections 3.2 and 3.3 present the error model and performance results for the selected and alternate system, respectively.

### 3.1 TRAJECTORY DEFINITIONS

MSFC supplied a reference trajectory to be used for the error analysis of the body fixed 3-axis reference system. A study of this trajectory shows that the reference trajectory was made in the following way:

- (1) A three dimensional simulation of the Saturn booster with a full engine model (not given explicitly),
- (2) A two dimensional pitch plane simulation using a calculus of variation techniques for both the Saturn S-IB and the Centaur (no lift considered), and
- (3) A circular orbit between the Centaur burns, but time in parking orbit equal to zero.

The coordinate system used is an Earth Centered Inertial (ECI) system with X along the azimuth, Y parallel to astronomic vertical at the launch site and passing through the center of the earth, and Z to complete an orthogonal triad.

To make direct use of the trajectory supplied would require copying of position, velocity, and acceleration components at each time point, transferring these data to punched cards, and coding a special program to convert the card data to the proper tape format used by the error analysis program. This would ignore the small difference between the ECI-plumb line system used by MSFC and the ECI-Greenwich or Vernal Equinox oriented system used by TRW.

The fastest and most economical way to make a trajectory similar to the MSFC reference trajectory, for use with the error analysis program, was to modify the Saturn-Centaur trajectory in existence at TRW for 25 June 1971 with a 7-min parking orbit, eliminating the coast and terminating the second Centaur burn at the same inertial velocity as the reference trajectory.

Figures 3-1 through 3-4 show how the TRW trajectory compares to the MSFC reference trajectory. Figure 3-1 is a plot of the inertial velocity as a function of time. Figure 3-2 shows the altitudes. Figure 3-3 is a plot of the flight path angles. The flight path angle as plotted is the complement of THETD given in the MSFC trajectory. Figure 3-4 shows the

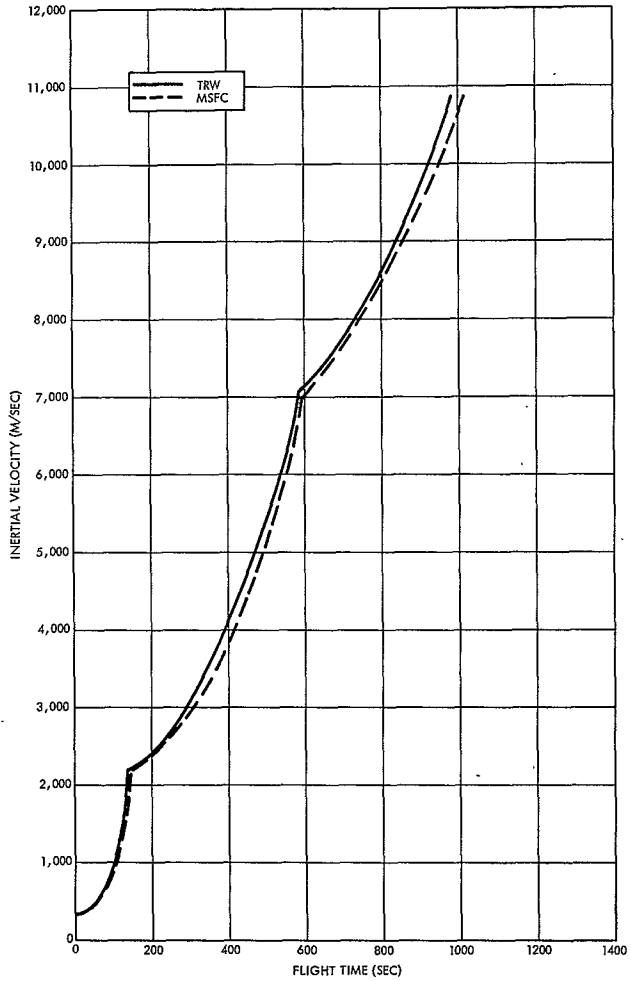


Figure 3-1. Inertial Velocity as a Function of Flight Time

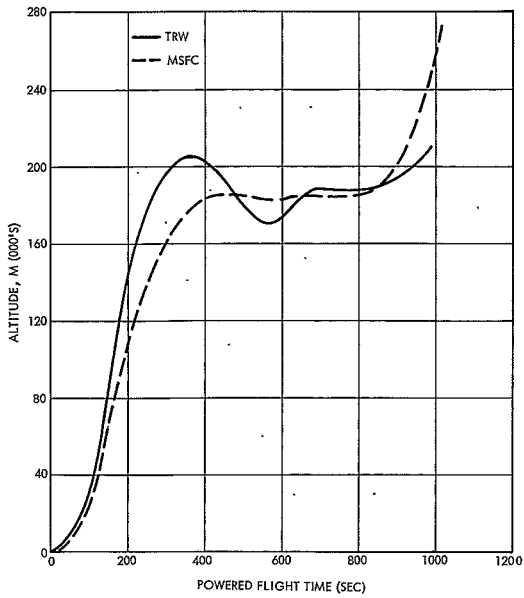


Figure 3-2. Altitude as a Function of Flight Time

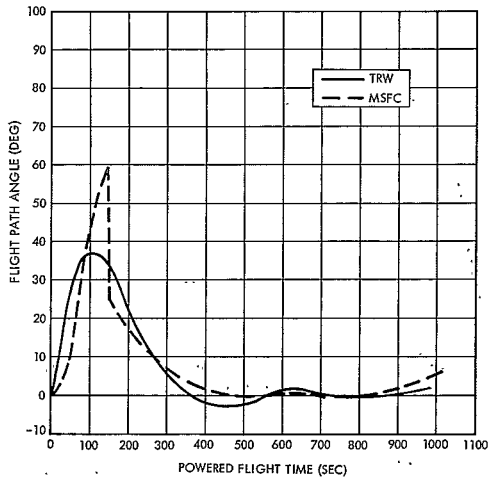


Figure 3-3. Flight Path Angle as a Function of Flight Time

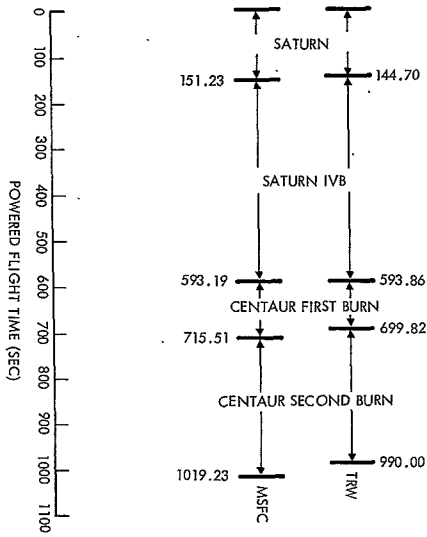


Figure 3-4. Comparison of Cutoff Times of Various Stages of Powered Flight

relative cutoff times of the various stages. This trajectory was accepted by MSFC for error analysis purposes.

### 3.2 SELECTED SYSTEM PERFORMANCE

#### 3.2.1 Error Model

The general system model is composed of instrument errors, equation errors, and computational truncation and roundoff errors. The equations and computer requirements were established to make most of these "software" errors negligible with respect to the "hardware" errors. Of these "software" errors, only the drift and alignment errors are large enough to require inclusion in the following discussion (see Section 5).

This section also presents the mathematical forms of the error model equations of the Strapped-down Inertial Reference Assembly (SIRA). These

equations constitute some modifications of the AB-5 gyro and AB-3 PIGA equations which reflect the strapped-down mode. The system model is completed by additional equations representing instrument misalignments.

### 3.2.2 SIRA Errors

Reference 7.4a gives the models used for the gyros and the accelerometers in the stable platform mode. These models are presented first.

#### 3.2.2.1 Stable Platform Mode

The AB-5 stabilization gyro coordinates of Reference 7.4a are as follows:

Using the coordinate system shown in Figure 3-5, the drift of each gyro is given by the equation:

$$\epsilon_p = C + M_{ep} a_o + M_{ubs} a_i + M_{ubi} a_s + E_o a_s a_i \quad (1)$$

where

C is the constant drift.

$M_{ep}$  is a coefficient which linearly relates a component of gyro drift to acceleration along the gyro output axis. This effect is caused by variations in turbine torques which result from acceleration induced loads acting on the output axis thrust pads.

$M_{ubs}$  is the mass unbalance along the spin reference axis.

$M_{ubi}$  is the mass unbalance along the input axis.

$E_o$  is the anisoelastic coefficient

$a_{o,s,i}$  are the sensed accelerations along the given axes.

o, s, i are output, spin, and input axes.

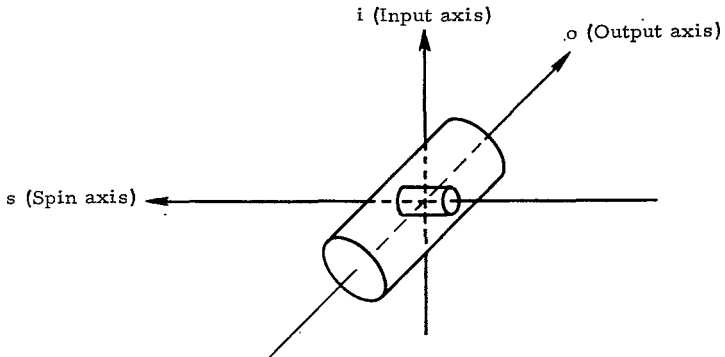


Figure 3-5. Gyro Model Coordinate

The equation which characterizes the AB3 PIGA is as follows:

$$\begin{aligned}
 a_m &= a_i + Aa_i + B + C_T(45 - \theta) + D(15 - p) + Ea_S \\
 &= (1 + A)a_i + [B + C_T(45 - \theta) + D(15 - p)] + Ea_S \\
 &= (1 + A)a_i + B' + Ea_S = a_i + \Delta a_i
 \end{aligned}
 \tag{2}$$

where

$a_m$  is instrument measured acceleration in g units

$a_i$  is actual acceleration along trunnion axis in g units

$$g = 9.79426 \text{ m/sec}^2$$

A is scale factor error coefficient

B is bias error

B' is bias error which includes effect of constant temperature and gas pressure

$C_T$  is temperature sensitivity coefficient

$\theta$  is temperature in degrees Centigrade (nominal 45°C)

D is gas pressure sensitivity coefficient

p is gas pressure in lb/in. (nominal 15 lb/in. <sup>2</sup>)

E is cross-coupling coefficient

$a_S$  is acceleration in g units along the accelerometer's gyro wheel spin axis.

In assembling the complete error model, all of the terms of Eq (1) are included except the anisoelastic term. Experience indicates that the effects of this term will be small.

Examination of Eq (2) for the indicated acceleration shows that when particular values of temperature and gas pressure are substituted in the appropriate terms, these terms become additional accelerometer biases and thus were not mechanized separately in the error model. For the particular values of  $\theta$  and  $p$ , the bias error coefficients are raised to account for temperature and pressure effects (see Paragraph 3.2.2.3). Because the spin reference axis is constantly rotating about the input axis and has an average value of angular position equal to zero, the accelerometer error term proportional to acceleration along the FIGA's gyro wheel spin axis can be neglected.

To make the error model complete, certain additional terms were added. Six terms which represent the nonorthogonality of the three accelerometers labeled  $X_b$ ,  $Y_b$ , and  $Z_b$  are included. The misalignments toward the pitch ( $Y_b$ ) axis of the yaw ( $Z_b$ ) and roll ( $X_b$ ) gyro input axes are also included.

### 3.2.2.2 Angular Rate Environment Sensitive Terms

Equations representing an AB-5 gyro mechanized as a SAP are presented in Section 7. Tabulated there are drift errors  $\epsilon_1$  through  $\epsilon_9$  attributed to the strapped-down mode. SAP error term  $\epsilon_1$  is equivalent to the conventional error terms of Eq (2). The drift rate resulting from  $\epsilon_2$  is negligible for this trajectory.

The remaining seven SAP error sources, resulting from environmental vibrational conditions, are combined with the constant drift term,  $C$ , by the RSS method (temperature and pressure induced error effects are similarly combined with the constant drift term,  $C$ ).

In summary, the portion of the SIRA error model that is attributed to a given SAP is Eq (3) and any axis misalignments:

$$\epsilon_p = C_{RSS} + M_{ep} a_o + M_{ubi} a_s + E_{o1} a_s + M_{ubs} a_I^* \quad (3)$$

---

\* Note that the accelerations  $a_I$  and  $a_s$  in Eq (3) refer to vehicle acceleration components resolved through a SAP rotation angle.

Eq (2) characterizes an AB-3 PIGA mounted on a non-rotating base. The equations for a body-mounted PIGA are shown in Section 7 ( $\Delta A_1$ ,  $\Delta A_2$ ,  $\Delta A_3$ ) where  $\Delta A_1$  is the error for the stable platform mode.

Error term  $\Delta A_2$  is analogous to drift rate term  $\epsilon_2$  and is likewise negligible for the reference trajectory. The third term,  $\Delta A_3$ , represents PIGA sensitivity to angular motion of the vehicle about the SAP input axis. This term is significant and is therefore compensated for in the computer.

### 3.2.2.3 Numerical Coefficients for Error Model\*

#### 3.2.3 Instrument Orientation

The orientation of the gyros and accelerometers is shown in Figure 3-7, where the input axes of the accelerometers make equal angles with the nominal thrusting direction ( $x_b$ ). The magnitude of the angle is  $\cos^{-1}(1/\sqrt{3})$  or 54.7355 deg.

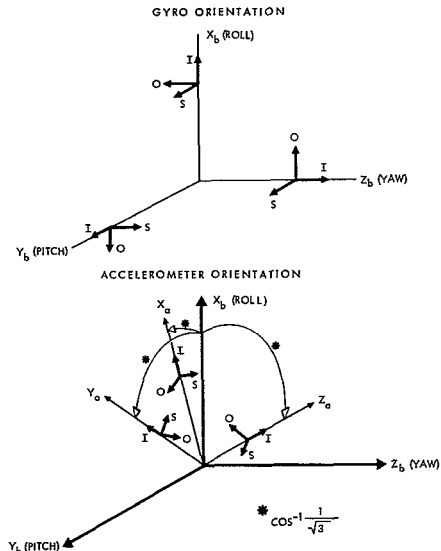


Figure 3-7. Instrument Orientation

\* This paragraph is in the Confidential Annex, "Annex of Error and Characteristics Tabulations (U)", TRW Document No. 4499-7200.13-001, and includes Eqs (4), (5), (6), (7), (8), (8a), (9), (10), and (11); Figure 3-6; and Table 3-I.

The advantage of the orientation is that it will tend to minimize the effect of accelerometer scale factor error on downrange velocity errors. It also reduces (on each axis) the maximum sensed acceleration by  $(1/\sqrt{3})$  and insures that each accelerometer will always sense a net positive acceleration. For the AB-3 FIGA the fact that the input axis acceleration is always a large positive value removes the problem of the threshold acceleration for alignment and insures that the error term proportional to spin axis acceleration has zero mean (because of the rotation of the FIGA about its input axis) and hence contributes negligible error during alignment and powered flight.

No study was made to determine whether the accelerometer orientation used was optimal.

It would be possible to initially orient the output axes of the pitch and yaw gyros such that the acceleration sensitive errors are minimized; however, there would be a serious penalty in added system complexity if this were done. To provide some indication of possible performance gains, two orientations of the gyro output axes were considered. The orientations relative to the body axes at launch are shown in Figure 3-8.

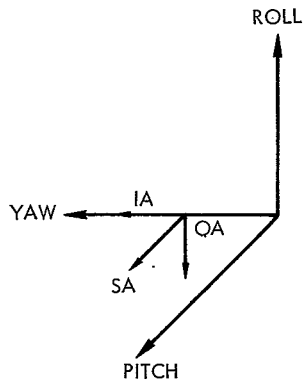
Because the reference trajectory has no yaw maneuvers, there is no rotation of the case of the yaw gyro about its input axis, and the initial gyro axis orientation relative to the body axes is maintained throughout the flight.

The orientation which leads to the smallest pitch or yaw gyro errors depends on the relative magnitude of the scales associated with the gyro input axis mass unbalance term and the term proportional to the acceleration along the gyro output axis.

Two orientations of the pitch gyro are also considered. Figure 3-9 shows the orientations of the pitch gyro at launch. Because the case of the pitch gyro rotates about the input axis of the gyro as the body rotates about the pitch axis, the output and spin reference axes do not retain the orientation relative to the body axes shown in Figure 3-9 throughout the flight (see Reference 7.10).

(a) YAW GYRO AT LAUNCH

- IA: YAW
- OA: -ROLL
- SA: PITCH



(b) YAW GYRO AT LAUNCH

- IA: YAW
- OA: PITCH
- SA: ROLL

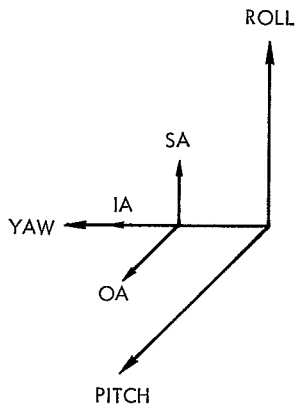


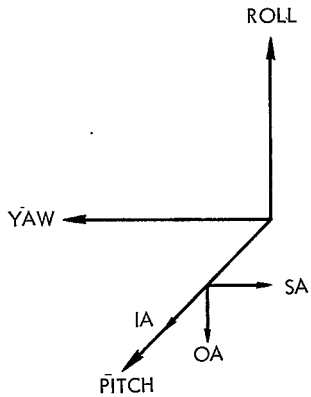
Figure 3-8. Two Orientations of Yaw Gyro at Launch

(a) PITCH GYRO AT LAUNCH

IA: PITCH

OA: -ROLL

SA: -YAW



(b) PITCH GYRO AT LAUNCH

IA: PITCH

OA: -YAW

SA: ROLL

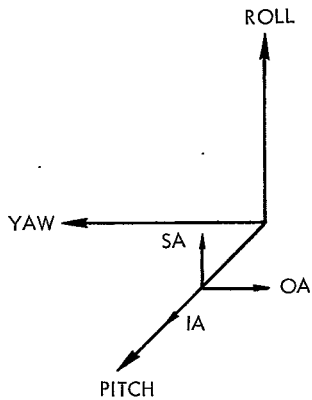


Figure 3-9. Two Orientations of Pitch Gyro at Launch

Table 3-II gives a comparison of the error terms which arise for the two different orientations of the yaw gyro. Here, because all of the thrust is along the body roll axis and the orientation of the gyro axes relative to the body axes does not change during flight, a different error term will dominate for each of the two different orientations.

The results are presented in the LV coordinate system,  $\bar{P}$ ,  $\bar{R}$ ,  $\bar{N}$ .

The LV coordinate system is established at each trajectory point by taking  $\bar{R}$  along the instantaneous radius vector from the center of the earth to the vehicle.  $\bar{N}$  is defined by

$$\bar{N} = \frac{\bar{V} \times \bar{R}}{|\bar{V} \times \bar{R}|}$$

where  $\bar{V}$  is the velocity vector, and

$$\bar{P} = \bar{R} \times \bar{N}$$

to complete the right handed system  $\bar{P}$ ,  $\bar{R}$ ,  $\bar{N}$ .

Table 3-II. Comparison of Injection Errors (LV)  
for Two Yaw Gyro Orientations \*\*

Yaw Gyro Orientation	Error Term	$\Delta P$ (ft)	$\Delta R$ (ft)	$\Delta N$ (ft)	$\Delta VP$ (ft/sec)	$\Delta VR$ (ft/sec)	$\Delta VN$ (ft/sec)												
*"a"	Output axis acceleration term	3 (1m)	2 (1m)	547 (167m)	-	-	1.0 (0.3 m/sec)												
*"b"	Input axis mass unbalance	7 (2m)	7 (2m)	1370 (418m)	-	-	2.8 (0.9 m/sec)												
<p>* Orientation of Gyro Axis Relative to Body Axes</p> <table style="margin-left: 100px;"> <tr> <td></td> <td style="text-align: center;"><u>"a"</u></td> <td style="text-align: center;"><u>"b"</u></td> </tr> <tr> <td>IA Input Axis</td> <td style="text-align: center;">Yaw</td> <td style="text-align: center;">Yaw</td> </tr> <tr> <td>OA Output Axis</td> <td style="text-align: center;">-Roll</td> <td style="text-align: center;">Pitch</td> </tr> <tr> <td>SA Spin Axis</td> <td style="text-align: center;">Pitch</td> <td style="text-align: center;">Roll</td> </tr> </table>									<u>"a"</u>	<u>"b"</u>	IA Input Axis	Yaw	Yaw	OA Output Axis	-Roll	Pitch	SA Spin Axis	Pitch	Roll
	<u>"a"</u>	<u>"b"</u>																	
IA Input Axis	Yaw	Yaw																	
OA Output Axis	-Roll	Pitch																	
SA Spin Axis	Pitch	Roll																	
<p>** Metric equivalent of the injection errors are shown in parentheses.</p>																			

For the particular scale values, orientation "a" leads to the position and velocity errors with smaller magnitudes. In the error analysis, orientation "a" was used, which has the yaw gyro output axis along the negative of the body roll axis and the spin axis along the body pitch axis.

Table 3-III compares the velocity and position errors in the Local Vertical (LV) coordinate system which arise for the two different orientations of the pitch gyro.

Examination of Table 3-III shows that, for the scale values used, slightly smaller injection errors arise for orientation "a" of the pitch gyro which has the output axis along the negative of the body roll axis and the spin axis along the negative of the body yaw axis. In the error analysis orientation "a" of the pitch gyro was used.

Table 3-III. Comparison of Injection Errors (LV) for Two Pitch Gyro Orientations\*\*

Pitch Gyro Orientation	Error Term	$\Delta P$ (ft)	$\Delta R$ (ft)	$\Delta N$ (ft)	$\Delta VP$ (ft/sec)	$\Delta VR$ (ft/sec)	$\Delta VN$ (ft/sec)
* <sub>a</sub>	Drift	1116 (340 m)	1104 (336 m)	8 (2 m)	1.7 (0.5 m/sec)	4.6 (1.4 m/sec)	-
	Spin axis mass unbalance	-	-	-	-	-	-
	Input axis mass unbalance	904 (276 m)	643 (196 m)	5 (2 m)	1.2 (0.4 m/sec)	2.1 (0.6 m/sec)	-
	Output axis acceleration term	365 (111 m)	391 (119 m)	2 (1 m)	0.5 (0.2 m/sec)	1.6 (0.5 m/sec)	-
	Aniselaastic term	-	-	-	-	-	-
	RSS	1482 (452 m)	1336 (407 m)	10 (3 m)	2.1 (0.7 m/sec)	5.3 (1.6 m/sec)	-
* <sub>b</sub>	Drift	1116 (340 m)	1104 (336 m)	8 (2 m)	1.7 (0.5 m/sec)	4.6 (1.4 m/sec)	-
	Spin axis mass unbalance	-	-	-	-	-	-
	Input axis mass unbalance	915 (279 m)	980 (299 m)	5 (2 m)	1.4 (0.4 m/sec)	4.0 (1.2 m/sec)	-
	Output axis acceleration term	360 (110 m)	250 (76 m)	2 (1 m)	0.5 (0.2 m/sec)	0.9 (0.3 m/sec)	-
	Aniselaastic term	-	-	-	-	-	-
	RSS	1487 (453 m)	1497 (456 m)	10 (3 m)	2.1 (0.7 m/sec)	6.2 (1.9 m/sec)	-
* Orientation of Gyro Axis Relative to Body Axes				"a" Pitch -Roll -Yaw	"b" Pitch -Yaw Roll		
** Metric equivalents of the injection errors are shown in parenthesis.							

### 3.2.4 Results

The error model with the  $3\sigma$  scale values of Table 3-I was used in TRW's generalized error analysis program. The resulting position and velocity errors are output in a number of coordinate systems.

The resulting injection errors are shown in Table 3-IV\*.

The injection errors are:

Position ( $3\sigma$ error)	1257m (4125 ft)
Velocity ( $3\sigma$ error)	3.0 m/sec (9.9 ft/sec)

The dominant in-plane error sources, both in position and velocity, are the initial alignment error of inertial reference frame about pitch and the pitch gyro drift rates.

The dominant out-of-plane error sources, both in position and velocity are the initial misalignment of the inertial reference about roll (azimuth) and the roll gyro fixed digit spin axis mass unbalance terms. Accelerometer error source contribution to the total navigation error is small.

The analysis indicates that the initial misalignments of the inertial reference frame about the roll (azimuth) and pitch (level) are important error contributions to the system's navigational capability. The estimates were based on a limited simulation of the alignment loops. Therefore, it is necessary to assess the alignment error sources more precisely and expand the analysis of the alignment loops in Phase 2 of the study.

---

\* Table 3-IV is in the Confidential Annex, "Annex of Error and Characteristics Tabulations (U)", TRW Document No. 4499-7200.13-001.

### 3.3 ALTERNATE SYSTEM

#### 3.3.1 Error Model

Performance of a modified inertial sensor assembly of the LEM Abort Guidance Section (AGS) on the reference trajectory is summarized in Table 3-V. The error source three  $\sigma$  magnitudes were computed from the sensor assembly design central specification.\* These error magnitudes apply to a worst-case system; the magnitude for a radian system should be lower. TRW Systems believes that these numbers are a conservative estimate of the capability of a strapped-down system which uses an SDF rate integrating gyro with continuous pulse rebalancing of the output axis. The budgeted error magnitudes were adjusted to reflect an accelerometer range of 0-10 g and a gyro range of 0-10 deg/sec. The budgeted values were also modified to reflect an on-vehicle updating of X accelerometer bias and X, Y, and Z gyro bias. The updating is automatic and was assumed to occur within 1/2 hr of launch. With the sensor assembly rigidly mounted to the vehicle, it is not possible to separate X accelerometer bias shifts from X scale factor shifts; likewise, X gyro bias shifts cannot be separated from X spin axis unbalance shifts. As a result, when updating is used, correlated errors are induced. This correlation effect is shown in the example below and has been included in the error model for the X accelerometer and X gyro.

Let  $a_o$  = accelerometer output in a +1 g field at the time of calibration and  $a_o'$  = accelerometer output at the time of updating. Then

$$a_o = K_o + K_1 \text{ measured in g units}$$

and

$$a_o' = K_o + \delta K_o + K_1 + \delta K_1$$

where  $K_o$  and  $K_1$  are the bias and scale factor, respectively, and the  $\delta$  terms represent the shifts in these parameters between calibration and updating.

---

\* Contributions from the computer to be used with the SIRA will be negligible when combined in an RSS manner with these numbers. These specifications include effects of vehicle dynamic environment.

Table 3-V. Summary of Performance Analysis, Typical Electrically Rebalanced Output Axis System

Error Source	Error Magnitude (3 $\sigma$ )	Position Error (ft)			Velocity Error (ft/sec)		
		$\Delta P$	$\Delta R$	$\Delta N$	$\Delta V_H$	$\Delta V_R$	$\Delta V_N$
<b>Accelerometer Chamber Errors</b>							
<b>Bias</b>							
X Accel	80 $\mu$ g	290	1020	--	1.0	2.2	--
Y Accel	80 $\mu$ g	--	--	1090	--	--	1.9
Z Accel	80 $\mu$ g	930	610	--	1.3	2.2	--
<b>Bias Correlated with Inertial Reference Alignment</b>							
Y Axis	190 $\mu$ g	--	--	1290	--	--	5.1
Z Axis	190 $\mu$ g	1100	100	--	1.1	0.8	--
<b>Rectification Error</b>							
X Accel	105 $\mu$ g	540	2070	--	1.8	3.9	--
Y Accel	150 $\mu$ g	--	--	2070	--	--	3.6
Z Accel	150 $\mu$ g	1740	1140	--	2.1	-3.9	--
<b>Bias Correlated with Scale Factor</b>							
X Accel	190 $\mu$ g/g	330	-1470	--	0.3	-2.8	--
<b>Scale Factor</b>							
X Accel	105 $\mu$ g/g	180	2250	--	1.2	4.5	--
<b>Nonlinearity</b>							
X Accel	90 $\mu$ g/g	150	1950	--	0.9	3.9	--
<b>Gyro Channel Errors</b>							
<b>Bias</b>							
X Gyro	0.16 deg/hr	--	--	1870	--	--	7.0
Y Gyro	0.16 deg/hr	3490	-3490	--	5.1	-13.9	--
Z Gyro	0.16 deg/hr	--	--	3900	--	--	8.0
<b>Spin Axis Mass Unbalance</b>							
X Gyro	0.12 deg/hr/g	--	--	2490	--	--	8.4
<b>Bias Correlated with Spin Axis Unbalance</b>							
X Gyro	0.60 deg/hr	--	--	5400	--	--	14.0
<b>Vibration Induced Drift Rate</b>							
X Gyro	0.06 deg/hr	--	--	690	--	--	2.7
Y Gyro	0.06 deg/hr	1380	1380	--	1.8	-5.1	--
Z Gyro	0.06 deg/hr	--	--	1290	--	--	3.0
<b>Scale Factor</b>							
Y Gyro	180 X 10 <sup>-6</sup> deg/deg	360	-450	--	0.3	-2.1	--
<b>Nonlinearity</b>							
Y Gyro	90 X 10 <sup>-6</sup> deg/deg	180	-210	--	0.3	-1.2	--
<b>Gyro Alignment</b>							
X Gyro to Y Accel	60 arc sec	--	--	150	--	--	2.1
<b>Inertial Reference Alignment</b>							
Azimuth	60 arc sec	--	--	4290	--	--	7.2
	RSS	4460	5710	8900	6.6	17.6	22.5
<b>RSS of <math>\Delta</math>Pos, <math>\Delta</math>Vel</b>		11,476 ft			29.3 ft/sec		
		3,498 m			8.9 m/sec		

At the time of updating, assume that some fraction  $(1/C)$  of the change in output  $(a'_0 - a_0)$  is due to bias and the remainder is due to scale factor. Therefore it is assumed  $\delta K_0 = 1/C (a'_0 - a_0)$  and  $\delta K_1 = (C-1)/C (a'_0 - a_0)$  where  $C$  is a constant. Based on these assumptions, new bias and scale factor terms are calculated for insertion in the guidance computer. The terms calculated are given by Eqs (12) and (13):

$$\begin{aligned}
 K_0 \text{ calculated} &= K_0 + \text{assumed } \delta K_0 \\
 &= K_0 + \frac{1}{C} (a'_0 - a_0) \\
 &= K_0 + \frac{\delta K_0 + \delta K_1}{C}
 \end{aligned} \tag{12}$$

and likewise  $K_1$  calculated =  $K_1 + \text{assumed } \delta K_1$

$$= K_1 + \frac{(\delta K_0 + \delta K_1) (C - 1)}{C} \tag{13}$$

The correct terms, however, are  $K_0 + \delta K_0$  and  $K_1 + \delta K_1$ . The errors after updating are therefore given by Eqs (14) and (15):

$$\begin{aligned}
 \text{Bias error} &= \epsilon K_0 = (K_0 + \delta K_0) - (K_0 \text{ calculated}) \\
 &= \left[ \frac{\delta K_0 (C - 1) - \delta K_1}{C} \right]
 \end{aligned} \tag{14}$$

$$\begin{aligned}
 \text{Scale factor error} &= \epsilon K_1 = (K_1 + \delta K_1) - (K_1 \text{ calculated}) \\
 &= - \left[ \frac{\delta K_0 (C - 1) - \delta K_1}{C} \right]
 \end{aligned} \tag{15}$$

Note that  $\epsilon K_0 = -\epsilon K_1$ . The errors after updating are correlated 1:1 and of opposite sign. In a similar manner, it can be shown that updating the X gyro results in correlation of the gyro bias and spin axis unbalance error terms. The gyro updating is made with the assumption that all the changes will be in the fixed drift term. The accelerometer updating is made with the assumption that all the changes will be in the scale factor term.

### 3.3.2 Instrument Orientation

The gyro and accelerometer input axes are oriented in the same direction in the unit being considered. The orientation of the unit would be such that these axes correspond to the gyro input axes of Paragraph 3.2.3. The output axes of the gyros whose input axis is normal to the thrust vector are oriented to make mass unbalance effects negligible.

## 4. KINEMATICAL REPRESENTATIONS

The treatment of kinematical representations is organized in three subsections. Subsection 4.1 is devoted to a description of the kinematical representations selected for study and the equations for each representation are explicitly given. Subsection 4.2 presents the second-order Taylor's series expansions of the Euler symmetrical parameters and the four gimbal Euler angle system. (The Taylor's series expansion for the direction cosines is given in Section 5.) Finally, Subsection 4.3 delineates the results of the computer sizing studies for the selected representations. A summary of the entire section is given in Subsection 2.3.

### 4.1 DESCRIPTION OF THE KINEMATICAL REPRESENTATIONS

#### 4.1.1 Direction Cosines

Eq (1) describes the transformation of vector components in vehicle coordinates  $X_b$ ,  $Y_b$ ,  $Z_b$  to vector components in inertial coordinates  $X_I$ ,  $Y_I$ ,  $Z_I$  in terms of the direction cosines. (In the interest of simplicity, the matrices of Eq (1) will be abbreviated as  $[X_b] = [a_{ij}] [X_I]$  from time to time.)

$$\begin{bmatrix} X_b \\ Y_b \\ Z_b \end{bmatrix} = \begin{bmatrix} a_{11} & a_{12} & a_{13} \\ a_{21} & a_{22} & a_{23} \\ a_{31} & a_{32} & a_{33} \end{bmatrix} \begin{bmatrix} X_I \\ Y_I \\ Z_I \end{bmatrix} \quad (1)$$

The directions cosine rates ( $da_{ij}/dt$ ) are a function of body rates, expressed by Eq (2).

$$\dot{a}_{ij} = a_{(i+1)j} \omega_{i+2} - a_{(i+2)j} \omega_{i+1} \quad (2)$$

where

$$i, j = 1, 2, 3$$

and

$$(i + 3) \equiv i$$

$$(i + 4) \equiv i + 1$$

$$(i + 5) \equiv i + 2$$

$\omega_i$ ,  $i = 1, 2, 3 \equiv$  angular rates about the indicated body axes.

The above equations are shorthand notations for nine equations representing the nine direction cosine rates as a function of the nine direction cosines and the three body rates. For example,

$$\dot{a}_{23} = a_{(2+1)3} \omega_{(2+2)} - a_{(2+2)3} \omega_{(1+2)} = a_{33} \omega_1 - a_{13} \omega_3$$

It can be demonstrated (for example, by Reference 4.2) that three independent coordinates are necessary and sufficient to describe the attitude of a rigid body. Thus the nine direction cosines are not independent.

Constraint equations that indicate the specific dependencies of the direction cosines are the cofactor relationships (Eq 3) and the ortho-normality constraints of (Eq 4):

$$a_{ij} = a_{i+1, j+1} a_{i+2, j+2} - a_{i+1, j+2} a_{i+2, j+1} \quad (3)$$

where the subscripts are handled as above.

$$\sum_{i=1}^3 a_{ij} a_{ik} = \delta_{jk} \quad \text{for } j, k = 1, 2, 3 \quad (4)$$

where

$$\delta_{jk} = 1 \quad \text{for } j = k$$

$$\delta_{jk} = 0 \quad \text{for } j \neq k$$

#### 4.1.2 Euler Symmetrical Parameters and Rodriguez Parameters

Euler's symmetrical parameters are defined in various places, including Reference 4.3. An Italian document (Reference 4.6) defines an equivalent set of parameters. (Only the notations in this set called "Rodriguez" parameters differ.) The former terminology will be used in this report.

Whittaker derives Euler's symmetrical parameters from geometrical considerations (Reference 4.1). The equations presented here and the approach used have been obtained from Mortensen's report, Reference 4.3.

Let  $\xi$ ,  $\eta$ ,  $\zeta$ , and  $\chi$  be the four Euler symmetrical parameters. Let  $\hat{e} = e_x \hat{i} + e_y \hat{j} + e_z \hat{k}$  be an eigenvector of the direction cosine matrix of Eq (1), specifically, a unit magnitude eigenvector associated with the eigenvalue +1. Then the following equations hold:

$$\begin{aligned}\xi &= e_x \sin \frac{\phi}{2} \\ \eta &= e_y \sin \frac{\phi}{2} \\ \zeta &= e_z \sin \frac{\phi}{2}\end{aligned}\tag{5}$$

where  $\phi$  and  $\hat{e}$  are defined as follows: Euler's theorem (Reference 4.2) states that the general displacement of a rigid body having one point fixed is a rotation about some axis;  $\hat{e}$  defines that axis and  $\phi$  represents the magnitude of the rotation.

The fourth parameter,  $\chi$ , can be determined from the constraint equation

$$\xi^2 + \eta^2 + \zeta^2 + \chi^2 = 1\tag{6}$$

This equation combined with Eq (5) produces the identity

$$\chi = \cos \frac{\phi}{2}\tag{7}$$

The equations relating parameter rates to body rates are

$$\begin{bmatrix} \dot{\xi} \\ \dot{\eta} \\ \dot{\zeta} \\ \dot{\chi} \end{bmatrix} = \frac{1}{2} \begin{bmatrix} \chi & -\zeta & \eta \\ \zeta & \chi & -\xi \\ -\eta & \xi & \chi \\ -\xi & -\eta & -\zeta \end{bmatrix} \begin{bmatrix} \omega_1 \\ \omega_2 \\ \omega_3 \end{bmatrix}\tag{8}$$

where  $\omega_i$ ,  $i = 1, 2, 3 \equiv$  angular rates about the indicated body axes. Once the Euler symmetrical parameters are found, they must be related to direction cosines:

$$\begin{aligned}
 a_{11} &= \xi^2 - \eta^2 - \zeta^2 + \chi^2 \\
 a_{12} &= 2(\xi\eta + \zeta\chi) \\
 a_{13} &= 2(\xi\zeta - \eta\chi) \\
 a_{21} &= 2(\xi\eta - \zeta\chi) \\
 a_{22} &= -\xi^2 + \eta^2 - \zeta^2 + \chi^2 \\
 a_{23} &= 2(\eta\zeta + \xi\chi) \\
 a_{31} &= 2(\xi\zeta + \eta\chi) \\
 a_{32} &= 2(\eta\zeta - \xi\chi) \\
 a_{33} &= -\xi^2 - \eta^2 + \zeta^2 + \chi^2
 \end{aligned} \tag{9}$$

#### 4.1.3 Quaternions

The background for quaternions given in this section can also be obtained from Reference 4.3. (In addition, the reference includes a discussion of the origin, use, and properties of quaternions.)

Quaternions involve the use of hypercomplex numbers that are defined by the following rules:

$$\begin{aligned}
 \bar{I}^2 &= \bar{J}^2 = \bar{K}^2 = -1 \\
 \bar{I}\bar{J} &= -\bar{J}\bar{I} = \bar{K} \\
 \bar{J}\bar{K} &= -\bar{K}\bar{J} = \bar{I} \\
 \bar{K}\bar{I} &= -\bar{I}\bar{K} = \bar{J}
 \end{aligned}$$

The quaternion defining the orientation of the body frame relative to the inertial frame can be written in terms of Euler's symmetrical parameters as follows:

$$q_{\mathbf{r}} = \mathbf{X} + \bar{\mathbf{I}}\xi + \bar{\mathbf{J}}\eta + \bar{\mathbf{K}}\zeta \quad (10)$$

and its conjugate is defined as

$$q_{\mathbf{r}}^* = \mathbf{X} - \bar{\mathbf{I}}\xi - \bar{\mathbf{J}}\eta - \bar{\mathbf{K}}\zeta \quad (11)$$

The norm of  $q_{\mathbf{r}}$  is defined as

$$q_{\mathbf{r}} q_{\mathbf{r}}^* = q_{\mathbf{r}}^* q_{\mathbf{r}} = X^2 + \xi^2 + \eta^2 + \zeta^2 = 1 \quad (12)$$

The vector  $\bar{X}_{\mathbf{I}}$  with components  $X_{\mathbf{I}}$ ,  $Y_{\mathbf{I}}$ ,  $Z_{\mathbf{I}}$  is represented in quaternion notation as

$$q(\bar{X}_{\mathbf{I}}) = \bar{\mathbf{I}}X_{\mathbf{I}} + \bar{\mathbf{J}}Y_{\mathbf{I}} + \bar{\mathbf{K}}Z_{\mathbf{I}} \quad (13)$$

and may be rotated to body space as

$$q(\bar{X}_{\mathbf{b}}) = q_{\mathbf{r}} q(\bar{X}_{\mathbf{I}}) q_{\mathbf{r}}^* = \bar{\mathbf{I}}X_{\mathbf{b}} + \bar{\mathbf{J}}Y_{\mathbf{b}} + \bar{\mathbf{K}}Z_{\mathbf{b}} \quad (14)$$

Now the updating of the  $q_{\mathbf{r}}$  coefficients is obviously done by Eq (8), i. e., in a fashion identical to the Euler's symmetrical parameters. It is further clear that Eq (9) can be derived from the quaternion form, and hence the Euler symmetrical and quaternion kinematic representatives are equivalent for purposes of this application.

#### 4.1.4 Cayley-Klein Parameters

An excellent discussion of Cayley-Klein parameters is available in Reference 4.2, which is the source for most of the material given here.

The transformation matrix  $Q$  composed of the complex Cayley-Klein parameters,  $\alpha, \beta, \gamma, \delta$ , (Eq 15) operates upon a complex matrix operator  $P_{\mathbf{b}}$  (Eq 16) as shown in Eq (17). The complex matrix operator  $P_{\mathbf{b}}$  contains the vector  $(X_{\mathbf{b}}, Y_{\mathbf{b}}, Z_{\mathbf{b}})$  to be transformed to inertial coordinates.

$$Q = \begin{bmatrix} \alpha & \beta \\ \gamma & \delta \end{bmatrix} \quad (15)$$

$$P_b = \begin{bmatrix} z & x - iy \\ x + iy & -z \end{bmatrix} \quad (16)$$

$$[P_I] = [Q] [P_b] [Q^\dagger] \quad (17)$$

where, as usual,  $i = \sqrt{-1}$ ,  $Q^\dagger$  is the adjoint of  $Q$ , and the resulting matrix  $P_I$  contains vector expressed in inertial coordinates,  $(X_I, Y_I, Z_I)$ .

The following identities are derived in Reference 4.2:

$$\gamma = -\beta^* \quad (18)$$

$$\delta = \alpha^* \quad (19)$$

$$\alpha\alpha^* = \beta\beta^* \quad (20)$$

where

\* indicates the complex conjugate

Body rates can be related to Cayley-Klein parameter rates as follows:

$$\begin{bmatrix} \dot{\alpha} \\ \dot{\beta} \\ \dot{\gamma} \\ \dot{\delta} \end{bmatrix} = \frac{1}{2} \begin{bmatrix} i\gamma & \gamma & i\delta \\ i\delta & \delta & i\beta \\ i\alpha & -\alpha & -i\gamma \\ i\beta & -\beta & -i\delta \end{bmatrix} \begin{bmatrix} \omega_1 \\ \omega_2 \\ \omega_3 \end{bmatrix} \quad (21)$$

The parameters are transformed into the direction cosine matrix by the ensuing relations (see Reference 4.2):

$$\begin{aligned}
 a_{11} &= \frac{1}{2} (a^2 - \gamma^2 + \delta^2 - \beta^2) \\
 a_{12} &= \frac{i}{2} (\gamma^2 - a^2 + \delta^2 - \beta^2) \\
 a_{13} &= \gamma\delta - \alpha\beta \\
 a_{21} &= \frac{i}{2} (a^2 + \gamma^2 - \beta^2 - \delta^2) \\
 a_{22} &= \frac{1}{2} (a^2 + \gamma^2 + \beta^2 + \delta^2) \\
 a_{23} &= -i(\alpha\beta + \gamma\delta) \\
 a_{31} &= \beta\delta - \alpha\gamma \\
 a_{32} &= i(\alpha\gamma + \beta\delta) \\
 a_{33} &= \alpha\delta + \beta\gamma
 \end{aligned} \tag{22}$$

It can be demonstrated that the Cayley-Klein and Euler symmetrical parameters are related as defined below:

$$\begin{aligned}
 \alpha &\equiv \text{re } a + i(\text{ima}) = \chi + i\xi \\
 \beta &\equiv \text{re } \beta + i(\text{im}\beta) = \eta + i\xi \\
 \gamma &\equiv \text{re } \gamma + i(\text{im}\gamma) = -\eta + i\xi \\
 \delta &\equiv \text{re } \delta + i(\text{im}\delta) = \chi - i\xi
 \end{aligned}$$

where

re  $a$  = real part of  $a$

im  $a$  = imaginary part of  $a$

and so on.

Thus, if Eq (22) is explicitly written in terms of the real and imaginary components of the  $\alpha$ ,  $\beta$ ,  $\gamma$ , and  $\epsilon$ , then all imaginary terms disappear and Eq (9) again results. Similarly, Eq (8) can be derived from Eq (21) by the same expansion of the Cayley-Klein parameters into real and imaginary components. Therefore, Cayley-Klein parameters are also equivalent to Euler's symmetrical parameters when used in this form.

#### 4.1.5 Four Parameter Euler Angle Representation

A four parameter system can be obtained using the mathematical equivalent of a four gimbal stable platform. It is commonly referred to as a "four gimbal Euler angle" representation, and that terminology will be used here. Several mechanizations are possible, and a typical one is given here. (See Reference 4.7.) The four rotations chosen are

$$\begin{bmatrix} X_I \\ \end{bmatrix} = \begin{bmatrix} -\theta_y \\ \end{bmatrix} \begin{bmatrix} -\psi_z \\ \end{bmatrix} \begin{bmatrix} -\gamma_y \\ \end{bmatrix} \begin{bmatrix} -\phi_x \\ \end{bmatrix} \begin{bmatrix} X_b \\ \end{bmatrix} \quad (23)$$

where

$\begin{bmatrix} \theta_y \\ \end{bmatrix}$ ,  $\begin{bmatrix} \psi_z \\ \end{bmatrix}$ ,  $\begin{bmatrix} \gamma_y \\ \end{bmatrix}$ ,  $\begin{bmatrix} \phi_x \\ \end{bmatrix}$   $\equiv$  matrices defining a rotation about the subscript axis; for example:

$$\begin{bmatrix} \theta_y \\ \end{bmatrix} = \begin{bmatrix} c\theta & 0 & -s\theta \\ 0 & 1 & 0 \\ s\theta & 0 & c\theta \end{bmatrix} \quad (23a)$$

where

$s \equiv \text{sine}$

$c \equiv \text{cosine}$

$\dot{\theta}$  is commanded such that  $\gamma$  remains small. Specifically, the constraint equation below is used

$$\dot{\theta} = \gamma K \operatorname{sgn} \cos \psi = \gamma K \frac{\cos \psi}{|\cos \psi|} \quad (23b)$$

where K is a gain factor.

The equations expressing the functional Euler relationship between body rates and Euler angle rates,  $\dot{\gamma}$ ,  $\dot{\psi}$ ,  $\dot{\phi}$  and the equations required to convert them to direction cosines are given below.

$$\begin{bmatrix} \dot{\gamma} \\ \dot{\psi} \\ \dot{\phi} \end{bmatrix} = \begin{bmatrix} -\dot{\theta} c\psi \\ -\gamma \dot{\theta} s\psi \\ \dot{\psi} \phi - \dot{\theta} s\psi \end{bmatrix} + \begin{bmatrix} 0 & c\phi & -s\phi \\ 0 & s\phi & c\phi \\ 1 & 0 & 0 \end{bmatrix} \begin{bmatrix} W_x \\ W_y \\ W_z \end{bmatrix} \quad (24)$$

$$\dot{\theta} = K\gamma \operatorname{sgn}(c\psi)$$

$$a_{11} = c\theta c\psi - \gamma s\theta$$

$$a_{12} = c\theta(\gamma s\phi c\psi - c\phi s\psi) + s\theta s\phi$$

$$a_{13} = c\theta(\gamma c\phi c\psi + s\phi s\psi) + c\phi s\theta$$

$$a_{21} = s\psi$$

$$a_{22} = \gamma s\phi s\psi + c\phi c\psi$$

$$a_{23} = \gamma c\phi s\psi - s\phi c\psi$$

$$a_{31} = -c\psi s\theta - \gamma c\theta$$

$$a_{32} = -s\theta(\gamma s\phi c\psi - c\phi s\psi) + c\theta s\phi$$

$$a_{33} = -s\theta(\gamma c\phi c\psi + s\phi s\psi) + c\theta c\phi$$

These equations assume a small angle approximation is valid for  $\gamma$ .

#### 4.1.6 Three Parameter Euler Angle Representation

Three non-consecutive rotations about two or three coordinate axes are generally referred to as Euler angles and suitably define an angular orientation. These parameters are so common that they will not be repeated here. Examples can be obtained from References 4.2 and 4.4. All such systems have singularities, e. g., for certain orientations (see Reference 4.4 for example) a finite body rate requires an infinite parameter rate to maintain the reference. Thus the computer cannot maintain the reference. The situation is directly analogous to gimbal lock in a three gimbal inertial platform.

#### 4.1.7 Rodriguez-Cayley, Gibbs Vector, and Vector Presentations

Equivalent three parameter representatives with notational changes only are variously labeled Rodriguez-Cayley, Gibbs Vector, and Vector presentations (References 4.4 and 4.5). The term Gibbs vector will be used for the immediate discussion.

Gibbs vector parameters are related to the Euler symmetrical parameters  $\xi$ ,  $\eta$ ,  $\zeta$ , and  $\chi$ , and  $\hat{e}$  and  $\Phi$  by the equations below.

$$A = \frac{\xi}{\chi} = e_x \tan \frac{\Phi}{2} \quad (25)$$

$$B = \frac{\eta}{\chi} = e_y \tan \frac{\Phi}{2} \quad (26)$$

$$C = \frac{\zeta}{\chi} = e_z \tan \frac{\Phi}{2} \quad (27)$$

$$\mu = 1 + \alpha^2 + \beta^2 + \gamma^2 = \frac{1}{\chi^2} = \sec^2 \frac{\Phi}{2} \quad (28)$$

where

A, B, C  $\equiv$  Rodriguez-Cayley parameters

$\xi$ ,  $\eta$ ,  $\zeta$ ,  $\chi$   $\equiv$  Euler symmetrical parameters

$\phi$ ,  $e_x$ ,  $e_y$ ,  $e_z$  are as previously defined.

The singularities of the above system are evident.

Then the parameters related to body rates are as follows  
(Reference 4.8):

$$\begin{bmatrix} \dot{A} \\ \dot{B} \\ \dot{C} \end{bmatrix} = \frac{1}{2\chi^2} \begin{bmatrix} \chi^2 + \xi^2 & \eta\xi - \chi\xi & \xi\xi + \chi\eta \\ \xi\eta + \chi\xi & \chi^2 + \eta^2 & \eta\xi - \chi\xi \\ \xi\xi - \chi\eta & \eta\xi + \chi\xi & \chi^2 + \xi^2 \end{bmatrix} \begin{bmatrix} \omega^1 \\ \omega^2 \\ \omega^3 \end{bmatrix} \quad (29)$$

and from the same source the direction cosine relationships are

$$[a_{ij}] = \frac{1}{1+A^2+B^2+C^2} \begin{bmatrix} 1 + A^2 - B^2 - C^2 & 2(AB+C) & 2(AC-B) \\ 2(AB-C) & 1 - A^2 + B^2 - C^2 & 2(BC+A) \\ 2(AC+B) & 2(BC-A) & 1 - A^2 - B^2 + C^2 \end{bmatrix} \quad (30)$$

#### 4.2 TAYLOR'S SERIES EXPANSIONS OF EULER'S SYMMETRICAL PARAMETERS AND THE FOUR GIMBAL EULER ANGLES

Only the parameters free from singularities were selected for further study. The second-order Taylor's series expansion of the direction cosine system is given in Paragraph 5.1.1. The second-order Taylor's series expansions for Euler symmetrical and the four-gimbal Euler angles are given below in Paragraphs 4.2.1 and 4.2.2, respectively. All three of these expansions were derived using the assumption that  $\dot{\omega} = \text{constant}$  during the measurement interval.

#### 4.2.1 Euler Symmetrical Parameters – Second-Order Taylor's Series Expansion

The second-order Taylor's series expansion for Euler's symmetrical parameters is:

$$\xi^m = \xi^{m-1} + \xi^{mI} + \frac{1}{4} \left( \chi^{mI} \Delta a_1^m - \zeta^{mI} \Delta a_2^m + \eta^{mI} \Delta a_3^m \right) \quad (31)$$

$$\eta^m = \eta^{m-1} + \eta^{mI} + \frac{1}{4} \left( \zeta^{mI} \Delta a_1^m - \chi^{mI} \Delta a_2^m + \xi^{mI} \Delta a_3^m \right) \quad (32)$$

$$\zeta^m = \zeta^{m-1} + \zeta^{mI} + \frac{1}{2} \left( -\eta^{mI} \Delta a_1^m + \xi^{mI} \Delta a_2^m + \chi^{mI} \Delta a_3^m \right) \quad (33)$$

$$\chi^m = \chi^{m-1} + \chi^{mI} + \frac{1}{2} \left( -\xi^{mI} \Delta a_1^m - \eta^{mI} \Delta a_2^m - \zeta^{mI} \Delta a_3^m \right) \quad (34)$$

where

$$\xi^{mI} = \frac{1}{2} \left( \chi^{m-1} \Delta a_1^m - \zeta^{m-1} \Delta a_2^m + \eta^{m-1} \Delta a_3^m \right) \quad (35)$$

$$\eta^{mI} = \frac{1}{2} \left( \zeta^{m-1} \Delta a_1^m + \chi^{m-1} \Delta a_2^m - \xi^{m-1} \Delta a_3^m \right) \quad (36)$$

$$\zeta^{mI} = \frac{1}{2} \left( -\eta^{m-1} \Delta a_1^m + \xi^{m-1} \Delta a_2^m + \chi^{m-1} \Delta a_3^m \right) \quad (37)$$

$$\chi^{mI} = \frac{1}{2} \left( -\xi^{m-1} \Delta a_1^m - \eta^{m-1} \Delta a_2^m - \zeta^{m-1} \Delta a_3^m \right) \quad (38)$$

and

$\xi, \eta, \zeta, \chi$  ■ Euler symmetrical parameters

$\Delta a_1, \Delta a_2, \Delta a_3$  ■ angular increments about the indicated body axes

$m, m-1$  ■ superscript denoting present or last value of a variable

$mI$  ■ superscript denoting an intermediate variable in the calculation of the present value of a variable

4. 2. 2 Four-Gimbal Euler Angle—Second-Order Taylor's Series Expansion

The second-order Taylor's series expansion is:

$$\begin{aligned}
 \phi^m &= \phi^{m-1} + \Delta a_1 - K\tau\gamma \sin \psi^{m-1} \operatorname{sgn} \cos \psi^{m-1} \\
 &+ \gamma^{m-1} (\Delta a_2^m \sin \phi^{m-1} + \Delta a_3^m \cos \phi^{m-1}) \\
 &+ \frac{1}{2} \left\{ K^2 \gamma^2 \sin^2 \psi^{m-1} \cos \psi^{m-1} \right. \\
 &\quad - K\tau (\Delta a_2^m \cos \phi^{m-1} - \Delta a_3^m \sin \phi^{m-1}) \sin \psi^{m-1} \operatorname{sgn} \cos \psi^{m-1} \\
 &\quad - 2K\tau^{m-1} (\Delta a_2^m \sin \phi^m + \Delta a_3^m \cos \phi^m) \left[ \cos \psi^{m-1} \right] \\
 &\quad + (\Delta a_2^m \cos \phi^{m-1} - \Delta a_3^m \sin \phi^{m-1}) \\
 &\quad \left. \cdot (\Delta a_2^m \sin \phi^{m-1} + \Delta a_3^m \cos \phi^{m-1}) \right\} \quad (39)
 \end{aligned}$$

$$\begin{aligned}
 \gamma^m &= \gamma^{m-1} - K\tau\gamma^{m-1} \left| \cos \psi^{m-1} \right| + (\Delta a_2^m \cos \phi^{m-1} - \Delta a_3^m \sin \phi^{m-1}) \\
 &+ \frac{1}{2} \left\{ K^2 \gamma^2 \cos^2 \psi^{m-1} - K\tau (\Delta a_2^m \cos \phi^{m-1} - \Delta a_3^m \sin \psi^{m-1}) \left| \cos \psi^{m-1} \right| \right. \\
 &\quad + 2K\tau\gamma^{m-1} (\Delta a_2^m \sin \phi^{m-1} + \Delta a_3^m \cos \phi^{m-1}) \sin \psi^{m-1} \operatorname{sgn} \cos \psi^{m-1} \\
 &\quad - \gamma^{m-1} (\Delta a_2^m \sin \phi^{m-1} + \Delta a_3^m \cos \phi^{m-1})^2 \\
 &\quad \left. - \Delta a_1^m \Delta a_2^m \sin \phi^{m-1} - \Delta a_1^m \Delta a_3^m \cos \phi^{m-1} \right\} \quad (40)
 \end{aligned}$$

$$\begin{aligned}
\psi^m = & \psi^{m-1} + \left( \Delta a_2^m \sin \psi^{m-1} + \Delta a_3^m \cos \psi^{m-1} \right) \\
& + \frac{1}{2} \left\{ -3K\tau\gamma^{m-1} \left( \Delta a_2^m \cos \phi^{m-1} - \Delta a_3^m \sin \phi^{m-1} \right) \cdot \sin \psi^{m-1} \operatorname{sgn} \cos \psi^{m-1} \right. \\
& + \Delta a_1 \left( \Delta a_2 \cos \phi - \Delta a_3 \sin \phi \right) \\
& + \gamma^{m-1} \left( \Delta a_2^m \phi^{m-1} + \Delta a_3^m \cos \phi^{m-1} \right) \\
& \left. \cdot \left( \Delta a_2^m \cos \phi^{m-1} - \Delta a_3^m \sin \phi^{m-1} \right) \right\} \quad (41)
\end{aligned}$$

$$\begin{aligned}
\theta^m = & \theta^{m-1} + K\tau\gamma^{m-1} \operatorname{sgn} \cos \psi^{m-1} \\
& - \frac{1}{2} \left\{ K^2 \tau^2 \gamma^{m-1} \cos \psi^{m-1} - K\tau \left( \Delta a_2^m \cos \phi^{m-1} - \Delta a_3^m \sin \phi^{m-1} \right) \right. \\
& \left. \operatorname{sgn} \cos \psi^{m-1} \right\} \quad (42)
\end{aligned}$$

where

$m$  = superscript denoting the present value of the variable

$\Delta a_1, \Delta a_2, \Delta a_3$  = angular increments about the indicated body axes

$\theta, \psi, \gamma, \phi$  = four-gimbal Euler angle parameters, previously defined

$K$  = gain factor, previously defined

## 4.3 COMPUTER REQUIREMENTS

### 4.3.1 General-Purpose Mechanization

The computer memory and timing estimates contained herein were made for a hypothetical random access, general purpose computer. The computer was assumed to use single address instructions and binary two's complement arithmetic operations. The following minimum instruction repertoire was assumed to exist:

CLA	-	Clear and add
ADD	-	Add
SUB	-	Subtract
MPY	-	Multiply
DVP	-	Divide
ALS	-	Accumulator left shift
ARS	-	Accumulator right shift
COM	-	Complement
STO	-	Store accumulator
TRA	-	Transfer control
TMI	-	Transfer on minus
AXT	-	Set index register
TIX	-	Transfer and decrement index

All instructions, with the exception of shifts, multiplies, and divides, were assumed to require the equivalent of one ADD time for execution. A shift instruction was assumed to require the equivalent of three ADD times for execution. Any input/output instruction necessary to interface with the input/output hardware was assumed to require the equivalent of one ADD time for execution. For simplicity, MPY and DVP instructions were assumed to require equal time for execution.\* In the following paragraphs, timing estimates are given in terms of equivalent ADD and MPY execution times. Specification of timing requirements in this manner allows rapid evaluation of timing requirements for any specific random access

\*The LEM AGS computer MPY and DVP time is seven ADD times.

aerospace computer by substitution of the appropriate execution times in the given expressions. Computer memory estimates were divided into two categories: (1) memory estimates for the program proper and (2) memory estimates for storage of constants and variables.

In all cases, the input/output hardware was assumed to contain the necessary summing registers to sum all incremental inputs. Program timing was assumed to be accomplished by means of a real-time interrupt. All computations were assumed to be single precision, with the exception of the direction cosine updating, where a pseudo-double precision technique was employed. The computer word length was not considered when making the estimates. It was assumed that the word length was large enough to meet the accuracy requirements of the system. The computer was assumed to contain a single index register for operand address modification.

It should be emphasized that use of the timing expressions can only yield a rough timing estimate for any specific computer. Existing aerospace computers contain many unique properties which make universal estimates extremely difficult. In particular, memory and timing estimates for the Univac 1824 (which contains 3 index registers, double precision instructions, and a square root instruction) would be significantly less than the following estimates would indicate if the full capability of this machine were used. At the other extreme, memory estimates for the Apollo Block I and Block II AGC/LGC computers would be significantly more than the following estimates would indicate because of the unusual instruction repertoire which this machine contains.

In addition to the timing expression, a fairly accurate timing estimate for the LEM AGS computer is given. All estimates reflect a 15 percent allowance for program housekeeping and scaling. Table 4-1 contains the results of this study.

#### 4.3.2 DDA Mechanization

The numbers of integrators required to update the parameters and resolve velocity increments are tabulated below:

<u>Parameter</u>	<u>Number of Integration</u>
Direction cosines	27
Euler symmetrical	50
Four-gimbal Euler angle	73
Quaternions*	33
Three-gimbal Euler angle*	46

Table 4-I. General Purpose Computer Requirements

Parameter	Memory Estimate (words)		Timing Estimate (msec)	
	Program	Constant and Variable	General	LEM AGS Computer
Direction Cosines				
First-order Taylor's series	38	21	132A + 18M	2.58
Second-order Taylor's series	88	21	156A + 30M	3.66
Euler Symmetrical Parameters				
First-order Taylor's series	143	28	154A + 22M	3.08
Second-order Taylor's series	163	28	167A + 29M	3.7
Four-Gimbal Euler Angle				
First-order Taylor's series	221	45	320A + 66M	7.82
Second-order Taylor's series	297	66	510A + 101M	12.17

\* Estimates made in Reference 4.5 and included for completeness.

## REFERENCES

- 4.1 E. T. Whittaker, "A Treatise on the Analytical Dynamics of Particles and Rigid Bodies," Cambridge University Press, Cambridge, Mass., 1960.
- 4.2 H. Goldstein, "Classical Mechanics," Addison-Wesley Publishing Company, Inc., June 1959.
- 4.3 R. E. Mortensen, "On Systems for Automatic Control of the Rotation of a Rigid Body," Report No. 63-23, Electronics Research Laboratory, University of California at Berkeley, 27 November 1963.
- 4.4 D. B. DeBra, "The Large Attitude Motions and Stability, Due to Gravity of a Satellite with Passive Sampling in an Orbit of Arbitrary Eccentricity About an Oblate Body," Stanford University, May 1962.
- 4.5 T. F. Wiener, "Theoretical Analysis of Gimballess Inertial Reference Equipment Using Delta-Modulated Instruments," LTJG, USN, Department of Aeronautics and Astronautics, Massachusetts Institute of Technology.
- 4.6 "Study for a No-Gimbal Space Reference System," Semi-annual Report N. 4, ASTIA No. AD 333 453, (Secret).
- 4.7 M. J. Friedenthal, "Analysis of a DDA Euler Angle Computer," 10 May 1963, Internal TRW Report No. 9352.8-209.
- 4.8 A. Sabroff, et al, "Investigation of the Acquisition Problem in Satellite Attitude Control," June 1955, TRW Report No. 4154-6008-RU001.

## 5. COMPUTER EQUATIONS AND PERFORMANCE

The purpose of this study was to determine the feasibility of an analytic-platform inertial reference for future space missions. Specifically, the study's principal aim was to examine the accuracy of a strapped-down inertial reference system that might replace the ST 124-M IMU, the present Saturn inertial reference. This section gives the equations to be programmed in the computer to be used and outlines performance data for certain critical computations.

TRW and MSFC personnel have agreed that certain functions should be included in the computer. These are described and the equations required for these operations are presented in the next few sections. In some cases, the equations are analyzed with respect to their inherent accuracies. However, in most cases, the analyses are only preliminary and disregard many facets of the problem that will be examined in the second phase of the study.

## 5.1 EQUATION DESCRIPTION

The replacement of the ST 124-M IMU by an equivalent strapped-down system requires the addition of certain functions to the present guidance and navigation software. These functions will be incorporated in a separate digital computer that will provide output signals equivalent to those presently available from the platform system.

A general block diagram of the software mechanization is shown in Figures 5-1, 5-2, and 5-3. These diagrams show the system input/output, signal flow, and give the computations programmed in the computer. Seven functions are incorporated in the block diagram:

- Instrument Error Compensation. The compensation block compensates for certain instrument errors; the accelerometer signals are compensated for errors due to bias and scale factor. In addition to the errors, vehicle angular rates about the accelerometer input axis must be accounted for. In view of the performance characteristics provided by MSFC and the results of Section 7, the gyro outputs will not be compensated.
- Attitude Reference. The attitude reference equations provide an accurate attitude reference matrix that relates the vehicle body axes to the desired Earth Centered Inertial (ECI) coordinate system. The ECI coordinate system used for navigation is defined as the  $X_s, Y_s, Z_s$  system. This system is local level at launch with the  $X_s$  axis an azimuth angle  $A_z$  clockwise from north and the  $Y_s$  axis vertical. The trajectory of the vehicle is in the  $X_s - Y_s$  plane (Reference 5.7).

Two other coordinate systems discussed in the text are the  $X_b, Y_b, Z_b$  and the  $X_a, Y_a, Z_a$  coordinate systems. These two coordinate systems are body-fixed with the  $X_a, Y_a, Z_a$  axes along the input axes of the accelerometers and the  $X_b, Y_b, Z_b$  axes along the input axes of the gyros. The  $X_b, Y_b, Z_b$  axes coincide with the yaw, roll, and pitch axes of the vehicle. The accelerometer and gyro axes are defined independently since the accelerometer errors may be reduced by an optimum orientation (see Section 3).

The attitude reference equations compute the direction cosines that relate the  $X_b, Y_b, Z_b$  axes to the  $X_s, Y_s, Z_s$  inertial axes. The selected design goal for the accuracy

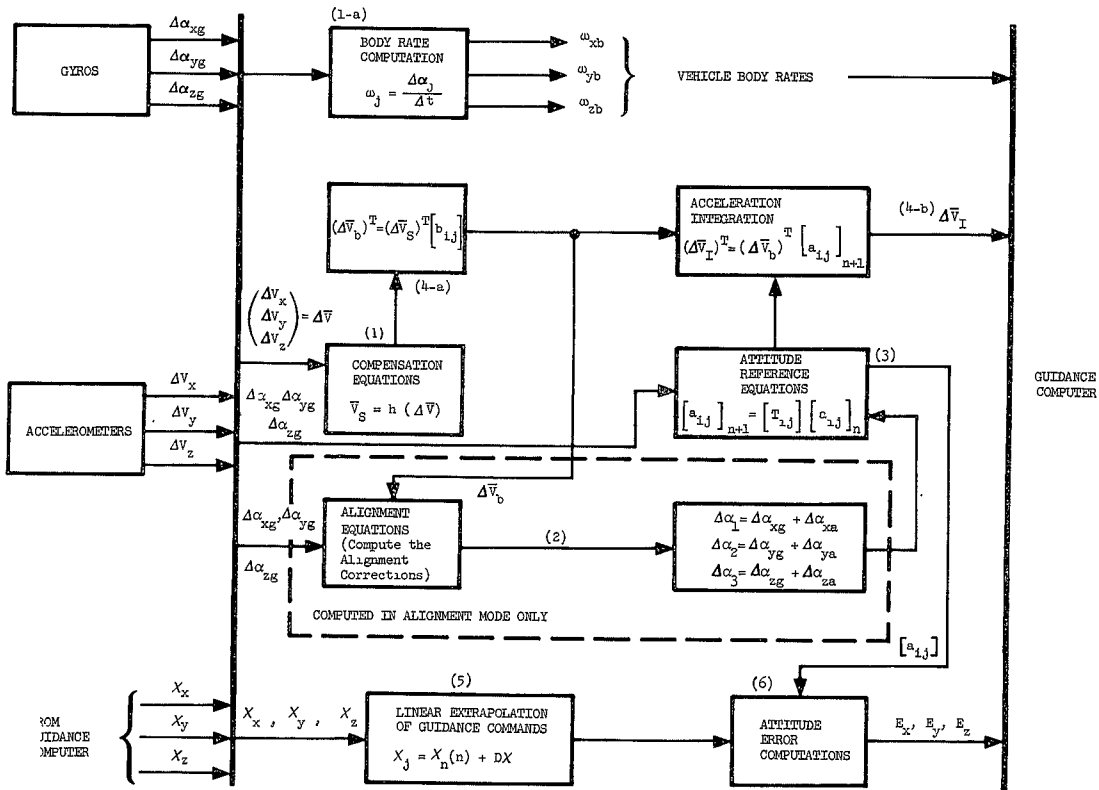


Figure 5-1. Software Mechanization

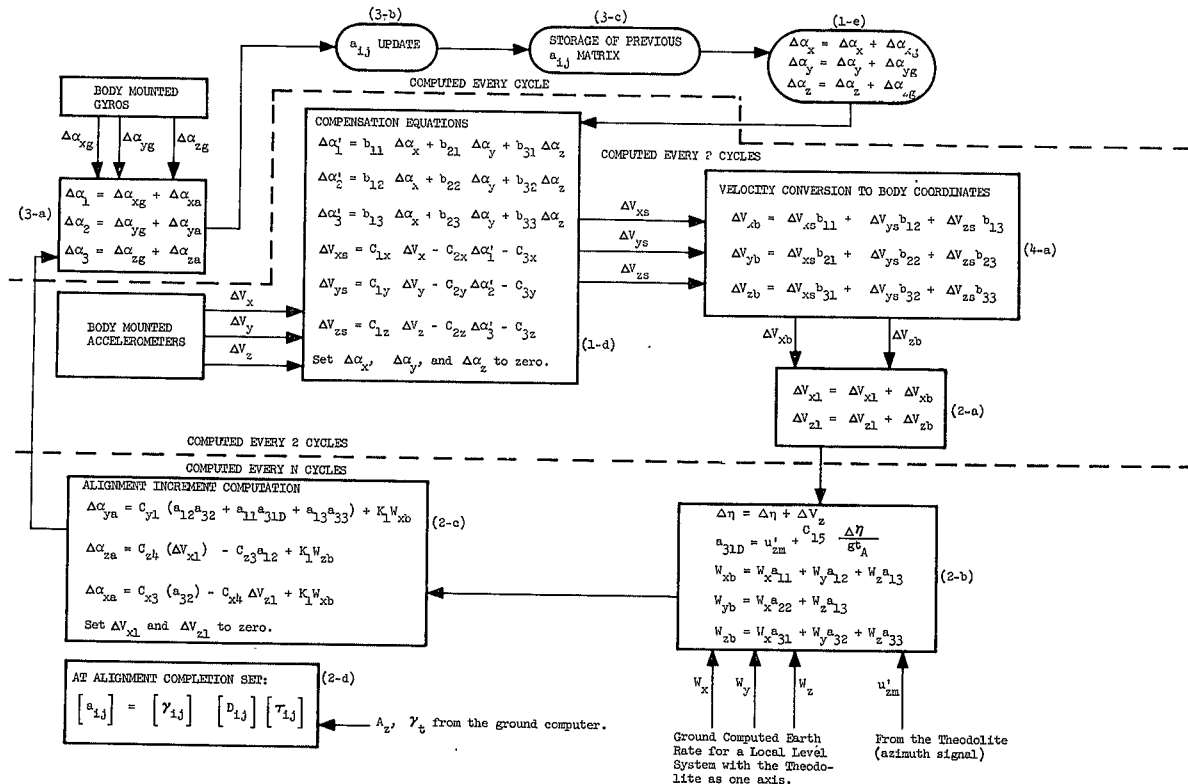


Figure 5-2. Alignment Equations

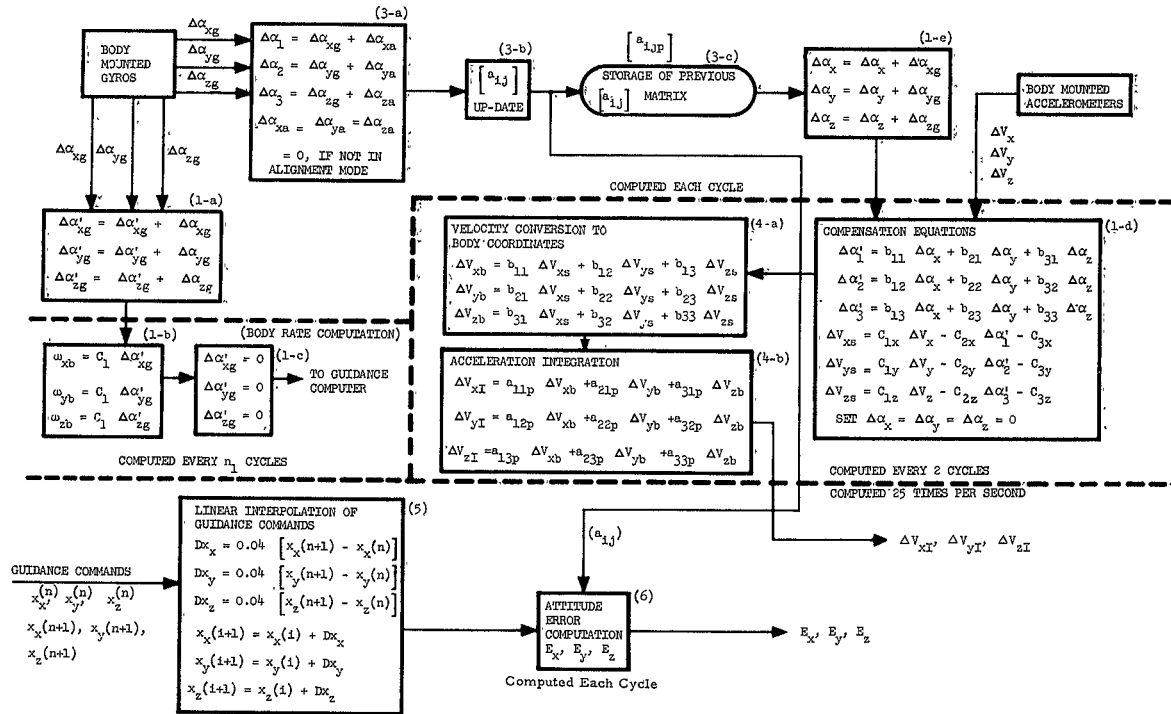


Figure 5-3. Flight Equations

of the attitude reference equations requires that these equations cause less than 20 arc sec attitude error at the end of a nominal flight. The system errors are based upon the following inputs:

- (1) Maximum vehicle slewing rates of 6 deg/sec\*
- (2) Worst-case vehicle coning of 3 cps at an amplitude of 0.05 deg.

- Acceleration Integration. The acceleration integration equations convert thrust velocity increments measured in vehicle coordinates to velocity increments in the navigation inertial coordinate system. The design goal for acceleration integration is that the computational error at the end of a nominal flight be less than 0.3 m/sec.
- Alignment. The alignment of a strapped-down system simply implies the computation of the correct direction cosines in the attitude reference transformation matrix. This alignment is performed prior to launch with the use of the accelerometer outputs for leveling corrections and theodolite information for azimuth alignment. The desired alignment accuracy is within 20 arc/sec about any vehicle axis. Also, the alignment must provide a variable launch azimuth capability.
- Linear Interpolation of Guidance Commands. Once each second\*\* the Saturn flight computer sends six attitude signals to the strapped-down digital computer. These signals are the present and predicted guidance command cycles. Since these angles are to be used to generate attitude error signals every 40 msec, the strapped-down digital computer will interpolate between the present and predicted angles. These interpolated values will be generated every 40 msec with the GP mechanization and every major cycle with the DDA mechanization.
- Attitude Error Signals. The commanded attitude is updated every 40 msec in the GP mechanization. However, the attitude error signals are not computed at the 40 msec rate but are computed as rapidly as the attitude reference equations. The DDA mechanization performs these operations every major cycle.

---

\* The system is designed to tolerate rates of 60 deg/sec. These are very unlikely to occur, and thus for error studies, 6 deg/sec (still very pessimistic) is used.

\*\* This number is currently slightly longer (1 to 2 sec).

- Vehicle Body Rate Computation. The strapped-down digital computer is also required to compute the vehicle body rates. It provides body rotation rates, attitude error signals, and the inertial velocity increments. Using the input signals of the body-mounted gyros and accelerometers, plus the guidance commands, the strapped-down computer provides these signals as well as a very accurate attitude reference.

In the next few subsections, the equations mechanizing these operations are analyzed and discussed and the merits of several possible mechanizations are presented. In some cases, several equations performing the same operation are presented. In these cases, the tradeoffs between the different concepts are discussed and the most satisfactory method is presented. Both DDA and GP equations are included, and the DDA mechanization is called out separately at the end of each section.

### 5.1.1 Attitude Reference Equations

The primary purpose of the attitude reference equations in a strapped-down system is to update and maintain the direction cosine matrix that relates the vehicle axes to the desired navigation or guidance coordinate system. (See Section 6 for further details on kinematical representation other than direction cosines.) For the Saturn application, the attitude reference equations update the matrix that relates the vehicle body axes  $X_b, Y_b, Z_b$  to the inertial navigation coordinate axes  $X_s, Y_s, Z_s$ .

$$\begin{bmatrix} X_b \\ Y_b \\ Z_b \end{bmatrix} = \begin{bmatrix} a_{ij} \end{bmatrix} \begin{bmatrix} X_s \\ Y_s \\ Z_s \end{bmatrix}$$

where

$X_b$  = vehicle yaw axis

$Y_b$  = vehicle roll axis

$Z_b$  = vehicle pitch axis

$X_s, Y_s, Z_s$  = inertial navigation axes, with  $Y_s$  vertical at launch,  $X_s$  at an azimuth  $A_z$  clockwise from north, and  $\bar{Z}_s = (\bar{X}_s) \times (\bar{Y}_s)$ . The vehicle's trajectory is in the  $\begin{bmatrix} X_s \\ Y_s \end{bmatrix}$  plane.

The direction cosines of the  $a_{ij}$  matrix are updated with the use of an algorithm that converts the angular increments obtained from the single axis platform-mounted gyroscopes into precise attitude updating signals. The selection of the best algorithm for the direction cosines integration depends primarily on the type and duration of the expected vehicle motions, the truncation of the algorithm, and the sampling rate of the gyro outputs.

From the studies made, it appears that the Taylor's series expansion provides good accuracy with a minimum of computer requirements. For this reason the Taylor's series expansion was selected as the basic integration algorithm. The derivation of the Taylor's series algorithm from gyro outputs is shown in the next few paragraphs.

The direction cosines used for maintaining the attitude reference of the vehicle relates the vehicle body axes to the ECI coordinate system. The transformation is defined by the  $a_{ij}$  transformation matrix shown below:

$$\begin{bmatrix} x_b \\ y_b \\ z_b \end{bmatrix} = \begin{bmatrix} a_{11} & a_{12} & a_{13} \\ a_{21} & a_{22} & a_{23} \\ a_{31} & a_{32} & a_{33} \end{bmatrix} \begin{bmatrix} x_s \\ y_s \\ z_s \end{bmatrix} \quad (1)$$

where

$\begin{bmatrix} a_{ij} \end{bmatrix}$  = the transformation matrix relating the vehicle body axes to the ECI coordinate frame

$x_b, y_b, z_b$  = unit vectors along the vehicle body axes

$x_s, y_s, z_s$  = unit vectors along the ECI coordinate system axes

It is easily demonstrated that direction cosine rates are related to body rates as follows:

$$\dot{a}_{ij} = a_{(i+1)j} \omega_{i+2} - a_{(i+2)j} \omega_{i+1}$$

where

$$i, j = 1, 2, 3$$

and

$$i + 3 = i$$

$$i + 4 = i + 1$$

$$i + 5 = i + 2$$

$\omega_1, \omega_2, \omega_3 =$  body rates about  $X_b, Y_b, Z_b$ , respectively

Body rate data cannot be obtained with the accuracy required; instead, an incremental angle is available. Thus an integration algorithm is required for the above equations.

If a second-order Taylor's series expansion is taken of

$$\int_t^{t+\Delta t} \dot{a}_{ij} dt = \Delta a_{ij}$$

subject to the assumption that  $\dot{\omega}_i =$  constant, the following general term is obtained for updating the direction cosine matrix:

$$a_{ij}(n+1) = a_{ij}(n) + \Delta a_{ij} \tag{2}$$

where

$$\begin{aligned} \Delta a_{ij} = & \Delta \alpha_{(i+2)} a_{(i+1)j}^{(n)} - \Delta \alpha_{(i+1)} a_{(i+2)j}^{(n)} \\ & + \left[ \frac{\Delta \alpha_{(i+2)} \Delta \alpha_i}{2} \right] a_{(i+2)j}^{(n)} - \left[ \frac{\Delta \alpha_{(i+2)}}{2} \right]^2 a_{ij}^{(n)} \\ & - \left[ \frac{\Delta \alpha_{(i+1)}}{2} \right]^2 a_{ij}^{(n)} + \frac{\Delta \alpha_{(i+1)} \Delta \alpha_i}{2} a_{(i+1)j}^{(n)} \end{aligned}$$

Where  $\Delta \alpha_i$  is the angular increment from the  $i^{\text{th}}$  gyro. The first-order Taylor's series can be obtained if terms with products of  $\Delta \alpha$  are neglected.

Eq (2) is used to update six direction cosines. The other three direction cosines are computed from the properties of the transformation matrices below:

$$\begin{aligned} a_{13}^{(n+1)} &= a_{21}^{(n+1)} a_{32}^{(n+1)} - a_{22}^{(n+1)} a_{31}^{(n+1)} \\ a_{23}^{(n+1)} &= a_{12}^{(n+1)} a_{31}^{(n+1)} - a_{11}^{(n+1)} a_{32}^{(n+1)} \\ a_{33}^{(n+1)} &= a_{11}^{(n+1)} a_{22}^{(n+1)} - a_{12}^{(n+1)} a_{21}^{(n+1)} \end{aligned} \quad (3)$$

(using the relation that  $a_{ij}$  = the cofactor of  $a_{ij}$ ). These equations might be put into another form to minimize computer storage requirements.

At the present time, the algorithm to be used in updating the  $a_{ij}$  matrix may be either a first- or second-order Taylor's series expansion. Although the second-order series requires more computer storage, the  $a_{ij}$  matrix may be updated at a slower rate than that required for the first-order Taylor's series. The second-order will be used for GP computations.

#### 5 1.1.1 DDA Equations

DDA computations for the model system (see Section 6) are rapid enough so that the first approximation is sufficient. The minimum complexity approach updates all nine direction cosines from gyro increments as follows:

$$\Delta\alpha_{ij} = a_{(i+1)j} \Delta\alpha_{i+2} - a_{(i+2)j} \Delta\alpha_{i+1} \quad (4)$$

DDA computations also use the following equations (see alignment discussion):

$$\Delta\alpha_1 = \Delta\alpha_{xg} + \Delta\alpha_{xa}$$

$$\Delta\alpha_2 = \Delta\alpha_{yg} + \Delta\alpha_{ya}$$

$$\Delta\alpha_3 = \Delta\alpha_{zg} + \Delta\alpha_{za} \quad (5)$$

#### 5.1.2 Acceleration Integration Equations

The equation for computing the inertial velocity increments from the velocity increments measured by the body-mounted accelerometers is

$$\begin{bmatrix} \Delta V_{xI} \\ \Delta V_{yI} \\ \Delta V_{zI} \end{bmatrix} = \begin{bmatrix} a_{ij} \end{bmatrix}^T_m \begin{bmatrix} b_{ij} \end{bmatrix} \begin{bmatrix} \Delta V_{xb} \\ \Delta V_{yb} \\ \Delta V_{zb} \end{bmatrix} \quad (6)$$

where

$\Delta V_{xI}, \Delta V_{yI}, \Delta V_{zI}$  = inertial velocity increments

$\Delta V_{xb}, \Delta V_{yb}, \Delta V_{zb}$  = velocity increments measured by the body mounted accelerometers

$\left[ a_{ij} \right]_m^T$  = matrix relating the inertial coordinates to the body coordinates.  $m$  signifies that the  $a_{ij}$  direction cosines were obtained at the  $m^{\text{th}}$  direction cosine update cycle. The superscript  $T$  indicates the transpose of the  $\left[ a_{ij} \right]$  matrix.

$\left[ b_{ij} \right]$  = matrix transforming the accelerometer recordings from accelerometer coordinates to gyro ( $X_b$ ) coordinates.

In Eq (6), the  $a_{ij}$  matrix is the direction cosine matrix obtained at the  $m^{\text{th}}$  direction cosine update cycle. If the velocity increments are computed every  $\Delta T$  sec, the accuracy of the inertial velocity increment computation may be increased by using the direction cosines present at the middle of the  $\Delta T$  interval. This is an implicit correction for the Coriolis term. An explicit correction could also be mechanized. Two methods are thus proposed for the acceleration integration equations, one using the  $a_{ij}$  matrix present at the end of  $\Delta T$  sec, and the other using the  $a_{ij}$  matrix present at the middle of the  $\Delta T$  interval. The choice of the acceleration integration method hinges on a tradeoff between computer storage requirements and the required accuracy of the integration equations.

#### 5.1.2.1 DDA Equations

- Velocity conversion to gyro body coordinates.

$$\begin{aligned} \Delta V_{xb} &= b_{11} \Delta V_{xs} + b_{12} \Delta V_{ys} + b_{13} \Delta V_{zs} \\ \Delta V_{yb} &= b_{21} \Delta V_{xs} + b_{22} \Delta V_{ys} + b_{23} \Delta V_{zs} \\ \Delta V_{zb} &= b_{31} \Delta V_{xs} + b_{32} \Delta V_{ys} + b_{33} \Delta V_{zs} \end{aligned} \quad (7)$$

where

$b_{ij}$  are constants.

• Velocity resolution to inertial space.

$$\begin{aligned}\Delta V'_{xI} &= a_{11} \Delta V_{xb} + a_{21} \Delta V_{zb} + a_{31} \Delta V_{zb} \\ \Delta V'_{yI} &= a_{12} \Delta V_{xb} + a_{22} \Delta V_{zb} + a_{32} \Delta V_{zb} \\ \Delta V'_{zI} &= a_{13} \Delta V_{xb} + a_{23} \Delta V_{zb} + a_{33} \Delta V_{zb}\end{aligned}\quad (8)$$

To provide a variable launch azimuth capability, the azimuth rotation  $\psi$  is performed.

$$\begin{aligned}\Delta V'_{xI} &= (C\psi) \Delta V'_{xI} + (S\psi) \Delta V'_{zI} \\ \Delta V'_{zI} &= (S\psi) \Delta V'_{xI} + (C\psi) \Delta V'_{zI}\end{aligned}\quad (9)$$

5.1.3 Compensation Equations

The compensation equations are used to correct the accelerometer outputs only.

The first step in the accelerometer compensation equations is to convert the gyro outputs from vehicle coordinates to the accelerometer input axes coordinate frame. This assumes the accelerometer input axes are not aligned with the gyro input axes. \* that is,

$$\begin{bmatrix} x_b \\ y_b \\ z_b \end{bmatrix} = \begin{bmatrix} b_{ij} \end{bmatrix} \begin{bmatrix} x_a \\ y_a \\ z_a \end{bmatrix}\quad (10)$$

---

\* It is likely that they will be colinear. If so, this rotation is not required.

where

$x_b, y_b, z_b$  = vehicle body axes which are aligned with the gyro input axes

$x_a, y_a, z_a$  = accelerometer input axes

$\begin{bmatrix} b_{ij} \end{bmatrix}$  = matrix with constant direction cosine elements

The gyro outputs  $\Delta\alpha_{xg}, \Delta\alpha_{yg}, \Delta\alpha_{zg}$  are thus converted to accelerometer coordinates as shown in Eq (11).

$$\begin{bmatrix} \Delta\alpha_1' \\ \Delta\alpha_2' \\ \Delta\alpha_3' \end{bmatrix} = \begin{bmatrix} b_{ji} \end{bmatrix} \begin{bmatrix} \Delta\alpha_{xg} \\ \Delta\alpha_{yg} \\ \Delta\alpha_{zg} \end{bmatrix} \quad (11)$$

where

$\Delta\alpha_1', \Delta\alpha_2', \Delta\alpha_3'$  = gyro outputs along the accelerometer input axes

$\Delta\alpha_{xg}, \Delta\alpha_{yg}, \Delta\alpha_{zg}$  = gyro outputs

If  $\Delta V_x, \Delta V_y,$  and  $\Delta V_z$  are the output increments of the body mounted accelerometers, the compensated velocity increments are:

$$\begin{aligned} \Delta V_{xs} &= C_{1x} \Delta V_x - C_{2x} \alpha_1' - C_{3x} \\ \Delta V_{ys} &= C_{1y} \Delta V_y - C_{2y} \alpha_2' - C_{3y} \\ \Delta V_{zs} &= C_{1z} \Delta V_z - C_{2z} \alpha_3' - C_{3z} \end{aligned} \quad (12)$$

where

$C_{1x}, C_{1y}, C_{1z}$  = scale factor corrections

$C_{2x}, C_{2y}, C_{2z}$  convert the  $\Delta\alpha_1^1, \Delta\alpha_1^1,$  and  $\Delta\alpha_3^1$  corrections to ft/sec

$C_{3x}, C_{3y}, C_{3z}$  = accelerometer bias corrections

Before these compensated velocity increments may be used in the acceleration integration equations, they must be transformed through the constant  $b_{ij}$  matrix from accelerometer coordinates to the vehicle axes coordinates:

$$\Delta\bar{V}_b = \begin{bmatrix} b_{ij} \end{bmatrix} \Delta\bar{V}_s \quad (13)$$

#### 5.1.3.1 DDA Equations

- Gyro rotation to accelerometer coordinate set.

$$\Delta\alpha_1^1 = b_{11} \Delta\alpha_{xg} + b_{21} \Delta\alpha_{yg} + b_{31} \Delta\alpha_{zg}$$

$$\Delta\alpha_2^1 = b_{12} \Delta\alpha_{xg} + b_{22} \Delta\alpha_{yg} + b_{32} \Delta\alpha_{zg}$$

$$\Delta\alpha_3^1 = b_{13} \Delta\alpha_{xg} + b_{23} \Delta\alpha_{yg} + b_{33} \Delta\alpha_{zg} \quad (14)$$

- Accelerometer compensation equations.

$$\Delta V_{xs} = C_{1x} \Delta V_x - C_{2x} \Delta\alpha_1^1 - C_{3x} \Delta t$$

$$\Delta V_{ys} = C_{1y} \Delta V_y - C_{2y} \Delta\alpha_2^1 - C_{3y} \Delta t$$

$$\Delta V_{zs} = C_{1z} \Delta V_z - C_{2z} \Delta\alpha_3^1 - C_{3z} \Delta t \quad (15)$$

#### 5.1.4 Body Rate Computation

The body rate computation is accomplished in a very simple manner by dividing the accumulated gyro outputs by the time interval in which they were accumulated.

$$\begin{aligned}
\omega_{xb} &= (\Delta \alpha_x) \left( \frac{1}{\Delta t} \right) \\
\omega_{yb} &= (\Delta \alpha_y) \left( \frac{1}{\Delta t} \right) \\
\omega_{zb} &= (\Delta \alpha_z) \left( \frac{1}{\Delta t} \right)
\end{aligned}
\tag{16}$$

The performance of the equations has not yet been established; but, if it is not adequate, it is certain that adjustments can be made to render it so.

#### 5.1.4.1 DDA Equations

The equations used here represent the DDA equivalent of a linear transfer function of  $s/(\tau s + 1)$ .

$$\begin{aligned}
\Delta \dot{\alpha}_{xb} &= 50 (\Delta \alpha_{xb} - \dot{\alpha}_{xb} \Delta t) \\
\Delta \dot{\alpha}_{yb} &= 50 (\Delta \alpha_{yb} - \dot{\alpha}_{yb} \Delta t) \\
\Delta \dot{\alpha}_{zb} &= 50 (\Delta \alpha_{zb} - \dot{\alpha}_{zb} \Delta t)
\end{aligned}
\tag{17}$$

#### 5.1.5 Linear Interpolation of Guidance Commands

Each second, six attitude signals are received from the guidance computer, three representing true gimbal angles and three representing predicted gimbal angles:

$$\begin{aligned}
&\chi_x(j), \chi_y(j), \chi_z(j) \\
&\chi_x(j+1), \chi_y(j+1), \chi_z(j+1)
\end{aligned}
\tag{18}$$

Interpolation between the computed and predicted  $\chi$  angles provides angle data 25 times/sec through the use of the following equations:

$$DX = \frac{1}{25} (\chi_{(j+1)} - \chi_{(j)}) \text{ for } \chi_x, \chi_y, \chi_z$$

$$\chi_{(i+1)} = \chi_{(i)} + DX \text{ for } \chi_x, \chi_y, \chi_z \quad (19)$$

#### 5.1.5.1 DDA Equations

See Section 6 for DDA discussion.

#### 5.1.6 Attitude Error Signals

The attitude error signals are computed by comparing two sets of direction cosines, one set termed the desired set computed from  $\chi_x$ ,  $\chi_y$ ,  $\chi_z$  and the other set the computed direction cosines. If the desired set of direction cosines is designated symbolically as  $a_{ijR}$ , the error signals are the positive right-hand rotations about the x, y, and z body axes as specified in Eq (20).

$$E_x = - \left[ a_{21} a_{31R} + a_{22} a_{32R} + a_{23} a_{33R} \right]$$

$$E_y = - \left[ a_{31} a_{11R} + a_{32} a_{12R} + a_{33} a_{13R} \right]$$

$$E_z = + \left[ a_{21} a_{11R} + a_{22} a_{12R} + a_{23} a_{13R} \right] \quad (20)$$

The command angles are assumed to be measured as they are shown in Figure 5-4.

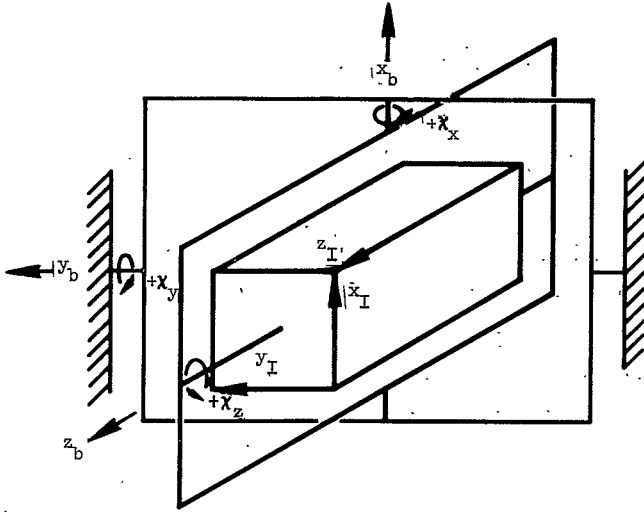


Figure 5-4. Gimbal Angle Orientation

Using this command angle sequence and sign,  $a_{ijR}$  becomes:

$$\begin{bmatrix} x_b \\ y_b \\ z_b \end{bmatrix} = \begin{bmatrix} CX_y & 0 & -SX_y \\ 0 & 1 & 0 \\ SX_y & 0 & CX_y \end{bmatrix} \begin{bmatrix} 1 & 0 & 0 \\ 0 & CX_x & SX_x \\ 0 & -SX_x & CX_x \end{bmatrix} \begin{bmatrix} CX_z & SX_z & 0 \\ -SX_z & CX_z & 0 \\ 0 & 0 & 1 \end{bmatrix} \begin{bmatrix} x_I \\ y_I \\ z_I \end{bmatrix} \quad (21)$$

$$\begin{bmatrix} x_b \\ y_b \\ z_b \end{bmatrix} = \begin{bmatrix} a_{ijR} \end{bmatrix} \begin{bmatrix} x_I \\ y_I \\ z_I \end{bmatrix} \quad (22)$$

$$\left( a_{ijR} \right) = \begin{bmatrix} (C\chi_z C\chi_y - S\chi_z S\chi_y S\chi_x) (C\chi_y S\chi_z + C_z S\chi_x S\chi_y) (-S\chi_y C\chi_x) \\ (-S\chi_z C\chi_x) & (C\chi_x C\chi_z) & (S\chi_x) \\ (S\chi_y C\chi_z + S\chi_z S\chi_x C\chi_y) (S\chi_y S\chi_z - S\chi_x C\chi_y C\chi_z) (C\chi_x C\chi_y) \end{bmatrix} \quad (23)$$

where

S = sine

C = cosine

#### 5.1.6.1 DDA Equations

$$\begin{aligned}
\Delta E_x &= - \left[ a_{21} \Delta a_{31R} + a_{31R} \Delta a_{21} + a_{22} \Delta a_{32R} + a_{32R} \Delta a_{22} \right. \\
&\quad \left. + a_{23} \Delta a_{33R} + a_{33R} \Delta a_{22} \right] \\
\Delta E_y &= - \left[ a_{31} \Delta a_{11R} + a_{11R} \Delta a_{31} + a_{32} \Delta a_{12R} + a_{12R} \Delta a_{32} \right. \\
&\quad \left. + a_{33} \Delta a_{13R} + a_{13R} \Delta a_{33} \right] \\
\Delta E_z &= + \left[ a_{21} \Delta a_{11R} + a_{11R} \Delta a_{21} + a_{22} \Delta a_{12R} + a_{12R} \Delta a_{22} \right. \\
&\quad \left. + a_{23} \Delta a_{13R} + a_{13R} \Delta a_{23} \right] \quad (24)
\end{aligned}$$

Consistent with the discussions of Subsections 2.4 and 2.5, the DDA equations for the  $\Delta a_{ijR}$  as a function of the  $\Delta \chi$ 's have not been derived. These derivations pose a straightforward task if it becomes desirable for Phase 2.

### 5.1.7 Prelaunch Alignment

The prelaunch alignment of the Saturn strapped-down system is performed while the vehicle is under the influence of small dynamic motions due to wind effects. The desired alignment accuracy is within 20 arc sec of all three axes and the porro prism rotational capability may be as much as 1 deg for the theodolite to acquire the reflected azimuth signals. Variable launch azimuth capability is to be provided.

The porro prism is installed along the  $z_b$  axis and in the  $x_b - z_b$  plane. Since the porro prism must cope with the theodolite acquisition problem resulting from vehicle sway, the porro prism's rotation must be in the  $x_b - z_b$  plane. The angle the porro prism is rotated must also be very accurately measured (within a few arc sec) for the azimuth alignment to meet the 20 arc sec accuracy requirement. This porro prism will be corrected in the alignment procedure by premultiplying the  $D_{ij}$  matrix with the matrix below (Eq 25), which compensates for the porro prism angle of rotation:

$$\begin{bmatrix} a'_{ij} \end{bmatrix} = \begin{bmatrix} \cos \gamma_T & 0 & \sin \gamma_T \\ 0 & 1 & 0 \\ -\sin \gamma_T & 0 & \cos \gamma_T \end{bmatrix} \begin{bmatrix} D_{ij} \end{bmatrix} \quad (25)$$

where

$\begin{bmatrix} a'_{ij} \end{bmatrix}$  = desired matrix relating the vehicle body axes with the local level reference axes

$\gamma_T$  = angle the porro prism is rotated in a clockwise direction about the  $y_b$  axis

$\begin{bmatrix} D_{ij} \end{bmatrix}$  = direction cosine matrix obtained during alignment

The capability of a variable launch azimuth is provided by multiplying the  $a'_{ij}$  matrix mentioned above by another matrix,  $c_{ij}$ , which relates the local level reference axes (used for alignment purposes) and the desired inertial navigation coordinate axes. The final matrix obtained provides the relationships between the vehicle body axes and the desired navigation coordinate axes:

$$\begin{bmatrix} a_{ij} \end{bmatrix} = \begin{bmatrix} a'_{ij} \end{bmatrix} \begin{bmatrix} \cos (A_z - A_o) & 0 & -\sin (A_z - A_o) \\ 0 & 1 & 0 \\ \sin (A_z - A_o) & 0 & \cos (A_z - A_o) \end{bmatrix} \quad (26)$$

where

$A_z$  = desired launch azimuth (clockwise from north)

$A_o$  = azimuth of the theodolite (clockwise from north)

$\begin{bmatrix} a'_{ij} \end{bmatrix}$  = matrix relating the alignment reference axes and the vehicle body axes

$\begin{bmatrix} a_{ij} \end{bmatrix}$  = matrix relating the vehicle body axes and the desired inertial navigation axes

Since the variable launch azimuth capability is provided by the multiplication of two matrices, the launch azimuth may be updated or changed until just a few seconds before launch.

In Reference 5.1, three schemes are presented for aligning the attitude reference equations with the use of the accelerometer outputs and a body-fixed porro prism. The alignment method tentatively chosen for implementation is a servoing technique and is shown in flow chart form by Figure 5-5. This method computes the alignment between the vehicle body axes and a local level coordinate system with one axis along the azimuth of the theodolite, which is represented by a  $D_{ij}$  matrix. Just prior to launch, three matrices must be multiplied to obtain the final  $a_{ij}$  direction cosine matrix relating the vehicle body axes and the desired ECI coordinate axes.

$$a_{31D} = u'_{zm} + \frac{\sum_{t=T}^{t-T_A} \Delta V_{z1}}{g(t-T_A)}$$

$$\omega_{xb} = W_x^a a_{11} + W_y^a a_{12} + W_z^a a_{13}$$

$$\omega_{yb} = W_x^a a_{21} + W_y^a a_{22} + W_z^a a_{23}$$

$$\omega_{zb} = W_x^a a_{31} + W_y^a a_{32} + W_z^a a_{33}$$

$$\Delta \alpha_{ya} = C_{y1} (a_{12} a_{32} + a_{11} a_{31a} + a_{13} a_{33}) - K_1 \omega_{yb}$$

$$\Delta \alpha_{xa} = C_{x3} (a_{32}) - C_{x4} \Delta V_{z1} - K_1 \omega_{xb}$$

$$\Delta \alpha_{za} = C_{z4} ((\Delta V_{x1}) - C_{z3} a_{12} - K_1 \omega_{zb})$$

$$\Delta \alpha_1 = \Delta \alpha_{xg} + \Delta \alpha_{xa}$$

$$\Delta \alpha_2 = \Delta \alpha_{yg} + \Delta \alpha_{ya}$$

$$\Delta \alpha_3 = \Delta \alpha_{zg} + \Delta \alpha_{za}$$

To Attitude Reference Equations ( $\begin{bmatrix} a_{ij} \end{bmatrix}$  computation)

Figure 5-5. Alignment Equations Flow Diagram

Another possible alignment mechanization is shown in Figure 5-6. Although this second method requires more computer memory than the first, the azimuth alignment should converge faster and with better accuracy. The decision between the two methods is based on a tradeoff between computer storage requirements and the alignment accuracy of the two methods.

If the scientific simulations of the two alignment equation sets do not meet accuracy requirements, it will be necessary to use a variable gain filter instead of the constant gains  $C_{y1}$ ,  $C_{x3}$ ,  $C_{x4}$ ,  $C_{z3}$ , and  $C_{z4}$ .

#### 5.1.7.1 DDA Equations

Only the servoing technique has been considered.

- Integrate velocity measurements.

$$\begin{aligned}\Delta V_{x1} &= (V_{xb} - 0.2V_{x1})\Delta t \\ \Delta V_{z1} &= (V_{zb} - 0.2V_{z1})\Delta t\end{aligned}\quad (27)$$

- Earth rate computations.

$$\begin{aligned}\Delta \theta_x &= \omega_x \Delta t \\ \Delta \theta_y &= \omega_y \Delta t \\ \Delta \theta_z &= \omega_z \Delta t\end{aligned}\quad (28)$$

- Resolve to body axis.

$$\begin{aligned}\Delta \theta'_x &= a_{11}\Delta \theta_x + a_{12}\Delta \theta_y + a_{13}\Delta \theta_z \\ \Delta \theta'_y &= a_{21}\Delta \theta_x + a_{22}\Delta \theta_y + a_{23}\Delta \theta_z \\ \Delta \theta'_z &= a_{31}\Delta \theta_x + a_{32}\Delta \theta_y + a_{33}\Delta \theta_z\end{aligned}\quad (29)$$

From an external source, obtain  $\Delta a_{31D}$ .

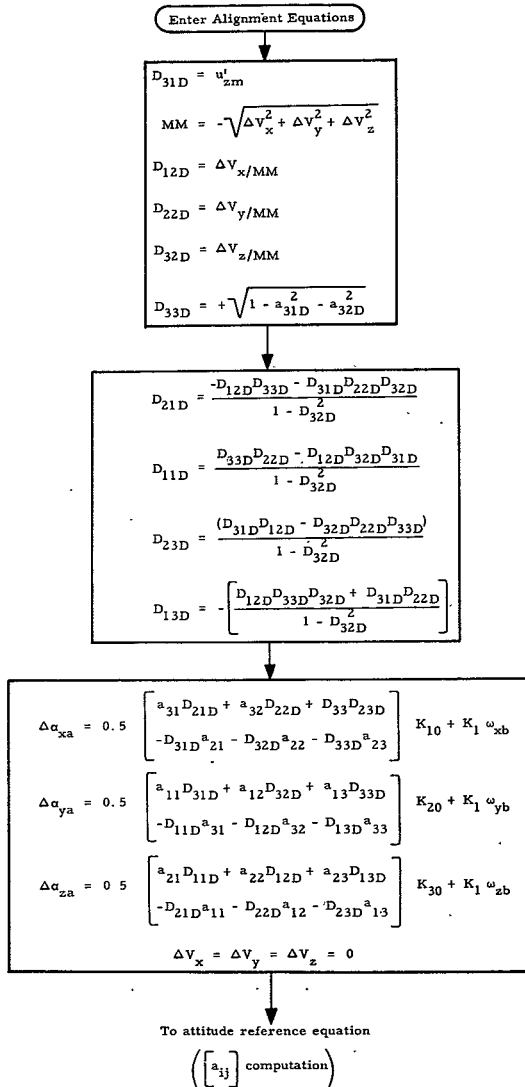


Figure 5-6. Alignment Equations Flow Diagram

- Alignment increment computation.

$$\begin{aligned}
 \Delta\alpha_{ya} &= \Delta\theta_x + C_{y1} \Delta t (a_{12}a_{32} + a_{11}a_{31D} + a_{13}a_{33}) \\
 \Delta\alpha_{za} &= C_{z4} \Delta V_{x1} - C_{z3} a_{12} + \Delta\theta_z \\
 \Delta\alpha_{xa} &= C_{x3} \Delta t a_{32} - C_{x4} \Delta V_{z1} + \Delta\theta_x
 \end{aligned} \tag{30}$$

Following alignment (i. e. , during boost),

$$\Delta\alpha_{ya} = 0 = \Delta\alpha_{za} = \Delta\alpha_{xa} \tag{31}$$

It is assumed that Eqs (25) and (26) are mechanized in a GSE computer.

## 5.2 ATTITUDE REFERENCE EQUATION ANALYSIS

This subsection analyzes the errors inherent in the Taylor's series expansions used to update the attitude reference direction cosines subject to constant slewing rates and vehicle coning (Reference 5.5). The slewing errors are derived analytically and are then verified for the second-order Taylor's series by scientific simulation tests. The errors due to vehicle coning are also presented and were obtained entirely from scientific simulations.

The results of these error analyses will be used in Paragraph 5.2.4 to compute the integration rate required for the two Taylor's series algorithms.

### 5.2.1 Taylor's Series Constant Slew Error Analysis

In this evaluation of the first- and second-order Taylor's series errors as a function of the number of constant slewing rate cycles the vehicle experiences, a mathematical method of F. B. Hildebrand will be used (Reference 5.2). In Subsection 1.22 of this book, Hildebrand states that a polynomial in  $[B]$ , where  $[B]$  is a square matrix, may be evaluated with the use of the eigenvalues of the matrix. This method is not valid if any two eigenvalues are equal. This method of evaluating matrix polynomials is illustrated as follows:

$$\text{If } P(B) = \text{polynomial in } [B] = C_1 [B]^{m-1} + C_2 [B]^{m-2} + \dots + C_m [I] \quad (32)$$

where  $I$  is the identity matrix, then

$$P(B) = \sum P(\lambda_K) [z_K(B)] \quad (33)$$

$$\text{where } [z_K(B)] = \frac{\prod_{r \neq K} ([B] - \lambda_r [I])}{\prod_{r \neq K} (\lambda_K - \lambda_r)} \quad (34)$$

$$\lambda_K, \text{ the } k^{\text{th}} \text{ eigenvalue, is found from} \quad (35)$$

$$\det [ [B] - \lambda [I] ] = 0$$

The transformation matrix  $a_{ij}$ , relating a vector in the vehicle frame to the inertial guidance frame is defined in Eq (36).

$$\begin{bmatrix} x_b \\ y_b \\ z_b \end{bmatrix} = \text{vehicle axes} = \begin{bmatrix} a_{ij} \end{bmatrix} \begin{bmatrix} x_I \\ y_I \\ z_I \end{bmatrix} \quad (36)$$

The direction cosines of the  $a_{ij}$  matrix are updated every  $\Delta t$  sec by a first- or second-order Taylor's series. (The value of  $\Delta t$  and the Taylor's series algorithm preference will be evaluated in the next few sections.) In matrix notation, the updating of the  $a_{ij}$  matrix using a first-order Taylor's series is shown in Eq (37), and the second-order Taylor's series updating is shown by Eq (38).

$$\begin{bmatrix} a_{ij} \end{bmatrix}_{(n+1)} = \begin{bmatrix} 1 & \Delta\alpha_3 & -\Delta\alpha_2 \\ -\Delta\alpha_3 & 1 & \Delta\alpha_1 \\ \Delta\alpha_2 & -\Delta\alpha_1 & 1 \end{bmatrix} \begin{bmatrix} a_{ij} \end{bmatrix}_{(n)} \quad (37)$$

$$\begin{bmatrix} a_{ij} \end{bmatrix}_{(n+1)} = \begin{bmatrix} \left[ 1 - \frac{1}{2} (\Delta\alpha_2^2 + \Delta\alpha_3^2) \right] \left[ \Delta\alpha_3 + \frac{1}{2} \Delta\alpha_1 \Delta\alpha_2 \right] \left[ -\Delta\alpha_2 + \frac{1}{2} \Delta\alpha_1 \Delta\alpha_3 \right] \\ \left[ -\Delta\alpha_3 + \frac{1}{2} \Delta\alpha_1 \Delta\alpha_2 \right] \left[ 1 - \frac{1}{2} (\Delta\alpha_1^2 + \Delta\alpha_3^2) \right] \left[ \Delta\alpha_1 + \frac{1}{2} \Delta\alpha_2 \Delta\alpha_3 \right] \\ \left[ \Delta\alpha_2 + \frac{1}{2} \Delta\alpha_1 \Delta\alpha_3 \right] \left[ -\Delta\alpha_1 + \frac{1}{2} \Delta\alpha_2 \Delta\alpha_3 \right] \left[ 1 - \frac{1}{2} (\Delta\alpha_1^2 + \Delta\alpha_2^2) \right] \end{bmatrix} \begin{bmatrix} a_{ij} \end{bmatrix}_{(n)} \quad (38)$$

where

$$\begin{bmatrix} a_{ij} \end{bmatrix}_{(n)} = a_{ij} \text{ matrix at the end of the } n^{\text{th}} \text{ compute cycle}$$

$$\begin{bmatrix} a_{ij} \end{bmatrix}_{(n+1)} = a_{ij} \text{ matrix at the end of the } (n+1)^{\text{th}} \text{ compute cycle}$$

$\Delta\alpha_1$  = accumulated output of the x gyro between the  $n^{\text{th}}$  cycle and the  $(n+1)^{\text{th}}$  cycle

$\Delta a_2$  = accumulated output of the y gyro

$\Delta a_3$  = accumulated output of the z gyro

In general, the updating of the  $a_{ij}$  matrix may be shown by multiplying the  $a_{ij}$  matrix by another matrix T:

$$\left[ a_{ij} \right]_{(n+1)} = [T]_{(n)} \left[ a_{ij} \right]_{(n)} \quad (39)$$

Furthermore,

$$\left[ a_{ij} \right]_{(n+1)} = [T]_{(n)} [T]_{(n-1)} [T]_{(n-2)} \dots [T]_{(1)} [T]_{(0)} \left[ a_{ij} \right]_{(0)} \quad (40)$$

For constant slewing rates, all  $[T]_{(i)}$  matrices are identical and Eq (40) may be rewritten as

$$\left[ a_{ij} \right]_{(n+1)} = [T]^n \left[ a_{ij} \right]_{(0)} \quad (41)$$

The errors of the first- and second-order Taylor's series algorithms are found by evaluating Eq (41) with Hildebrand's method described in Eqs (32) through (35).

For the constant rate slewing analysis, the original  $a_{ij}$  matrix is defined to be the unit matrix  $[I]$ . The attitude errors are defined as angular errors of rotation about the three vehicle axes  $x_b$ ,  $y_b$ ,  $z_b$ :

$$\sin E_x = \frac{\left[ (z_b)' (y_{bD}') \right] - \left[ (y_b)' (z_{bD}') \right]}{2}$$

$$\sin E_y = \frac{\left[ (x_b)' (z_{bD}') \right] - \left[ (z_b)' (x_{bD}') \right]}{2}$$

$$\sin E_z = \frac{[(y_b) (x_{bD})] - [(x_b) (y_{bD})]}{2} \quad (42)$$

where

$x_b, y_b, z_b$  = vehicle body axes orientation

$x_{bD}, y_{bD}, z_{bD}$  = desired orientation of the vehicle body axes

### 5. 2. 1. 1 First-Order Taylor's Series Errors

5. 2. 1. 1. 1 Single Axis Slew Errors. The constant rate slewing analysis which follows is performed for a constant slew about the x axis, which produces a T matrix as shown in Eq (42). Due to symmetry, slews about the y or z axis will have the same errors.

$$[T] = \begin{bmatrix} 1 & 0 & 0 \\ 0 & 1 & \Delta \\ 0 & -\Delta & 1 \end{bmatrix} \quad (43)$$

where  $\Delta$  is the angle rotated about the x body axis in the positive right-hand rule direction in  $\Delta t$  sec.

The eigenvalues are obtained by solving the determinant equation:

$$\begin{vmatrix} 1-\lambda & 0 & 0 \\ 0 & 1-\lambda & \Delta \\ 0 & -\Delta & 1-\lambda \end{vmatrix} = 0 \quad (44)$$

From Eq (44), the eigenvalues were found to be

$$\lambda_1 = 1, \lambda_2 = 1 + j\Delta, \lambda_3 = 1 - j\Delta \quad (45)$$

After combining these eigenvalues with the T matrix as in Eq (43),

$$\begin{bmatrix} a_{ij} \end{bmatrix}_{(n+1)} = [T]^n = \begin{bmatrix} 1 & 0 & 0 \\ 0 & R^n \cos n\Delta & R^n \sin n\Delta \\ 0 & -R^n \sin n\Delta & R^n \cos n\Delta \end{bmatrix} \quad (46)$$

where

$$\tan \alpha = \Delta$$

$$R^2 = 1 + \Delta^2$$

n = number of computation cycles

After slewing for n cycles, the  $[T]^n$  matrix should be, ideally

$$[T]^n = \begin{bmatrix} 1 & 0 & 0 \\ 0 & \cos n\Delta & \sin n\Delta \\ 0 & -\sin n\Delta & \cos n\Delta \end{bmatrix} \quad (47)$$

With the error criteria specified in Eq (42), the desired orientation in Eq (47), and the computed orientation in Eq (46), the attitude errors are

$$\begin{aligned} \sin E_y &= 0 \\ \sin E_z &= 0 \end{aligned} \quad (48)$$

$$\begin{aligned} \sin E_x &= R^n \sin(n(\alpha - \Delta)) = R^n \sin n\epsilon \\ -\epsilon &= \Delta \tan^{-1} \Delta = \Delta \left( \Delta - \frac{\Delta^3}{3} + \frac{\Delta^5}{5} - \frac{\Delta^7}{7} \right) \\ -\epsilon &= \frac{\Delta^3}{3} + \frac{\Delta^5}{5} - \frac{\Delta^7}{7} + \dots \approx \frac{\Delta^3}{3} \end{aligned} \quad (49)$$

Thus the errors due to the first-order Taylor's series expansion are

$$\begin{aligned} \text{scale factor } R &= + \sqrt{1 + \Delta^2} \\ \text{angle error per cycle} &\approx -\frac{\Delta^3}{3} \end{aligned} \quad (50)$$

5.2.1.1.2 Three Axis Slew Errors. The T matrix for a three axis slew is shown in Eq (51), its eigenvalues in Eq (52), and the resulting  $T^n$  matrix in Eq (53).

$$[T] = \begin{bmatrix} 1 & \Delta & -\Delta \\ -\Delta & 1 & \Delta \\ \Delta & -\Delta & 1 \end{bmatrix} \quad (51)$$

where  $\Delta =$  the angle rotated about each axis in  $\Delta t$  sec

$$\lambda_1 = 1, \lambda_2 = 1 - j\sqrt{3}\Delta, \lambda_3 = 1 + j\sqrt{3}\Delta \quad (52)$$

$$[T]^n = \begin{bmatrix} \frac{1}{3}(1+2R^n \cos na) & \frac{1}{3}[1-R^n(\cos na - \sqrt{3}\sin na)] & \frac{1}{3}[1-R^n(\cos na + \sqrt{3}\sin na)] \\ \frac{1}{3}[1-R^n(\cos na + \sqrt{3}\sin na)] & \frac{1}{3}[1+2R^n \cos na] & \frac{1}{3}[1-R^n(\cos na - \sqrt{3}\sin na)] \\ \frac{1}{3}[1-R^n(\cos na - \sqrt{3}\sin na)] & \frac{1}{3}[1-R^n(\cos na + \sqrt{3}\sin na)] & \frac{1}{3}(1+2R^n \cos na) \end{bmatrix} \quad (53)$$

where

$$R^2 = 1 + 3\Delta^2$$

$$\tan \alpha = \sqrt{3}\Delta$$

$n =$  the number of compute cycles.

The true or desired direction cosines are shown in Eq (54).

$$[T]^n = \begin{bmatrix} \frac{1}{3}(1 + 2 \cos n\omega) & \frac{1}{3}(1 - \cos n\omega + \sqrt{3} \sin n\omega) & \frac{1}{3}(1 - \cos n\omega - \sqrt{3} \sin n\omega) \\ \frac{1}{3}(1 - \cos n\omega - \sqrt{3} \sin n\omega) & \frac{1}{3}(1 + 2 \cos n\omega) & \frac{1}{3}(1 - \cos n\omega + \sqrt{3} \sin n\omega) \\ \frac{1}{3}(1 - \cos n\omega + \sqrt{3} \sin n\omega) & \frac{1}{3}(1 - \cos n\omega - \sqrt{3} \sin n\omega) & \frac{1}{3}(1 + 2 \cos n\omega) \end{bmatrix} \quad (54)$$

where

$$\omega = \sqrt{3} \Delta$$

The error terms defined in Eq (42) are shown below:

$$\begin{aligned} \sin E_x &= \frac{1}{3} \left[ 1 - R^n (\cos [n(\omega - a)] - \sqrt{3} \sin [n(\omega - a)]) \right] \\ \sin E_y &= \frac{1}{3} \left[ 1 - R^n (\cos [n(\omega - a)] - \sqrt{3} \sin [n(\omega - a)]) \right] \\ \sin E_z &= \frac{1}{3} \left[ 1 - R^n (\cos [n(\omega - a)] - \sqrt{3} \sin [n(\omega - a)]) \right] \end{aligned} \quad (55)$$

for small error angles ( $R = 1$ ),  $\sin E_x = \sin E_y = \sin E_z = -\sqrt{\frac{3}{3}} \sin [n(\omega - a)]$ .

Thus the errors for a three axis slew are functions of

$$\begin{aligned} \text{scale factor } R, R &\cong \sqrt{1 + 3\Delta^2} \\ \text{angle error per cycle } \sim &= \Delta^3 \end{aligned} \quad (56)$$

### 5.2.1.2 Second-Order Taylor's Series Errors

5.2.1.2.1 Single Axis Slew Errors. For the second-order Taylor's series, the T matrix for an x axis constant rate slew is

$$[T] = \begin{bmatrix} 1 & 0 & 0 \\ 0 & 1 - \frac{\Delta^2}{2} & \Delta \\ 0 & \Delta & 1 - \frac{\Delta^2}{2} \end{bmatrix} \quad (57)$$

and the matrix eigenvalues are

$$\lambda_1 = 1, \lambda_2 = 1 - \frac{\Delta^2}{2} + j\Delta, \lambda_3 = 1 - \frac{\Delta^2}{2} - j\Delta \quad (58)$$

After computing  $T^n$ , it was found that  $T^n$  for the second-order series is identical with the  $T^n$  matrix shown in Eq (46) except for the values of  $a$  and  $R$ . For the second-order Taylor's series,

$$\tan \alpha = \frac{\Delta}{1 - \frac{\Delta^2}{2}}$$

$$R^2 = 1 + \frac{\Delta^4}{4} \quad (59)$$

Based upon the error criteria in Eq (42), the attitude errors for the single axis slew are

$$E_y = 0$$

$$E_z = 0$$

$$E_x = R^n \sin n\epsilon$$

where

$$R^2 = 1 + \frac{\Delta^4}{4} \quad (60)$$

$$\epsilon = \Delta - \alpha$$

$$\alpha = \tan^{-1} \left( \frac{\Delta}{1 - \frac{\Delta^2}{2}} \right) \cong \Delta + \frac{\Delta^3}{2} + \frac{\Delta^5}{4} - \frac{\Delta^3}{3} \left[ 1 + \frac{3}{2} \Delta^2 + \frac{9}{4} \Delta^4 \right]$$

$$\alpha \approx \Delta + \frac{1}{6} \Delta^3 \quad (61)$$

$$\epsilon = \Delta - \alpha \approx -\frac{\Delta^3}{6}$$

Thus, for a single axis slew, the second-order Taylor's series errors are

$$\text{scale factor error } R = \sqrt{1 + \frac{\Delta^4}{4}} \quad (62)$$

$$\text{per cycle angle error} \sim -\frac{\Delta^3}{6}$$

Although the angle error for the second-order Taylor's series is only 1/2 the error for the first-order series, the scale factor is decreased to a large extent.

5.2.1.2.2 Three Axis Slewing Errors. The T matrix for a three axis slew using the second-order Taylor's series is shown in Eq (63) and the matrix eigenvalues are shown in Eq (64).

$$[T] = \begin{bmatrix} 1 - \Delta^2 & \Delta + \frac{\Delta^2}{2} & -\Delta + \frac{\Delta^2}{2} \\ -\Delta + \frac{\Delta^2}{2} & 1 - \Delta^2 & \Delta + \frac{\Delta^2}{2} \\ \Delta + \frac{\Delta^2}{2} & -\Delta + \frac{\Delta^2}{2} & 1 - \Delta^2 \end{bmatrix} \quad (63)$$

$$\lambda_1 = 1, \lambda_2 = 1 - \frac{3\Delta^2}{2} + j\sqrt{3}\Delta, \lambda_3 = 1 - \frac{3\Delta^2}{2} - j\sqrt{3}\Delta \quad (64)$$

The multiplication of T by itself n times was found to be the identical matrix shown in Eq (53), except that

$$R^2 = 1 + 9\frac{\Delta^4}{4} \quad (65)$$

$$\tan \alpha = \sqrt{3} \left( \frac{\Delta}{1 - 3\frac{\Delta^2}{2}} \right)$$

As in Eq (55), the attitude errors after n compute cycles are

$$\sin E_x = \sin E_y = \sin E_z = \frac{1}{3} \left[ 1 - R^n \left( \cos[n(\omega - \alpha)] - \sqrt{3} \sin[n(\omega - \alpha)] \right) \right] \quad (66)$$

$$\alpha = \tan^{-1} \left[ \frac{\sqrt{3} \Delta}{1 - 3\frac{\Delta^2}{2}} \right] \approx \frac{\sqrt{3} \Delta}{1 - 3\frac{\Delta^2}{2}} - \frac{\sqrt{3} \Delta^3}{(1 - 9\frac{\Delta^2}{2})} + \dots$$

$$\alpha \approx \sqrt{3} \left[ \Delta + \frac{\Delta^3}{2} \right] \quad (67)$$

$$\omega - \alpha \approx \frac{-\sqrt{3} \Delta^3}{2}$$

Thus, for a 3 axis slew, the second-order Taylor's series errors are

$$\begin{aligned} \text{scale factor } R &= +\sqrt{1 + \frac{9\Delta^4}{4}} \\ \text{angle error per cycle} &\approx -\frac{\Delta^3}{2} \end{aligned} \tag{68}$$

### 5. 2. 1. 3 Summary

The results of the analysis shown in this section are summarized in Table 5-I. Although the second-order Taylor's series reduces the angle error 50 percent, its primary advantage is the reduction of the scale factor error. However, the choice of the Taylor's series algorithm calls for a tradeoff between the available computer space and the required accuracy.

Table 5-I. Summary of Attitude Reference Equation Analysis

Algorithm	Single Axis Slew		Three Axis Slew	
	Scale Factor Error	Per Cycle Angle Error	Scale Factor Error	Per-Cycle Angle Error
First-Order Taylor's Series	$\sqrt{1 + \Delta^2}$	$\frac{\Delta^3}{3}$	$\sqrt{1 + 3\Delta^2}$	$-\Delta^3$
Second-Order Taylor's Series	$\sqrt{1 + \frac{\Delta^4}{4}}$	$\frac{\Delta^3}{6}$	$\sqrt{1 + 9\frac{\Delta^4}{4}}$	$-\frac{\Delta^3}{2}$

### 5. 2. 2 Scientific Simulation Test Results

In accordance with Reference 5.5, several tests of the attitude reference equations were performed on the 7094 computer. The errors obtained from these runs are entirely algorithm accuracy errors since the words used were 27 bits in length and the attitude increments (gyro outputs) were not quantized.

Several constant-rate single and three axis slewing tests were run for rates that varied from 25 deg/sec to 1.15 deg/sec. The results of these performance runs are tabulated in Table 5-II, and perform exactly

as expected from the analytical analysis just covered. All runs were performed at a direction cosine integration rate of 20 msec. Since the errors are proportional to the cube of the rotation increment, the errors would be decreased by a factor of one-eighth if a 10-msec integration interval were used.

The angular acceleration tests assess the accuracy of the attitude reference equations while under the influence of square wave angular accelerations about one or three axes. These angular accelerations are shown pictorially for a typical test in Figure 5-7. The rotation rate and rotation angle are shown in Figures 5-8 and 5-9.

The angular acceleration tests were designed so that the maximum rotation rate is  $\leq 25$  deg/sec. Consequently, the errors for the angular acceleration runs should be less than the errors obtained for the single axis slew of 25 deg/sec. The results of runs 10, 11, 12, and 12A in Table 5-II show that the errors are of the same form as the attitude angle plotted in Figure 5-9.

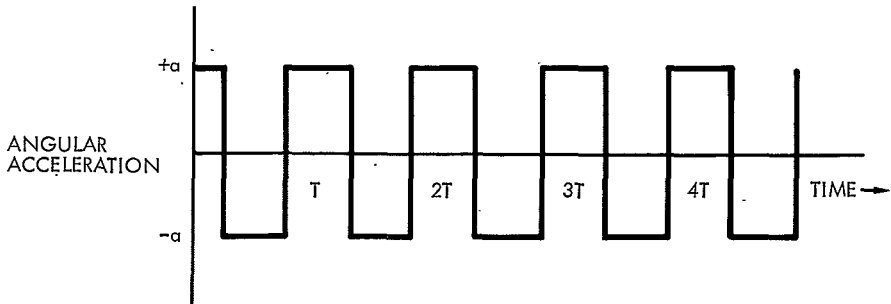


Figure 5-7. Angular Acceleration Profile

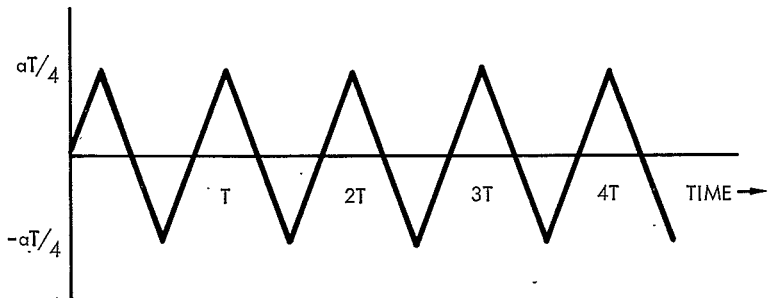


Figure 5-8. Resulting Rotation Rate Profile

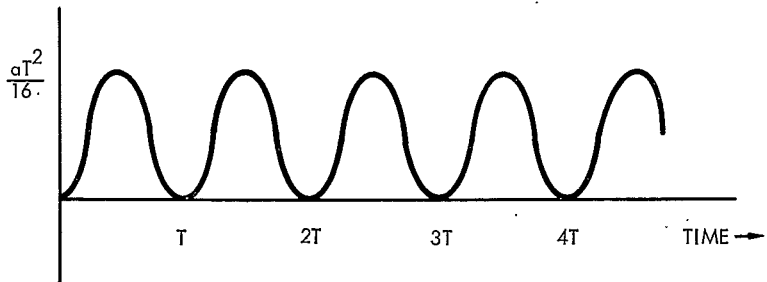


Figure 5-9. Resulting Attitude Rotation Angle

Table 5-II. Slewing Performance Results, Second-Order Taylor's Series

Attitude Errors						
Run No.	Description	$E_x$ ( $\mu$ rad)	$E_y$ ( $\mu$ rad)	$E_z$ ( $\mu$ rad)	Compute Cycles (n)	Attitude (deg)
1	X axis slew at 25 deg/sec	0.	0.	0.	0	0
		-0.0685	0.	0.	180	90
		-0.1370	0.	0.	360	180
		-0.205	0.	0.	540	270
		-0.274	0.	0.	720	360
2	Y axis slew at 25 deg/sec	0.	0.	0.	0	0
		0.	-0.0685	0.	180	90
		0.	-0.1368	0.	360	180
		0.	-0.2050	0.	540	270
		0.	-0.274	0.	720	360
3	Z axis slew at 25 deg/sec	0.	0.	0.	0	0
		0.	0.	-0.0685	180	90
		0.	0.	-0.1368	360	180
		0.	0.	-0.2050	540	270
		0.	0.	-0.274	720	360
4	X axis slew +1.15 deg/sec for 10 sec -1.15 deg/sec for 20 sec +1.15 deg/sec, etc.	$-2.54 \times 10^{-4}$	0.	0.	500	+11.5
		$-3.06 \times 10^{-4}$	0.	0.	1500	-11.5
		$-2.33 \times 10^{-4}$	0.	0.	2500	+11.5
		$-3.3 \times 10^{-4}$	0.	0.	3500	-11.5
5	Y axis slew +1.15 deg/sec for 10 sec -1.15 deg/sec for 10 sec	0.	$-6.24 \times 10^{-4}$	0.	1000	0
6	Three axis slew at 25.102186 deg/sec/axis	-0.16	-0.16	-0.16	138	120
		-0.317	-0.316	-0.318	276	240
		-0.475	-0.475	-0.474	414	360

Table 5-II. Slewing Performance Results, Second-Order Taylor's Series  
(Continued)

Attitude Errors						
Run No.	Description	$E_x$ ( $\mu$ rad)	$E_y$ ( $\mu$ rad)	$E_z$ ( $\mu$ rad)	Compute Cycles (n)	Attitude (deg)
7	Three axis slew at 10.011855 deg/sec/axis	-0.0255	-0.0262	-0.0258	346	120
		-0.0517	-0.0518	-0.0512	692	240
		-0.0775	-0.0775	-0.0775	1038	360
8	Three axis slew at +1.15 deg/sec/ axis for 10 sec -1.15 deg/sec for 10 sec	$1.1 \times 10^{-3}$	$1.1 \times 10^{-3}$	$5.6 \times 10^{-4}$	1000	0.
9	Three axis slew +25.102186 deg/sec for 3.4 sec and -25.102186 deg/sec for 3.4 sec	$7.4 \times 10^{-4}$	$-1.53 \times 10^{-3}$	$1.24 \times 10^{-3}$	340	0.
10	X axis angular acceleration 20.8 deg/sec <sup>2</sup> for 1.2 sec; -20.8 deg/sec <sup>2</sup> for 2.4 sec; 20.8 deg/sec <sup>2</sup> for 1.2 sec	0.0017	0.	0.	60	15
		0.01675	0.	0.	120	30
		0.017	0.	0.	180	15
		$1.675 \times 10^{-4}$	0.	0.	240	0.
11	Y axis angular acceleration  21.6 deg/sec <sup>2</sup> for 1.1 sec;  -21.6 deg/sec <sup>2</sup> for 2.2 sec;  21.6 deg/sec <sup>2</sup> for 1.1 sec	0.	$1.24 \times 10^{-4}$	0.	220	0.

Table 5-II. Slewing Performance Results, Second-Order Taylor's Series  
(Continued)

Attitude Errors						
Run No.	Description	$E_x$ ( $\mu$ rad)	$E_y$ ( $\mu$ rad)	$E_z$ ( $\mu$ rad)	Compute Cycles (n)	Attitude (deg)
12A	Z axis angular acceleration 39.2 deg/sec <sup>2</sup> for 0.6 sec; -39.2 deg/sec <sup>2</sup> for 1.2 sec; 39.2 deg/sec <sup>2</sup> for 0.6 sec	0.	0.	$4.16 \times 10^{-5}$	120	0.
12B	Three axis acceleration max $\dot{\alpha} = 23.5$ deg/sec accel = 39.2 deg/sec <sup>2</sup> for 0.6 sec, then -39.2 deg/sec <sup>2</sup> for 1.2 sec, etc.	0. 0.0025 $10^{-6}$ $2.86 \times 10^{-5}$ $4.37 \times 10^{-5}$ $6.5 \times 10^{-4}$	0. 0.014 $0.9 \times 10^{-3}$ $2. \times 10^{-4}$ $2.6 \times 10^{-4}$ $6.5 \times 10^{-4}$	0. 0.014 $3.8 \times 10^{-4}$ $8.35 \times 10^{-4}$ $1.25 \times 10^{-3}$ $6.5 \times 10^{-4}$	0 60 120 240 360 480	0. $14.1\sqrt{3}$ 0. 0. 0.
1A*	X axis slew at +25 deg/sec with a period of 4 sec initial direction cosines:	0. -2.7738 -5.5239 -8.308889	0. 0. 0. 0.	0. 0. 0. 0.	0 25 50 75	-25 -12.5 0. 12.5
$a_{ij}$	$\begin{bmatrix} 1 & 0 & 0 \\ 0 \cos 25^\circ & -\sin 25^\circ & 0 \\ 0 \sin 25^\circ & \cos 25^\circ & 0 \end{bmatrix}$	-11.059 -8.308889 -5.5239 -2.7738	0. 0. 0. 0.	0. 0. 0. 0.	100 125 150 175	25 12.5 0. -12.5
		0. -2.7738 -5.5239 -8.308889 -11.059 -8.308889	0. 0. 0. 0.	0. 0. 0. 0.	200 225 250 275	-25 -12.5 0. 12.5
		0. -2.7738 -5.5239 -8.308889 -11.059 -8.308889	0. 0. 0. 0.	0. 0. 0. 0.	300 325	25 12.5

\*Errors for Run 1A are in  $\mu$ rad.

Table 5-II. Slewing Performance Results, Second Order Taylor's Series  
(Continued)

Attitude Errors						
Run No.	Description	$E_x$ ( $\mu$ rad)	$E_y$ ( $\mu$ rad)	$E_z$ ( $\mu$ rad)	Compute Cycles (n)	Attitude (deg)
		-5.5239	0.	0.	350	0
		-2.7738	0.	0.	375	-12.5
		0.	0.	0.	400	-25
		-2.7738	0.	0.	425	-12.5
		-5.5239	0.	0.	450	0.
		-8.308889	0.	0.	475	12.5
		-11.059	0.	0.	500	25
		-8.308889	0.	0.	525	12.5
		-5.5239	0.	0.	550	0.
		-2.7738	0.	0.	575	-12.5
		0.	0.	0.	600	-25
		-2.7738	0.	0.	625	-12.5
		-5.5239	0.	0.	650	0.
		-8.03889	0.	0.	675	12.5
		-11.059	0.	0.	700	25
		etc.	0.	0.	etc.	etc.

### 5.2.3 Direction Cosines Coning Studies

One of the more critical areas of an analytical platform system is the integration algorithm used to compute the transformation between the vehicle and the desired navigation coordinate frame. These algorithms have at least two common error sources, (1) small angle approximations (truncation errors) and (2) computer quantization errors. One other error source of these algorithms is a loss of information with resultant drift under conditions of vehicle coning. A study of this last problem is presented below (Reference 5.4).

Vehicle coning is caused by limit cycles being applied to two of the vehicle's axes, the pitch and yaw axes for instance. If the two limit cycles are in phase, coning will not occur. The vehicle will experience no net rotation. If the limit cycles are out of phase, the vehicle will cone, with the maximum coning occurring for a 90-deg phase shift. For this study, the two limit cycle inputs are of the same frequency, the same amplitude, and have a 90-deg phase shift.

The errors of an algorithm experiencing coning are functions of:

- (1) The computer sampling interval,  $\Delta t$
- (2) The limit cycle frequency,  $f$ , (or the limit cycle period,  $T$ )
- (3) The limit cycle amplitude,  $A$
- (4) The phase shift between the two limit cycles.

Following a summary below, the errors of four algorithms will be examined as a function of these four parameters,  $\Delta t$ ,  $f$ ,  $T$ , and  $A$ .

Four algorithms were studied, namely the first- and second-order Taylor's series, backwards differencing, and a modified Runge-Kutta algorithm termed Algorithm A. A scientific computer program was used in the analysis and was designed for two limit cycle inputs (sinusoids) of the same frequency, amplitude, and a 90-deg phase shift.

The errors of the four algorithms are plotted as a percentage of the total vehicle coning rate versus the computer sampling interval normalized to the limit cycle period in Figure 5-10. When portrayed as a percentage of nominal coning rate, the errors are independent of the limit cycle amplitude, and they are independent of frequency if the sampling interval is

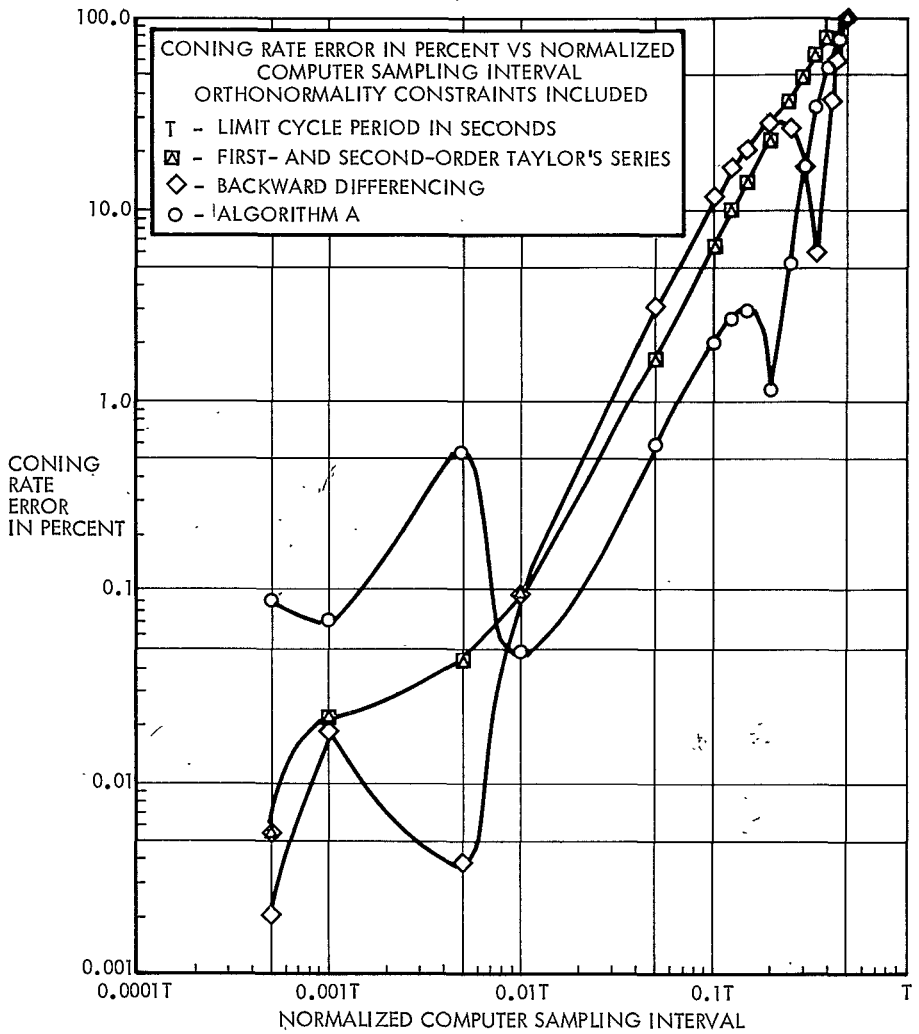


Figure 5-10. Coning Study Results

plotted proportional to the limit cycle period. That is, the percentage figure of the error is unaffected by the frequency if the limit cycle is sampled the same number of times per cycle. The normalized error is converted to a coning error in rad/sec by calculating  $W'$

where

$$W' = \frac{A^2 \omega}{2} = \text{the true vehicle coning rate, rad/sec}$$

$A$  = limit cycle amplitude, rad

$\omega$  = limit cycle frequency, rad/sec

Algorithm A has three distinct disadvantages:

- (1) Longest time lag
- (2) Longest computation time
- (3) Greatest computer memory requirements

Before Algorithm A could be used in a computer program, the effects of the time lag and its performance under alternate dynamic conditions must be investigated. When accuracy and computer requirements are both considered, the Taylor's series is the best algorithm.

#### 5.2.3.1 Algorithm Equations

The four algorithms examined in this study are:

- (1) First-order Taylor's series
- (2) Second-order Taylor's series
- (3) Backward Differencing
- (4) Algorithm A, a modified Runge-Kutta

The unmodified Runge-Kutta algorithm was not included because it appeared to be inadequate from previous study results.

The equations of the four algorithms are presented below in matrix notation. These equations also contain some orthonormality correction terms. \* The following notation is used:

$$\begin{aligned}
 E_1 &= 1 - \left( a_{11}^{n-1} \right)^2 - \left( a_{12}^{n-1} \right)^2 - \left( a_{13}^{n-1} \right)^2 \\
 E_2 &= 1 - \left( a_{21}^{n-1} \right)^2 - \left( a_{22}^{n-1} \right)^2 - \left( a_{23}^{n-1} \right)^2 \\
 E_3 &= 1 - \left( a_{31}^{n-1} \right)^2 - \left( a_{32}^{n-1} \right)^2 - \left( a_{33}^{n-1} \right)^2 \\
 E_{13} &= \left( a_{11}^{n-1} \right) \left( a_{13}^{n-1} \right) + \left( a_{21}^{n-1} \right) \left( a_{23}^{n-1} \right) \left( a_{33}^{n-1} \right)
 \end{aligned}
 \tag{69}$$

ortho-  
normality  
correction  
terms

$C_1, C_2$  are constants with a value of 0.5 for all computer simulations

$\begin{bmatrix} a_{ij}^n \end{bmatrix}$  is the nth direction cosine matrix

$\Delta\alpha_1, \Delta\alpha_2,$  and  $\Delta\alpha_3$  are the positive right-hand rule rotations about the respective x, y, z vehicle axes.

---

\*At this writing, complete evaluation of the requirement for the orthonormality terms had not been obtained. Indications are that they are not required.

5. 2. 3. 1. 1 Second-Order Taylor's Series

$$\left[ a_{ij}^n \right] = \begin{bmatrix} \left( 1 - \frac{\Delta a_3^2 + \Delta a_2^2}{2} \right) \left( \frac{\Delta a_1^2}{2} + \Delta a_3 \right) \left( \frac{\Delta a_3 \Delta a_1}{2} - \Delta a_2 \right) \\ \left( \frac{\Delta a_2 \Delta a_1}{2} - \Delta a_3 \right) \left( 1 - \frac{\Delta a_1^2 + \Delta a_3^2}{2} \right) \left( \frac{\Delta a_3 \Delta a_2}{2} + \Delta a_1 \right) \\ \left( \frac{\Delta a_3 \Delta a_1}{2} - \Delta a_2 \right) \left( \frac{\Delta a_2 \Delta a_3}{2} - \Delta a_1 \right) \left( 1 - \frac{\Delta a_2^2 + \Delta a_1^2}{2} \right) \end{bmatrix}$$

$$+ \left( a_{ij}^{n-1} \right) \begin{bmatrix} C_1 E_1 & C_1 E_1 & (C_1 E_1 - C_2 E_{13}) \\ C_1 E_2 & C_1 E_2 & C_1 E_2 \\ (C_1 E_3 - C_2 E_{13}) & C_1 E_3 & C_1 E_3 \end{bmatrix} \quad (70)$$

5. 2. 3. 1. 2 First-Order Taylor's Series

$$\left( a_{ij}^n \right) = \begin{bmatrix} 1 & \Delta a_3 & -\Delta a_2 \\ -\Delta a_3 & 1 & \Delta a_1 \\ \Delta a_2 & -\Delta a_1 & 1 \end{bmatrix} \left( a_{ij}^{n-1} \right) + \left( a_{ij}^{n-1} \right) \begin{bmatrix} C_1 E_1 & C_1 E_1 & (C_1 E_1 - C_2 E_{13}) \\ C_1 E_2 & C_1 E_2 & C_1 E_2 \\ (C_1 E_3 - C_2 E_{13}) & C_1 E_3 & C_1 E_3 \end{bmatrix} \quad (71)$$

5. 2. 3. 1. 3 Backward Differencing

$$\left( a_{ij}^n \right) = \left( a_{ij}^{n-1} \right) + \begin{bmatrix} 0 & \frac{\Delta a_3}{2} & -\frac{\Delta a_2}{2} \\ -\frac{\Delta a_3}{2} & 0 & \frac{\Delta a_1}{2} \\ \frac{\Delta a_2}{2} & -\frac{\Delta a_1}{2} & 0 \end{bmatrix} \left[ \left( 3a_{ij}^{n-1} \right) - \left( a_{ij}^{n-2} \right) \right]$$

$$+ \begin{pmatrix} a_{ij}^{n-1} \end{pmatrix} \begin{bmatrix} C_1 E_1 & C_1 E_1 & (C_1 E_1 - C_2 E_{13}) \\ C_1 E_2 & C_1 E_2 & C_1 E_2 \\ (C_1 E_3 - C_2 E_{13}) & C_1 E_3 & C_1 E_3 \end{bmatrix} \quad (72)$$

5.2.3.1.4 Algorithm A

$$\begin{pmatrix} a_{ij}^n \end{pmatrix} = \begin{bmatrix} \left( 1 - \frac{\Delta \alpha_3^{n-1} \Delta \alpha_3^n + \Delta \alpha_2^{n-1} \Delta \alpha_2^n}{2} \right) \left( \frac{\Delta \alpha_3^{n-1} + \Delta \alpha_3^n + \Delta \alpha_1^{n-1} \Delta \alpha_2^n}{2} \right) \left( \frac{-\Delta \alpha_2^{n-1} + \Delta \alpha_2^n - \Delta \alpha_1^{n-1} \Delta \alpha_3^n}{2} \right) \\ \left( -\frac{\Delta \alpha_3^{n-1} + \Delta \alpha_3^n - \Delta \alpha_2^{n-1} \Delta \alpha_1^n}{2} \right) \left( 1 - \frac{\Delta \alpha_1^{n-1} \Delta \alpha_1^n + \Delta \alpha_2^n \Delta \alpha_3^{n-1}}{2} \right) \left( \frac{\Delta \alpha_1^{n-1} + \Delta \alpha_1^n + \Delta \alpha_2^{n-1} \Delta \alpha_3^n}{2} \right) \\ \left( \frac{\Delta \alpha_2^{n-1} + \Delta \alpha_2^n + \Delta \alpha_3^{n-1} \Delta \alpha_1^n}{2} \right) \left( \frac{-\Delta \alpha_1^n + \Delta \alpha_1^{n-1} - \Delta \alpha_3^{n-1} \Delta \alpha_2^n}{2} \right) \left( 1 - \frac{\Delta \alpha_2^n \Delta \alpha_2^{n-1} + \Delta \alpha_1^n \Delta \alpha_3^{n-1}}{2} \right) \end{bmatrix} \begin{pmatrix} a_{ij}^{n-1} \end{pmatrix} + \begin{pmatrix} a_{ij}^{n-1} \end{pmatrix} \begin{bmatrix} C_1 E_1 & C_1 E_1 & (C_1 E_1 - C_2 E_{13}) \\ C_1 E_2 & C_1 E_2 & C_1 E_2 \\ (C_1 E_3 - C_2 E_{13}) & C_1 E_3 & C_1 E_3 \end{bmatrix} \quad (73)$$

### 5.2.3.2 Discussion

Typical coning study results can be seen in Figure 5-11. The following paragraphs are devoted to a discussion of the empirical observation that such results can be normalized into one extremely convenient curve, previously shown in Figure 5-10.

5.2.3.2.1 Frequency Normalization. Consider two sinusoidal signals of frequencies  $f_1$  and  $f_2$  with corresponding periods  $T_1$  and  $T_2$ . If signal 1 is sampled every  $T_1/K$  sec and signal 2 is sampled every  $T_2/K$  sec, the same body angular rotation will have occurred for both signals.

To investigate the coning error as a function of the limit cycle frequency, several scientific simulations were run for one limit cycle amplitude at different limit cycle frequencies and computer sampling intervals. The data of these simulations is tabulated later in Table 5-VII. The same data is shown in Table 5-III below, except as a percentage of the true vehicle coning rate. An examination of the data shows that the percentage error of the Taylor's series algorithm apparently is invariable for different frequencies as long as the computer samples the limit cycles the same number of times per cycle, i. e., computations are made for the same angular change between computation intervals.\*

Table 5-III. Taylor's Series Error in True Vehicle Coning Rate

$\Delta t$ (computer sampling interval)	0.5T	0.1T	0.05T	0.01T
Taylor's series error in %f = 1 cps	100	6.48	1.667	0.1
Taylor's series error in %f = 10 cps	100	6.48	1.667	0.097
Taylor's series error in %f = 100 cps	100	6.5	1.677	--

So, the data obtained for the four algorithms may be converted to any frequency by normalizing the output data with respect to the period of the input limit cycle.

---

\*It is likely that this result could be demonstrated analytically with little difficulty.

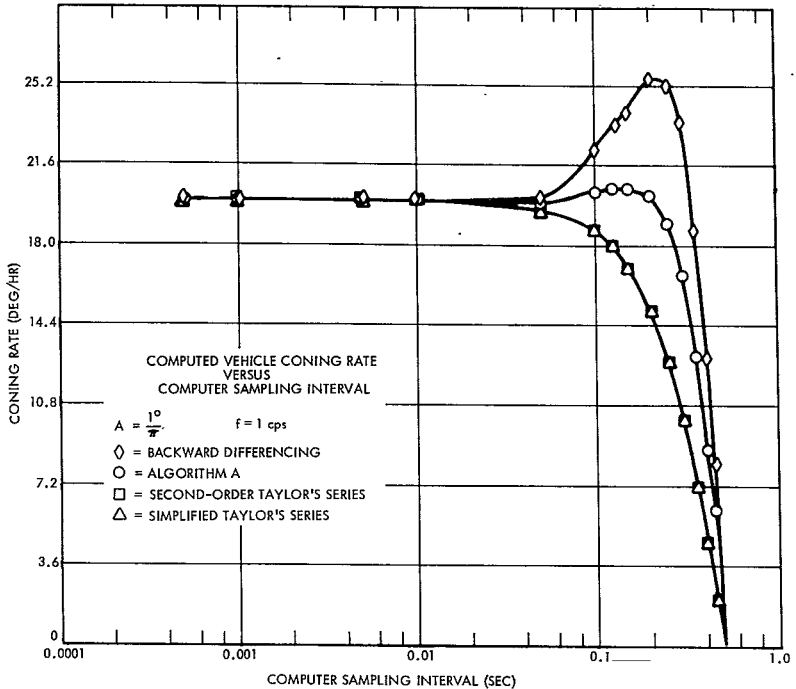


Figure 5-11. Typical Coning Study Results

5.2.3.2.2 Error Amplitude Variation. For each algorithm, several computer simulations were run for different limit cycle amplitudes and frequencies. After examining the output data, the following observations were made:

- (1) The vehicle normally experiences a coning rate proportional to the limit cycle frequency and the square of the limit cycle amplitude.\* (Refer to Paragraph 5.2.3.)

\*This checks with the Goodman and Robinson derivation in The American Society of Mechanical Engineers - Applied Mechanics Division, dated 11 January 1957, Paper No. 57-A-30.

Table 5-IV. Algorithm Coning Rate Error in Degrees Per Hour

Computer Sampling Interval (sec) $\Delta t$	Algorithm A			Taylor's Series			Backward Differencing			Simplified Taylor's Series		
	A = $1/2\pi^\circ$ f = 1 cps	A = $1/\pi^\circ$ f = 1 cps	A = $3/2\pi^\circ$ f = 1 cps	A = $1/2\pi^\circ$ f = 1 cps	A = $1/\pi^\circ$ f = 1 cps	A = $3/2\pi^\circ$ f = 1 cps	A = $1/2\pi^\circ$ f = 1 cps	A = $1/\pi^\circ$ f = 1 cps	A = $3/2\pi^\circ$ f = 1 cps	A = $1/2\pi^\circ$ f = 1 cps	A = $1/\pi^\circ$ f = 1 cps	A = $3/2\pi^\circ$ f = 1 cps
0.5	5.0	20.0	45.	5.0	20.0	45.	5.0	20.0	45.	5.0	20.0	45.
0.45	3.719	14.876	33.45	4.46	17.84	40.13	2.96	11.84	26.65	4.22	16.88	37.99
0.4	2.79	11.17	25.12	3.831	15.33	34.48	1.76	7.05	15.8	3.831	15.33	34.5
0.35	1.733	6.931	15.593	3.18	12.71	28.6	0.2964	1.185	2.666	3.18	12.71	28.6
0.3	0.841	3.363	7.566	2.492	9.877	22.22	-0.832	3.32	-7.481	2.492	9.877	22.22
0.25	0.261	1.046	2.354	1.82	7.268	16.36	-1.325	-5.299	-11.91	1.82	7.268	16.36
0.20	-0.057	0.2287	-0.5134	1.217	4.865	10.95	-1.37	-5.486	-12.34	1.217	4.865	10.95
0.15	-0.151	0.604	-1.359	0.71	2.84	6.4	-1.01	-4.05	-9.12	0.71	2.84	6.4
0.125	-0.135	-0.543	-1.219	0.50	2.01	4.5	-0.81	-3.237	-7.3	0.50	2.01	-1.219
0.1	-0.105	-0.416	-0.936	0.33	1.30	2.915	-0.56	-2.26	-5.1	0.33	1.3	2.915
0.05	-0.03	-0.118	-0.2658	0.0833	0.333	0.75	-0.157	-0.62	-1.4	0.0833	0.333	0.75
0.01	-0.025	-0.0105	-0.024	0.005	0.019	0.05	-0.005	-0.021	-0.045	0.005	0.019	0.05
0.005	-0.025	-0.0108	-0.025	0.0023	0.009	0.022	-0.0002	-0.0008	-0.0016	0.0023	0.009	0.022
0.001	-0.0036	-0.014	-0.033	0.00103	0.0045	0.011	0.00095	0.004	0.01	0.00103	0.0045	0.011
0.0005	-0.0046	-0.018	-0.042	$10^{-4}$	0.0005	0.002	0.00011	0.0004	0.0038	0.0001	0.0005	0.002

- (2) In all the scientific simulation results, the error in computing the vehicle coning rate is proportional to the square of the limit cycle amplitude (see Table 5-IV). Thus, it appears that if the error is known at an amplitude  $A_o$ , frequency  $f_o$ , and computer sampling interval  $\Delta t_o$ , the error for a different amplitude  $A$  at the same frequency and the same sampling interval may be found as

$$\text{Error}(f_o, A_o, \Delta t_o) = \text{Error}(f_o, A, \Delta t_o) (A/A_o)^2$$

- (3) The data shown in Table 5-V was obtained from a scientific simulation for three frequencies, 1, 10, and 100 cps, at the same amplitude of  $1/2\pi$ . After normalizing the computer sampling interval with respect to the period of the limit cycles, the error is found to be directly proportional to the frequency. The error at a new frequency may be apparently found by:

$$\text{Error}\left(f, A_o, \frac{\Delta t_o}{T_o}\right) = \text{Error}\left(f_o, A_o, \frac{\Delta t_o}{T_o}\right) (f/f_o)$$

Table 5-V. Taylor's Series Error

$\Delta t$ (computer sampling interval)	$0.5T^{**}$	$0.1T$	$0.05T$	$0.01T$
Taylor's series error in deg/hr at $f = 1$ cps	5	0.334	0.083	0.005
Taylor's series error in deg/hr at $f = 10$ cps	50	3.34	0.83	0.0485
Taylor's series error in deg/hr at $f = 100$ cps	500	33.5	8.38	--

\*\*  $T$  is the period of the limit cycle input

- (4) In view of observations (1) through (3), and since the vehicle coning rate and the algorithms' error in computing the coning rate are both proportional to the limit cycle frequency and the square of the limit cycle amplitude, the algorithms' errors, when portrayed as a percent of the true vehicle coning rate, will be independent of the limit cycle amplitude and frequency when the computer samples the limit cycles the same number of times per cycle.

The output data of several scientific simulations verifies the above, and this data is tabulated in Tables 5-VI and 5-VII. Three graphs of some simulation results are also shown in Figures 5-11, 5-12, and 5-13.

(5) A graph of the percentage error for the four algorithms versus the computer sampling interval normalized to the limit cycle period is plotted as Figure 5-11. From this graph, the error of any of the four algorithms for any limit cycle amplitude, frequency, and computer sampling interval may be found as follows:

- (a) Normalize the computer sampling interval with respect to the limit cycle period. For example, the normalized sampling interval for a 0.5 cps signal and a 20 msec sampling interval is  $\frac{0.02T}{2.0} = 0.01T$ .
- (b) Obtain the percentage error from the normalized graph (Figure 5-11). For instance, the percentage error for the Taylor's series is 0.1 percent for the 0.5 cps signal and a 20 msec sampling interval.

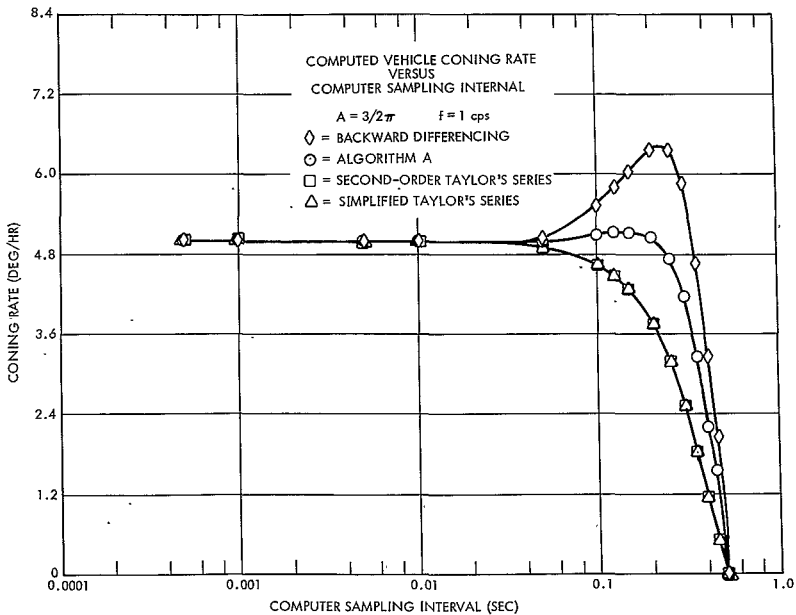


Figure 5-12. Typical Coning Study Results

- (c) Calculate the correct vehicle coning rate in the desired units. For a 0.5 cps signal with an amplitude of 0.01 rad, the vehicle coning rate is

$$\omega' = (0.01)^2 (\pi) (0.5) = 1.5708 \times 10^{-4} \text{ rad/sec}$$

$$\omega' = 0.5655 \text{ rad/hr} = 32.403 \text{ deg/hr}$$

- (d) The coning error is 0.1 percent of 32.4 deg/hr or an equivalent drift of 0.034 deg/hr.

5.2.3.2.3 Sample Calculation. In this paragraph, the coning error for three algorithms will be computed for 10 cps limit cycles of 0.03 deg amplitude using the graphical method described in the previous paragraphs. These calculations will be performed for computer sampling intervals varying from 2 to 50 msec. These results will then be compared with the output data of several scientific simulations to verify the accuracy of this analytical method of computing each algorithm's coning error. Although sample calculations are shown only for the Taylor's series algorithm, the same method was used for all the algorithms shown on the normalized graph.

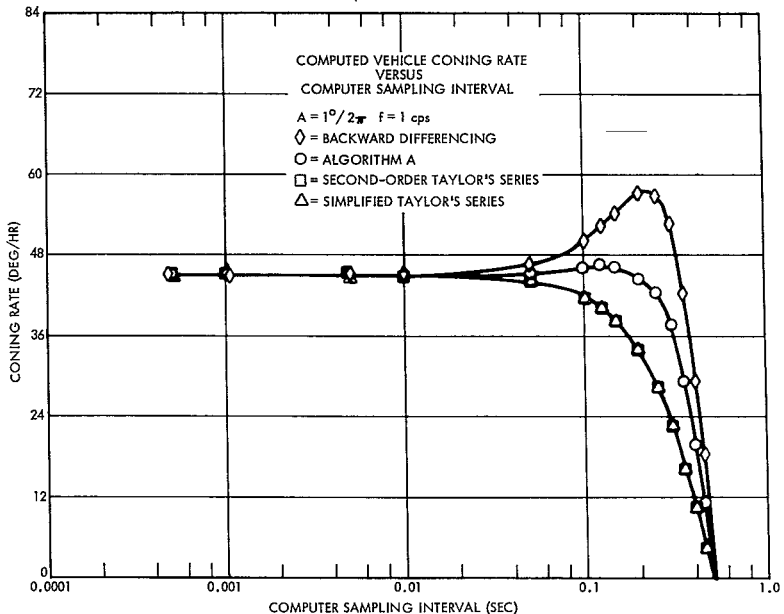


Figure 5-13. Typical Coning Study Results

Table 5-VI. Algorithm Coning Rate Error in Percent

Computer Sampling Interval (sec) $\Delta t$	Algorithm A			Taylor's Series			Backward Differencing			Simplified Taylor's Series		
	A = $1/2\pi^\circ$ f = 1 cps	A = $1/\pi^\circ$ f = 1 cps	A = $3/2\pi^\circ$ f = 1 cps	A = $1/2\pi^\circ$ f = 1 cps	A = $1/\pi^\circ$ f = 1 cps	A = $3/2\pi^\circ$ f = 1 cps	A = $1/2\pi^\circ$ f = 1 cps	A = $1/\pi^\circ$ f = 1 cps	A = $3/2\pi^\circ$ f = 1 cps	A = $1/2\pi^\circ$ f = 1 cps	A = $1/\pi^\circ$ f = 1 cps	A = $3/2\pi^\circ$ f = 1 cps
0.5	100	100	100	100	100	100	100	100	100	100	100	100
0.45	74.38	74.38	74.38	89.2	89.20	89.18	59.2	59.20	59.22	84.4	84.40	84.4
0.4	55.8	55.85	55.83	76.62	76.65	76.62	35.16	35.15	35.13	76.62	76.65	76.62
0.35	34.654	34.655	34.651	63.56	63.55	63.55	5.93	5.926	5.92	63.46	63.55	63.55
0.3	16.82	16.815	16.81	49.4	49.4	49.4	16.64	16.636	16.62	49.4	49.4	49.4
0.25	5.22	5.23	5.23	36.36	36.340	36.35	26.5	26.49	26.48	36.36	36.34	36.35
0.20	1.14	1.143	1.141	24.34	24.325	24.33	27.4	27.430	27.42	24.34	24.325	24.33
0.15	3.02	3.02	3.02	14.2	14.2	14.22	20.2	20.25	20.26	14.2	14.2	14.22
0.125	2.72	2.715	2.72	10.0	10.05	10.0	16.20	16.20	16.22	10.0	10.05	10.0
0.1	2.08	2.08	2.08	6.48	6.5	6.48	11.29	11.30	11.33	6.48	6.5	6.48
0.05	0.594	0.591	0.5906	1.667	1.667	1.667	3.13	3.1	3.11	1.667	1.667	1.667
0.01	0.052	0.051	0.051	0.1	0.095	0.11	0.10	0.105	0.10	0.1	0.095	0.11
0.005	0.52	0.54	0.55	0.045	0.045	0.049	0.004	0.0038	0.0036	0.045	0.045	0.049
0.001	0.072	0.070	0.073	0.02	0.022	0.023	0.0190	0.020	0.021	0.02	0.022	0.023
0.0005	0.092	0.090	0.092	0.002	0.0105	0.004	0.0023	0.002	0.002	0.002	0.01	0.004

Table 5-VII. Algorithm Coning Rate Error

Computer Sampling Interval $\Delta t$	Taylor's Series		
	A = $1/2\pi$ deg f = 1 cps	A = $1/2\pi$ deg f = 10 cps	A = $1/2\pi$ deg f = 100 cps
0.5	5.0		
0.45	4.46		
0.4	3.83		
0.35	3.18		
0.3	2.47		
0.25	1.82		
0.2	1.23		
0.15	0.73		
0.125	0.50		
0.1	0.33		
0.05	0.08	50	
0.01	0.005	3.28	
0.005	0.002	0.83	500
0.001	0.001	0.046	33.5
0.0005	$10^{-4}$	0.01	8.4

(1) Taylor's Series

Limit cycle frequency = 10 cps

Limit cycle amplitude = 0.03 deg

Computer sampling interval = 2 to 50 msec

For a limit cycle frequency of 10 cps and an amplitude of 0.03 deg, the true vehicle coning rate is

$$\omega' = \frac{1}{2} (0.03) (0.03) \left(\frac{\pi}{180}\right) (20\pi) (3600) \text{ arc deg/hr}$$

$$\omega' = 1.7765 \text{ arc deg/hr}$$

- (a) Computer sampling interval is 10 msec. The normalized sampling interval is

$$\frac{0.01}{0.1} T = 0.1T$$

From the normalized graph the error for the Taylor's series is 6.5 percent. Thus, the Taylor's series algorithm's coning error is 6.5 percent of 1.7765 arc deg/hr or 0.115 deg/hr.

- (b) Computer sampling interval is 5 msec. The normalized computer sampling interval is

$$\frac{0.005}{0.1} T = 0.05T$$

From the normalized graph, the error for the Taylor's series is 1.68 percent. Thus, the Taylor's series algorithm's coning error is 1.68 percent of 1.7765 arc deg/hr or 0.0297 deg/hr.

The coning errors of the Taylor's series algorithm at other computer cycle times were computed in the same manner and are presented in Table 5-VIII. The coning errors obtained from the scientific

Table 5-VIII. Coning Error for Taylor's Series Algorithm

$\Delta T$ (Sec)	Computer Simulation Taylor's Series Coning Error (arc deg/hr)	Graphical Computation of the Taylor's Series Coning Error (arc deg/hr)	Difference (arc deg/hr)
0.002	0.005	0.00515	$10^{-4}$
0.003	0.0109	0.0103	$6 \times 10^{-4}$
0.005	0.0295	0.0297	$2 \times 10^{-4}$
0.010	0.115	0.115	0
0.015	0.26	0.259	0.001
0.020	0.432	0.434	0.002
0.025	0.646	0.647	0.0011
0.040	1.36	1.35	0.011
0.050	1.7763	1.7763	0*

\*No information is obtained from a sinusoidal signal when it is sampled two times per cycle.

simulations are tabulated here and show that the graphical computation method obtains approximately the same values (within 0.01 deg/hr in most cases) as the scientific simulations.

(2) Backward Differencing

The coning errors of the backward differencing algorithm at several computer times were computed in the same manner, and are presented in Table 5-IX.

Limit cycle frequency = 10 cps

Limit cycle amplitude = 0.03 deg

Computer sampling interval = 2 to 50 msec

Table 5-IX. Coning Errors for Backward Differencing Algorithm

Computer Interval (Sec)	Computer Simulation Backward Differencing Coning Error (arc deg/hr)	Graphical Computation of the Backward Differencing Error (arc deg/hr)	Difference (arc deg/hr)
0.002	0.0096	0.0083	0.0013
0.003	0.0213	0.0213	0
0.005	0.0556	0.0587	0.0031
0.010	0.2046	0.1971	0.0075
0.012	0.2764	0.266	0.0104
0.015	0.3636	0.362	0.0016
0.020	0.4887	0.487	0.0017
0.025	0.4618	0.471	0.0009
0.040	0.6611	0.626	0.035
0.050	1.7765	1.7765	0

(3) Algorithm A

The coning errors of the Algorithm A at several computer times were computed in the same manner, and are presented in Table 5-X.

Limit cycle frequency = 10 cps

Limit cycle amplitude = 0.03 deg

Computer sampling interval = 2 to 50 msec

Table 5-X. Coning Errors for Algorithm A

Computer Sampling $\Delta t$ (sec)	Computer Simulator Algorithm A Coning Error (arc deg/hr)	Graphical Computation of Algorithm A Coning Error (arc deg/hr)	Difference (arc deg/hr)
0.002	0.0135	0.0012	0.012
0.005	0.0220	0.01065	0.01135
0.010	0.0487	0.0373	0.0114
0.012	0.0594	0.0465	0.0129
0.015	0.0568	0.0462	0.0106
0.020	0.0318	0.0202	0.0116
0.040	0.9804	0.991	0.0106
0.050	1.7765	1.7765	0

#### 5.2.4 The Attitude Reference Integration Rate

This paragraph determines the required attitude reference equation updating computation rate based upon the previous error analyses. The desired attitude reference equation drift rate is less than  $10^{-2}$  deg/hr, subject to the following assumed environment. Booster data from MSFC indicates that the vehicle pitched at a rate of 1.17 deg/sec (nominal) during a portion of the flight and that the maximum rate experienced during the flight was 3 deg/sec. Since the slewing errors increase with increased rates, a maximum rate of 6 deg/sec will be used for design purposes. During staging, the 6 deg/sec value is exceeded; however, this rate is present for a very short time and should cause only negligible errors (Reference 5.3).

The worst-case angular oscillation condition is assumed to be a coning with a 0.05 deg amplitude at 3 cps.

#### 5.2.4.1 Slewing Error Criteria

The slewing errors for the first- and second-order Taylor's series are shown in Table 5-XI. Because the angular error per cycle is largest for a three axis slew, this case will be used for design purposes.

From Table 5-XI, the angular error per cycle is  $\Delta^3$  for a first-order series and  $-\frac{\Delta^3}{2}$  for a second-order series.

Table 5-XI. First- and Second-Order Taylor's Series Slewing Errors

	Drift Errors of the First-Order Taylor's Series ( $10^{-2}$ deg/hr)					Drift Errors of the Second-Order Taylor's Series ( $10^{-2}$ deg/hr)				
	15	10	7.5	5	2	15	10	7.5	5	2
Computer Sampling Rate in msec										
Slewing Errors (maximum rate = 6 deg/sec)	5.37	2.3	1.34	0.6	0.0956	2.69	1.15	0.67	0.3	0.033
Coning Errors (0.05 deg at 3 cps)	2.07	1.0	0.044	0.028	0.0081	2.07	1.0	0.044	0.028	0.0081
RSS $3\sigma$	5.76	2.51	1.34	0.6	0.096	3.39	1.52	0.67	0.3	0.033

The scale factor errors are  $R = \sqrt{1 + 3\Delta^2}$  for a first-order series and  $R = \sqrt{1 + 9\frac{\Delta^4}{4}}$  for a second-order series. The primary advantage of using the second-order Taylor's series, naturally, is the scale factor error reduction.

Since  $\Delta$  in the above equations is defined to be

$$\Delta = \int_0^{\Delta t} \omega dt = \omega \Delta t$$

$$\Delta = (6) (3600) (4.85 \times 10^{-6}) \Delta t$$

$$\Delta = 0.105 \Delta t \text{ rad}$$

$$\Delta \theta_1 = -\Delta^3 = -1.16 \Delta t^3 \times 10^{-3}$$

$$\Delta \theta_2 = -\frac{\Delta^3}{2} = -0.581 \Delta t^3 \times 10^{-3} \quad (74)$$

$$\Delta \dot{\theta}_1 = \text{first-order drift rate} = \frac{\Delta \theta_1}{\Delta t} = -1.16 \Delta t^2 \times 10^{-3}$$

$$\Delta \dot{\theta}_2 = \text{second-order drift rate} = \frac{\Delta \theta_2}{\Delta t} = -0.581 \Delta t^2 \times 10^{-3} \quad (75)$$

For the drift in the attitude reference equations to be between  $<0.01$  deg/hr, the sampling interval  $\Delta t$  for the first- and second-order Taylor's series must be:

(1) First-order Taylor's series

$$\Delta t \leq 6.5 \text{ msec}$$

(2) Second-order Taylor's series

$$\Delta t \leq 9.14 \text{ msec}$$

#### 5.2.4.2 Coning Error Criteria

The true vehicle coning rate for the 3 cps, 0.05 deg amplitude limit cycles is  $\omega' = A^2 \omega / 2 = 1.48 \text{ deg/hr}$ .

For the drift rate of  $10^{-3} \text{ deg/hr}$ , the error is 0.0677 percent. Using the graph of Figure 5-11,

$$\Delta t = 0.007 T = 0.007 \left(\frac{1}{3}\right) = 2.33 \text{ msec}$$

For the drift rate of  $10^{-2} \text{ deg/hr}$ , the error is 0.677 percent. From Figure 5-11,

$$\Delta t = 0.03 T = 0.03 \left(\frac{1}{3}\right) = 10 \text{ msec}$$

Therefore, the coning errors require the computer integration period to be less than 10 msec.

In Table 5-XIII the errors for both algorithms are tabulated for five different sampling rates. From the table, it appears that the first-order Taylor's series meets the drift criteria if sampled every 5 msec, and the second-order Taylor's series meets the drift criteria if sampled every 10 msec.

However, these error calculations do not represent the total algorithm errors since the computer word size restrictions are not included. The errors due to the computer word size will be analyzed in Phase 2 with hypocomp simulations.

### 5.2.5 Attitude Reference Equation Quantization

#### 5.2.5.1 GP Mechanization

As mentioned in Subsection 5.1, the accuracy sought in the attitude reference equations will hold attitude errors about any axis at injection to less than 20 arc sec. The errors listed in Paragraph 5.2.4 cause a maximum ( $3 \sigma$ ) drift error of 0.0152 arc sec/sec during the flight, which would be approximately 15.2 arc sec attitude error at injection for a 1000 sec flight. During the 1000 sec, the second-order Taylor's series would update the direction cosines 100,000 times. For the RSS attitude errors to equal 20 sec, the attitude error due to quantization must be less than 13.0 sec.

Conservatively then, if the errors were additive, the required quantization must be less than

$$\frac{13 \text{ arc sec} \times 4.85 \times 10^{-6} \text{ rad/sec}}{10^5} = 6.31 \times 10^{-10} \text{ rad}$$

which would require 31 digits.

A much less conservative approach is to divide the attitude error at injection by the  $\sqrt{n}$  :

$$\Delta\theta = \frac{13 \times 4.85 \times 10^{-6}}{\sqrt{10^5}} = \frac{10^{-8} \times 4.85 \times 13}{3.16} = 2 \times 10^{-7}$$

which is equivalent to a word length of 23 bits.

Thus, the estimated word length required for the attitude reference equations is between 23 and 31 bits. The actual word length required will be obtained during Phase 2 of the MSFC study by ICS and hypocomp simulations of typical trajectories, and it is very likely that 23 bits will suffice.

#### 5.2.5.2 DDA Mechanization

It is likely that the quantization errors for the DDA will not be propagated as they are in the GP because of the DDA's integrator operation, so an 18 bit word is assumed sufficient (10 sec resolution). If the DDA is chosen for further study, this assumption will be verified in Phase 2.

### 5.3 ALIGNMENT STUDY

The attitude reference of a strapped-down system is maintained by a direction cosine matrix  $\begin{bmatrix} a_{ij} \end{bmatrix}$  relating the vehicle body axes to the desired guidance coordinate axes (refer to Paragraph 5.1.1).

The alignment of a strapped-down system simply requires the presence of correct direction cosines in the computer at the time the IMU "goes inertial." If the vehicle is perfectly motionless and vertical, the alignment could be accomplished simply by transferring the correct direction cosines to the computer. Since the vehicle is not motionless on the launch pad, the alignment must be performed in a manner similar to the alignment of an inertial platform. For this system, alignment will be accomplished by using the accelerometer outputs to compute leveling signals and a theodolite to compute azimuth error signals. Two sets of alignment equations are presently considered and are shown in Paragraph 5.1.7.

To analyze the errors of the alignment methods, scientific simulations of the two methods were performed on an IBM 7094 computer. This computer program obtained the errors which would result from the effects of vehicle sway, alignment equation inaccuracy, and theodolite signal errors. No computer quantization errors were included. Computer iteration rate was a parameter in the simulation, but quantization was not simulated.

#### 5.3.1 Scientific Simulation Description

The scientific simulation programmed for the IBM 7094 computer simulates acceleration and rotation rates experienced by the body-mounted gyros and accelerometers.

The inertial instruments experience the effects of gravity and the earth's rotation rate, as well as acceleration and rotation rates due to vehicle sway. The vehicle sway effects are programmed for a constant wind, the data for which was obtained from MSFC (Reference 5.6). Sample data received from MSFC is shown in Figures 5-14 through 5-16. As the vehicle sway data points out, the amount the vehicle sways depends on the station of the vehicle. For all simulations performed, the station was assumed to be 82.5 m.

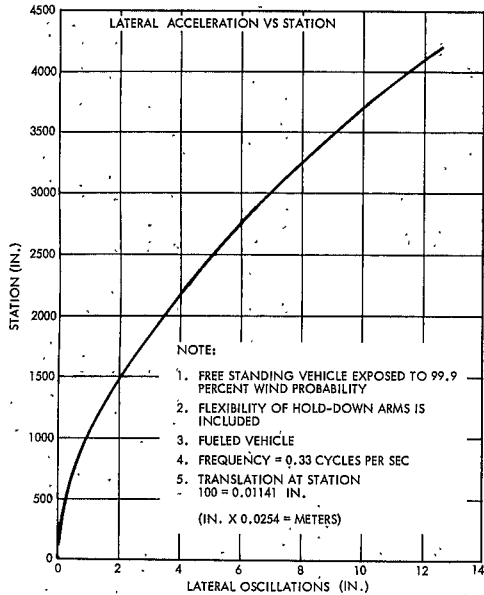


Figure 5-14. Saturn C-5 LOR (Suborbital Start) Vehicle on the Launcher/Umbilical Tower

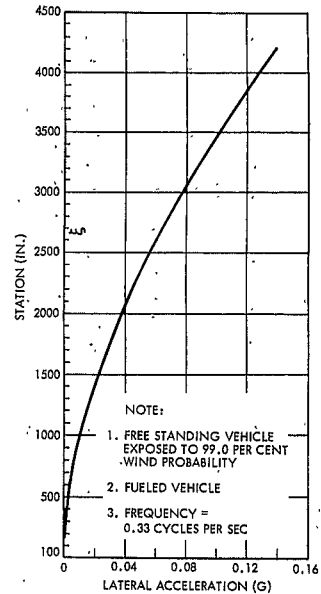


Figure 5-15. Saturn V LOR Vehicle on the Launcher/Umbilical Tower

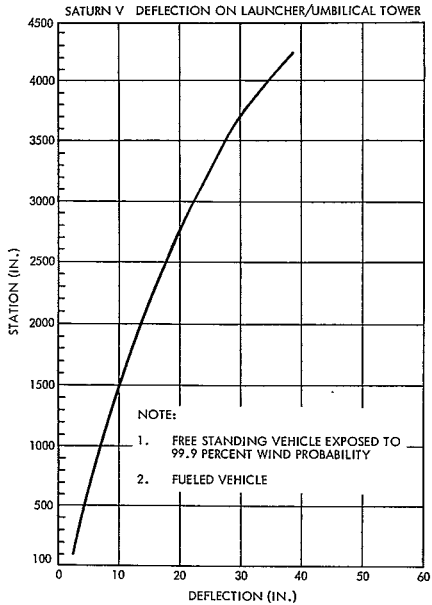


Figure 5-16. Saturn V Deflection on Launcher/Umbilical Tower

Due to the vehicle sway, the inertial instruments experience oscillatory accelerations as well as oscillatory rotation rates. Since MSFC's vehicle sway data quotes a frequency of 0.33 cps or 0.8 cps, the lateral motions of the vehicle were assumed to be of the following form:

$$D = D_0 \sin \omega_0 t$$

$$r = a_0 \sin \omega_0 t$$

$$\omega_s = a_0 \omega_0 \cos \omega_0 t \tag{76}$$

where

$D_o$  = maximum lateral deflection, m

$\alpha_o$  = maximum lateral deflection angle, rad

$\omega_o$  = vehicle sway radial frequency

$D$  = instantaneous lateral deflection, m

$\alpha$  = instantaneous lateral deflection angle, rad

The vehicle sway induced accelerations are derived from the equations for  $\alpha$ ,  $D$ , and  $\omega$ . The resulting accelerations have two components,  $A_D$  and  $A_F$ , where  $A_D$  is a lateral acceleration and  $A_F$  is a vertical acceleration.

$$A_D = D_o \omega_o^2 \sin \omega_o t \left[ \frac{\alpha_o^2}{2} (1 + \cos 2 \omega_o t) \right]$$

$$A_F = \frac{-\alpha_o D_o \omega_o^2}{2} [1 + 3 \cos 2 \omega_o t] \quad (77)$$

These acceleration components are oscillatory and attain maximum amplitudes of

$$A_D \text{ max.} = 0.84 \text{ m/sec}^2 \text{ (2.74 ft/sec}^2\text{)}$$

$$A_F \text{ max.} = 0.00182 \text{ m/sec}^2 \text{ (0.00598 ft/sec}^2\text{)}$$

when  $D_o = 0.20$  m (0.64 ft),  $\alpha_o = 0.00436$  rad, and  $\omega_o$  is 2.07 rad/sec.  $A_D$  causes the largest leveling error because it reaches a value of 0.085 g for the stated values of  $\alpha_o$ ,  $D_o$ , and  $\omega_o$ .

Using gravity, earth's rotation rate,  $\alpha$ ,  $\omega_s$ ,  $A_D$ , and  $A_F$ , the simulation computes the true vehicle orientation relative to a north-east-vertical coordinate system and computes the accelerometer and gyro outputs. The gyro outputs update the  $a_{ij}$  matrix relating the body axes to this coordinate system. The accelerometer outputs are then sent to the attitude reference equations to compute the leveling signals.

The azimuth reference signal is provided by a theodolite which is located along the astronomical north axis for simulation purposes, with an angle of inclination of 26 deg with the horizontal. Due to this inclination angle, the theodolite measures the azimuth with an error proportional to the tangent of the inclination angle and the deflection angle of the vehicle.

The porro prism is aligned with the  $z_b$  body axis ( $z_b$ ) in the  $x_b - z_b$  plane. The reflected signal is essentially a dot product of the  $z_b$  body axis with a vector colinear with the line of sight from the theodolite to the porro prism.

The unit vector defining the theodolite's line of sight to the porro prism is

$$\hat{i}_{th} = \cos i \hat{i}_N - \sin i \hat{i}_V$$

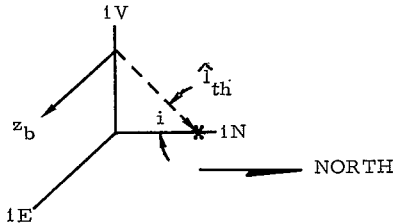
The  $z_b$  axis is defined to be

$$\hat{z}_b = a_{31T} \hat{i}_N + a_{32T} \hat{i}_V + a_{33T} \hat{i}_E$$

Thus the theodolite signal is

$$\hat{z}_b \cdot \hat{i}_{th} = \cos i a_{31T} - \sin i a_{32T}$$

$$u'_{zm} = \frac{\hat{z}_b \cdot \hat{i}_{th}}{\cos i} = a_{31T} - \tan i a_{32T}$$



The error in the theodolite signal is  $(\tan i) (a_{32T})$ , which is approximately one-half the vehicle deflection angle about the  $x_b$  axis. Since  $a_{32T}$  may be as large as 0.01 rad, this signal will cause an azimuth error as large as 0.6 deg if uncorrected.

### 5.3.2 Simulation Results

The preliminary simulation results of the strapped-down alignment equations verify that

- (1) The alignment gains must be very small to filter out the vehicle sway accelerations in the leveling signals.
- (2) The theodolite signal errors must be corrected for inclination angle errors, which can produce azimuth errors as large as 0.6 deg.
- (3) The alignment correction signals must be updated at a rate greater than twice per vehicle sway cycle.

As a consequence, the desired scientific simulation results are a combination of finding (1) the alignment computation interval, (2) the alignment gains required to obtain less than 20 arc sec alignment error, and (3) the correction of the theodolite azimuth reference signal.

#### 5.3.2.1 Alignment Gain Selection

Since the alignment gains must be very small to meet accuracy requirements, the reduction of the initial alignment error to 20 arc sec would require many computation or alignment cycles. For instance, consider the number of cycles required to reduce an error of 36 arc min to 20 arc sec using a feedback gain of  $5 \times 10^{-4}$ . That is, only  $5 \times 10^{-4}$  of the computed attitude error is corrected each alignment cycle. The attitude error as a function of time is approximately  $E = 2160 (0.9995)^n$  arc sec. For this error to be reduced to 20 arc sec, 4760 iterations would be needed:

$$(0.9995)^n = 0.0927$$

$$n = \frac{\ln(0.0927)}{\ln(0.9995)} = \frac{-2.38}{-0.0005}$$

$$n = 4760 \text{ iterations}$$

As a result, a very short iteration rate is required or the alignment time will be extremely long. Therefore, the alignment update interval is tentatively chosen to be 20 msec for all the following runs even though this interval requires that the alignment must run for at least 95.2 sec to reduce the error to 20 arc sec. (Moreover, the problems of erroneous accelerations due to vehicle sway add to the alignment time required.)

The first alignment gain used was 0.001 and was used in simulations with alignment update intervals of 20 msec. Although this gain converged fast, it did not provide the desired alignment leveling accuracy.

The gain was reduced to  $5 \times 10^{-4}$  at the same interval; this small gain reduced the leveling error considerably. However, leveling error was cyclic with a frequency equal to the vehicle sway frequency and reached a peak magnitude of  $10^{-3}$  rad ( $\sim 200$  arc sec). The gain was further reduced to  $10^{-4}$ , which reduced the leveling errors to  $\Delta\theta = 25 \sin 2.07t$  arc sec (see Figure 5-17), but the alignment gain must be decreased to  $10^{-5}$  for the specified leveling accuracy. At this time, however, no simulations have been performed for this gain value.

However, if the gain value of  $10^{-5}$  is used, the reduction of 36 arc min error to 20 arc sec error would require at least 238,000 alignment cycles, or a running period in real time of 79 1/3 min for a 20 msec alignment cycle. Since this period is extremely long, the alignment should be completed in four modes:

- Mode 1. Perform the alignment with alignment gains of  $10^{-3}$  for 60 sec. This mode will reduce alignment errors of 1 arc-deg to errors of 18 arc min.
- Mode 2. Continue the alignment with alignment gains of  $5 \times 10^{-4}$  for 60 sec. This will reduce the 18 arc min error to 240 arc sec.
- Mode 3. Continue the alignment with alignment gains of  $10^{-4}$  for 400 sec. This will reduce the alignment error from 240 arc sec to 35 arc sec.
- Mode 4. Continue the alignment with alignment gains of  $10^{-5}$  for at least 1200 sec. This will reduce the alignment error to 20 arc sec. To reduce the error to 10 arc sec, this set of gains must be used at least 2500 sec (41 2/3 min).

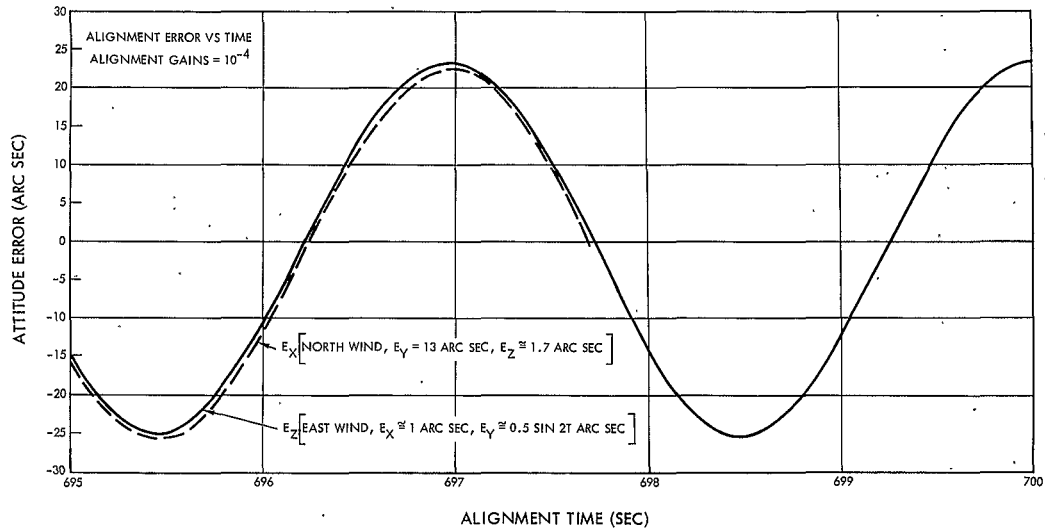


Figure 5-17. Alignment Gain Plot .

These four modes will reduce the error from 1 arc deg to 10 arc sec in 53 minutes. Since this method requires such a long time, it is recommended that a Kalman filter be used until the misalignment is reduced to 10 arc sec. At this time the alignment gains of the Kalman filter will be replaced with constant gains of  $10^{-5}$ . In this manner, the alignment will be performed much faster for the same accuracy. The Kalman filter to 10 arc sec is recommended because the errors due to computer quantization, accelerometer bias, and other theodolite instrument errors (such as bias) are not included.

### 5.3.2.2 Theodolite Signal Correction

As mentioned earlier, the theodolite error due to the theodolite inclination angle error may cause an azimuth error as large as 0.6 deg if uncorrected. To correct this error, the theodolite signal was modified in several ways.

The first correction method was to add a quantity to the theodolite signal  $u'_{zm}$  which is proportional to the attitude reference equations value for  $a_{31}$ . That is,

$$a_{31D} = u'_{zm} + \tan i a_{32} \quad (78)$$

However, since  $a_{31D}$  is small, this method may correct the  $u'_{zm}$  in the wrong direction. For instance, let  $a_{31T} = 0.004$ ,  $a_{32T} = 0.01$ , and  $\tan i = 0.5$ , then,  $u'_{zm} = 0.004 - 0.005 = -0.001$ . If the computed value for  $a_{31}$  is negative,  $u'_{zm}$  will become more negative and will cause the azimuth alignment to become unstable.

The second correction method was to use the velocity increments from the accelerometer:

$$a_{31D} = u'_{zm} + \tan i \left( \frac{\Delta V_z}{g T_a} \right) \quad (79)$$

If the vehicle sway causes accelerations along the z axis, this method becomes as inaccurate as the original  $u'_{zm}$ . For instance, let  $T_a = 0.02$ ,  $A_z = g a_{32T} + A_d$ . Then

$$u'_{zm} = a_{31T} + \tan i \left[ -a_{32T} + \frac{g a_{32T} T_a}{g T_a} + \frac{2.74}{g T_a} \times 1/2 (\cos \omega_0 t - \cos \omega_0 t) \right]$$

$$u'_{zm} = a_{31T} + \tan i \left[ \frac{1.37}{g} \right]$$

$$u'_{zm} = a_{31T} + \tan i [0.04]$$

or  $u'_{zm}$  is in error by 0.05 rad.

Although this error is cyclic, it is larger than the original azimuth error.

The third correction method was to accumulate the z accelerometer outputs and then compensate for  $a_{32T}$ . That is,

$$a_{31D} = u'_{zm} + \tan i \left( \frac{\Delta \xi}{gt} \right)$$

$$\Delta \xi = \Delta \xi + \Delta V_z \quad (80)$$

This method reduces the theodolite inclination error nearly to zero. That is,

$$a_{31D} = a_{31T} + \tan i \left[ -a_{32T} + \frac{g a_{32T} t}{gt} + \frac{\int_0^t A \sin \omega_0 t}{gt} \right]$$

$$a_{31D} \cong a_{31T} + \frac{\tan i}{gt} \left[ \frac{A}{\omega} (1 - \cos \omega_0 t) \right]$$

$$\lim_{t \rightarrow \infty} a_{31D} \cong a_{31T} \quad (81)$$

The scientific simulations show that this method reduces the azimuth error to less than 10 arc sec.

#### 5.3.2.3 Conclusions

Constant gain filter methods may be used for alignment purposes but will require almost 1 hr to reduce an initial error of 1 arc deg to less than 20 arc sec. Also, both alignment methods presented (refer to Subsection 5.3) may be used although the first method is preferable.

Since the constant gain filters require a long calibration time, it is recommended that a variable gain filter be used (such as a Kalman filter). Since it is desirable to align until launch time, it is also suggested that the variable gains be changed to constant gains of  $10^{-5}$  when the alignment has attained an accuracy around 10 arc sec.

## 5.4 ACCELERATION INTEGRATION ANALYSIS

In this subsection, the acceleration integration equations presented in Paragraph 5.1.2 are discussed with regard to software errors. No consideration is given to computer quantization errors nor to errors associated with the fact that the accelerometers are not located at the same point. These errors will be analyzed in Phase 2 of the MSFC study. It seems likely, though, that they will be small.

Furthermore, the work performed to date is not sufficient to support a specific prediction in the velocity and position errors at the end of a flight. (These are errors that result from computer errors in integrating velocity, of course.) Nonetheless, sufficient work has been done to indicate the possibility that these errors can be kept under 0.3 msec (1 ft/sec) per axis ( $3\sigma$ ), so this number is used in Section 3 but is subject to verification during the Phase 2 study.

Acceleration equation errors resulting from any of the limit cycling effects will be functions of the limit cycle frequency, the acceleration integration frequency, and the attitude reference matrix updating frequency. In Phase 2 of the study, these velocity errors will be examined for the effects of the sampling frequency, limit cycle frequency, acceleration amplitude and time variation, and computer quantization effects. If possible, these results will be arranged in a form similar to that of the direction cosines coning results (see Paragraph 5.2.3) to facilitate the design of strapped-down systems.

The acceleration integration errors are a function of the vehicle dynamics and can only be approximated in the simulations. Nonetheless, meaningful results can be obtained by considering the effects of specific inputs as was done with the attitude reference studies. In this respect, it is convenient to consider the following motions:

(1) Vehicle Rotations

(a) Constant Slewing Rates

- About one axis only
- About two or more axes, in phase
- About two or more axes, out of phase

- (b) Constant Rate Limit Cycling
  - About one axis only
  - About two or more axes, in phase
  - About two or more axes, out of phase
- (c) Sinusoidal Limit Cycling
  - About one axis only
  - About two or more axes, in phase
  - About two or more axes, out of phase  
(usually referred to as vehicle coning)

(2) Vehicle Accelerations

- (a) Constant Accelerations  $A_0$
- (b) Ramp accelerations  $A_1 t$
- (c) Parabolic accelerations  $A_2 t^2$
- (d) In general, the acceleration is of the form

$$A = A_0 + A_1 t + A_2 t^2 + \dots$$

During powered flight, the vehicle may experience any combination of these motions. So for a complete representation of the errors due to the acceleration integration equations, each of the vehicle rotational motions should be analyzed during each of the possible accelerations, constant, ramp, or parabolic. Then the errors should be computed during combinations of several vehicle motions while the vehicle is subjected to the three types of accelerations, because the errors are apparently non-linear functions of the vehicle dynamics being discussed.

At this time, the complete analysis of the acceleration integration equations is not available. Only preliminary results are available for constant slews about one axis, under the influence of constant accelerations. The other errors and their combinations must be analyzed at a later time.

5. 4. 1 Acceleration Integration Errors

The acceleration integration methods presented in Paragraph 5. 1. 2 are very similar, and may be represented as in Eq (82).

$$\begin{bmatrix} \Delta V_{xI} \\ \Delta V_{yI} \\ \Delta V_{zI} \end{bmatrix} = \begin{bmatrix} a_{11} & a_{21} & a_{31} \\ a_{12} & a_{22} & a_{32} \\ a_{13} & a_{23} & a_{33} \end{bmatrix} \begin{bmatrix} \Delta V_{xb} \\ \Delta V_{yb} \\ \Delta V_{zb} \end{bmatrix} \quad (82)$$

where

$\Delta V_{xI}$ ,  $\Delta V_{yI}$ ,  $\Delta V_{zI}$  = velocity increments accumulated over  $\Delta t$  sec along the x, y, z inertial axes.

$\Delta V_{xb}$ ,  $\Delta V_{yb}$ ,  $\Delta V_{zb}$  = velocity increments accumulated by the x, y, z body-mounted accelerometers

$\begin{bmatrix} a_{ji} \end{bmatrix}$  = transpose of the  $a_{ij}$  matrix relating the vehicle body axes to the inertial navigation axis.

The velocity increments along the inertial axes and the vehicle body axes were accumulated for  $\Delta t$  sec. The values used for the direction cosines in the  $a_{ji}$  matrix may be the values at the end of the  $\Delta t$  interval the velocity increments were accumulated (Method 1) or they may be the values of the direction cosines present at the middle of the interval  $\frac{\Delta t}{2}$  (Method 2).

The accuracy of these two methods is evaluated analytically while the vehicle experiences several dynamic conditions of accelerations and rotations. The errors of the two proposed acceleration integration methods will be obtained where these results are compared with the correct integral of the dynamic conditions.

#### 5. 4. 2 Error Analysis for Single Axis Slews and Constant Accelerations

The accelerations and body rates for the error analysis are

$$\bar{A} = \text{vehicle acceleration} = A_1 x_b + A_2 y_b + A_3 z_b$$

$$\bar{\omega} = \text{vehicle rotation rate} = \omega_1 x_b$$

For this constant rotation rate  $\omega_1$ , the  $a_{ij}$  matrix as a function of time is

$$\begin{bmatrix} x_b \\ y_b \\ z_b \end{bmatrix} = \begin{bmatrix} 1 & 0 & 0 \\ 0 & \cos \omega_1 t & \sin \omega_1 t \\ 0 & -\sin \omega_1 t & \cos \omega_1 t \end{bmatrix} \begin{bmatrix} x_s \\ y_s \\ z_s \end{bmatrix} \quad (83)$$

assuming the  $a_{ij}$  matrix at the start of the rotation is the identity matrix  $[\mathbf{I}]$ . The inertial accelerations are

$$\bar{A} = A_1 x_s + (A_2 \cos \omega_1 t - A_3 \sin \omega_1 t) y_s + (A_2 \sin \omega_1 t + A_3 \cos \omega_1 t) z_s \quad (84)$$

The true inertial velocity increments over T sec are

$$\begin{aligned} \Delta V'_{xs} &= A_1 \Delta t \\ \Delta V'_{ys} &= \frac{A_2}{\omega_1} \left[ \sin (\omega_1 (t_0 + T)) - \sin \omega_1 t_0 \right] + \frac{A_3}{\omega_1} \left[ \cos \omega_1 (t_0 + T) - \cos \omega_1 t_0 \right] \\ \Delta V'_{zs} &= \frac{A_2}{\omega_1} \left[ \cos \omega_1 (t_0 + T) - \cos \omega_1 t_0 \right] + \frac{A_3}{\omega_1} \left[ \sin \omega_1 (t_0 + T) - \sin \omega_1 t_0 \right] \end{aligned} \quad (85)$$

However, the integration performed by the acceleration integration equations, using the direction cosines at the end of an interval  $\Delta t$ , provides the following inertial velocity increments:

$$\begin{bmatrix} \Delta V'_{xs} \\ \Delta V'_{ys} \\ \Delta V'_{zs} \end{bmatrix} = \begin{bmatrix} A_1 \Delta t & A_2 \Delta t & A_3 \Delta t \end{bmatrix} \begin{bmatrix} 1 & 0 & 0 \\ 0 & \cos \omega_1 (t_0 + \Delta t) & \sin \omega_1 (t_0 + \Delta t) \\ 0 & -\sin \omega_1 (t_0 + \Delta t) & \cos \omega_1 (t_0 + \Delta t) \end{bmatrix} \quad (86)$$

$$\Delta V_{xs} = A_1 \Delta t$$

$$\Delta V_{ys} = A_2 \Delta t \cos \omega_1 (t_0 + \Delta t) - A_3 \Delta t - A_3 \Delta t \sin \omega_1 (t_0 + \Delta t)$$

$$\Delta V_{zs} = A_3 \Delta t \cos \omega_1 (t_0 + \Delta t) + A_2 \Delta t \sin \omega_1 (t_0 + \Delta t)$$

The accumulated velocity increments, after T sec, are

$$\Delta V_{xs} = \sum_{n=1}^{\frac{T}{\Delta t}} A_1 n \Delta t$$

$$\Delta V_{ys} = A_2 \Delta t \sum_{n=1}^{\frac{T}{\Delta t}} \cos \left[ \omega_1 (t_0 + n \Delta t) \right] - A_3 \Delta t \sum_{n=1}^{\frac{T}{\Delta t}} \sin \left[ \omega_1 (t_0 + n \Delta t) \right] \quad (87)$$

$$\Delta V_{zs} = A_2 \Delta t \sum_{n=1}^{\frac{T}{\Delta t}} \sin \left[ \omega_1 (t_0 + n \Delta t) \right] + A_3 \Delta t \sum_{n=1}^{\frac{T}{\Delta t}} \cos \left[ \omega_1 (t_0 + n \Delta t) \right]$$

After T sec, the velocity errors may be found by subtracting  $\Delta V_{js}$  from the  $\Delta V_{js}^!$  values, as shown below:

$$\Delta V_x = \Delta V_x^! - \Delta V_{xs}$$

$$\Delta V_y = \Delta V_y^! - \Delta V_{ys} \quad (88)$$

$$\Delta V_z = \Delta V_z^! - \Delta V_{zs}$$

Consider the second integration method using the direction cosines at the middle of the interval. These equations provide the following inertial velocity increments:

$$\begin{bmatrix} \Delta V_{xs} \\ \Delta V_{ys} \\ \Delta V_{zs} \end{bmatrix} = \begin{bmatrix} A_1 \Delta t & A_2 \Delta t & A_3 \Delta t \end{bmatrix} \begin{bmatrix} 1 & 0 & 0 \\ 0 & \cos \left[ \omega_1 \left( t_0 + \frac{\Delta t}{2} \right) \right] & \sin \left[ \omega_1 \left( t_0 + \frac{\Delta t}{2} \right) \right] \\ 0 & -\sin \left[ \omega_1 \left( t_0 + \frac{\Delta t}{2} \right) \right] & \cos \left[ \omega_1 \left( t_0 + \frac{\Delta t}{2} \right) \right] \end{bmatrix} \quad (89)$$

$$\Delta V_{xs} = A_1 \Delta t$$

$$\Delta V_{ys} = A_2 \Delta t \cos \left[ \omega_1 \left( t_0 + \frac{\Delta t}{2} \right) \right] - A_3 \Delta t \sin \left[ \omega_1 \left( t_0 + \frac{\Delta t}{2} \right) \right]$$

$$\Delta V_{zs} = A_3 \Delta t \cos \left[ \omega_1 \left( t_0 + \frac{\Delta t}{2} \right) \right] + A_2 \Delta t \sin \left[ \omega_1 \left( t_0 + \frac{\Delta t}{2} \right) \right]$$

After T sec, the accumulated velocity increments are

$$\Delta V_{xs} = \sum_{n=1}^{\frac{T}{\Delta t} - 1} A_1 n \Delta t$$

$$\Delta V_{ys} = A_2 \Delta t \sum_{n=0}^{\frac{T}{\Delta t} - 1} \cos \left[ \omega_1 \left( t_0 + \frac{\Delta t}{2} + n \Delta t \right) \right] - A_3 \Delta t \sum_{n=1}^{\frac{T}{\Delta t} - 1} \sin \left[ \omega_1 \left( t_0 + \frac{\Delta t}{2} + n \Delta t \right) \right]$$

$$\Delta V_{zs} = A_2 \Delta t \sum_{n=0}^{\frac{T}{\Delta t} - 1} \sin \left[ \omega_1 \left( t_0 + \frac{\Delta t}{2} + n \Delta t \right) \right] + A_3 \Delta t \sum_{n=0}^{\frac{T}{\Delta t} - 1} \cos \left[ \omega_1 \left( t_0 + \frac{\Delta t}{2} + n \Delta t \right) \right]$$

(90)

The errors of both integration methods are shown in Table 5-XII. The errors are decreased considerably by using the direction cosines at the middle of the interval for the constant acceleration and X axis slew. Further analysis must be performed, however, to reveal which method is the best. Some scientific simulation results are shown in Table 5-XIII, which also shows that Method 2 is a major improvement.

#### 5.4.3 Estimated Computer Word Length

The quantization errors will be made to cause velocity errors of 0.09 m/sec (0.3 ft/sec) or less after the 1000 sec flight. These errors will be based on a maximum acceleration estimate of 4 g.

If the velocity increments are updated every 20 msec, the quantization error for  $n$  iterations will be between  $1.8 \times 10^{-6}$  msec ( $6 \times 10^{-6}$  ft/sec) ( $0.3/n$ ) and  $0.4 \times 10^{-3}$  msec ( $1.34 \times 10^{-3}$  ft/sec) ( $0.3/\sqrt{n}$ ). To provide the velocity register with the capability of containing velocity changes as large as 61 m/sec (200 ft/sec) and still not cause unreasonable quantization errors, a word size between 18 and 26 bits would be required. For the same considerations with velocity increments to be updated every 10 msec, the word size would have to be between 19 and 27 bits.

Table 5-XII. Acceleration-Integration Errors for a Constant 5 deg/sec Slew about the  $X_b$  Axis and a Constant 3-g Acceleration Along the Y Body Axis

Acceleration Integration Method		Time	$\Delta V_{x_s}$	$\Delta V_y$	$\Delta V_z$
Method 1	$\begin{bmatrix} 1 & 0 & 0 \\ 0 & 1 & 0 \\ 0 & 0 & 1 \end{bmatrix}$	0.1	0	$3 \times 10^{-5}$	-0.00838
		0.2	0	$1.3 \times 10^{-4}$	-0.01675
		0.3	0	$3 \times 10^{-4}$	-0.02513
	$\begin{bmatrix} 1 & 0 & 0 \\ 0 & 0.707 & -0.707 \\ 0 & 0.707 & 0.707 \end{bmatrix}$	0.1	0	0.00594	-0.00590
		0.2	0	0.0119	-0.0117
		0.3	0	0.017989	-0.0175
	$\begin{bmatrix} 1 & 0 & 0 \\ 0 & 0 & -1 \\ 0 & 1 & 0 \end{bmatrix}$	0.1	0	+0.00838	$3 \times 10^{-5}$
		0.2	0	+0.01675	$1.3 \times 10^{-4}$
		0.3	0	0.02513	$3 \times 10^{-4}$
Method 2	$\begin{bmatrix} 1 & 0 & 0 \\ 0 & 1 & 0 \\ 0 & 0 & 1 \end{bmatrix}$	0.1	0	---	---
		0.2	0	$-2 \times 10^{-5}$	$-2 \times 10^{-7}$
		0.3	0	$-3 \times 10^{-5}$	$-3 \times 10^{-7}$
	$\begin{bmatrix} 1 & 0 & 0 \\ 0.707 & -0.707 \\ 0.707 & 0.707 \end{bmatrix}$	0.1	0	$-6 \times 10^{-6}$	$-7 \times 10^{-6}$
		0.2	0	$-1.3 \times 10^{-5}$	$-1.4 \times 10^{-5}$
		0.3	0	$-2 \times 10^{-5}$	$-2.1 \times 10^{-5}$
	$\begin{bmatrix} 1 & 0 & 0 \\ 0 & 0 & -1 \\ 0 & 1 & 0 \end{bmatrix}$	0.1	0	$-2 \times 10^{-7}$	$-2 \times 10^{-5}$
		0.2	0	$-3 \times 10^{-7}$	$-3 \times 10^{-5}$
		0.3	0	$-7 \times 10^{-6}$	$-6 \times 10^{-6}$

Table 5-XIII. Summary of Velocity Transformation Equation Errors with no Vehicle Limit Cycling

	20 msec Compute Cycle		40 msec Compute Cycle		Modified 40 msec Compute Cycle	
	$\Delta V_{X_S}$ Error (ft/sec)	$\Delta V_{Z_S}$ Error (ft/sec)	$\Delta V_{X_S}$ Error (ft/sec)	$\Delta V_{Z_X}$ Error (ft/sec)	$\Delta V_{X_S}$ Error (ft/sec)	$\Delta V_{Z_S}$ Error (ft/sec)
Case 17 (400 sec burn) $\omega = 0.15$ deg/sec; $A = 16$ ft/sec <sup>2</sup>	-0.158	+0.036	-0.316	0.072	-0.0060	0.0068
Case 18 (5 sec burn) $\omega = 10$ deg/sec, $A = 11$ ft/sec <sup>2</sup>	-0.03907	+0.08436	-0.07762	+0.16900	+0.00008	+0.00004
New Case (2 sec burn) $\omega = 25$ deg/sec, $A = 11$ ft/sec <sup>2</sup>	-0.03869	+0.07397	-0.07613	+0.16965	+0.00024	+0.00011

## REFERENCES

- 5.1 D. F. McAlister, "MSFC Strapdown Preliminary Alignment Study," TRW IOC 9351.4-197, dated 28 September 1965.
- 5.2 F. B. Hildebrand, "Methods of Applied Mathematics," Prentice Hall Inc., Englewood Hills, New Jersey, 1952.
- 5.3 M. W. Klotz, "Information Regarding Space Booster Angular Rate Environments," TRW IOC 9351.6-625, dated 2 December 1965.
- 5.4 K. L. Baker, "Summary of LEM-AGS Preliminary Attitude Reference and Navigation Equation Performance," TRW IOC 9351.4-220, dated 26 October 1965.
- 5.5 R. Eshbaugh, R. D. Davis, and K. Baker, "Attitude Reference and Navigation Scientific Simulation Results — LEM AGS," TRW IOC 7221.7-4, dated 8 February 1966.
- 5.6 "Saturn Wind Induced Motion on Launcher," dated 8 October 1965, (no author, hand carried from MSFC).
- 5.7 "Astrionics System Handbook, Saturn Launch Vehicle," 1 August 1965, George C. Marshall Space Flight Center, NASA.

## 6. COMPUTER STUDIES

Basically, the objective of the strapped-down guidance study is to define a particular set of platform equations that will permit the use of a strapped-down gyro assembly for an attitude reference system. The unit that mechanizes these computations, the computer, is the subject of this section. The incremental digital pickoff instrumentation of gyros and accelerometers suggests the use of a computational unit that can accept, perform arithmetic operations on, and deliver information in incremental form. The most satisfactory means of implementing these operations is the Digital Differential Analyzer (DDA).

The primary difficulty with conventional DDA mechanizations is that a large amount of equipment is needed for any substantial number of equations. Therefore, the feasibility of using such a device depends upon the organization of the element itself. It is apparent at the outset that each minor computation cannot have a significant amount of hardware reserved solely to itself, so if the device is to be practical, the arithmetic section must be time-shared with many of the computations.

The other means suggested for solving the required equations is the more conventional GP digital computer. Since GP digital computers offer flexibility advantages, a study was made to determine the characteristics such a device would require in order to satisfy the strapped-down system demands. Pertinent information regarding solution time, number of components, etc., is included in this section following the DDA analysis.

### 6.1 DDA CONCEPT

#### 6.1.1 Preliminary Considerations

Accuracy requirements and computation rate are the two most critical factors governing the structure of the DDA. The word length necessary to maintain the desired accuracy was tentatively selected as 16 binary bits. Since the DDA is to operate on the data incrementally, it is desirable for the unit to process data as rapidly as possible so that time buffering of data (either input or output) is minimized. The

time buffering hardware can be minimized by iterating at a rate fast enough to service inputs as they occur, which also results in a short response time for the computational unit. The accelerometer inputs can vary at a maximum rate of 805 bits/sec. The DDA can iterate at a rate fast enough to accept this. The gyro inputs on the other hand can vary up to 60 deg/sec. This equates to a rate of 22,000 bits/sec for a 10 arc sec increment size. The reciprocal of this (45.4  $\mu$ sec/bit) is difficult to fit into any DDA mechanization. As a result, it becomes necessary either to provide for accumulating and time buffering gyro inputs when they are changing at their maximum rate or to increase the gyro increment size. The latter would degrade the system accuracy for nominal inputs and hence will not be considered further. Thus there will be an inherent lag in the solution (for rates greater than 1.4 deg/sec) and an upper time limit on just how long high rates can be present before information is lost.

The maximum data rate for the accelerometers, 805 bits/sec, implies that there exists 1/805 or 1.25 msec between data pulses. If all the computations are to be done sequentially, this yields an iteration time of 1.25 msec. The least complex flight program requires 134 minor computational cycles (see Table 6-II). The minor cycle time is then  $1.25/134 = 9.4 \mu$ sec.

Recall that the minor cycle involves a  $y$  (16 bits);  $\Delta y$  (8 bits);  $R$  (16 bits);  $\Delta x$  (2 bits). Adding 10 control bits gives a total of 52 bits. If serial (bit-by-bit) operation is considered, this results in a bit rate of 0.180  $\mu$ sec/bit. This requirement is not consistent with present, low power, high reliability memory systems. Even if a memory system were available, present integrated logic circuits could not process the data within the bit time.

Consider then the accessing of more than one bit per memory cycle and the associated required memory cycle time.

<u>Number of Bits</u>	<u>Required Cycle Time (μsec)</u>	
1	0.18	} Difficult to Achieve
2	0.36	
4	0.72	
8	1.44	
16	2.88	} Easy to Achieve
26	4.70	
32	5.71	
52	9.4	

But the memory is only one section of the device; other considerations such as the complexity of the arithmetic unit, control units, etc., will influence final mechanization choices.

In general, the arithmetic sequence involves combining two quantities ( $y$  and  $\Delta y$ ), sensing a third ( $\Delta x$ ) and on the basis of  $\Delta x$  combining a fourth,  $R$ , with the previous combination of  $y$  and  $\Delta y$ . It is convenient to package all these quantities into two words at most. By grouping  $y$ ,  $\Delta y$ , and  $\Delta x$  into the first word, and  $R$ , scale, and control bits into the second word, very efficient use is made of both the memory and the arithmetic unit. This arrangement also results in a reasonable word length for the memory and associated cycle time.

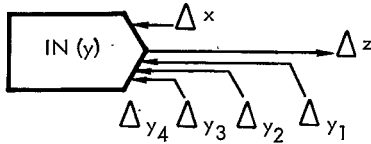
Due to the nature and number of equations to be solved, it is necessary to use the output ( $\Delta z$ ) of a particular computational cycle in as many as eight other cycles. The  $\Delta z$ 's could be given absolute addresses and the individual cycles could address the required  $\Delta y$ 's and  $\Delta x$ 's. The former approach implies the use of a large addressing scheme since a minor cycle might need up to five different  $\Delta$ 's. The difficulty can be avoided by use of a nonstandard core matrix for the memory device. With this approach, the normal core matrix addressing coupled with a specific wiring pattern facilitates the transfer of the  $\Delta z$ 's to their respective destinations. An added feature of this technique permits sign inversion when required.

### 6.1.2 DDA Computational Elements

During the course of this study, several different computational elements were deemed necessary to implement the various sets of equations. The final set of equations dictates the use of three different elements (operations). These elements are in reality programmed instructions but can be interpreted as the equivalent of conventional DDA integrators, adders, and samplers.

#### 6.1.2.1 Integrator

The integrator element accepts an initial value for  $y$ , one  $\Delta x$ , and up to four  $\Delta y$ 's. The output is called  $\Delta z$ . Schematically it is described as follows:

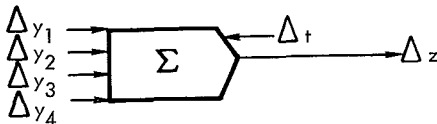


It is composed of a 16 bit R (remainder register) and a 16 bit  $y$  register. The  $y$  and  $\Delta y$  information is summed to provide the up-to-date magnitude of  $y$ . A plus or minus  $\Delta x$  signal causes the new  $y$  to be added to or subtracted from the R register. Overflow is detected on the final sum or difference and becomes the output  $\Delta z$  from this element. The overflow point (scale point) is variable within certain limits. These elements are connected in such a manner that they facilitate all the multiplications involved in solving the platform equations.

#### 6.1.2.2 Adder

The adder element is similar to the integrator except that the  $\Delta x$  input is a fixed rate, namely, the highest iteration rate. It can accumulate

up to four  $\Delta y$ 's per iteration and then issues a corresponding  $\Delta z$  on the same and next three iterations. Schematically, the adder appears as shown below.

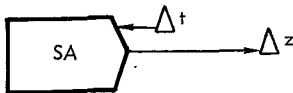


The adder is essentially a time buffer for  $\Delta z$ 's. Consider the summing of the outputs of three integrator elements, each of which might emit a plus  $\Delta z$ . If these were to be summed and used as a  $\Delta x$  input to another integrator, they must be time buffered since an integrator can accept only a +1, 0, -1  $\Delta x$  during any one iteration.

#### 6.1.2.3 Sampler

The sampler element simply routes a selected input, say  $\Delta Vx$ , to its preselected destinations. This element was deemed necessary since an input may be needed in many different elements.

A slight variation on this operation will be used to enable the loading of constants, initial conditions, etc.



#### 6.1.3 System Description

It is convenient to use two 26 bit memory cells to store the data associated with each minor computational cycle. This permits the time sharing of much of the memory hardware and of much of the arithmetic unit. The data can be stored as shown below.

Cell n	$\Delta y(8)$	$\Delta x(2)$	$y(16)$	}	Integrator N
Cell n + 1	OPN(7)	Scale (3)	R(16)		
Cell n + 2	$\Delta y(8)$	$\Delta x(2)$	$y(16)$	}	Integrator N + 1
Cell n + 3	OPN(7)	Scale (3)	R(16)		

So far in the study, no attempt has been made to scale the equations. It is estimated that 3 bits will suffice to enable the scaling to be accomplished. This scaling information is envisioned as being used to specify the overflow of the R register used in an integration cycle. The OPN or operation code will be used to specify the type operation required to execute the given instruction. Presently the need is for three different operations; however, the 7 bits will facilitate the handling of input and output data. The 7 bit control word can be utilized in the following manner. Two bits can be decoded fully to specify the particular operation (i. e., integrate; ADD cycle; ADD cycle and output; sample). The remaining 5 bits can be used to select 1 out of 12 incremental inputs or 1 out of 9 incremental outputs.

Two bits are allowed for  $\Delta x$ . A ternary scheme will transmit this incremental data. Using +1 = 01, zero = 00, -1 = 10 provides a simple means for changing the sign of the increment. A simple inversion or a juxtaposition of the two binary bits yields a sign change. This coding enables the memory system to accommodate  $+\Delta z$ 's to one location and  $-\Delta z$ 's (the same  $\Delta z$ ) to another location. The specific manner in which this is accomplished is described under "Special Techniques" in Paragraph 6.1.6.

Table 6-I illustrates the sequence of events during an integration cycle. For simplicity, most of the detailed operations are excluded. The cycle time has been tentatively set at 8  $\mu$ sec, yielding an iteration time of 1.07 msec for the flight program. This computation rate will permit additional computations up to 22 to be added if they are so needed. The present flight program iteration rate then is 945 iterations/sec.

Table 6-I. Sequence of Operations During Integration Cycle Consecutive Integrations Followed by ADD Cycle

Memory Function	Arithmetic Unit Function
1. Write ( OPN, SC, R) N-2	Sum (R + $\Delta X = R'$ ) N-1 Set $\Delta Z_{N-1}$
2. Read ( $\Delta Y, \Delta X, Y$ ) <sub>N</sub>	
3. Store ( $\Delta Y, \Delta X, Y$ ) N-1	Sum (Y + $\Delta Y = Y'$ ) <sub>N</sub>
4. Read (OPN, SC, R) <sub>N</sub>	
5. Store (OPN, SC, R) N-1	Sum (R + $Y' \Delta X = R'$ ) <sub>N</sub> . Set $\Delta Z_N$
6. Read ( $\Delta Y, \Delta X, Y$ ) N+1	
7. Store ( $\Delta Y, \Delta X, Y$ ) <sub>N</sub>	Sum (Y + $\Delta Y = Y'$ ) N+1
8. Read (OPN, SC, R) N+1	
9. Store (OPN, SC, R) <sub>N</sub>	If $Y' \neq 0$ , Set $\neq \Delta Z$ and set $y'' = y' \mp \Delta Z$

#### 6.1.4 DDA Operation

DDA operation is initiated by an external command setting the load program indiscrete. Data is fed serially into the input register; the DDA places the 26 bit word into the first cell in the memory. This is followed by identical cycles in which all appropriate cells could be initialized. The DDA accomplishes this by presetting the address counter to zero, enabling the write buffer to load serially, and initiating a write command to the memory electronics when the buffer is filled. The address register can be advanced at the end of each cycle.

The load program discrete is then reset and the alignment program discrete set. This causes the DDA to access cell zero. A sample instruction is the first command to be executed. This command, when placed in the control register, causes the selected input (as determined by the 5 bit address) to be routed to the  $\Delta z$  logic. A subsequent write cycle places

the  $\Delta z$  (now  $\Delta x$ 's and  $\Delta y$ 's) in those cells requiring it. (Recall that the unique wiring arrangement routes the  $\Delta z$  to several cells simultaneously.)

The inherent serial nature of a DDA affords some freedom which can be taken advantage of in the design of the memory. Serial operation means that each minor cycle is followed by the same minor cycle each iteration. In other words, the program does not change from one iteration to the next.

Since data is broken up into two DDA words, a read cell  $N$ , read cell  $N + 1$ , restore cell  $N$ , and restore cell  $N + 1$  sequence is required. The arithmetic operations could be done concurrently. However, it is desirable to use a read, write/read, write sequence instead. Figure 6-1 delineates how the data is sequenced in and out of the memory. One of the advantages of the technique shown here is that the data is present in the arithmetic unit longer than if a read, read/write, write cycle is used. Thus the retrieval and storage of data for two consecutive instructions are interleaved. The manner in which this is accomplished in the memory is treated in Paragraph 6.1.6.

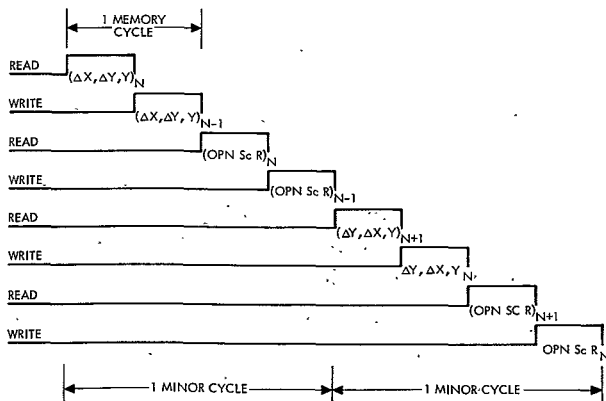


Figure 6-1. In and Out of Memory Data Sequence

The specific operations which occur during a minor cycle have been shown in Table 6-I. Those operations relating to the Nth cycle are underlined. Note that the N + 1 cycle illustrates typical operations for an ADD instruction.

#### 6.1.5 Input/Output

##### 6.1.5.1 Mode Control

The present equation set implies three modes of operation for the DDA. It is anticipated that some external source will control these three mode discrettes.

These three discrettes cause the DDA to perform either the load program function, the alignment equations, or the flight equations.

##### 6.1.5.2 Load Program

The ability to load the entire program (initial conditions, etc.) all in one continuous operation appears to be the only requirement on loading. This can be accomplished by use of the 26 bit write buffer register internal to the DDA which will accept serial information. When the register is loaded, the control logic places the contents of it into a cell in the core matrix. The loading scheme requires that the program be loaded sequentially, proceeding from cell zero to the highest numbered cell.

##### 6.1.5.3 Incremental Inputs

The gyro inputs are accepted into 15 bit buffer registers which, in turn, permit a 60 deg change at the maximum 60 deg/sec rate. If this rate is maintained longer than 1 sec, information will be lost due to overflow of the 15 bit buffers.

For purposes of this study, three options were considered for the implementation of the interpolation of guidance commands. The simplest implementation is to assume that the commanded direction cosine matrix (6 terms) is transferred incrementally to the DDA. This implies 12 lines with appropriate buffer circuits.

The second implementation assumes that the six  $\Delta A_{ijR}$ 's are fed to the DDA and that the DDA will linearly extrapolate this information over the 1 sec interval.

The third implementation assumes that the change in three angles from one predicted point to the next is transferred to the DDA. The DDA then must calculate the appropriate sines and cosines and generate the new  $\Delta a_{ijR}$  matrix and linearly extrapolate the information over the 1 sec interval.

Since the third implementation requires that a significant number of computations be executed, it would increase the iteration time and thus necessitate time buffering on the accelerometer inputs. This method also would place an upper limit on the length of time the accelerometers could operate at their maximum rate. The effects of these three approaches appear in the summary.

The accelerometer inputs are sampled directly by the DDA in those configurations which do not require the DDA to compute the commanded direction cosine matrix. In the case where the cosines are computed, time buffer registers are also required due to the reduction in major cycle rate. These accumulators will permit the accelerometers to maintain their maximum data rate (805 pps) for 10 sec. The buffer registers are then 7 bits.

#### 6.1.5.4 Incremental Outputs

The outputs from the DDA appear on nine channels; present design is predicated on the assumption that the external equipment will be able to accept this incremental pulse type information.

#### 6.1.6 DDA Memory System

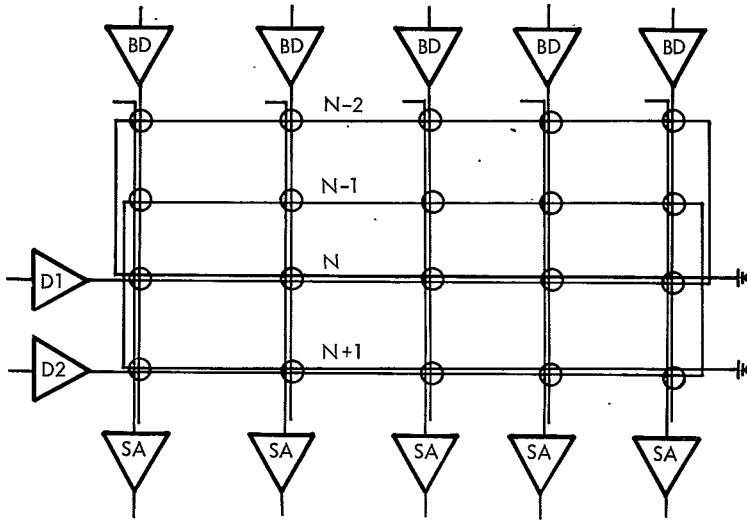
##### 6.1.6.1 General Description

The memory function of the DDA is performed by a 354 word, 26 bit, sequentially addressed, ferrite core memory. Data is written in and read out in parallel (26 bits). The cycle time (read followed by write) is 4  $\mu$ sec. The block diagram for the DDA includes the items associated directly with the memory.

##### 6.1.6.2 Special Techniques

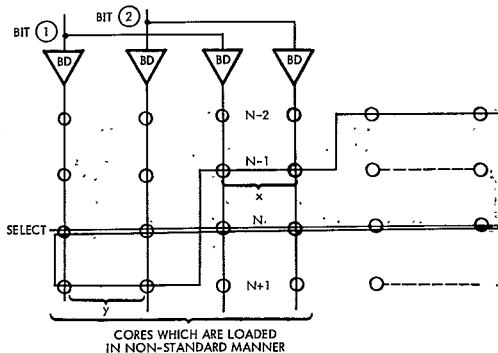
It is convenient to explain each of the three special techniques separately and to superimpose them on each other for the final array.

The manner in which one word is read out and another is written into is shown below.



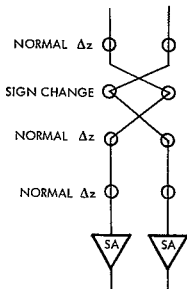
Pulsing driver D causes the cores in row N to turn over (if they store 1's) and a resultant sense amplifier output. Currently, row N-2 is half selected in the write direction. Immediately after the readout data is retrieved, the row N-2 can be written into by simply pulsing those bit drivers where 1's are to be stored. Note that each cell  $j$  is also connected to cell  $j-2$  by the drive (select) line.

To transmit  $\Delta z$ 's to several different cells, it is only necessary to route the select line for say cell  $j$  to the other cores in the other cells into which data is required. However, the information (data) must be duplicated on all the bit drivers requiring it. The technique is shown below.



During the write portion of the memory cycle, a half select current is routed through the core pairs  $x$  and  $y$ . Data bits ① and ② are used to turn on the bit drivers (if 1's are to be written) such that cells  $N-1$  and  $N+1$  will be written into during the same time interval that cell  $N-2$  is loaded.

In order to effectively transmit a  $+\Delta z$  to one cell and a  $-\Delta z$  to another, the following scheme is used. The code for  $+1$ ,  $0$ ,  $-1$  is chosen as  $01$ ,  $00$ ,  $10$ , respectively. Thus  $+1$  differs from  $-1$  either by a simple inversion or a juxtaposition of the bits. In those instances where a  $-\Delta z$  is required, the sense windings for the bit pair can be interchanged as shown below.



The physical location of quantities within a word is shown below.

Row				
1.	$\Delta y(8)$	$\Delta x(2)$	$y(16)$	] Integrator N
2	OPN (7)	Scale (3)	$r(16)$	
3	$\Delta y(8)$	$\Delta x(2)$	$y(16)$	] Integrator N+1
4	OPN (7)	Scale (3)	$r(16)$	

The overall block diagram for the DDA is shown in Figure 6-2.

#### 6.1.7 DDA Signal Flow

The functional flow of signals within the DDA is depicted in Figure 6-3. Detailed equations for the DDA are given in Section 5, and typical DDA schematics for these equations are given in the following pages.

##### 6.1.7.1 Flight Equations

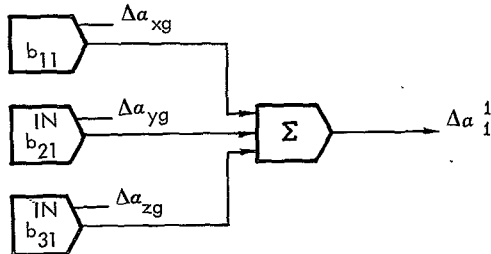
- Gyro Rotation to Acceleration Coordinate Set

$$\Delta a_1^1 = b_{11}\Delta a_{xg} + b_{21}\Delta a_{yg} + b_{31}\Delta a_{zg}$$

$$\Delta a_2^1 = b_{12}\Delta a_{xg} + b_{22}\Delta a_{yg} + b_{32}\Delta a_{zg}$$

$$\Delta a_3^1 = b_{13}\Delta a_{xg} + b_{23}\Delta a_{yg} + b_{33}\Delta a_{zg}$$

Typical implementation: 9 integrators, 3 adders



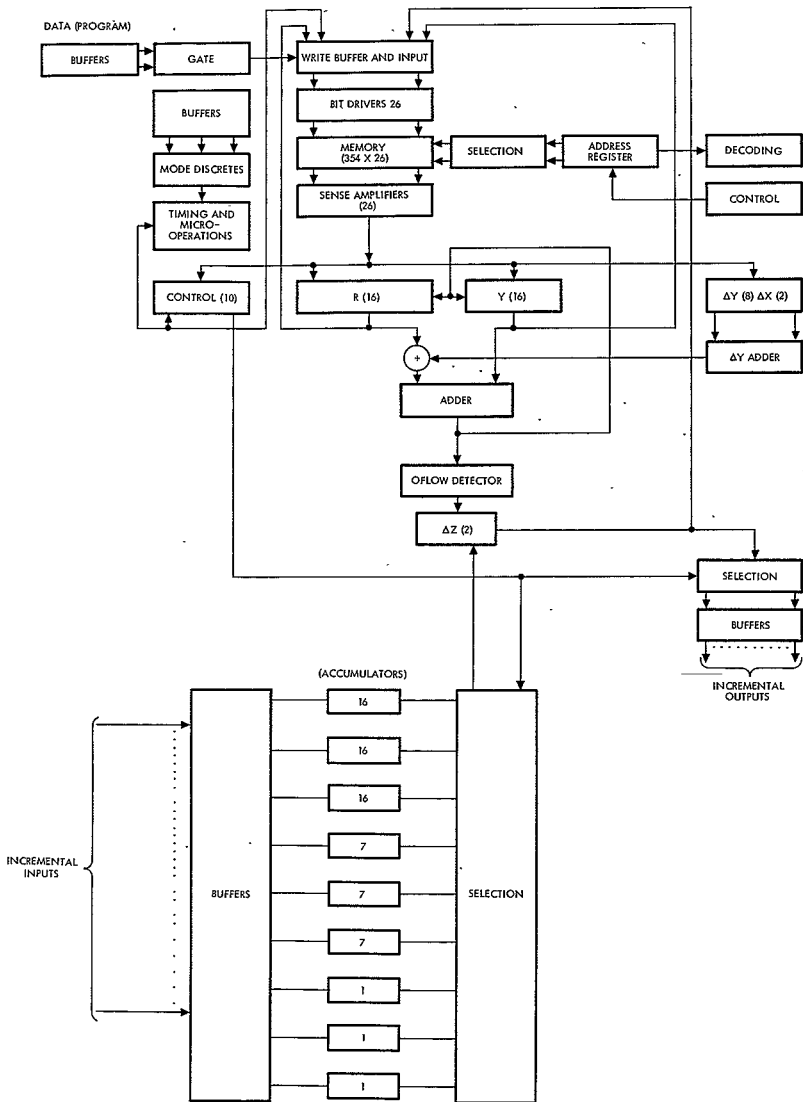


Figure 6-2. DDA Block Diagram

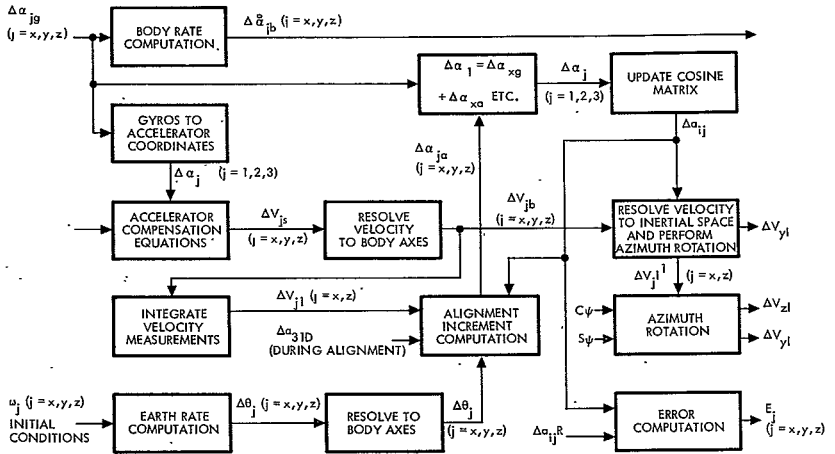
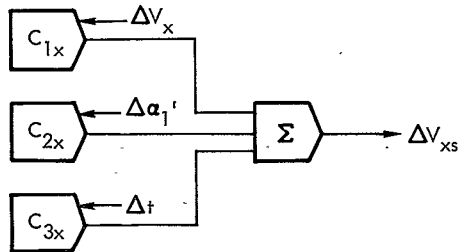


Figure 6-3. DDA Signal Flow Block Diagram

• Acceleration Compensation Equations

$$\begin{aligned} \Delta V_{xs} &= C_{1x} \Delta V_x - C_{2x} \Delta \alpha_1^1 - C_{3x} \Delta t \\ \Delta V_{ys} &= C_{1y} \Delta V_y - C_{2y} \Delta \alpha_2^1 - C_{3y} \Delta t \\ \Delta V_{zs} &= C_{1z} \Delta V_z - C_{2z} \Delta \alpha_3^1 - C_{3z} \Delta t \end{aligned}$$

Typical Implementation: 9 integrators, 3 adders



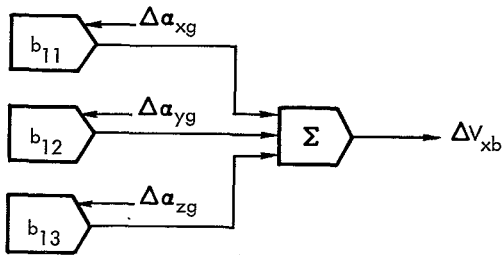
• Velocity Conversion to Gyro Body Coordinates

$$\Delta V_{xb} = b_{11} \Delta V_{xs} + b_{12} \Delta V_{ys} + b_{13} \Delta V_{zs}$$

$$\Delta V_{yb} = b_{21} \Delta V_{xs} + b_{22} \Delta V_{ys} + b_{23} \Delta V_{zs}$$

$$\Delta V_{zb} = b_{31} \Delta V_{xs} + b_{32} \Delta V_{ys} + b_{33} \Delta V_{zs}$$

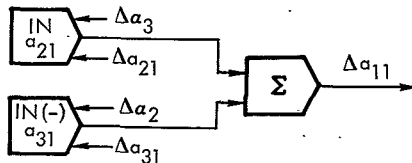
Typical Implementation: 9 integrators, 3 adders



• Attitude Reference Equation

$$\Delta a_{ij} = \Delta a_{(i+2) a(i+1)j} - \Delta a_{(i+1) a(i+2)j}$$

Typical Implementation: 18 integrators, 9 Adders



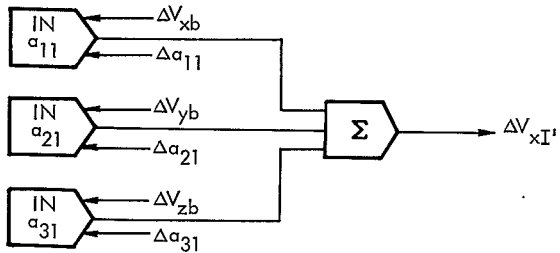
- Velocity Resolution to Inertial Space

$$\Delta V_{xi}' = a_{11}\Delta V_{xb} + a_{21}\Delta V_{yb} + a_{31}\Delta V_{zb}$$

$$\Delta V_{yi}' = a_{12}\Delta V_{xb} + a_{22}\Delta V_{yb} + a_{32}\Delta V_{zb}$$

$$\Delta V_{zi}' = a_{13}\Delta V_{xb} + a_{23}\Delta V_{yb} + a_{33}\Delta V_{zb}$$

Typical Implementation: 9 integrators, 3 adders

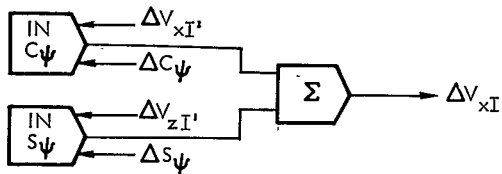


- Azimuth Rotation

$$\Delta V_{xi} = C\psi\Delta V_{xi}' + S\psi\Delta V_{zi}'$$

$$\Delta V_{zi} = S\psi\Delta V_{xi}' + C\psi\Delta V_{zi}'$$

Typical Implementation: 6 integrators, 3 adders



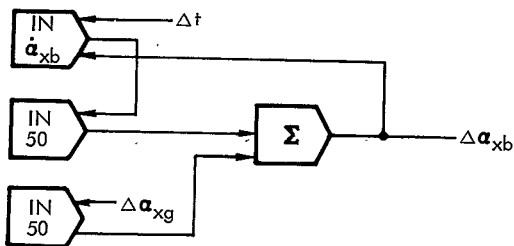
- Body Rate Computation

$$\Delta \dot{a}_{xb} = 50 (\Delta a_{xg} - \dot{a}_{xb} \Delta t)$$

$$\Delta \dot{a}_{yb} = 50 (\Delta a_{yg} - \dot{a}_{yb} \Delta t)$$

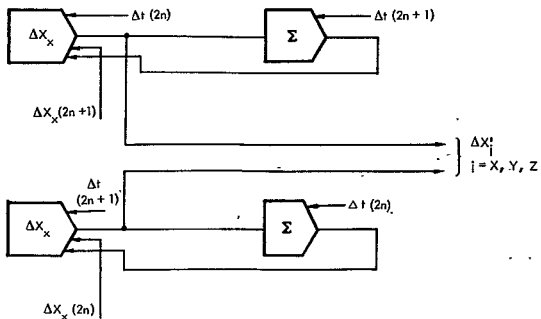
$$\Delta \dot{a}_{zb} = 50 (\Delta a_{zg} - \dot{a}_{zb} \Delta t)$$

Typical Implementation: 9 integrators, 3 adders



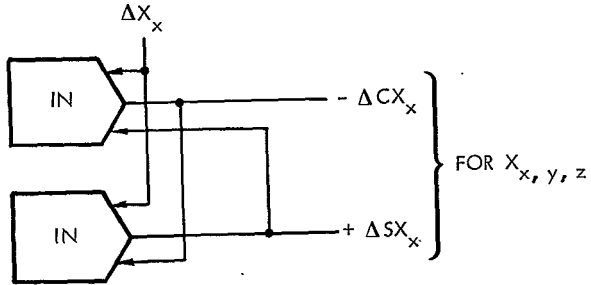
- Extrapolation of Guidance Commands

Typical Implementation: 6 integrators, 6 adders



- Sine Cosine Generation

Typical Implementation: 6 integrators



- Formulation of  $\Delta a_{ijR}$  (Commanded Angles)

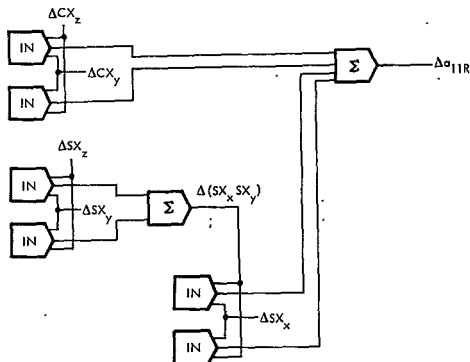
$$\Delta a_{11R} = (CX_z CX_y - SX_x SX_y SX_z)$$

$$\Delta a_{12R} = (CX_y SX_z + CX_z SX_x SX_y)$$

$$\Delta a_{31R} = (SX_y CX_z + SX_z SX_x CX_y)$$

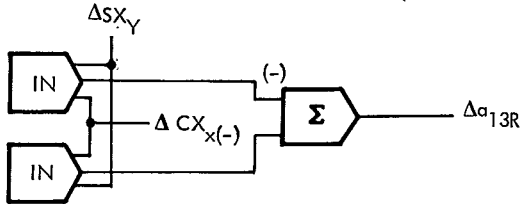
$$\Delta a_{32R} = (SX_y SX_z - SX_x CX_y CX_z)$$

Typical Implementation: 24 integrators, 8 adders



$$\begin{aligned}\Delta a_{13R} &= -S X_y C X_x \\ \Delta a_{21R} &= -S X_z C X_x \\ \Delta a_{22R} &= C X_x C X_z \\ \Delta a_{33R} &= C X_x C X_y\end{aligned}$$

Typical Implementation: 8 integrators, 4 adders



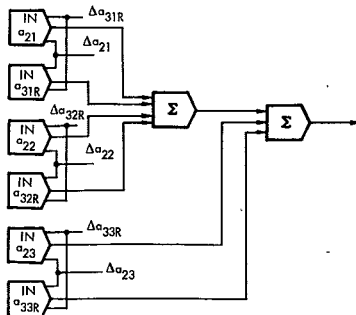
• Attitude Error Signals

$$\begin{aligned}\Delta E_x = & - a_{21} \Delta a_{31R} + a_{31R} \Delta a_{21} + a_{22} \Delta a_{32R} + a_{32R} \Delta a_{22} \\ & + a_{23} \Delta a_{32R} + a_{33R} \Delta a_{22}\end{aligned}$$

$$\begin{aligned}\Delta E_y = & - a_{31} \Delta a_{11R} + a_{11R} \Delta a_{31} + a_{32} \Delta a_{12R} + a_{12R} \Delta a_{32} \\ & + a_{33} \Delta a_{13R} + a_{13R} \Delta a_{33}\end{aligned}$$

$$\begin{aligned}\Delta E_z = & - a_{21} \Delta a_{11R} + a_{11R} \Delta a_{21} + a_{22} \Delta a_{12R} + a_{12R} \Delta a_{22} \\ & + a_{23} \Delta a_{13R} + a_{13R} \Delta a_{23}\end{aligned}$$

Typical Implementation: 18 integrators, 6 adders



- Integrate Velocity Measurements

$$\Delta V_{x1} = (V_{xb} - 0.2V_{x1}) \Delta t$$

$$\Delta V_{z1} = (V_{zb} - 0.2V_{z1}) \Delta t$$

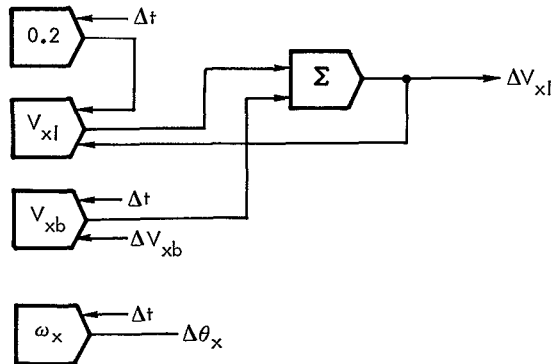
- Earth Rate Computation

$$\Delta \theta_x = W_x \Delta t$$

$$\Delta \theta_y = W_y \Delta t$$

$$\Delta \theta_z = W_z \Delta t$$

Typical Implementation: 9 integrators, 3 adders



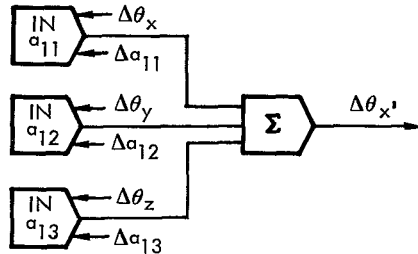
- Resolve Earth Rate Computations to Body Axes

$$\Delta\theta_x^i = a_{11}\Delta\theta_x + a_{12}\Delta\theta_y + a_{13}\Delta\theta_z$$

$$\Delta\theta_y^i = a_{21}\Delta\theta_x + a_{22}\Delta\theta_y + a_{23}\Delta\theta_z$$

$$\Delta\theta_z^i = a_{31}\Delta\theta_x + a_{32}\Delta\theta_y + a_{33}\Delta\theta_z$$

Typical Implementation: 9 Integrators, 3 adders



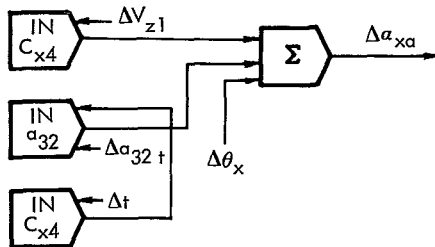
- Alignment Increment Equations

$$\Delta\alpha_{xa} = C_{x3} a_{32} \Delta\tau - C_{x4} \Delta V_{z1} + \Delta\theta_x$$

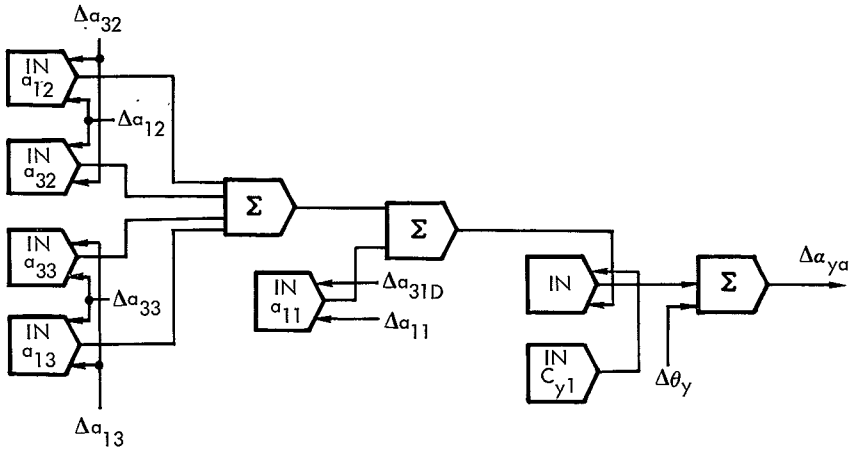
$$\Delta\alpha_{ya} = C_{y1} (a_{12} a_{32} + a_{11} a_{310} + a_{13} a_{33}) \Delta\tau + \Delta\theta_y$$

$$\Delta\alpha_{za} = C_{z3} a_{12} \Delta\tau + C_{z4} \Delta V_{x1} + \Delta\theta_z$$

Typical Implementation for  $\Delta\alpha_{xa}$  and  $\Delta\alpha_{za}$ : 6 integrators, 2 adders



Typical Implementation for  $\Delta a_{ya}$ : 7 integrators, 3 adders



### 6.1.8 DDA Computational and Component Requirements

#### 6.1.8.1 Computational Element Count

Table 6-II itemizes the number of computational elements needed to implement the three main approaches.

Table 6-II. DDA Element Count

Approach	Inte-grators	Adders	Samplers	Number of Elements
Flight Equations (without extrapolation of guidance commands)	87	33	14	134
Flight Equations (with extrapolation of $\Delta a_{ijR}$ 's)	99	51	14	164
Flight Equations (with extrapolation of $\Delta a_{ijR}$ and inputs)	133	51	11	196
Alignment Equations	31	11	1	43
Total Number of Elements, Maximum	162	62	15	239

#### 6.1.8.2 Component Count

Preliminary logic design of the DDA yields the following component requirements.

Standard Logic Elements	No Extrapolation	Power (w)	Extrapolation $\Delta a_{ijR}$	Power (w)
Flip-flops	210	4.20	255	5.10
Two input gates	275	4.95	300	5.40
Four input gates	12	0.10	12	0.10
High speed gates	40	1.36	50	1.70
Clock drivers	16	1.52	19	1.80
Totals	553 Flat-packs	12.13	636 Flat-packs	14.10

## Input/Output

	<u>Quantity</u>
Input buffer circuits	35
Output buffer circuits	18

## Memory

	<u>Quantity</u>
Stack	400 x 28 bits
Sense amplifiers	28
Drivers	20
Digit drivers	28
Switches	20

## 6.2 GP COMPUTER CONCEPT

This subsection is functionally divided into two main areas. The first discusses the hardware required for a typical GP implementation of the analytic platform. The second discusses the results of the timing and memory estimates made for the various equations of Section 5. (Assumptions underlying the timing and memory estimates appear in Section 5, also).

### 6.2.1 Hardware Considerations

A study was carried out to determine the effects on the overall system if a GP computing device is used to solve the guidance equations.

The instruction repertoire selected is used in several available space computers, one of which is manufactured by TRW. The following GP approach assumes the use of TRW's Aerospace Computer (currently used with a strapped-down guidance system) with special input/output equipment to facilitate the integration with the MSFC strapped-down guidance system.

The computer is a binary fixed-point machine operating in parallel on 18 bit words at 10  $\mu$ sec/instruction rate. It is a single address system using a 4096 word core matrix as memory element. Its instruction repertoire includes addition, subtraction, multiplication, division, conditional transfer instructions, and special input/output commands. Figure 6-4 illustrates the special input/output equipment required.

The iteration time varies between 7.5 and 8.66  $\mu$ sec, depending upon the specific sets of equations to be solved. The GP program takes advantage of the fact that many computations need not be done each iteration; they can be spread out over a long interval, reducing individual iteration times. The DDA does not permit this freedom to be used to any advantage.

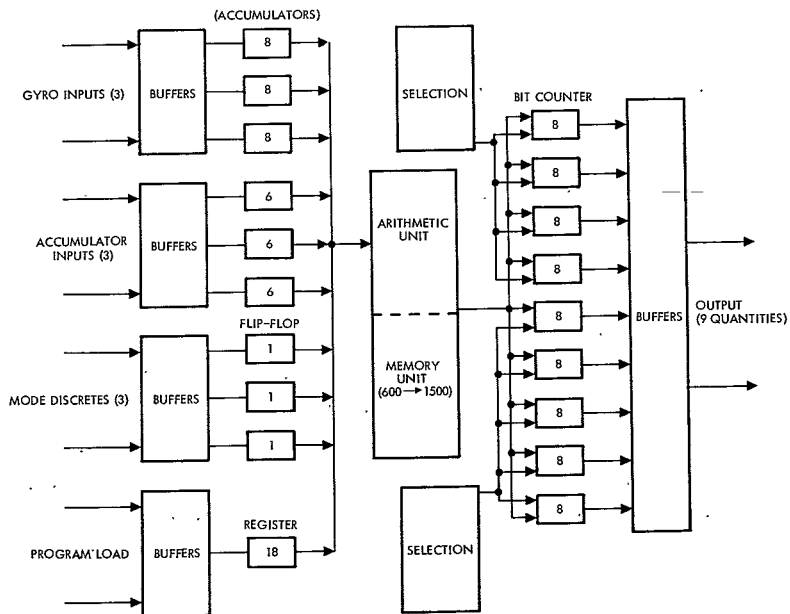


Figure 6-4. Special Input/Output Equipment

### 6.2.1.1 Component Count

#### Input/Output Equipment and Arithmetic Unit

	<u>Quantity</u>	<u>Power (W)</u>
Flip-flops	306	6.10
Gates	636	11.40
High speed gates	85	2.90
Drivers	58	1.74
Clock drivers	<u>26</u>	<u>2.47</u>
Totals	1111 Flat-packs	24.61

#### Buffers

	<u>Quantity</u>
Input	35
Output	18

#### Memory

	<u>Quantity</u>
Stack	18 x 1024
Sense Amps	18
Inhibit Drivers	18
Drivers	16
Switches	12

### 6.2.2 Sizing Results

All GP equations of Section 5 have been assumed to be mechanized as independent routines, which require program linkage to form the composite program. It is assumed that two modes, selected by input discrettes, will be required for the computer program. These modes are the Alignment Mode and the Flight Mode. Transition between these modes will require a Flight Mode initialization routine to set the necessary flags and initial conditions for the Flight Mode.

The program linkage flow required for the MSFC strapped-down system is shown in Figure 6-5. The program linkage selects all routines required for any given mode. It also contains the necessary cycle counters for determining which routines are to be linked during each computational cycle.

Computer memory and timing estimates for the proposed MSFC strapped-down system equations are summarized in Table 6-III. Estimates have been made for several sets of alignment equations and attitude reference equations. For simplification estimates are listed only for those equations requiring minimum and maximum memory and timing.

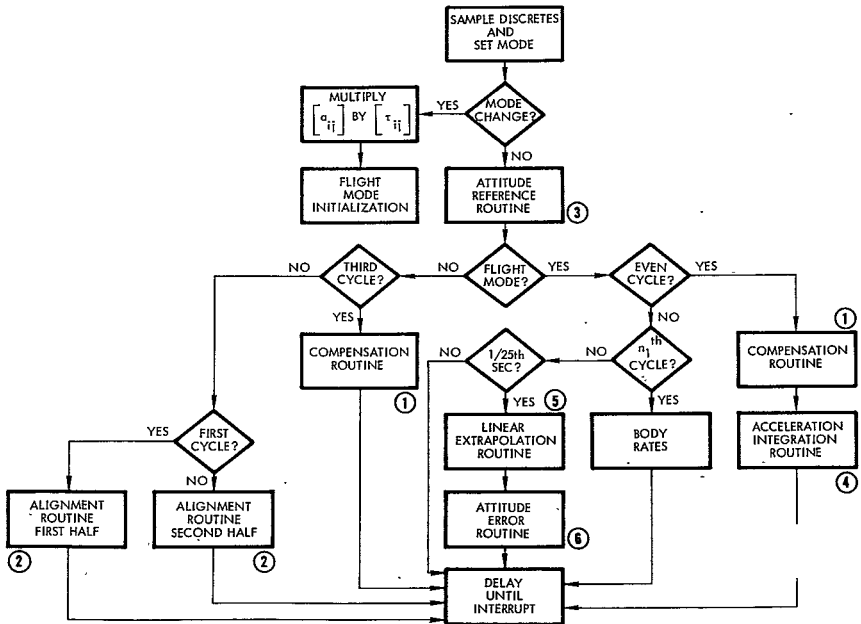


Figure 6-5. Program Linkage Flow Required for Strapped-Down System

Table 6-III Summary of MSFC Strapped-down System Memory and Timing Requirements

Function	Block (Figures 5-2 and 5-3)	Program Words (N)	Constant and Vari- able Words (N)	Computa- tion Rate	Total Words (N)	Adds A	Multiplies M	LEM AEA Computer Computation Time (msec)
Compensation equations	1e, 1d, 4a	57	40	every 3 cycles	97	121	27	3.1
Body rate computation	1a, 1b 1c	14	10	every $n_1$ cycles	24	28	3	0.49
Alignment Eq (Method 1)	2a, 2b, 2c	102	33	every 3 cycles	135	120	25	2.95
(Method 2)	*	233	38		271	194	74	7.12
Matrix multi- plication at alignment end	2d	49	39	once	88	117	30	4.5
Subroutines								
Sine/cosine		42			42	16	14	1.14
Square root		44			44	32	12	1.6
Attitude Refer- ence equations	3b			every cycle				
(1) First-order Taylor's series		68	30		98	234	18	3.6
(2) Second-order Taylor's series (using secondary direction cosines)		88	21		109	156	30	3.66
(3) First-order Taylor's series (using secondary direction cosines)		58	21		79	132	18	2.58

\*These equations are defined in Reference 5.1 as "Scheme 1." This is a technique involving matrix multiplication.

Table 6-III. Summary of MSFC Strapped-down System Memory and Timing Requirements (continued)

Function	Block (Figures 5-2 and 5-3)	Program Words (N)	Constant and Vari- able Words (N)	Computa- tion Rate	Total Words (N)	Adds A	Multiplies M	LEM AEA Computer Computation Time (msec)
Storage of Pre- vious $a_{ij}$ matrix	3c	6	9	every cycle	15	27	0	0.27
Acceleration integration	4b	15	4	every 2 cycles	19	35	9	0.98
Linear extra- polation of guid- ance commands	5	30	15	25 times/ sec	45	27	3	0.48
Attitude error computation (with Xi input) With Xi2R input	6	165	34	25 times/ sec	199	231	52	5.95
		38	12	25 times/ sec	50	28	10	0.98
Mode discrete processing and routine linkage		72	19	every cycle	91	65	0	0.65
Total Memory Estimates								
Minimum		<u>558</u>	<u>198</u>					
Maximum		719	248					

A rough estimate of the required program cycle time can be determined from the various timing expressions by use of the flow chart in Figure 6-5. The computational path that consumes the most time per cycle is that path that solves the attitude reference equations, the compensation equations, and the acceleration integration equations. Implementation of the equations requiring minimum memory capacity will require a minimum computational cycle of  $380A + 54M$  (7.58 msec using the LEM AEA computer). Implementation of the equations requiring maximum memory capacity will require a minimum computational cycle of  $415A + 104M$  (8.66 msec).

## 7. SAP AND PIGA ANALYSIS

### 7.1 DERIVATION OF EQUATIONS OF MOTION

#### 7.1.1 Model

The following schematic (Figure 7-1) will represent the SAP.

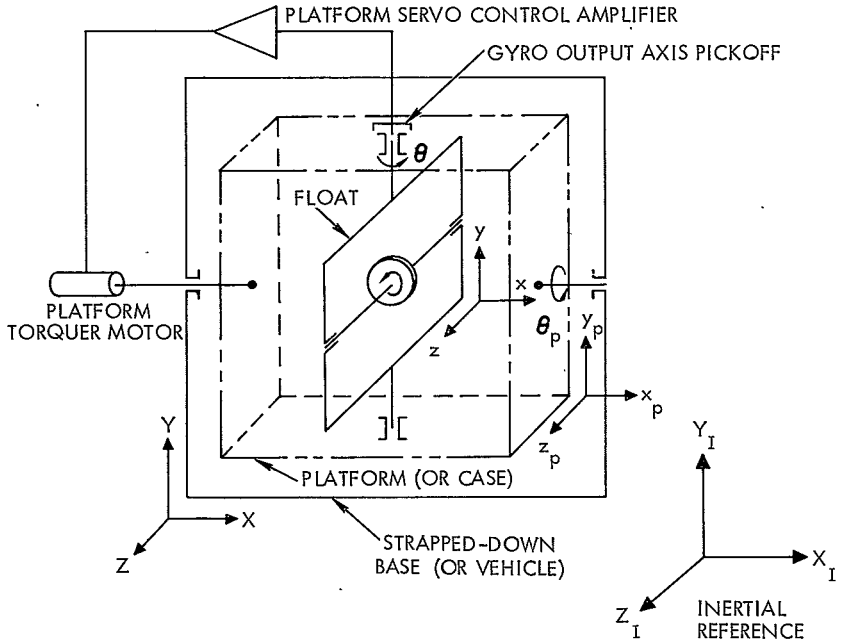


Figure 7-1. SAP Model

where

$X, Y, Z$  indicate a reference system fixed to and rotating with the vehicle.

$x_p, y_p, z_p$  indicate a reference system fixed to and rotating with the platform.

(Note: This reference differs from the vehicle reference by angle  $\theta_p$ .)

$x, y, z$  indicate a reference system fixed to and rotating with the float.

(Note: This reference differs from the platform reference by angle  $\theta$ .)

### 7.1.2 Preliminary Equations

The equations to be developed will express SAP motions relative to an arbitrarily established inertial reference ( $X_I, Y_I, Z_I$ ). The angular rate vector of the vehicle axes ( $X, Y, Z$ ) relative to the inertial set ( $X_I, Y_I, Z_I$ ) is denoted as  $\bar{\omega}$  and is resolved into components along the vehicle axes as follows:

$$\bar{\omega} = \omega_X \hat{i}_X + \omega_Y \hat{i}_Y + \omega_Z \hat{i}_Z \quad (1)$$

where the  $\hat{i}_X, \hat{i}_Y, \hat{i}_Z$  represent unit vectors along the indicated vehicle axis.

Newton's Law in rational form is obtained by applying the Coriolis Equation to the angular momentum vector of a rigid body (see Reference 7.1). In equation form this is

$$\frac{d}{dt} (\bar{H})_I = \frac{d}{dt} (\bar{H})_j + \bar{\omega}_j \times \bar{H} = \bar{L}_{I/j} \quad (2)$$

(Note: In Eq (2) subscripts I and j refer to inertial space and an arbitrary j<sup>th</sup> set of axes, respectively.)

It remains in this derivation then to apply this equation once to the float and again to the platform and then to investigate the component of interest in each application. Since the angular momentums and angular rates are expressed in different coordinate systems, transformation relationships must be established. These are developed as follows:\*

The transformation relating the vehicle and platform coordinates is

$$\begin{bmatrix} X \\ Y \\ Z \end{bmatrix} = \begin{bmatrix} 1 & 0 & 0 \\ 0 & \cos\theta_p & \sin\theta_p \\ 0 & -\sin\theta_p & \cos\theta_p \end{bmatrix} \begin{bmatrix} x_p \\ y_p \\ z_p \end{bmatrix} \quad (3)$$

It should be noted at this point that in the strapped-down application the angle  $\theta_p$  is not necessarily a small angle and in general is not. Therefore small angle approximations cannot be permitted as is generally done in textbooks. (See References 7.1 and 7.2.)

\*The transformations used in Eqs (3), (4), and (5) are consistent with those employed in Reference 7.2.

Similarly, the transformation relating the float and platform coordinates is

$$\begin{bmatrix} x_p \\ y_p \\ z_p \end{bmatrix} = \begin{bmatrix} \cos\theta & 0 & -\sin\theta \\ 0 & 1 & 0 \\ \sin\theta & 0 & \cos\theta \end{bmatrix} \begin{bmatrix} x \\ y \\ z \end{bmatrix} \quad (4)$$

However, since the SAP is intended to null the float motion relative to the platform, the small angle approximation can be permitted in this transformation equation. Eq (4) can then be written as

$$\begin{bmatrix} x_p \\ y_p \\ z_p \end{bmatrix} = \begin{bmatrix} 1 & 0 & -\theta \\ 0 & 1 & 0 \\ \theta & 0 & 1 \end{bmatrix} \begin{bmatrix} x \\ y \\ z \end{bmatrix} \quad (5)$$

### 7.1.3 Angular Velocities

The next step is to describe the angular velocities of the platform and the float with respect to inertial space. These are the  $\bar{\omega}_j$  for use in Eq (2). The angular velocity of the platform is that of the vehicle less the angular rate  $\dot{\theta}_p$  about the X (or  $x_p$ ) axis.\* In vector form

$$\bar{\omega}_p = \bar{\omega} - \dot{\theta}_p \hat{x}_p \quad (6)$$

In Eq (6)  $\hat{x}_p$  indicates a unit vector in the  $x_p$  direction. Similarly  $\hat{y}_p \rightarrow y_p$  and  $\hat{z}_p \rightarrow z_p$ . Substituting Eq (1) into Eq (6) yields

$$\bar{\omega}_p = \omega_X \hat{X} + \omega_Y \hat{Y} + \omega_Z \hat{Z} - \dot{\theta}_p \hat{x}_p \quad (7)$$

Transforming the  $\bar{\omega}$  components (i. e.,  $\omega_X, \omega_Y, \omega_Z$ ) into the platform axes by use of Eq (3), Eq (7) takes the form

\*The relative motions implied by Eqs (6) and (9) are compatible with the coordinate transformations defined by Eqs (3), (4), and (5). See Reference 7.2.

$$\bar{\omega}_p = (\omega_X - \dot{\theta}_p) \hat{x}_p + (\omega_Y \cos \theta_p - \omega_Z \sin \theta_p) \hat{y}_p + (\omega_Y \sin \theta_p + \omega_Z \cos \theta_p) \hat{z}_p \quad (8)$$

For calculation purposes Eq (8) can be written as

$$\bar{\omega}_p = \omega_1 \hat{x}_p + \omega_2 \hat{y}_p + \omega_3 \hat{z}_p \quad (8a)$$

where

$$\omega_1 = \omega_X - \dot{\theta}_p \quad (8b)$$

$$\omega_2 = \omega_Y \cos \theta_p - \omega_Z \sin \theta_p \quad (8c)$$

$$\omega_3 = \omega_Y \sin \theta_p + \omega_Z \cos \theta_p \quad (8d)$$

Similar to the previous steps the inertial angular velocity of the float is that of the platform less the angular rate  $\dot{\theta}$  about the y (or  $y_p$ ) axis. In vector form,

$$\bar{\omega}_f = \bar{\omega}_p - \dot{\theta} \hat{y} \quad (9)$$

In Eq (9)  $\hat{y}$  indicates a unit vector in the y direction. Similarly,  $\hat{x} \rightarrow x$  and  $\hat{z} \rightarrow z$ . Substitute Eq (8a) into Eq (9):

$$\bar{\omega}_f = \omega_1 \hat{x}_p + \omega_2 \hat{y}_p + \omega_3 \hat{z}_p - \dot{\theta} \hat{y} \quad (10)$$

Transforming the  $\bar{\omega}_p$  components into the float axes by use of Eq (5), Eq (10) becomes

$$\bar{\omega}_f = (\omega_1 + \theta \omega_3) \hat{x} + (\omega_2 - \dot{\theta}) \hat{y} + (-\theta \omega_1 + \omega_3) \hat{z} \quad (11)$$

By use of Eqs (8b), (8c), and (8d),  $\omega_1$ ,  $\omega_2$ , and  $\omega_3$  can be eliminated from Eq (11):

$$\begin{aligned} \bar{\omega}_f = & \left( \omega_X - \dot{\theta}_p + \theta \left[ \omega_Y \sin \theta_p + \omega_Z \cos \theta_p \right] \right) \hat{x} + (\omega_Y \cos \theta_p - \omega_Z \sin \theta_p - \dot{\theta}) \hat{y} \\ & + \left( \omega_Y \sin \theta_p + \omega_Z \cos \theta_p - \theta \left[ \omega_X - \dot{\theta}_p \right] \right) \hat{z} \end{aligned} \quad (12)$$

For calculation purposes, Eq (12) can be written as

$$\bar{\omega}_f = \omega_x \hat{x} + \omega_y \hat{y} + \omega_z \hat{z} \quad (12a)$$

where

$$\omega_x = \omega_X - \dot{\theta}_p + \theta \left[ \omega_Y \sin\theta_p + \omega_Z \cos\theta_p \right] \quad (12b)$$

$$\omega_y = \omega_Y \cos\theta_p - \omega_Z \sin\theta_p - \dot{\theta} \quad (12c)$$

$$\omega_z = \omega_Y \sin\theta_p + \omega_Z \cos\theta_p - \theta(\omega_Z - \dot{\theta}_p) \quad (12d)$$

#### 7.1.4 Output Axis Equation

Applying the Coriolis Equation, Eq (2), to the float,

$$\frac{d}{dt}(\bar{H}_f)_I = \frac{d}{dt}(\bar{H}_f)_f + \bar{\omega}_f \times \bar{H}_f = \bar{L}_{I/f} \quad (13)$$

where

$$\bar{H}_f = I_x \omega_x \hat{x} + I_y \omega_y \hat{y} + (I_z \omega_z + H_x) \hat{z} \quad (14)$$

Here the I symbols represent the principal moments of inertia of the float about its center of gravity (c. g.). This statement implies that the principal axes are in line with the gyro output and spin axis. This assumption will not degrade the accuracy of this analysis since the values of the products of inertia are two orders of magnitude lower than those about the float axes (see Reference 7.4b). For every torque term pertaining to float axes inertias there is a nearly identical torque term associated with the products of inertia. Therefore, due to the gross differences in magnitudes, the product of inertial torque terms can be safely dropped. The symbol  $H_x$  represents the angular momentum of the gyro wheel due to spin.

Eq (14) can be simplified for calculations to

$$\overline{H}_f = H_x \hat{x} + H_y \hat{y} + H_z \hat{z} \quad (14a)$$

where

$$H_x = I_x \omega_x \quad (14b)$$

$$H_y = I_y \omega_y \quad (14c)$$

$$H_z = I_z \omega_z + H_r \quad (14d)$$

Using the simplified forms of Eqs (12a) and (14a) in Eq (13),

$$\begin{aligned} \frac{d}{dt}(\overline{H}_f)_I = \overline{L}_{I/f} = & \dot{H}_x \hat{x} + \dot{H}_y \hat{y} + \dot{H}_z \hat{z} + (\omega_y H_z - \omega_z H_y) \hat{x} + (\omega_z H_x - \omega_x H_z) \hat{y} \\ & + (\omega_x H_y - \omega_y H_x) \hat{z} \end{aligned} \quad (15)$$

where

$$\dot{H}_x = I_x \dot{\omega}_x \quad (15a)$$

$$\dot{H}_y = I_y \dot{\omega}_y \quad (15b)$$

$$\dot{H}_z = I_z \dot{\omega}_z \quad (15c)$$

(Note: There is no time rate of change of either the moments of inertia or the unit vectors with regard to the float reference axes.)

The torque term,  $\overline{L}_{I/f}$ , can be expressed in components along the float axes, i. e.,

$$\overline{L}_{I/f} = L_x \hat{x} + L_y \hat{y} + L_z \hat{z} \quad (16)$$

At this point only the component along the  $\hat{y}$  unit vector is of interest, so the scalar magnitudes of that component can be equated:

$$\therefore L_y = I_y \dot{\omega}_y + \omega_z H_x - \omega_x H_z \quad (17)$$

Eliminating  $H_x$  and  $H_z$  by means of Eqs (14b) and (14d), respectively, and grouping similar terms

$$L_y = I_y \dot{\omega}_y + (I_x - I_z) \omega_x \omega_z - H_r \omega_x \quad (17a)$$

A comparison of the latter two torque terms in Eq (17a) permits the term  $(I_x - I_z) \omega_x \omega_z$  to be neglected. This comparison merely relates  $(I_x - I_z) \omega_z$  to  $H_r$  which is itself of the form  $I'_z \omega_s$  ( $\omega_s$  = spin rate and  $I'_z$  is the wheel inertia about axis z;  $I'_z \approx I_z$ ).  $I_x$  and  $I_z$  are approximately of the same magnitude so that their difference is small. Also  $\omega_z$  is quite small with respect to  $\omega_s$  so that the product is indeed very small relative to  $H_r$ .

The terms that are neglected by  $(I_x - I_z) \omega_x \omega_z$ , i. e., after  $\omega_x$  and  $\omega_z$  have been eliminated by Eqs (12b) and (12d), are shown in Table 7-I.

After removal of the negligible terms, Eq (17a) becomes

$$L_y = I_y \dot{\omega}_y - H_r \omega_x \quad (17b)$$

Table 7-I. Neglected Output Axis Torques

A)	$(I_x - I_z) (\omega_x - \dot{\theta}_p) (\omega_y \sin \theta_p + \omega_z \cos \theta_p)$
B)	$(I_x - I_z) \theta (\omega_x - \dot{\theta}_p)^2$
C)	$(I_x - I_z) \theta (\omega_y \sin \theta_p + \omega_z \cos \theta_p)^2$
D)	$(I_x - I_z) \theta^2 (\omega_y \sin \theta_p + \omega_z \cos \theta_p) (\omega_x - \dot{\theta}_p)$

Substituting Eqs (12b) and (12c) into Eq (17b) yields

$$L_y = I_y \frac{d}{dt} \left[ \omega_Y \cos \theta_p - \omega_Z \sin \theta_p - \dot{\theta} \right] - H_r \left[ \omega_X - \dot{\theta}_p + \theta (\omega_Y \sin \theta_p + \omega_Z \cos \theta_p) \right] \quad (17c)$$

The external torques ( $L_y$ ) will be considered to act either in the form of error torques about the output (y) axis or control torques about the output axis, i. e.,

$$L_y = L_e' + L_a \quad (18)$$

where

$L_e'$  = Error torques about y such as bias, mass unbalance, anisoelectricity, etc.

and

$L_a$  = Control torques about y.

Any external torques resulting from damping or spring effects are negligible in a gas bearing gyro such as that considered in this study. See Reference 7.3.

By carrying out the indicated differentiation, substituting Eq (18), and rearranging, Eq (17c) becomes

$$I_y \ddot{\theta} - H_r \dot{\theta}_p = -H_r \omega_X + I_y (\dot{\omega}_Y \cos \theta_p - \dot{\omega}_Z \sin \theta_p) - I_y \dot{\theta}_p (\omega_Y \sin \theta_p + \omega_Z \cos \theta_p) - H_r \theta (\omega_Y \sin \theta_p + \omega_Z \cos \theta_p) - L_e' - L_a \quad (19)$$

If a new error torque,  $-L_E$ , is defined to include all terms on the right hand side of Eq (19) except  $-H_r \omega_X$ ,  $I_y (\dot{\omega}_Y \cos \theta_p - \dot{\omega}_Z \sin \theta_p)$ , and  $-L_a$ , Eq (19) can be rewritten as

$$I_y \ddot{\theta} - H_r \dot{\theta}_p = -H_r \omega_X + I_y (\dot{\omega}_Y \cos \theta_p - \dot{\omega}_Z \sin \theta_p) - L_E - L_a \quad (20)$$

where

$$L_E = L_e' + I_y \dot{\theta}_p (\omega_Y \sin \theta_p + \omega_Z \cos \theta_p) + H_r \theta (\omega_Y \sin \theta_p + \omega_Z \cos \theta_p) \quad (20a)$$

Assuming no initial conditions exist, and that  $\sin\theta_p$  and  $\cos\theta_p$  are approximately constant, then Eq. (20) can be written in Laplace notation as

$$I_y S^2 \theta - H_r S \theta_p = -H_r \omega_X + I_y \left( [S \omega_Y] \cos\theta_p - [S \omega_Z] \sin\theta_p \right) - L_E - L_a \quad (21)$$

Eq. (21) is a linearized "Output Axis Equation." Note that general forms of torques  $L_E$  (as well as the sine and cosine of  $\theta_p$ ) cannot be Laplace transformed because of their nonlinear characteristics.\* The development of SAP error terms in Section 8 is based on the  $L_E$  being restricted to average or constant values. The linearization is performed for convenience in establishing a block diagram of the loop. This loop is operated on by the average values of these nonlinear torques in order to obtain the resulting drift rates.

To complete the closed loop diagram, an input axis equation must be determined. This equation, employing similar linearization techniques, is derived next.

#### 7.1.5 Input Axis Equation

The input axis equation is derived with nearly identical steps to those of the output axis equation, the difference being that the angular momentum of the so-called "rigid body" platform consists of both that of the float and the platform excluding the float. Actually, because of the relative motion  $\theta$  between the two, the moments of inertia of the float change with time when viewed from the platform axes. However, the eigenvectors of the float and platform never substantially deviate from each other. Therefore, it is sufficient to transform the float angular momentum to the platform reference axes without including time rate of change of inertias.

---

\* General solutions to the output axis equation and the input axis equation (in Section 7) are to be performed employing computer techniques. Such solutions will not restrict the  $L_E$  torques or  $\theta_p$  motion.

Eq (2) to the platform-float combination gives

$$\frac{d}{dt} (\bar{H}_{pf})_I = \frac{d}{dt} (\bar{H}_{pf})_P + \bar{\omega}_P \times \bar{H}_{pf} = \bar{L}_{I/P} \quad (22)$$

where

$$\bar{H}_{pf} = \bar{H}_P + \bar{H}_f \quad (23)$$

The float angular momentum  $\bar{H}_f$  has already been defined in Eq (14). The term  $\bar{H}_P$  then is

$$\bar{H}_P = I_{P_x} \omega_1 \hat{x}_P + I_{P_y} \omega_2 \hat{y}_P + I_{P_z} \omega_3 \hat{z}_P \quad (24)$$

where the  $\omega_1, \omega_2, \omega_3$  are defined in Eqs (8b), (8c), and (8d), respectively, and the  $I_P$  symbols represent principal moments of inertia of the platform alone about its c. g.

Since the input axis, which is along the platform  $x_P$  (or X), is the axis of interest it is necessary to transform the float angular momentum into platform coordinates by use of Eqs (5) and (14a):

$$\begin{bmatrix} H_{f_{xp}} \\ H_{f_{yp}} \\ H_{f_{zp}} \end{bmatrix} = \begin{bmatrix} 1 & 0 & -\theta \\ 0 & 1 & 0 \\ \theta & 0 & 1 \end{bmatrix} \begin{bmatrix} H_x \\ H_y \\ H_z \end{bmatrix} \quad (25)$$

which yields

$$\overline{H}_f^{i*} = \left( H_x - \theta H_z \right) \hat{x}_p + \left( H_y \right) \hat{y}_p + \left( H_z + \theta H_x \right) \hat{z}_p \quad (25a)$$

Substituting Eqs (14b), (14c), and (14d) gives

$$\overline{H}_f^{i*} = \left( I_x \omega_x - \theta \left[ I_z \omega_z + H_r \right] \right) \hat{x}_p + \left( I_y \omega_y \right) \hat{y}_p + \left( I_z \omega_z + H_r + \theta \left[ I_x \omega_x \right] \right) \hat{z}_p \quad (25b)$$

Now from Eqs (24) and (25b), Eq (23) takes the form of

$$\begin{aligned} \overline{H}_{pf} = & \left( I_{p_x} \omega_1 + I_x \omega_x - \theta \left[ I_z \omega_z + H_r \right] \right) \hat{x}_p + \left( I_{p_y} \omega_2 + I_y \omega_y \right) \hat{y}_p \\ & + \left( I_{p_z} \omega_3 + I_z \omega_z + H_r + \theta \left[ I_x \omega_x \right] \right) \hat{z}_p \end{aligned} \quad (26)$$

Again for the sake of simplification,

$$\overline{H}_{pf} = H_{x_{pf}} \hat{x}_p + H_{y_{pf}} \hat{y}_p + H_{z_{pf}} \hat{z}_p \quad (26a)$$

where

$$H_{x_{pf}} = I_{p_x} \omega_1 + I_x \omega_x - \theta \left[ I_z \omega_z + H_r \right] \quad (26b)$$

$$H_{y_{pf}} = I_{p_y} \omega_2 + I_y \omega_y \quad (26c)$$

$$H_{z_{pf}} = I_{p_z} \omega_3 + I_z \omega_z + \theta \left[ I_x \omega_x \right] + H_r \quad (26d)$$

\*  $\overline{H}_f$  represents  $\overline{H}_f$  expressed in platform coordinates.

Substituting Eqs (26a) and (8a) into Eq (22) yields

$$\begin{aligned} \frac{d}{dt} \left( \overline{H}_{pf} \right) / I = \overline{L}_{I/p} = \dot{H}_{x_{pf}} \hat{x}_p + \dot{H}_{y_{pf}} \hat{y}_p + \dot{H}_{z_{pf}} \hat{z}_p + \left( \omega_2 H_{z_{pf}} - \omega_3 H_{y_{pf}} \right) \hat{x}_p \\ + \left( \omega_3 H_{x_{pf}} - \omega_1 H_{z_{pf}} \right) \hat{y}_p + \left( \omega_1 H_{y_{pf}} - \omega_2 H_{x_{pf}} \right) \hat{z}_p \end{aligned} \quad (27)$$

The torque term  $\overline{L}_{I/p}$  can be expressed in components along the platform axes, i. e.,

$$\overline{L}_{I/p} = L_{x_p} \hat{x}_p + L_{y_p} \hat{y}_p + L_{z_p} \hat{z}_p \quad (28)$$

Since we are interested only in the component along the  $\hat{x}_p$  unit vector, the scalar coefficients of that vector can be equated:

$$\therefore L_{x_p} = \dot{H}_{x_{pf}} + \omega_2 H_{z_{pf}} - \omega_3 H_{y_{pf}} \quad (28a)$$

The time rate of change of  $H_{x_{pf}}$  is obtained from Eq (26b):

$$\dot{H}_{x_{pf}} = I_{p_x} \dot{\omega}_1 + I_{x_x} \dot{\omega}_x - \dot{\theta} \left[ I_z \dot{\omega}_z + H_r \right] - \theta \left[ I_z \dot{\omega}_z \right] \quad (29)$$

Substituting Eqs (29), 26c), and (26d) into Eq (28a) yields

$$\begin{aligned} L_{x_p} = I_{p_x} \dot{\omega}_1 + I_{x_x} \dot{\omega}_x - \dot{\theta} \left[ I_z \dot{\omega}_z + H_r \right] - \theta \left[ I_z \dot{\omega}_z \right] \\ + \omega_2 \left( I_{p_z} \omega_3 + I_z \omega_z + \theta \left[ I_{x_x} \dot{\omega}_x \right] + H_r \right) - \omega_3 \left( I_{p_y} \omega_2 + I_y \dot{\omega}_y \right) \end{aligned} \quad (30)$$

As Eq (17a) does, the wheel momentum  $H_x$  is considered to be sufficiently predominant over any  $\omega$  terms that it is compared against such that they are neglected. Also  $\theta$  is sufficiently small and the expected angular accelerations indicated by MSFC data are slow so  $\theta I_z \dot{\omega}_z$  can be suppressed. The remaining terms in Eq (30) are then

$$L_{x_p} = I_{P_x} \dot{\omega}_x + I_x \dot{\omega}_x - \dot{\theta} H_r + H_r \dot{\omega}_z \quad (30a)$$

The torque terms that have been neglected here are presented in Table 7-II after  $\omega_2$ ,  $\omega_3$ ,  $\omega_x$ ,  $\omega_y$ ,  $\omega_z$  have been removed by Eqs (8c), (8d), (12b), (12c), and (12d), respectively.

Substituting Eqs (8b), (8c), and (12b) into Eq (30a) yields

$$L_{x_p} = I_{P_x} \frac{d}{dt} (\omega_x - \dot{\theta}_p) + I_x \frac{d}{dt} (\omega_x - \dot{\theta}_p) + \theta [\omega_Y \sin \theta_p + \omega_Z \cos \theta_p] - \dot{\theta} H_r + H_r (\omega_Y \cos \theta_p - \omega_Z \sin \theta_p) \quad (30b)$$

Table 7-II. Neglected Input Axis Torques

A) $I_z (\omega_Y^2 - \omega_Z^2) \sin \theta_p \cos \theta_p$	*J) $\Delta I_p \omega_Y \omega_Z (\cos^2 \theta_p - \sin^2 \theta_p)$
B) $I_z \omega_Y \omega_Z (\cos^2 \theta_p - \sin^2 \theta_p)$	K) $-I_x \theta (\dot{\theta}_p - \dot{\omega}_X) [\omega_Y \cos \theta_p - \omega_Z \sin \theta_p]$
C) $I_z \theta (\dot{\theta}_p - \dot{\omega}_X) [\omega_Y \cos \theta_p - \omega_Z \sin \theta_p]$	
D) $-I_z \dot{\theta} (\omega_Y \sin \theta_p + \omega_Z \cos \theta_p)$	L) $I_x \theta^2 (\omega_Y^2 - \omega_Z^2) \overline{\sin \theta_p \cos \theta_p}$
E) $-2I_z \theta \dot{\theta} (\dot{\theta}_p - \dot{\omega}_X)$	M) $I_x \theta^2 \omega_Y \omega_Z (\cos^2 \theta_p - \sin^2 \theta_p)$
F) $-I_z \theta (\dot{\omega}_Y \sin \theta_p + \dot{\omega}_Z \cos \theta_p)$	N) $-I_y (\omega_Y^2 - \omega_Z^2) \sin \theta_p \cos \theta_p$
G) $-I_z \theta^2 (\dot{\theta}_p - \dot{\omega}_X)$	O) $-I_y \omega_Y \omega_Z (\cos^2 \theta_p - \sin^2 \theta_p)$
H) $-I_z \dot{\theta}_p (\omega_Y \cos \theta_p - \omega_Z \sin \theta_p)$	P) $I_y \dot{\theta} (\omega_Y \sin \theta_p + \omega_Z \cos \theta_p)$
*I) $\Delta I_p (\omega_Y^2 - \omega_Z^2) \cos \theta_p \sin \theta_p$	
*Note. $\Delta I_p$ is defined as $I_{P_z} - I_{P_y}$	

Again consider the external torques acting about the SAP input axis to be composed of either error torques or control torques such that

$$L_{x_p} = L_{pe}' + L_{pa} \quad (31)$$

where

$L_{pe}'$  = Error torques about  $x_p$  such as friction, torquer errors, etc.

and

$L_{pa}$  = Control torques about  $x_p$

By carrying out the indicated differentiation, substituting Eq (31), and rearranging, Eq (30b) takes the form

$$\begin{aligned} (I_{p_x} + I_x) (\ddot{\theta}_p - \dot{\omega}_X) + H_r \dot{\theta} &= H_r (\omega_Y \cos \theta_p - \omega_Z \sin \theta_p) \\ &+ I_x \theta (\omega_Y \sin \theta_p + \omega_Z \cos \theta_p) \\ &+ I_x \theta (\dot{\omega}_Y \sin \theta_p + \dot{\omega}_Z \cos \theta_p) \\ &+ I_x \theta \dot{\theta} (\omega_Y \cos \theta_p - \omega_Z \sin \theta_p) - L_{pe}' - L_{pa} \end{aligned} \quad (32)$$

If a new error torque term,  $-L_{pE}$ , is defined to include all terms on the right hand side of Eq (32) except  $H_r (\omega_Y \cos \theta_p - \omega_Z \sin \theta_p)$  and  $-L_{pa}$ , Eq (32) can be rewritten as

$$(I_{p_x} + I_x) (\ddot{\theta}_p - \dot{\omega}_X) + H_r \dot{\theta} = H_r (\omega_Y \cos \theta_p - \omega_Z \sin \theta_p) - L_{pE} - L_{pa} \quad (32a)$$

where

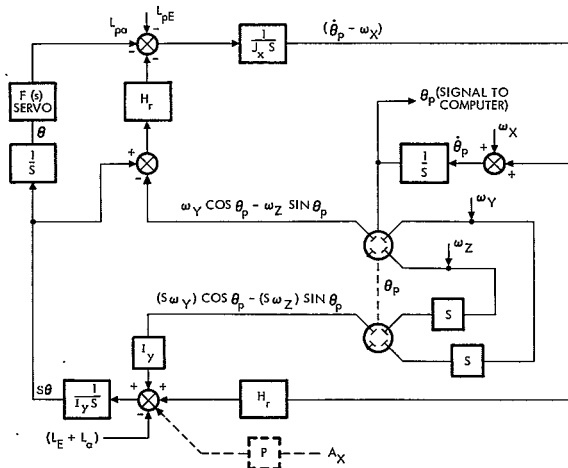
$$\begin{aligned} L_{pE} &= L_{pe}' + I_x \theta (\omega_Y \sin \theta_p + \omega_Z \cos \theta_p) + I_x \theta (\dot{\omega}_Y \sin \theta_p + \dot{\omega}_Z \cos \theta_p) \\ &+ I_x \theta \dot{\theta} (\omega_Y \cos \theta_p - \omega_Z \sin \theta_p) \end{aligned} \quad (32b)$$

With no initial conditions, and restricting  $\sin\theta_p$  and  $\cos\theta_p$  to be approximately constant, Eq (32a) can be written in Laplace notation as

$$\left( I_{P_x} + I_x \right) S \left( \dot{\theta}_p - \omega_x \right) + H_r S \theta = H_r \left( \omega_y \cos \theta_p - \omega_z \sin \theta_p \right) - L_{pE} - L_{pa} \quad (33)$$

Eq (33) is a linearized "Input Axis Equation."

A block diagram representation of Eqs (21) and (33) is shown below in Figure 7-2. The diagram includes several symbols defined below it which will be used during the remainder of this section.



where:

$$J_x \triangleq I_{px} + I_x$$

$$L_{pa} \triangleq F(s)\theta, \quad (F(s) \text{ is the platform control})$$

$$P \triangleq \text{pendulosity of FIGA}$$

$$A_x \triangleq \text{acceleration along the vehicle X axis}$$

Figure 7-2. SAP Block Diagram

## 7.2 SAP ERROR TERMS

Now that the equations of motion have been determined, there remains to be evaluated those terms in the equations that contribute error effects. Due to their nonlinear implications on Eqs (21) and (33), certain approximations will be made here to determine the effects of the error torques,  $L_E$  and  $L_{pE}$  in Eqs (20a) and (32a). Such approximations involve the treatment of each effect acting independently of the others rather than being coupled together. In this manner a set of error contributions based on closed-loop operation can be developed for use in error analyses.

These approximations imply the validity of superposition which is generally not a property of nonlinear systems. However, the following derivations suggest that a reasonable degree of superposition does exist in the SAP.

A more rigorous evaluation of the error effects (which would serve as a verification of any preliminary supposition) would necessitate the solution of the nonlinear equations, Eq (19) and Eq (32). This type of evaluation could be implemented by means of either digital or analog computer techniques. However, the scope of the current SAP strapped-down study can be satisfied by the error equations which will be derived here. Any future studies should include computerized solutions to Eq (19) and Eq (32).

If an even broader scope of error evaluation is desirable, the neglected terms in Tables 7-I and 7-II as well as product-of-inertia type errors should be investigated. As it was pointed out previously, their effects on rate measurement are at least two orders of magnitude smaller than those terms that were retained. The cost of such a simulation goes beyond the merits which could be expected.

### 7.2.1 Derivation of SAP Error Terms

If the linearized Eq (21) and Eq (33) are combined such that

- (1)  $\theta$  is eliminated
- (2)  $L_{pa} = F(s)\theta$  ( $F(s) = F$  in remainder of report)
- (3)  $\left(\dot{\theta}_p - \omega_X\right)$  is explicit

then the resulting equation is

$$\begin{aligned} (\dot{\theta}_P - \omega_X) = & \frac{H_R I_Y S^2 (\dot{\omega}_Y \cos \theta_P - \dot{\omega}_Z \sin \theta_P) - L_{PE} I_Y S^2}{J_X I_Y S^3 + H_R^2 S + H_R F} \\ & + \frac{-I_Y (H_R S + F) \left( [S \omega_Y] \cos \theta_P - [S \omega_Z] \sin \theta_P \right) + (H_R S + F) (L_E + L_a^*)}{J_X I_Y S^3 + H_R^2 S + H_R F} \end{aligned} \quad (34)$$

The terms on the right side of Eq (32) are all "error terms" in one form or another since ideally

$$(\dot{\theta}_P - \omega_X) = 0 \quad (34a)$$

The right hand side of Eq (34) is then the drift rate about the SAP input axis, and will be designated as  $\epsilon_p(s)$ .

Eq (34), in conjunction with the block diagram of Figure 7-2, shows that  $\epsilon_p(s)$  is a function of the vehicle angular rates and the error torques acting about both the input and output axes. Included in the output axis error torques ( $L_E$ ) are the more conventional drift rate effects due to such phenomena as fixed torque and mass unbalances. These effects, lumped into a single term ( $L_e$ ), will be developed first.

Next a more specialized case (where the component of vehicle angular rate along the SAP output axis is a ramp function) is evolved. Finally, and with particular emphasis, the error effects due to vehicle angular rates and output-axis or input-axis error torques that are oscillatory in nature are investigated.

The errors to be developed and a brief description of their associated causes were presented in Subsection 2.5 and are repeated here in Table 7-III for convenience. Following this error listing is an explanation of the steps to be used in obtaining expressions for the errors. Finally, the steps are demonstrated and the expressions tabulated.

\* Both forms of output axis torques, i.e.,  $L_E$  and  $L_a$ , will be retained in general throughout much of the derivation of the SAP equations. The  $L_a$  are retained for convenience in the deriving of the FIGA equations in the next section. The  $L_a$  are undefined for the SAP at this time and therefore have significance only for the FIGA.

Table 7-III. Drift Rate Errors and Causes

Error No.	Error Cause
$\epsilon_1$	$L_e'$ are fixed torques, mass unbalances, and anisoelectricity (MSFC error model)
$\epsilon_2$	Ramp input of $\omega_2$ (constant angular acceleration during finite time interval)
$\epsilon_3$	Rectification due to sinusoidal inputs of $\omega_2$ and $\omega_3$
$\epsilon_4$	Rectification due to sinusoidal inputs of $L_e'$ and $\omega_3$ ( $L_e'$ are $M_{ubs}$ and $M_{ubi}$ activated by vibration vibration inputs)
$\epsilon_5$	Rectification due to sinusoidal inputs of $L_e'$ and $\omega_3$ ( $L_{pe}'$ are friction torques or mass unbalances excited by vibration)
$\epsilon_6$	Rectification due to sinusoidal inputs of $\omega_2$ and $\omega_3$ (different propagation through loop than $\epsilon_3$ )
$\epsilon_7$	Rectification due to sinusoidal inputs of $L_e'$ and $\omega_3$ (different propagation through loop than $\epsilon_4$ )
$\epsilon_8$	Rectification due to sinusoidal inputs of $L_{pe}'$ and $\omega_3$ (different propagation through loop than $\epsilon_5$ )
$\epsilon_9$	Rectification due to sinusoidal inputs of $\omega_X$ and $\omega_3$ (maximum value occurs when $\omega_X$ and $\omega_3$ are in phase)

Error term  $\epsilon_1$  can be obtained by simply applying the final value theorem to Eq (34) and considering  $L_a$  and the nonlinear contributions to Eq (20a) to be zero.

Similarly, error term  $\epsilon_2$  can be found by again applying the final value theorem to Eq (34), treating the angular acceleration component along the SAP output axis as a constant, and considering  $L_E$  and  $L_a$  torques to be equal to zero.

Error terms  $\epsilon_3$  through  $\epsilon_9$  all fall into the general classification of drift errors induced by rectification. These rectified drift rates are contained within the nonlinear portions of Eq (20a) which describe output-axis error torques,  $L_E$ . Each of the nonlinear terms in Eq (20a) serves to produce a class of drift errors.

The first class involves the product of the float angle,  $\theta$  and the component of vehicle rate along the SAP spin axis,  $\omega_3$  (defined in Eq 8d). However, an expression of  $\theta$  can be derived from a rearrangement of Eqs (21) and (33). This expression shows  $\theta$  to be a direct function of  $L_e'$ ,  $L_{pe}'$ , and  $\omega_2$  (defined in Eq 8c), which is apparent in the block diagram of Figure 7-2. By restricting these latter three forcing functions to be sinusoidal, the frequency response of  $\theta$  with regard to each of them can be obtained. Rectifications resulting from the product of each of these frequency responses and  $\omega_3$  lead to the first class of errors.

The second class is similarly based on the product of  $\theta_p$  and  $\omega_3$ . Either Eq (34) or Figure 7-2 clearly demonstrates that  $\theta_p$  is a direct function of  $\omega_x$  in addition to  $L_e'$ ,  $L_{pe}'$ , and  $\omega_2$ . The frequency responses of  $\theta_p$  due to oscillatory forms of these four inputs are inspected for rectifications with  $\omega_3$ .

#### 7.2.2 Error Term $\epsilon_1$ (Fixed Torque, G-Sensitive)

Inspection of Eq (34) or Figure 7-2 assures that for constant values of the inputs  $L_E$ ,  $L_a$ ,  $L_{pE}$  and  $\omega_2$  (defined in Eq 8c), only those due to  $L_E$  and  $L_a$  contribute to steady-state drift rate. This can be verified by

applying the final value theorem after assuming\* that the servo is such that it permits the theorem's application. Also, since the use of controlled electrical output axis torquing is undefined at this stage, the errors associated with  $L_a$  (such as scale factor) are not treated here. The steady-state drift rate is then

$$\epsilon_p = \frac{\overline{L_E}}{H_r} \quad (35)$$

where the  $\overline{L_E}$  are the average values of the error torques defined in Eq (20a) (which is repeated here):

$$L_E = L_e' + I_y \theta_p (\omega_Y \sin \theta_p + \omega_Z \cos \theta_p) + H_r \theta (\omega_Y \sin \theta_p + \omega_Z \cos \theta_p)$$

If  $\omega_3$  is substituted by Eq (8d) into Eq (20a), then Eq (35) becomes

$$\epsilon_p = \frac{1}{H_r} (L_e' + I_y \theta_p \omega_3 + H_r \theta \omega_3) \quad (35a)$$

Error term  $\epsilon_1$  pertains only to the drift effects of fixed torque and g sensitive phenomena such as mass unbalances and anisoelasticity. These error torques are implied by  $L_e'$  in Eq (20a). Therefore,  $\epsilon_1$  can be readily determined as

$$\epsilon_1 = \frac{L_e'}{H_r} \quad (36)$$

### 7.2.3 Error Term $\epsilon_2$ (Ramp Input of $\omega_2$ )

A review of Eq (34) reveals that a ramp type input form of  $\omega_2$  (equivalent to a constant or "average" value of  $\dot{\omega}_2$ ) creates a steady-state

---

\* The assumption here pertains to the servo being of form  $F(s) = KG(s)$  with poles of  $G(s)$  existing in left half plane and  $F(s) = K(1)$  (i. e.,  $G(s) = 1$ ) at frequencies of interest.

drift rate in addition to  $\bar{L}_E$ . \* Such a forcing function could occur in the form of constant angular acceleration during some finite time interval. The dc value of drift rate caused by constant  $\dot{\omega}_2$  can be found by application of the final value theorem to Eq (34),

$$\epsilon_2 = -\frac{I_y}{H_r} \dot{\omega}_2 \quad (37)$$

#### 7.2.4 Error Terms $\epsilon_3$ to $\epsilon_9$ (Rectification)

In this section it will be shown how vibratory inputs, both linear and angular, can result in SAP drift rate errors. The method to be used can most easily be described by means of Figure 7-3 together with the relationships developed in deriving the expression (Eq 35a) for error source  $\epsilon_1$ . Figure 7-3 is a simplified version of Figure 7-2 that employs substitution of  $\omega_2$  and  $\omega_3$  by Eq (8c) and (8d), respectively.

As may be observed by examination of Figure 7-3 the following disturbance inputs to the SAP may be independently specified:  $\omega_2$ ,  $\omega_3$ ,  $\omega_X$ ,  $L_{e'}$ , and  $L_{pe'}$ . The first three are angular rates about the gyro output, spin reference, and input axis, respectively. The fourth term represents, in this case, torques about the gyro output axis due to linear

---

\* In Eq (34) recall the assumption that  $\sin\theta_p$  and  $\cos\theta_p$  remain essentially constant. Then by Eq (8c)

$$\dot{\omega}_2 = S\omega_2 = S(\omega_Y \cos\theta_p - \omega_Z \sin\theta_p)$$

and from Eq (34),

$$\epsilon_2 = \frac{I_y (H_r S + F)}{J_x I_y S^3 + H_r^2 S + H_r F}$$



an error model of the SAP excited by the above five input, the following assumptions will apply:

- (1) Each input will be a sinusoidal function of time.
- (2) These inputs will be considered acting two at a time. As will be shown below, rectification errors are excited in this manner.
- (3) The SAP rate,  $\dot{\theta}_p$  is sufficiently small such that  $\sin \theta_p$  and  $\cos \theta_p$  can be considered as constant parameters.

In developing the error  $\epsilon_1$  it was shown by Eqs (35) and (36) that a constant torque acting around the gyro output axis ( $L_e'$ ) will result in a SAP drift, while a constant input axis torque ( $L_{pe}'$ ) does not produce such an error. Referring to Figure 7-3 it is seen that the  $L_E$  error term is composed of two product terms in addition to  $L_e'$ . Hence, any constant value in these two product error terms will also yield a SAP drift rate.

On the other hand, since  $L_{pe}'$  does not produce a constant drift rate error, then any constant component in the nonlinear terms in  $L_{pE}$  will also fail to produce such drift errors. Hence, rectification errors will only be evaluated for the two nonlinear terms in  $L_E$ . The errors from these two terms will be divided into two classes:

$$\text{Class 1: } H_r \theta \omega_3$$

$$\text{Class 2: } I_y \dot{\theta}_p \omega_3$$

These two classes of errors will be treated separately in the following subsections.

### Class 1 Rectification Errors: $H_r \theta \omega_3$

Considering the first nonlinear term ( $H_r \theta \omega_3$ ) in  $L_E$ , a constant value can occur if  $\theta$  and  $\omega_3$  are sinusoidal functions of time. To demonstrate, let

$$\omega_3 = \Omega_3 \sin \omega_o t \quad (38)$$

and

$$\theta = \theta_{\max} \sin(\omega_o t + \phi_1) \quad (39)$$

Therefore, the product  $H_r \theta \omega_3$  is

$$H_r \theta \omega_3 = H_r \theta_m \Omega_3 \sin \omega_o t \sin(\omega_o t + \phi_1) \quad (40)$$

or by using trigonometric identities,

$$H_r \theta \omega_3 = \frac{H_r \theta_m \Omega_3}{2} \left[ \cos(-\phi_1) - \cos(2\omega_o t + \phi_1) \right] \quad (40a)$$

The average value of  $H_r \theta \omega_3$  during one cycle is

$$\overline{H_r \theta \omega_3} = \frac{H_r \theta_m \Omega_3}{2} \cos(-\phi_1) \quad (40b)$$

Now consider the effect of the term  $H_r \theta \omega_3$  for the case where  $\omega_3$  and  $\omega_2$  are acting simultaneously and  $\omega_X$ ,  $L_e$ , and  $L_{pe}$  are assumed zero.

Whereas the rate  $\omega_3$  can be specified independently, the float angle  $\theta$  will be excited by  $\omega_2$ . However, the float angle  $\theta$  will also be excited by

the nonlinear terms (included in  $L_{pE}$  and  $L_E$ ) containing  $\theta$  itself and  $\omega_3$ . For sufficiently small values of  $\omega_3$ , the influence of these nonlinear terms on  $\theta$  in comparison with that of  $\omega_2$  can be made negligible. It is then possible to define  $\theta$  due to  $\omega_2$  by a linear transfer function relating  $\theta$  and  $\omega_2$ .

To obtain a closed-loop expression for  $\theta$ , the linearized equations, Eqs (21) and (33), can again be used by rearranging in the following manner:

- (1)  $\left(\dot{\theta}_p - \omega_x\right)$  is eliminated
- (2)  $L_{pa} = F\theta$
- (3)  $\theta$  is explicit
- (4) Substitute Eq (8c).

The resulting equation is

$$\theta = \frac{\left(H_r^2 + J_x I_y S^2\right) \omega_2 - H_r L_{pE} - J_x S \left(L_E + L_a^*\right)}{J_x I_y S^3 + H_r^2 S + H_r F} \quad (41)$$

The transfer function between  $\theta$  and  $\omega_2$  as indicated by Eq (41) is

$$\theta = \left( \frac{H_r^2 + J_x I_y S^2}{J_x I_y S^3 + H_r^2 S + H_r F} \right) \omega_2 = \frac{\theta}{\omega_2}(s) \omega_2 \quad (42)$$

---

\*  $L_a$  is retained here only for reference to PIGA applications.

If  $\omega_2$  (phased relative to  $\omega_3$ ) is

$$\omega_2 = \Omega_2 \sin(\omega_0 t + \psi_1) \quad (43)$$

then  $\theta$  can be expressed as

$$\theta = \left| \frac{\theta}{\omega_2}(j\omega) \right| \Omega_2 \sin\left(\omega_0 t + \psi_1 - \angle \frac{\theta}{\omega_2}(j\omega)\right) \quad (44)$$

where

$$\Omega_2 = \text{Amplitude of } \omega_2 \quad (44a)$$

$$\left| \frac{\theta}{\omega_2}(j\omega) \right| = \text{Amplitude ratio between } \theta \text{ and } \omega_2 \quad (44b)$$

$$\angle \frac{\theta}{\omega_2}(j\omega) = \text{Phase angle between } \theta \text{ and } \omega_2 \quad (44c)$$

Substituting Eq (44) for Eq (39), the average value of  $H_r \theta \omega_3$  can be obtained directly from Eq (40b), i. e.,

$$\overline{H_r \theta \omega_3} = \frac{H_r \left| \frac{\theta}{\omega_2}(j\omega) \right| \Omega_2 \Omega_3}{2} \cos\left(\angle \frac{\theta}{\omega_2}(j\omega) - \psi_1\right) \quad (45)$$

Hence by Eq (35) the average drift rate due to  $\omega_2$  and  $\omega_3$  is

$$\epsilon_3 = \frac{1}{H_r} \overline{H_r \theta \omega_3} = \frac{\left| \frac{\theta}{\omega_2} \right| \Omega_2 \Omega_3}{2} \cos\left(\angle \frac{\theta}{\omega_2} - \psi_1\right)^* \quad (46)$$

\* Note that the  $j\omega$  notation has been deleted in Eq (46). It will be deleted throughout the remainder of the report for convenience.

It should be noted that the validity of Eq (46) is based on the assumption that any float angular motion  $\theta$  is induced only by  $\omega_2$ , and is unaffected by  $\omega_3$ . Obviously, when  $\omega_3$  reaches a sufficiently large magnitude, relative to  $\omega_2$ , this assumption will no longer be valid. The maximum value of  $\omega_3$  for which the above linearized method of analysis holds true cannot be accurately established without benefit of a nonlinear analysis.

Two remaining Class 1 errors can be determined by utilizing the same technique used to obtain  $\epsilon_3$  in Eq (46). Error term  $\epsilon_4$  results from oscillations of  $L_e'$  rather than  $\omega_2$ . In this case, the magnitude of  $\omega_3$  must again be considered as being less than some specified value, only this time with regard to an  $L_e'$  magnitude. A transfer function between  $\theta$  and  $L_e'$  is obtained from Eq (41) and is solved for explicitly in terms of  $\theta$ . After substituting a sinusoidal form of  $L_e'$  (phased relative to  $\omega_3$ ) the average value of the product  $\theta\omega_3$  over one period yields  $\epsilon_4$ ,

$$\epsilon_4 = \frac{1}{2} \left| \frac{\theta}{L_e'} \right| \cdot \left| L_e' \right|^* \Omega_3 \cos \left( \left| \frac{\theta}{L_e'} \right| - \psi_2 \right) \quad (47)$$

Similarly, the same steps with  $L_{pe}'$  in place of  $L_e'$  yield  $\epsilon_5$ ,

$$\epsilon_5 = \frac{1}{2} \left| \frac{\theta}{L_{pe}'} \right| \cdot \left| L_{pe}' \right|^* \Omega_3 \cos \left( \left| \frac{\theta}{L_{pe}'} \right| - \psi_3 \right) \quad (48)$$

### Class 2 Rectification Errors: $I_y \dot{\theta}_p \omega_3$

Class 2 errors originate from the second nonlinear term  $(I_y \dot{\theta}_p \omega_3)$  in  $L_E$ . In this class, drift errors occur if  $\dot{\theta}_p$  and  $\omega_3$  are sinusoidal functions of time. Much the same approach as that used to determine the Class 1 errors is adopted to develop this second group. First,  $\omega_3$  is

---

\*  $\left| L_e' \right|$  and  $\left| L_{pe}' \right|$  refer to amplitudes of sinusoidal  $L_e'$  and  $L_{pe}'$ .

again expressed as in Eq (38) and  $\theta_p$  is shown in the form of  $\theta$  in Eq (39):

$$\dot{\theta}_p = \dot{\theta}_{p_{\max}} \sin(\omega_o t + \phi_2) \quad (49)$$

From these two equations an average value resembling Eq (40b) can be obtained, i.e.,

$$\frac{\dot{\theta}_p}{I_y \dot{\theta}_{p_{\max}} \omega_3} = \frac{I_y \dot{\theta}_{p_{\max}} \Omega_3 \cos(-\phi_2)}{2} \quad (50)$$

Eq (34) can be rewritten to provide a closed-loop expression for  $\dot{\theta}_p$  necessary in Eq (50):

$$\dot{\theta}_p = \omega_X - \frac{I_y F S \omega_2 + I_y S^2 L_{pE} - (H_r S + F)(L_E + L_a^*)}{J_x I_y S^3 + H_r^2 S + H_r F} \quad (51)$$

Pursuing the same procedure as that of the Class 1 errors, it is pertinent that  $\omega_3$  can be specified independently but  $\dot{\theta}_p$  in Eq (51) results from four forcing functions  $\omega_2$ ,  $L_{pe}'$ ,  $L_e'$ , and  $\omega_X$ . Up to certain magnitudes of  $\omega_3$  with regard to  $\omega_2$ ,  $L_{pe}'$ ,  $L_e'$ , and  $\omega_X$ , respectively,  $\dot{\theta}_p$  is not a function of  $\omega_3$ . Further,  $\dot{\theta}_p$  can be identified as being affected only by the particular forcing function of interest, the other three being suppressed.

Within these restrictions, transfer functions between  $\dot{\theta}_p$  and each of the four external sources are evolved from Eq (51). These expressions, solved explicitly for  $\dot{\theta}_p$ , are used with the sinusoidal forms of the external sources implied in Eqs (38), (43), (46), (47), and (48). The transfer function between  $\dot{\theta}_p$  and  $\omega_X$  is unity. The drift error in each case then is the average value of the product of the particular transfer function amplitude, the associated sinusoidal forcing function, and a periodic  $\omega_3$ . In each case, the other three inputs are suppressed while the input of interest is being investigated.

---

\*  $L_a$  is retained here only for reference to PIGA applications.

Drift errors  $\epsilon_6$ ,  $\epsilon_7$ , and  $\epsilon_8$  are therefore due to the same external causes as  $\epsilon_3$ ,  $\epsilon_4$ ,  $\epsilon_5$ , respectively. The respective differences are due to different propagations through the loop. Accordingly, the frequency responses will differ. Error  $\epsilon_6$  is derived as an example:

From Eq (51)

$$\frac{\dot{\theta}_p}{\omega_2}(s) = \frac{-I_y FS}{J_x I_y S^3 + H_r^2 S + H_r F} \quad (52)$$

From Eq (52) the frequency response (using Eq (43) ) is

$$\theta_p = \left| \frac{\dot{\theta}_p}{\omega_2} \right| \Omega_2 \sin\left(\omega_o t + \psi_1 - \angle \frac{\dot{\theta}_p}{\omega_2}\right) \quad (53)$$

The average value of  $I_y \dot{\theta}_p \omega_3$  indicated in Eq (50) is then

$$\overline{I_y \dot{\theta}_p \omega_3} = \frac{I_y}{2} \left| \frac{\dot{\theta}_p}{\omega_2} \right| \Omega_2 \Omega_3 \cos\left(\angle \frac{\dot{\theta}_p}{\omega_2} - \psi_1\right) \quad (54)$$

From Eqs (35) and (54) the drift rate  $\epsilon_6$  is

$$\epsilon_6 = \frac{1}{2} \frac{I_y}{H_r} \left| \frac{\dot{\theta}_p}{\omega_2} \right| \Omega_2 \Omega_3 \cos\left(\angle \frac{\dot{\theta}_p}{\omega_2} - \psi_1\right) \quad (54a)$$

Similarly, sinusoidal inputs of  $L_e'$  and  $L_{pe}'$  rectify individually with  $\omega_3$  as

$$\epsilon_7 = \frac{1}{2} \frac{I_y}{H_r} \left| \frac{\dot{\theta}_p}{L_e'} \right| \cdot \left| L_e' \right| \Omega_3 \cos\left(\angle \frac{\dot{\theta}_p}{L_e'} - \psi_2\right) \quad (55)$$

and

$$\epsilon_8 = \frac{1}{2} \frac{I_y}{H_r} \left| \frac{\dot{\theta}_p}{L_{pe}} \right| \cdot \left| L_{pe} \right| \Omega_3 \cos \left( \left| \frac{\dot{\theta}_p}{L_{pe}} \right| - \psi_3 \right) \quad (56)$$

For the case of  $\omega_X$  the drift rate is simply

$$\epsilon_9 = \frac{I_y}{H_r} \omega_X \omega_3 \quad (57)$$

This error is due to oscillatory coupling between components of vehicle rate along the platform input and spin axes. If the form of  $\omega_X$  (phased relative to  $\omega_3$ ) is

$$\omega_X = \Omega_X \sin(\omega_0 t + \psi_4) \quad (58)$$

then the average value of their product over one cycle will yield a frequency independent of drift rate equal to

$$\epsilon_9 = \frac{1}{2} \frac{I_y}{H_r} \Omega_X \Omega_3 \cos \psi_4 \quad (59)$$

When the two oscillations are in phase their maximum rectification effect is reached, i.e.,

$$\epsilon_{9_{\max}} = \frac{1}{2} \frac{I_y}{H_r} \Omega_X \Omega_3 \quad (59a)$$

The algebraic expressions for the drift errors are listed in Subsection 2.5. In summary, there are four significant features associated with these expressions:

- (1) They are restricted to the conditions that  $\cos \theta_p$  and  $\sin \theta_p$  remain essentially constant.
- (2) Forcing functions are periodic in nature (exceptions are  $\epsilon_1$  and  $\epsilon_2$ ).
- (3) The SAP float angle  $\theta$  and platform angle rate  $\dot{\theta}_p$  are not excited by the SAP spin axis component of vehicle angular velocity ( $\omega_3$ ).
- (4) The extent to which superposition may be used in evaluating the effects of more than one error source (acting concurrently) is unknown. Its validity must await further nonlinear analysis for resolution.

### 7.3 PIGA ERROR TERMS

If the control torque term  $L_a$  in Eq. (51) is considered to be the torque due to instrument pendulosity and input axis acceleration; i.e.,  $L_a = P \cdot A_X$ , and the vehicle rates and error torques are suppressed, then the nominal equation for a PIGA results,

$$\dot{\theta}_p = \frac{P(H_r S + F)}{J_x I_y S^3 + H_r^2 S + H_r F} A_X \quad (60)$$

(Note:  $P$  and  $A_X$  are pendulosity and input axis acceleration, respectively.)

In steady-state operation, Eq (60) becomes

$$\theta_p = \frac{P}{H_r} A_X \quad (60a)$$

where the ratio  $P/H_r$  is the nominal value of the scale factor relating SAP angular rate to input axis acceleration. This same scale factor serves to relate increments of SAP angles to increments of input velocity after integrating Eq (60a). The ideal acceleration measurement, then, is the SAP motion in Eq (60a) multiplied by the inverse of the scale factor,

$$A_m = \frac{H_r}{P} \dot{\theta}_p = A_X \quad (60b)$$

Similarly, Eq (60) becomes

$$A_m = \frac{(H_r^2 S + H_r F)}{J_x I_y S^3 + H_r^2 S + H_r F} A_X \quad (60c)$$

However, the existence of vehicle angular rates and error torques suggest discrepancies in the acceleration measurement. The extent to which such rates and torques affect the PIGA measurements involves a more complex treatment than that of the SAP. The additional complexity arises from functional differences in the two modes of operation.

One of the primary suppositions used in deriving the SAP error terms was the restricting of the sine and cosine of the input angle  $\theta_p$  to be constant during a limited time interval. In the case of the PIGA, the same assumption can be allowed only during special conditions. Such conditions would exist when the vehicular acceleration component acting along the PIGA input axis is either zero or nearly zero. When these conditions are satisfied, the PIGA is susceptible to rectification errors that are nearly identical to those of the SAP. The forms of such rectification errors would comply with those of SAP drift rate errors  $\epsilon_3$  through  $\epsilon_9$  in Table 7-VI multiplied by the ratio  $H_r/P$ .

When this condition is not satisfied, and input axis acceleration components do exist, the PIGA is designed to freely rotate proportionally to the magnitudes of such acceleration components. As a result, the sine and cosine of  $\theta_p$  are not maintained constant. Therefore, the techniques utilized to develop SAP errors  $\epsilon_3$  through  $\epsilon_9$  are not applicable to the PIGA operation during an environment of input axis acceleration.

Actually, an advantage of the PIGA is its capability to utilize its free rotation feature to average unwanted error torques to a zero value. Hopefully, this averaging feature will eliminate or at least minimize any rectification effects. An accurate determination of any rectification effects should be performed using computer techniques. Until such verification of errors can be performed, it will be assumed that the PIGA's averaging feature will eliminate rectification errors.

Only one further mention of the rectification-type errors is appropriate at this time. If it is determined later that rectification does play a significant role in the PIGA performance, then particular emphasis should be placed on such errors involving  $L_e'$  and  $L_{pe}'$  type error torques. These torques are stressed since they involve periodic accelerations acting on mass unbalances. Due to the built-in pendulosity, which is intentionally orders of magnitude greater than nonperfect mass unbalances, much larger  $L_e'$  and  $L_{pe}'$  magnitudes can be expected.

Under the criteria of neglecting rectification effects, only three types of errors will be considered as being meaningful. They are

- (1) Errors due to error torques about the output axis such as bias, scale factor, etc.
- (2) Errors due to ramp inputs of  $\omega_2$
- (3) Errors due to any vehicle rotation about the PIGA input axis.

The first two of these error types are analogous to SAP errors  $\epsilon_1$  and  $\epsilon_2$ . The third is an effect which must be compensated. The mathematical expressions for each of the errors will be developed next.

### 7.3.1 Derivation of PIGA Error Terms

In the development of the SAP equations, an expression was first determined explicitly for the drift rate error term  $\epsilon(s)$ , Eq (34). In order to evaluate the PIGA error terms, a similar expression for the acceleration measurement errors can be obtained by

- (1) Multiplying Eq (51) through by  $H_r/P$ ,
- (2) Subtracting Eq (60c),
- (3) Substituting  $\omega_2$  by Eq (8c).

The resulting error equation is

$$\Delta A_m = \frac{H_r}{P} \omega_X + \frac{H_r}{P} \left( \frac{(H_r S + F)L_E - I_y S^2 L_{pE} - I_y F S \omega_2}{J_x I_y S^3 + H_r^2 S + H_r F} \right). \quad (61)$$

By applying the final value theorem to Eq (61), the steady-state acceleration errors can be determined, i. e.,

$$\Delta A_m = \frac{H_r}{P} \omega_X + \frac{\bar{L}_E}{P} \quad (61a)$$

Also note that, if the time function of  $\omega_2$  in Eq (61) is a ramp function, Eq (61) implies an additional term to Eq (61a),

$$\Delta A_m = - \frac{I_y}{P} \dot{\omega}_2 \quad (61b)$$

The three types of acceleration measurement errors, discussed previously, are apparent in Eqs (61a) and (61b). They will be designated as follows:

$$\Delta A_1 = \frac{L_e}{P} \dot{\epsilon}_1 \quad (62)$$

$$\Delta A_2 = - \frac{I}{P} \dot{\omega}_2 \quad (63)$$

$$\Delta A_3 = \frac{H_r}{P} \omega_X \quad (64)$$

Note that Eqs (62) and (63) are analogous to SAP Eqs (36) and (37), respectively. Following the criteria previously set forth, the nonlinear product terms of  $\overline{L_E}$  in Eq (61a) and originally from Eq (20a), are considered to have average values equivalent to zero.

The error designated as  $\Delta A_3$  in Eq (64) is attributed directly to input axis angular rate components. This error did not appear in the SAP error equations since the SAP was intended only to measure that angular rate component. In contrast, the PIGA would ideally measure only input axis acceleration on a nonrotating vehicle. Thus, any form of vehicle rotation about the PIGA input axis becomes an acceleration measurement error. This error, the rotation rate multiplied by the PIGA scale factor, is independent of loop dynamics and should be compensated for in the acceleration measurement equations.

The acceleration errors, their expressions, and their causes are summarized in Subsection 2.5.

#### 7.4 VIBRATION ENVIRONMENT

This subsection analyzes angular and linear vibration conditions and discusses their implications for the strapped-down guidance system. The criteria for establishing the characteristics of these conditions are discussed individually in the following sections.

### 7.4.1 Angular Vibration

The angular motion environment consists of both sinusoidal and random components. The random angular motion was obtained from Reference 7.5, entitled "Working Paper, Angular Motions in Instrument Unit on Saturn Flights," supplied to TRW by MSFC. By mutual agreement, the two agencies chose the random component to be a constant  $0.0005 \frac{(\text{deg}/\text{sec})^2}{\text{cps}}$  rate spectral density up to 40 cps. This flat spectrum of random angular motion is to be interpreted as an equivalent to the actual spectrum shown in Figure 7-4. The RMS value of angular rate associated with this spectrum is 0.14 deg/sec. This figure was extracted

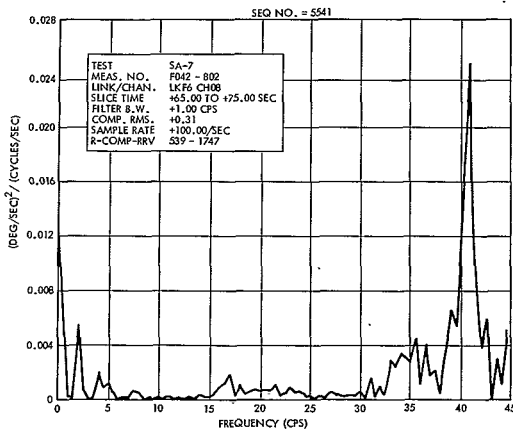


Figure 7-4. Angular Vibration Spectrum

from Reference 7.5. Reference 7.5 states that the high energy spikes appearing above 30 cps were likely due to local mechanical conditions within the rate measuring instruments. During advanced phases of system design, such phenomena should be carefully evaluated by a larger sample of data with a broader bandwidth since their effects on accuracy could be pronounced. An initial summary of a visual inspection of the recordings of Reference 7.11 angular rate data measured on a Saturn flight is shown in Figure 7-5. Figure 7-5 presents the approximate rate amplitudes and frequencies of the angular oscillations that occurred about each axis during particular time intervals. An interpretation of the graph may

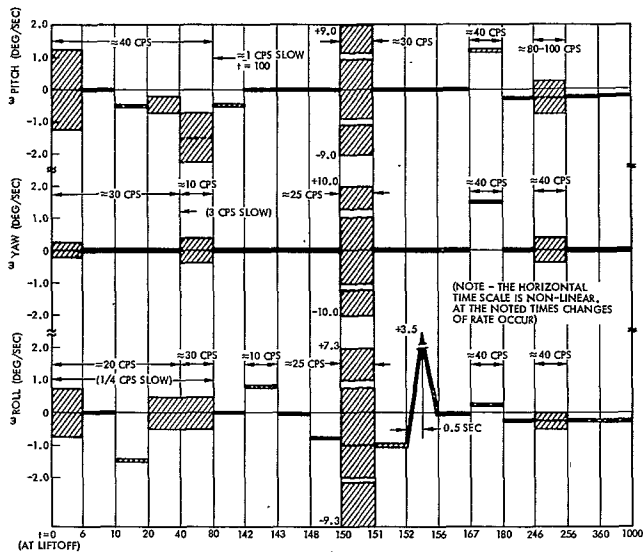


Figure 7-5. Summary of Visual Inspection of Recordings

be demonstrated in the following manner: consider the roll axis trace. During the first 6 sec following liftoff an oscillation with a 0.8 deg/sec amplitude acting at 20 cps exists. During the 6- to 10-sec time interval the amplitude is reduced to a 0.1 deg/sec amplitude. Between 10 and 20 sec the 0.1 deg/sec amplitude is biased so as to center about a -1.5 deg/sec value. From 20 to 80 sec the amplitude changes to 0.5 deg/sec. Also, during the first 80 sec the previously described oscillations are being carried on a slowly varying wave at 1/4 cps. Other frequencies of oscillation are indicated in the appropriate time intervals. The amplitudes shown include large 30 to 40 cps components consistent with Reference 7.5 (which was derived from the same flight data). If these higher frequency components are assumed to be instrumentation errors and are ignored, then two basic frequencies exist about each axis. These rate components are summarized in Table 7-IV. The values used to establish the SAP and FIGA errors are described as follows. First, an extreme condition assuming a peak angular rate amplitude of 1.0 deg/sec acting at frequencies of up to 40 cps about each axis is used and yields small errors. The maximum

Table 7-IV. Equivalent Sinusoidal Angular Oscillations

Axis	Low Frequency Component		Higher Harmonic Component	
	Frequency (cps)	Amplitude (deg/sec)	Frequency (cps)	Amplitude (deg/sec)
Pitch	0.6	0.15	3.0	0.20
Yaw	0.5	0.10	2.7	0.15
Roll	0.6	0.10	6.0	0.15

frequency assumed, although somewhat arbitrary, generally spans the frequency range of greatest sensitivity of the instruments (Subsections 4.2 and 7.5) and still complies with the 40 cps limit agreed upon with MSFC. Effects of potential extension of this frequency limit are discussed in Paragraphs 7.5.2 and 7.5.3. Based on the review of the flight data of Reference 7.11, the assumed magnitude of peak rate appears to be a realistic worst-case value for the intended analysis of this report.

The angular rate environment established here generally agrees with the data presented in Reference 7.6 also. This reference provides a summary of angular rate environments of in-house data on Thor and Atlas. The summary was prepared from Centaur as well as the SA-10 flight data referred to above.

#### 7.4.2 Linear Vibration

The definition of a linear vibration environment is predicated on the basis of flight test data from Reference 7.11 and general considerations of current spacecraft. Both sinusoidal and random components are assumed. This assumption is supported by state-of-the-art concepts of booster environment (see References 7.7 and 7.8). Furthermore, by establishing both random and nonrandom components of vibration, the effects of coupling between angular and linear oscillations of the two components can be investigated.

The vibration environment is inspected only up to 40 cps. Beyond that frequency no angular oscillations have been defined so that coupling

has been neglected.\* The worst-case philosophy employed to set the angular-oscillational environment is again used here for reasons of consistency. The maximum sinusoidal level below 40 cps indicated in References 7.7 and 7.8 is 1.0g. The peak level extracted from the SA-10 flight test data is approximately 0.25g. TRW has selected the former level (1.0g) for purposes of investigating SAP and PIGA rectification effects. This amplitude is considered to be constant up to 40 cps.

Similarly, a conservative estimate of a constant acceleration spectral density of  $0.01 \text{ g}^2/\text{cps}$  is selected for the random component. This level corresponds to the highest value shown below 40 cps in Reference 7.7. The RMS value of acceleration associated with this spectrum is a conservative 0.63g.

## 7.5 ERROR SOURCE MAGNITUDES

This subsection is concerned with the error magnitudes resulting from angular transients and from linear and angular vibrations.

### 7.5.1 Angular Transients

The forcing function implied by Eqs (37) or (63) is that of a constant angular acceleration acting about the gyro output axis of either the SAP or PIGA during a finite time interval. Such a sustained condition does not exist in the expected environment (see Figure 7-5). However, properly interpreted in terms of the applicable environment, this error source can be shown to result in a form of SAP or PIGA error. Such an alternate form is developed next.

In the derivation of Eqs (37) and (63), the error was defined in terms of a SAP drift rate for consistency with the forms of all the other error terms considered. However, the significance of this error may be more readily appreciated if expressed as a platform angle error by simple

---

\* Coupling referred to here is drift rectification. Such coupling has been shown to be a function of the angular and linear vibrations.

integration of Eq (37). This integration is performed for the case of  $\omega_X = 0$  to single out the effect:

$$\epsilon_2 \Big|_{\omega_X = 0} = \frac{d\theta_p}{dt} = -\frac{I_y}{H_r} \dot{\omega}_2 \quad (65a)$$

or after integration (assuming zero initial conditions),

$$\Delta\theta_p = -\frac{I_y}{H_r} \omega_2 \quad (65b)$$

One point at which this error could be induced is during staging. At such time the largest vehicle angular velocity transients occur. The maximum instantaneous SAP angular error  $\Delta\theta_p$  would be proportional to the maximum instantaneous angular rate and would correspondingly reduce to zero as the angular rate transients subside. For the maximum value of angular rate shown in Figure 7-5 (10 deg/sec), the SAP angular hang-off would be 18 arc sec. This is obtained from the following numerical values:

$$\begin{aligned} I_y &= 1210 \text{ gr-cm}^2 \\ H_r &= 2.5 \times 10^6 \text{ gr-cm}^2/\text{sec} \\ \omega_2 &= 10 \text{ deg/sec} \end{aligned}$$

Since the average value of  $\omega_2$  is zero over any significant portion of the trajectory, this error term (as given by Eq 65b) will not result in SAP drift rates having some average value over the boost flight profile. Furthermore, since the average value of  $\omega_2$  is also zero or small for the reference trajectory, the average error over the flight profile in SAP angle  $\theta_p$  (as given by Eq 65) will approach zero. Assuming an average missile pitch rate of 0.25 deg/sec during powered flight, the resulting SAP error would be 0.4 arc sec, which is certainly a negligible value. Thus, this error term is negligible.

The same discussion holds true for the PIGA error of Eq (63). In addition, the rotational mode of the PIGA will tend to reduce this effect to an even smaller value. On this basis, the PIGA error source  $\Delta A_2$  is neglected.

### 7.5.2 Sinusoidal Errors

The SAP error magnitudes of  $\epsilon_3$  to  $\epsilon_9$  (Eqs 46, 47, 48, 54a, 55, 59) are numerically calculated below. These error equations are presented as a function of oscillatory amplitudes of vehicle angular rate components and error torques. The angular rate amplitudes have been specified in Paragraph 7.4.1 (1.0 deg/sec). The error torque amplitudes considered here are due to the mass unbalance of the SAP gyro about the output and input axes.

The error torque about the output axis of the SAP gyro is calculated from the MSFC determined coefficients of spin-axis mass-unbalance  $M_{\text{ubs}}$ . The error torque for use in Eqs (47) and (55) associated with the environment of Subsection 7.4 is

$$L_{e'} = \left| M_{\text{ubs}} \right| \times H_r \times Ng = 0.51 \text{ gr-cm} \quad (66)$$

where

$$\left| M_{\text{ubs}} \right| = 0.040 \frac{\text{deg/hr}}{\text{g}}$$

$$N = 1 \text{ (number of g units acting)}$$

The second error torque contributed by vibration (for use in Eqs 48 and 56) involves combined platform and float mass unbalance effects. As vibrational acceleration acts perpendicular to the input axis, any off-axis c.g. location will induce error torques. Error source  $\epsilon_5$  indicates a high sensitivity to the magnitude of this error torque. Therefore, a close tolerance of dynamic balance is recommended for the SAP about their input axes. It is assumed for purposes of this report that the balance will be maintained less than 5 gr-cm/g.\* Based on this unbalance and the vibrational environment ( $Ng = 1$ ) the input axis error torque is

$$L_{pe'} = 5 \frac{\text{gr-cm}}{\text{g}} \times Ng = 5 \text{ gr-cm} \quad (67)$$

\* While some degree of precision balancing is required to meet this magnitude, it is well within the state-of-the-art.

Each of the calculations of drift rates involves a series of steps. Rather than presenting all calculations, one term,  $\epsilon_3$  is selected to demonstrate the procedure to calculate these rectified drift rates (see Eq 46). However, the results of the calculations of each term are presented as a normalized graph for each term. Each term is numerically developed as a function of the steady-state frequency of vehicle angular velocity.

An essential step in the calculation of the drift rates is the determination of the SAP closed-loop stability. The error equations (Subsection 7.2) are based on use of the final value theorem which requires the poles of the SAP closed-loop servo system to be in the left-half plane of a root-locus plot. The open-loop parameters of the SAP were furnished to TRW by MSFC along with estimates of the closed-loop parameters. The open-loop parameters include the poles and zeros of the platform servo control amplifier and torquer motor. The closed-loop poles were verified at TRW by means of a digital computer root-locus program.

By use of these poles the closed-loop amplitude and phase characteristics of the transfer functions ( $\frac{\theta}{\omega_2}(j\omega)$ , etc.) in Eqs (46), (47), (48), (54a), (55), and (59) may be readily determined. Drift rates normalized to the product of the forcing function amplitudes are then calculated for a worst-case condition. Such a condition will occur when these forcing functions are in phase (i. e.,  $\psi_i = 0$ ,  $i = 1, 2, 3, 4$ ). SAP drift rates can then be computed from these curves and the associated environments.

The five-step procedure to obtain the  $\epsilon_3$  drift rate is

- (1) Presentation of open-loop gyro, amplifier, and torquer parameters
- (2) Determination of closed-loop poles
- (3) Calculation of Bode diagram of  $\frac{\theta}{\omega_2}(j\omega)$
- (4) Calculation of  $\epsilon_3 k_2 \Omega_3$  vs frequency
- (5) Computation of  $\epsilon_3$  for angular rate environment.

### (1) Open-Loop Parameters

A line diagram of the SAP control system from gyro through to the input axis torque motor is shown in Figure 7-6. The third order function representing the platform mounted gyro corresponds directly to the open-loop portion of the characteristic equation in Eq (34). This relationship is

$$\frac{K_g}{S \left( \frac{S^2}{\omega_n^2} + 1 \right)} = \frac{1/H_r}{S \left( \frac{J_x I_y}{H_r^2} S^2 + 1 \right)} \quad (68)$$

The natural frequency of the SAP-mounted AB-5 gyro has been determined by MSFC to be  $\omega_n = 400$  rad/sec. The SAP gain  $K_g$  is  $2.25 \times 10^{-2} \frac{\text{deg}}{\text{gr-cm}}$ . The output axis of this gyro has a gas-bearing suspension and therefore has an effective damping ratio of zero.\*

The remaining gains and functions of Figure 7-6 are lumped together to represent the platform control (F(s)). This group begins at the gyro pickoff and ends at the platform torque motor, i. e.,

$$F(s) = K_F \frac{\left( \frac{S}{r_1} + 1 \right) \left( \frac{S^2}{r_2^2} + \frac{2k_a}{r_2} S + 1 \right)}{\left( \frac{S}{q_1} + 1 \right) \left( \frac{S^2}{q_2^2} + \frac{2k_b}{q_2} S + 1 \right) \left( \frac{S}{q_3} + 1 \right)} \quad (69)$$

\* Because of this type of suspension, a second natural frequency occurs at 2850 rad/sec. TRW was informed by MSFC of this second frequency subsequent to completion of this analysis so it does not appear in the closed-loop configuration. Preliminary analysis indicates that no significant differences occur between the root-loci of these two loop configurations.

PLATFORM	PICKOFF	NETWORK	MODULATION	TORQUER
$K_g = 2.25 \times 10^{-2} \frac{\text{deg}}{\text{gr-cm}}$	$K_{po} = 10 \frac{\text{volt}}{\text{deg}}$	$K_n = 1.0 \frac{\text{volt}}{\text{volt}}$	$K_m = 150 \frac{\text{volt}}{\text{volt}}$	$K_{tg} = 261 \frac{\text{gr-cm}}{\text{volt}}$
$\frac{K_g}{s \left( \frac{s}{400} + 1 \right)}$	$K_{po}$	$\frac{K_n \left( \frac{s}{50} + 1 \right) \left( \frac{s}{100} + 1 \right) \left( \frac{s}{200} + 1 \right) \left( \frac{s}{666} + 1 \right)}{\left( \frac{s}{1} + 1 \right) \left( \frac{s}{1500} + 1 \right) \left( \frac{s}{3000} + 1 \right)}$	$K_m$	$\frac{K_{tg}}{\left( \frac{s}{666} + 1 \right)}$
$\xrightarrow{\hspace{10em} F(s) \hspace{10em}}$ (Gain, $K_F = 3.92 \times 10^5 \frac{\text{gr-cm}}{\text{deg}}$ )				
$\xrightarrow{\hspace{10em} \text{Open Loop Function} \hspace{10em}}$ (Gain, $K_{olb} = 8.8 \times 10^3$ )				

Figure 7-6. Line Diagram of SAP Control System

(Note that a zero of the amplifier and the pole of the torque motor cancel each other.)

The numerical values of the  $F(s)$  parameters are:

$$\begin{aligned}
 K_F &= 3.92 \times 10^3 \\
 r_1 &= 50 \text{ rad/sec} \\
 r_2 &= 224 \text{ rad/sec, } \xi_a = 0.45 \\
 q_1 &= 1 \text{ rad/sec} \\
 q_2 &= 1800 \text{ rad/sec, } \xi_b = 0.84 \\
 q_3 &= 6000 \text{ rad/sec.}
 \end{aligned}$$

The product of Eqs (68) and (69) provide the open-loop transfer function from which the closed-loop poles may be determined.

## (2) Closed-Loop Poles

The closed-loop poles were calculated by means of a digital computer program. Figure 7-7 is a reproduction of the program print-out sheet. The printout data includes the input data and the resulting nominal closed-loop poles. Note that complex poles and zeros are given in terms of their real and imaginary parts rather than in the form used in Eq (69).

Figure 7-8 presents traces of the root locus for gain changes of 30 db above nominal to 24 db below nominal. Inspection of these traces shows that adequate stability occurs at the nominal gain poles.

Converting the programmed poles back to frequency/damping ratio form, the closed-loop equivalent of Figure 7-6 is

$$G_{c.l.}(s) = \frac{\left(\frac{S}{r_1} + 1\right) \left(\frac{S^2}{r_2} + \frac{2\xi_a}{r_2} S + 1\right)}{\left(\frac{S^2}{p_1} + \frac{2\xi_c}{p_1} S + 1\right) \left(\frac{S}{p} + 1\right) \left(\frac{S^2}{p_3} + \frac{2\xi_d}{p_3} S + 1\right) \left(\frac{S}{p_4} + 1\right) \left(\frac{S}{p_5} + 1\right)} \quad (70)$$

or numerically,

$$p_1 = 82 \text{ rad/sec}, \xi_c = 0.87$$

$$p_2 = 654 \text{ rad/sec}$$

$$p_3 = 738 \text{ rad/sec}, \xi_d = 0.24$$

$$p_4 = 1933 \text{ rad/sec}$$

$$p_5 = 5913 \text{ rad/sec.}$$

## (3) Bode Diagram of $\frac{\theta}{\omega_2}(j\omega)$

It can be readily determined that the relationship between the  $\frac{\theta}{\omega_2}(S)$  transfer functions in Eq (42) of Subsection 7-2 and Eq (70) of this section is as follows:

$$\frac{\theta}{\omega_2}(S) = \frac{1/S}{1 + \frac{F/H_r}{S \left( \frac{J_x I_y}{H_r} S^2 + 1 \right)}} = G_{c.l.}(s) \times \left( \frac{J_x I_y}{H_r} S^2 + 1 \right) \times \frac{H_r}{F} \quad (71)$$

SAP TRW TRANSFER FUNCTION

EXTENT OF TRACE			
D1	D2	D3	D4
.30000000 02	.24000000 02	.00000000 00	.00000000 00
STEP SIZE LIMIT			
L1	L2	L3	L4
.60000000 01	.60000000 01	.00000000 00	.00000000 00
OPEN LOOP ZEROS		OPEN LOOP POLES	
.10000000 03	.20000000 03	.00000000 00	.00000000 00
-.11000000 03	-.20000000 03	.00000000 00	.40000000 03
-.50000000 02	.00000000 00	.00000000 00	-.40000000 03
		-.10000000 01	.00000000 00
		-.15000000 04	.10000000 04
		-.15000000 04	-.10000000 04
		-.60000000 04	.00000000 00
ESTIMATES FOR NOMINAL CLOSED LOOP POLES		NOMINAL CLOSED LOOP POLES	
-.52000000 02	.48000000 02	-.71583994 02	.40183049 02
-.15000000 03	.40000000 03	-.71583994 02	-.40183049 02
-.75000000 03	-.40000000 03	-.65454488 03	.34362452-05
-.10000000 01	.00000000 00	-.17820937 03	.71599727 03
-.15000000 04	.10000000 04	-.19335010 04	.73325039 05
-.15000000 04	-.10000000 04	-.17820937 03	-.71599728 03
-.60000000 04	.00000000 00	-.59133674 04	.35678667-06
BODE GAIN	INPUT BODE GAIN	GAMMA	PHASE
.88000000 04	.88000000 04	.12479999 10	.18000000 03
ROOT LOCUS GAIN	INPUT ROOT LOCUS GAIN	CENTROID	
.10982399 14	.00000000 00	-.2187500 04	

Figure 7-7. Reproduction of Root Locus Printout

7-46

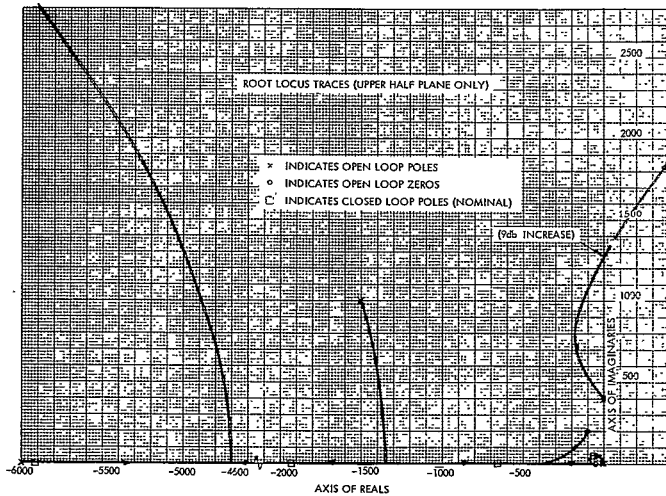


Figure 7-8. Root Locus Traces  
(Upper Half Plane Only)

Bode diagram techniques can be employed to readily evaluate the frequency response of Eq (49), i. e.,  $\frac{\theta}{\omega_2}(j\omega)$ . The amplitude curve is shown in Figure 7-9 and the phase in Figure 7-10. From these characteristics a normalized form of error term  $\epsilon_3$  may be calculated.

(4) Calculation of  $\frac{\epsilon_3}{\Omega_2 \Omega_3}(j\omega)$

In review of the basic form of  $\epsilon_3$  in Eq (46), two phase angles are involved. Inspection of the Bode diagrams in Step (3) reveals that the peak value of  $\left| \frac{\theta}{\omega_2} \right|$  occurs approximately at the same frequency as the zero phase of  $\frac{\theta}{\omega_2}$ . If  $\psi_1$  were also at a zero value, then  $\cos(\sqrt{\frac{\theta}{\omega_2}} - \psi_1)$  would equal 1.0 and a worst-case condition would be established. Therefore, vehicle angular rate components  $\omega_2$  and  $\omega_3$  will be considered as effectively acting in phase such that  $\psi_1 = 0$ . Drift rate  $\epsilon_3$  can then be normalized to the remaining two independent variables  $\Omega_2$  and  $\Omega_3$ . In this manner the indicated nonlinear product  $\frac{1}{2} \left| \frac{\theta}{\omega_2} \right| \cos \angle \frac{\theta}{\omega_2}$  can be calculated.

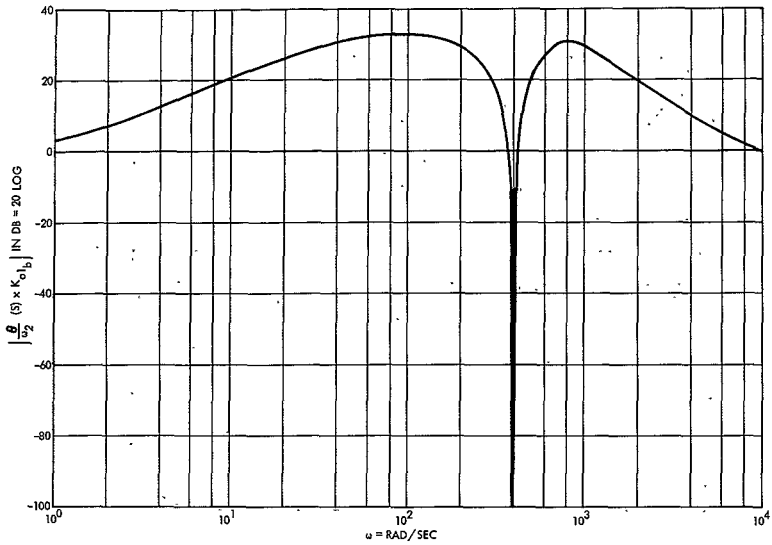


Figure 7-9. Amplitude of  $\frac{\theta}{\omega_2}(j\omega)$

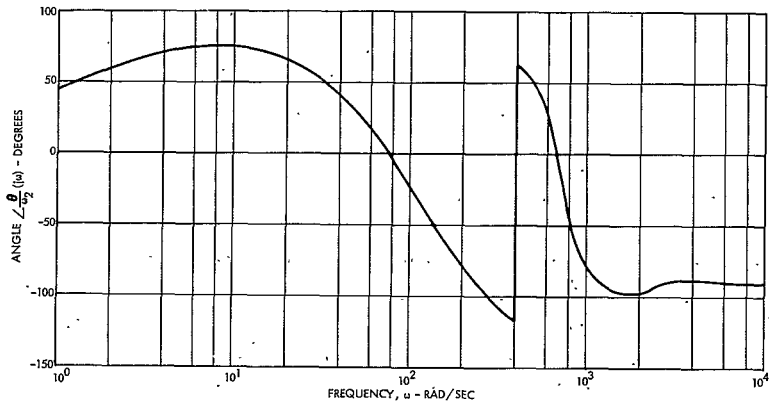


Figure 7-10. Phase Angle of  $\frac{\theta}{\omega_2}(j\omega)$

This computation is performed in Table 7-V and the resulting curve shown in Figure 7-11. Particular emphasis should be placed on the peak value of  $\frac{\epsilon_3}{\Omega_2 \Omega_3}$ . This magnitude is  $2.92 \times 10^{-3} \frac{\text{deg/hr}}{(\text{deg/sec})^2}$  and occurs at 16 cps. The units of the graph have been converted so that vehicle rate amplitudes  $\Omega_2$  and  $\Omega_3$  may be expressed in conventional deg/sec units.

(5) Computation of  $\epsilon_3$

The drift error is calculated by multiplying the normalized drift error curve in Figure 7-11 by the rate environment amplitudes of Sub-section 7.4 (i. e., 1 deg/sec). Comparison of the peak characteristics of Figure 7-11 and the flat environmental spectrum reveals that the maximum SAP  $\epsilon_3$  drift error would occur if the vehicle were to be excited by angular oscillations of approximately 16 cps. This error is

$$\epsilon_{3 \text{ max}} = 2.93 \times 10^{-3} \frac{\text{deg/hr}}{(\text{deg/sec})^2} \times (1.0 \text{ deg/sec})^2 = 0.0029 \text{ deg/hr} \quad (72)$$

Drift rate errors of this magnitude would have negligible effects on SAP performance. This statement is made with regard to the present fixed drift rate. In fact, not until angular oscillations reach amplitudes of approximately 3 deg/sec should any concern be associated with this error source. Under these conditions,

$$\epsilon_{3 \text{ max}}^* = 2.93 \times 10^{-3} \times (3.0)^2 = 0.026 \text{ deg/hr.} \quad (72a)$$

For use in the error model the maximum value of 0.0029 deg/hr is selected for the value of  $\epsilon_3$ . This worst-case philosophy is applied to the other six error sources. The normalized drift rate curves of errors  $\epsilon_4$  through  $\epsilon_8$  are shown in Figures 7-12 through 7-16. Drift rate  $\epsilon_9$  is independent of frequency and accordingly has no curve associated with it. Table 7-VI presents the peak values of each normalized error source below the upper environment frequency of 40 cps and the maximum drift rates corresponding to these peak values. The forcing function amplitudes are repeated for convenience.

---

\*  $\epsilon_{3 \text{ max}}$  in Eq (72a) is not applicable to this study. It is presented only to demonstrate environmental regions of potential concern.

Table 7-V.  $\epsilon_3/\Omega_2\Omega_3$  Calculations

$\omega$	$\left  \frac{\theta}{\omega_2} \times K_{o1b}^* \right $	$\left  \frac{\theta}{\omega_2} \times K_{o1b} \right $	$\frac{1}{K_{o1b}} \times \frac{3600}{(57.3)^2}$	$\frac{1}{2} \left  \frac{\theta}{\omega_2} \right $	$\frac{\theta}{\omega_2}$	$\cos \frac{\theta}{\omega_2}$	$\frac{\epsilon_3}{\Omega_2\Omega_3}$
rad sec	db	Numerical		$\frac{\text{deg/hr}}{(\text{deg/sec})^2}$	deg		$\frac{\text{deg/hr}}{(\text{deg/sec})^2}$
0.1	0	1.0	$1.26 \times 10^{-4}$	$0.63 \times 10^{-4}$	+7	0.993	$0.63 \times 10^{-4}$
0.5	1.0	1.12		0.71 x	+26	0.900	0.64 x
1.0	3.0	1.41		0.89 x	+45	0.707	0.63 x
1.5	5.0	1.8		1.14 x	+53	0.602	0.69 x
2.0	7.0	2.24		1.41 x	+62	0.469	0.66 x
3.0	10.0	3.20		2.01 x	+68	0.375	0.75 x
5.0	14.0	5.0		3.15 x	+73	0.292	0.92 x
7.0	17.0	7.1		4.48 x	+75	0.259	1.16 x
10	20.0	10.0		6.3 x	+74	0.285	1.79 x
15	24.0	15.85		10 x	+71	0.326	3.26 x
20	26.0	20.0		12.6 x	+66	0.407	5.13 x
30	29.0	28.1		17.7 x	+53	0.602	10.66 x
36	30.5	33.6		21.1 x	+45	0.707	14.92 x
50	32.0	40.5		25.5 x	+33	0.839	21.39 x
70	33.0	45.1		28.4 x	+3	0.999	28.27 x
100	34.0	50.2		31.6 x	-22	0.927	29.29 x
150	32.0	39.6		25.0 x	-60	0.500	12.50 x
200	30.0	31.8		20.0 x	-80	0.174	3.48 x
300	21.0	11.1		7.0 x	-100	-0.174	-1.22 x
400	-∞	0		0	117	-0.454	0
400	-∞	0		0	63	0.454	0
500	19.0	9.0		5.7 x	50	0.643	3.79 x
600	26.0	20.3		12.8 x	42	0.743	9.51 x
700	30.0	31.8		20.1 x	-4	0.998	20.26 x
850	31.5	36.5		23.0 x	-53	0.602	13.85 x
1000	28.0	25.2		16.0 x	-76	0.242	3.87 x
1500	22.0	12.6	$1.26 \times 10^{-4}$	$8.0 \times 10^{-4}$	-100	-0.174	$1.53 \times 10^{-4}$

$K_{o1b}$  is defined as the Bode gain of the open-loop function.

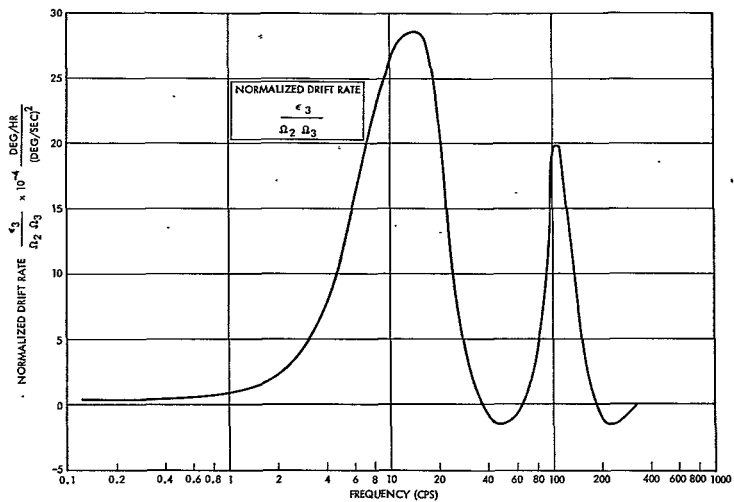


Figure 7-11. Normalized Drift Rate  $\frac{\epsilon_3}{\Omega_2 \Omega_3}$

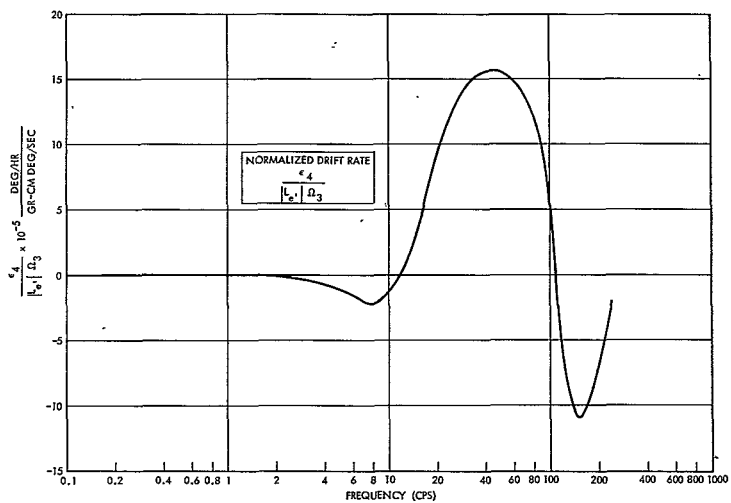


Figure 7-12. Normalized Drift Rate  $\frac{\epsilon_4}{|L_e| \Omega_3}$

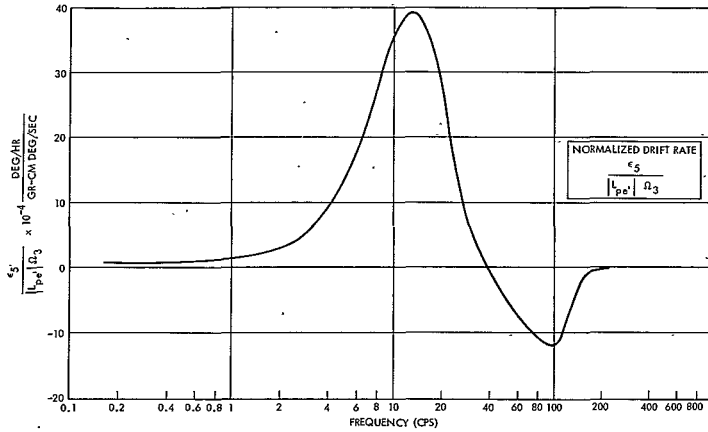


Figure 7-13. Normalized Drift Rate  $\frac{\epsilon_5}{|L_{pe}| \Omega_3}$

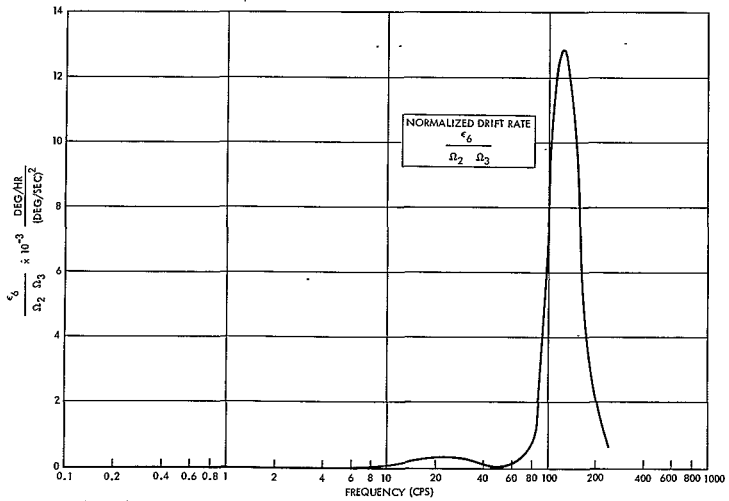


Figure 7-14. Normalized Drift Rate  $\frac{\epsilon_6}{\Omega_2 \Omega_3}$

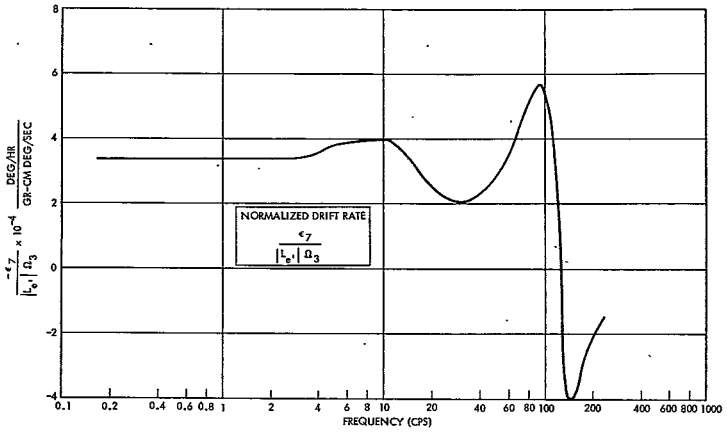


Figure 7-15. Normalized Drift Rate  $\frac{\epsilon_7}{|L_e| \Omega_3}$

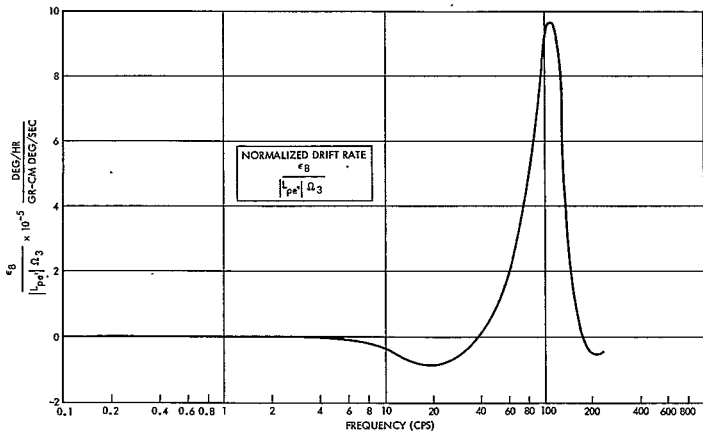


Figure 7-16. Normalized Drift Rate  $\frac{\epsilon_8}{|L_{pe}| \Omega_3}$

Table 7-VI. Drift Rectification Error Magnitudes (Sinusoidal)

<u>Error</u>	<u>Forcing Function Product</u>	<u>Normalized Drift Rate</u>	<u>Figure or Equation</u>	<u>Error Magnitude (deg/hr)</u>
$\epsilon_3$	$\Omega_2 \Omega_3$	$2.93 \times 10^{-3} \frac{\text{deg/hr}}{(\text{deg/sec})^2}$	Fig. 7-11 and Eq (72)	0.0029
$\epsilon_4$	$L_e' \Omega_3$	$1.58 \times 10^{-4} \frac{\text{deg/hr}}{(\text{gr-cm})(\text{deg/sec})}$	Fig. 7-12	$8.05 \times 10^{-5}$
$\epsilon_5$	$L_{pe}' \Omega_3$	$3.98 \times 10^{-3} \frac{\text{deg/hr}}{(\text{gr-cm})(\text{deg/sec})}$	Fig. 7-13	0.020
$\epsilon_6$	$\Omega_2 \Omega_3$	$3.30 \times 10^{-4} \frac{\text{deg/hr}}{(\text{deg/sec})^2}$	Fig. 7-14	$3.30 \times 10^{-4}$
$\epsilon_7$	$L_e' \Omega_3$	$4.00 \times 10^{-4} \frac{\text{deg/hr}}{(\text{gr-cm})(\text{deg/sec})}$	Fig. 7-15	$2.04 \times 10^{-4}$
$\epsilon_8$	$L_{pe}' \Omega_3$	$8.29 \times 10^{-6} \frac{\text{deg/hr}}{(\text{gr-cm})(\text{deg/sec})}$	Fig. 7-16	$4.14 \times 10^{-5}$
$\epsilon_9$	$\Omega_X \Omega_3$	$1.52 \times 10^{-2} \frac{(\text{deg/hr})}{(\text{deg/sec})^2}$	Eq (59)	0.0152

Note:  $\Omega_X = \Omega_2 = \Omega_3 = 1.0 \text{ deg/sec}$

$L_e' = 0.51 \text{ gr-cm}$

$L_{pe}' = 5.0 \text{ gr-cm}$

Maximum frequency of data is 40 cps

Further inspection of Figures 7-11 through 7-16 reveals that these normalized curves achieve additional peak values above the 40 cps frequency cutoff of environment. In fact for errors  $\epsilon_6$ ,  $\epsilon_7$ ,  $\epsilon_8$ , the peak values occur around 100 cps and are considerably higher than the maximum value below 40 cps. For purposes of evaluating these higher frequency effects, the vibration environment is assumed to be "extended" to include these higher peaks. The extended environmental effects are tabulated in Table 7-VII. Only error  $\epsilon_6$  has any significance as an error source (0.013 deg/hr). However, even this value will cause a small change to the constant drift term when combined by finding the RSS.

Table 7-VII. Drift Rectification Error Magnitudes (Sinusoidal) for Extended Environment

<u>Error</u>	<u>Normalized Drift Rate (peak)</u>	<u>Frequency (cps)</u>	<u>Error Magnitude (deg/hr)</u>
$\epsilon_3$	$2.06 \times 10^{-3} \frac{\text{deg/hr}}{(\text{deg/sec})^2} *$	110	0.0021
$\epsilon_6$	$1.30 \times 10^{-2} \frac{\text{deg/hr}}{(\text{gr-cm})(\text{deg/sec})}$	125	0.013
$\epsilon_7$	$5.70 \times 10^{-4} \frac{\text{deg/hr}}{(\text{gr-cm})(\text{deg/sec})}$	95	$2.91 \times 10^{-4}$
$\epsilon_8$	$9.70 \times 10^{-5} \frac{\text{deg/hr}}{(\text{gr-cm})(\text{deg/sec})}$	110	$4.85 \times 10^{-4}$

\*Note in Figure 7-11 that the indicated peak value at 110 cps is a secondary peak to that occurring at 16 cps.

### 7.5.3 Random Errors

The same error terms that were evaluated in Paragraph 7.5.2 for sinusoidal inputs are investigated in this section for random environmental conditions. An equivalent sinusoidal form of the random inputs is established. By means of this form the resulting drift rate errors can be computed by a procedure similar to that just used. Here again the result of each computation is presented, but only one term is selected to serve as a demonstration.

Consider an element of power,  $\Phi(\omega_o)\Delta\omega_o$ , of the random input defined by the spectral density function  $\Phi(\omega_o)$ . As  $\Delta\omega_o$  approaches zero, the signal represented by this element of power may be approximated by a single frequency sinusoid with amplitude  $\gamma_o$ . If the power in this single frequency signal is equated to the power in the element of the random signal,

$$\frac{\gamma_o^2}{2} = \Phi(\omega_o)\Delta\omega_o \quad (73)$$

or

$$\gamma_o = \sqrt{2\Phi(\omega_o)\Delta\omega_o} \quad (73a)$$

If this equivalent sinusoid is assumed to act at 45 deg to both the SAP-gyro output axis and spin axis, then the amplitudes of the components of rate along the gyro output axis ( $\Omega_2$ ) and gyro spin axis ( $\Omega_3$ ) are

$$\Omega_2 = \Omega_3 = \frac{\gamma_o}{2} = \sqrt{\Phi(\omega_o)d\omega_o} \quad (74)$$

The error source  $\epsilon_3$  is again selected to serve as a demonstration. The contribution to  $\epsilon_3$  resulting from the above element of power (or its single frequency equivalent signal) is

$$\Delta \epsilon_{3_i} = \left[ \frac{\epsilon_3}{\Omega_2 \Omega_3} (\omega_o) \right] \Omega_2 \Omega_3 = \left[ \frac{\epsilon_3}{\Omega_2 \Omega_3} (\omega_o) \right] \Phi(\omega_o) \Delta \omega_{o_i} \quad (75)$$

where  $\left[ \frac{\epsilon_3}{\Omega_2 \Omega_3} (\omega_o) \right]$  is the error coefficient obtained previously. The total value of the error  $\epsilon_3$  can be obtained by summing all elements  $\Phi(\omega) \Delta \omega_i$  contained in the bandwidth defined by  $\Phi(\omega_o)$ . This may be expressed by the integral

$$\epsilon_3 = \int_0^{\infty} \left[ \frac{\epsilon_3}{\Omega_2 \Omega_3} (\omega_o) \right] \Phi(\omega_o) d\omega_o \quad (75a)$$

Since  $\Phi(\omega)$  is assumed to be constant from  $\omega_o = 0$  to  $\omega_o = \omega_{o_{\max}}$  and zero for  $\omega_o$  to  $\omega_{o_{\max}}$ , the above integral can be rewritten as

$$\epsilon_3 = \Phi(\omega_o) \int_0^{\omega_{oM}} \left[ \frac{\epsilon_3}{\Omega_2 \Omega_3} (\omega_o) \right] d\omega_o \quad (75b)$$

The indicated integration of Eq (75b) is by inspection of the area under the curve of Figure 7-11. This area is numerically integrated to be  $4.30 \times 10^{-2} \frac{\text{deg/hr}}{(\text{deg/sec})^2}$  (cps).

The product of this area and the constant angular rate spectral density of  $0.0005 \frac{(\text{deg/sec})^2}{\text{cps}}$  is  $2.15 \times 10^{-5}$  deg/hr.

The random drift errors are tabulated in Table 7-VIII. This table includes the numerically integrated area-under-the curve values up to 40 cps of Figures 7-11 through 7-16 plus forcing function products. The values of random induced error torques for terms  $\epsilon_4$ ,  $\epsilon_5$ ,  $\epsilon_7$ ,  $\epsilon_8$  are the torque per unit g values calculated previously.

The extended environment introduced earlier is again applied to the random case. This environment extends the vibrational frequency to include the higher magnitudes that appear in the spectra of Figures 7-11 through 7-16. These calculations are shown in Table 7-IX. It is noteworthy that these overall random errors are essentially noncontributory to the error model.

Table 7-VIII. Drift Rectification Error Magnitudes (Random)

Error	Forcing Function Product	Area-Under-Curve	Figure or Equation	Error Magnitude (deg/hr)
$\epsilon_3$	$\sqrt{\Phi_2} \sqrt{\Phi_3} = \Phi_T$	$4.30 \times 10^{-2} \frac{\text{deg/hr}}{(\text{deg/sec})^2}$ (cps)	Fig. 7-11, Eq (75b)	$2.15 \times 10^{-5}$
$\epsilon_4$	$\sqrt{\Phi_e} \sqrt{\Phi_3} *$	$2.92 \times 10^{-3} \frac{\text{deg/hr}}{(\text{gr-cm})(\text{deg/sec})}$ (cps)	Fig. 7-12	$3.26 \times 10^{-6}$
$\epsilon_5$	$\sqrt{\Phi_{pe}} \sqrt{\Phi_3} **$	$6.99 \times 10^{-2} \frac{\text{deg/hr}}{(\text{gr-cm})(\text{deg/sec})}$ (cps)	Fig. 7-13	$7.84 \times 10^{-4}$
$\epsilon_6$	$\sqrt{\Phi_2} \sqrt{\Phi_3} = \Phi_T$	$7.13 \times 10^{-3} \frac{\text{deg/hr}}{(\text{deg/sec})^2}$ (cps)	Fig. 7-14	$3.75 \times 10^{-6}$
$\epsilon_7$	$\sqrt{\Phi_e} \sqrt{\Phi_3} *$	$1.14 \times 10^{-2} \frac{\text{deg/hr}}{(\text{gr-cm})(\text{deg/sec})}$ (cps)	Fig. 7-15	$1.28 \times 10^{-4}$
$\epsilon_8$	$\sqrt{\Phi_{pe}} \sqrt{\Phi_3} **$	$1.73 \times 10^{-4} \frac{\text{deg/hr}}{(\text{gr-cm})(\text{deg/sec})}$ (cps)	Fig. 7-16	$1.94 \times 10^{-6}$
$\epsilon_9$	$\sqrt{\Phi_X} \sqrt{\Phi_3}$	$6.08 \times 10^{-1} \frac{\text{deg/hr}}{(\text{deg/sec})^2}$ (cps)	Eq (59)	$3.04 \times 10^{-4}$

Note:  $\Phi_T = \Phi_X = \Phi_2 = \Phi_3 = 0.0005 \frac{(\text{deg/sec})^2}{\text{cps}}$

$\Phi_e = \Phi_{pe} = 0.01 \text{ g}^2/\text{cps}$

\*  $\epsilon_4$  and  $\epsilon_7$  computations must be multiplied by 0.51 gr-cm/g

\*\*  $\epsilon_5$  and  $\epsilon_8$  computations must be multiplied by 5.0 gr-cm/g

Table 7-IX. Drift Rectification Error Magnitudes (Random)  
for Extended Environment

<u>Error</u>	<u>Area-Under-Curve</u>	<u>Bandpass (cps)</u>	<u>Magnitude (deg/hr)</u>
$\epsilon_3$	$1.44 \times 10^{-1} \frac{\text{deg/hr}}{(\text{deg/sec})^2} \text{ (cps)}$	300	$7.20 \times 10^{-5}$
$\epsilon_4$	$9.80 \times 10^{-4} \frac{\text{deg/hr}}{(\text{gr-cm})(\text{deg/sec})} \text{ (cps)}$	250	$1.09 \times 10^{-6}$
$\epsilon_5$	$1.91 \times 10^{-2} \frac{\text{deg/hr}}{(\text{gr-cm})(\text{deg/sec})} \text{ (cps)}$	250	$2.24 \times 10^{-4}$
$\epsilon_6$	$9.35 \times 10^{-1} \frac{\text{deg/hr}}{(\text{deg/sec})^2} \text{ (cps)}$	230	$4.65 \times 10^{-4}$
$\epsilon_7$	$1.75 \times 10^{-2} \frac{\text{deg/hr}}{(\text{gr-cm})(\text{deg/sec})} \text{ (cps)}$	250	$1.96 \times 10^{-4}$
$\epsilon_8$	$5.50 \times 10^{-3} \frac{\text{deg/hr}}{(\text{gr-cm})(\text{deg/sec})} \text{ (cps)}$	240	$6.18 \times 10^{-5}$

Table of Symbols for Section 7

$A_x$	- Acceleration along the vehicle X axis
$A_m$	- Measured value of $A_x$
$\Delta A_m$	- Acceleration measurement errors
$F(s)$	- Transfer function of platform servo
$g$	- A unit of gravity
$G_{c.l.}$	- SAP closed-loop transfer function
$\vec{H}$	- Angular momentum vector; appropriate use of an $\vec{H}$ vector is identified with each reference system and each application
$H_r$	- Magnitude of angular momentum component pertaining to gyro spinning wheel along float spin axis (z); equal to $I_z \omega_s$
$\vec{H}_f$	- Angular momentum vector of float; includes $H_r$ component
$H_x, H_y, H_z$	- Component magnitudes of $\vec{H}_f$ along the float axes (x, y, z); $H_z$ includes float angular momentum along z and $H_r$
$\vec{H}_p$	- Angular momentum vector of platform isolated from float
$\vec{H}_{pf}$	- Angular momentum vector of platform and float together; vector sum of $\vec{H}_f + \vec{H}_p$
$H_{x_{pf}}, H_{y_{pf}}, H_{z_{pf}}$	- Component magnitudes of $\vec{H}_{pf}$ along the platform axes ( $x_p, y_p, z_p$ )
$I_x, I_y, I_z$	- Mass moments of inertia of float (including wheel) about float axes ( $I_z$ is wheel inertia about $I_z$ )
$I_{p_x}, I_{p_y}, I_{p_z}$	- Mass moments of inertia of platform (not including float) about platform axes
$J_x$	- Mass moments of inertia of platform (including float) about input axis; sum of $I_{p_x}$ and $I_x$
$K_i$	- Servo gains; particular usage is denoted in text.

Table of Symbols for Section 7 (Continued)

$\bar{L}$	- Moment vector; equivalent to the total time rate or change of $\bar{H}$
$\bar{L}_{I/f}$	- Moment vector acting on float; equal to total time rate of change of $\bar{H}_f$
$L_y$	- Component magnitude of $\bar{L}_{I/f}$ along the output axis (y); composed of possible error or control torques
$L_E$	- Error torques acting about output axis (y); composed of both external ( $L_e'$ ) torques and internal (nonlinear) torques
$L_e'$	- Error torques acting on float about output axis (y) such as fixed torque, mass unbalance effects, and includes vibrational torques
$L_a$	- Control torques acting on float about output axis (y) such as earth rate compensation or intentional mass unbalance for FIGA
$\bar{L}_{I/p}$	- Moment vector acting on platform (including float); equal to total time rate of change $\bar{H}_{pf}$
$L_{x_p}$	- Component magnitude of $\bar{L}_{I/p}$ along the input axis ( $x_p$ ); composed of possible error or control torques
$L_{pE}$	- Error torques acting about input axis ( $x_p$ ); composed of both external ( $L_{pe}'$ ) torques and internal (nonlinear) torques
$L_{pe}'$	- Error torques acting on SAP about input axis ( $x_p$ ) such as friction, torque errors, and includes vibrational torques
$L_{pa}$	- Control torques acting on SAP about input axis ( $x_p$ ); such torques are due to closed-loop torque motor control; $L_{pa} = F(s)\theta$
$ M_{ubs} $	- Error model coefficient representing float mass unbalance along gyro spin axis
N	- Number of gravity units
P	- Pendulosity of FIGA

Table of Symbols for Section 7 (Continued)

$p_i$	- Closed loop poles
$q_i$	- Open loop poles
$r_i$	- Open loop zeros
$S$	- Laplace transform notation
$X_I, Y_I, Z_I$	- Inertial reference coordinates
$X, Y, Z$	- Vehicle fixed coordinates
$x_p, y_p, z_p$	- Platform fixed coordinates
$x, y, z$	- Float fixed coordinates
$\hat{x}_p, \hat{y}_p, \hat{z}_p$	- Unit vectors along platform fixed axes
$\hat{x}, \hat{y}, \hat{z}$	- Unit vectors along float fixed axes
$\hat{i}_X, \hat{i}_Y, \hat{i}_Z$	- Unit vectors along vehicle fixed axes
$\gamma_0$	- General amplitude of a random/sinusoid equivalent (see Eq 73)
$\epsilon_p, \epsilon_i (i = 1 \text{ to } 9)$	- Drift rate errors; deviation of $\dot{\theta}_p$ from $\omega_X$
$\theta$	- Output axis angle; angle between float $(x, y, z)$ and platform $(x_p, y_p, z_p)$
$\theta_p$	- Input axis angle; angle between platform $(x_p, y_p, z_p)$ and vehicle $(X, Y, Z)$
$\theta_m, \dot{\theta}_{pm}$	- Maximum amplitudes of vibrational forms of $\theta$ , and $\dot{\theta}_p$ , respectively
$\phi_1, \phi_2$	- Phase angles of $\theta$ relative to $\omega_3$ and $\dot{\theta}_p$ relative to $\omega_3$ , respectively

Table of Symbols of Section (Continued)

$\Phi(\omega_0)$	- Power spectral density (particular usage is denoted in text)
$\psi_1, \psi_2, \psi_3, \psi_4$	- Phase angles of $\omega_2$ relative to $\omega_3$ , $L_e'$ relative to $\omega_3$ , $L_{pe}'$ relative to $\omega_3$ , and $\omega_X$ relative to $\omega_3$ , respectively
$\bar{\omega}$	- Angular velocity vector representing motion of vehicle axes (X, Y, Z) relative to inertial axes ( $X_I, Y_I, Z_I$ )
$\omega_X, \omega_Y, \omega_Z$	- Component magnitudes of $\bar{\omega}$ along the vehicle axes (X, Y, Z)
$\bar{\omega}_p$	- Angular velocity vector representing motion of platform axes ( $x_p, y_p, z_p$ ) relative to inertial axes ( $X_I, Y_I, Z_I$ )
$\omega_1, \omega_2, \omega_3$	- Component magnitudes of $\bar{\omega}_p$ along the platform axes ( $x_p, y_p, z_p$ )
$\bar{\omega}_f$	- Angular velocity vector representing motion of float axes (x, y, z) relative to inertial axes ( $X_I, Y_I, Z_I$ )
$\omega_x, \omega_y, \omega_z$	- Component magnitudes of $\bar{\omega}_f$ along the float axes (x, y, z)
$\omega_s$	- Magnitude of gyro wheel spin rate
$\omega_0$	- Frequency of oscillation
$\Omega_X, \Omega_2, \Omega_3$	- Amplitudes of vibrational forms of $\omega_X, \omega_2, \omega_3$ , respectively
	- Amplitude value symbols
∠	- Phase angle symbols

## REFERENCES

- 7.1 G. R. Pitman, "Inertial Guidance," John Wiley and Sons, New York, 1962, Chart 3.
- 7.2 C. T. Leondes, "Guidance and Control of Aerospace Vehicles," McGraw-Hill Book Company, New York, 1963, pgs 87-100.
- 7.3 H. E. Thomason, "A General Description of the ST124-M Inertial Platform System," NASA Technical Note D-2983, Marshall Space Flight Center, September, 1965, pgs 53-64.
- 7.4 F. P. Daniel, (Marshall Space Flight Center), Letter (R-ASTR-AG) to E. I. Ergin (TRW), 26 August 1965, including enclosures:
  - a) G. B. Doane, "Instrumentation Error Modeling for Analytic Platform Study," (U), Memo No. 369-65, 26 July 1965, Conf.
  - b) "Float Inertias for AB5 Gyro and AB3 Accelerometer," Unclassified document.
- 7.5 F. P. Daniel, "Working Paper, Angular Motions in Instrument Unit on Saturn Flight," Marshall Space Flight Center, March 30, 1965.
- 7.6 M. W. Klotz, "Information Regarding Space Booster Angular Rate Environments," Memo No. 9351.6-625, TRW Systems, December 2, 1965.
- 7.7 "Apollo Technical Manual Structural Dynamics (Vibrations, Acoustics, Explosion)," Exhibit I Paragraph 5.1, SID 64-182 (ARM 5-2), North American Aviation, Inc., Downey, California, March 1, 1964.
- 7.8 "Military Standard Environmental Test Methods for Aerospace and Ground Equipment," MIL-STD-810 (USAF).
- 7.9 D. D. Otten, "Second Progress Report, Body Fixed Three Axis Inertial Reference System," Report No. 4499-20-RU000, TRW Systems, Redondo Beach, California, September 30, 1965.
- 7.10 M. J. Laubenstein, "Error Analysis for MSFC Body Fixed Three Axis Reference System (U)," Report No. 4499-6005-T7000, TRW Systems, Redondo Beach, California, 16 December 1965.
- 7.11 "Saturn Flight S/A-10 Digital Printout — Linear Acceleration and Angular Rate Telemetry," Flight Test Data (including oscillograph tapes), Marshall Space Flight Center, 8 September 1965.

## 8. ENCODER STUDIES

This section is devoted to a TRW-conducted survey of shaft encoder state-of-the-art. The survey was limited to the types of encoding systems that could comply with angular accuracy and resolution requirements of 10 arc sec or better.

The survey itself involved a literature search (see references following this section) and direct communication with manufacturers of encoding hardware.

The encoding devices selected for in-depth examination are discussed in Subsection 8.1 according to their primary detection concepts. Brief functional descriptions for each class of device are given, and a more detailed treatment of the inductosyn (including circuit implementation) and the theodosyn systems is given because of their more promising features. Subsection 2.6 includes the findings of the tradeoff study that support the view that the inductosyn or theodosyn system is suitable for use in this system.

### 8.1 DESCRIPTION OF ENCODERS AND SURVEY RESULTS

Digital shaft encoders produce digital output signals proportional either to the absolute magnitude of the shaft displacement or an angular increment thereof. The flow of information from the whole angle digital encoders is presented either in serial or parallel form. The outputs of the serial or parallel systems are usually in the form of gray-coded binary signals. The conversion to straight binary can be easily accomplished in the digital computer or in peripheral circuitry.

The encoding devices may be categorized in terms of their principal detection concepts, namely,

- Optical
- Variable reluctance
- Variable capacitance
- Magnetic
- Variable inductance
- Mechanical

### 8.1.1 Optical Concept

The simplest single-channel optical disc encoder consists of a light source, glass disc, and masked photodetector. As the illuminated disc rotates, the alternate opaque and transparent radial bars near the disc's periphery move past the detector, interrupting the light beam. Additional wave shaping results in an incremental pulse output.

Another optical encoder employs two adjacent glass discs with slightly different radial bar frequencies. The numbers of bars are  $N$  and  $N+1$ . Four source-detector combinations are used to record the rotation of the grading interference patterns.

An absolute disc encoder output is obtained with multiple tracks. The tracks are normally coded in natural or gray binary.

### 8.1.2 Variable Reluctance Concept

A typical variable reluctance encoder (Figure 8-1) consists of an  $N$  segmented disc and two differentially wound E core pickoffs. The pickoffs are mounted such that their outputs are in electrical quadrature. As a tooth (a segment of the disc) passes the E core, the reluctance path between the stationary E core poles and the rotating tooth will vary as the subtended angle of the E core and the number of the disc's teeth enclosed by that angle. Thus, equally spaced pulses will be generated as a function of the rotating disc displacement and its number of teeth.

For example, if six teeth are enclosed by the subtended angle of the E core,  $N$  equal pulses per disc revolution will be generated. If 12 teeth are enclosed by the subtended angle of the E core,  $2N$  pulses per revolution will result. Commercially, options are available up to  $12^{12}$  pulses per revolution (8N system). An interrogating carrier frequency greater than the product of the desired number of pulses per revolution and the maximum angular velocity of the disc is fed into the pickoffs. This operation produces as an output an AM carrier signal in quadrature with approximately sinusoidal envelope variations. (The modulating signal itself is position dependent.) These signals are then amplified, demodulated, and converted into square waves that are appropriately processed via digital logic and are indicative of the angular position of the disc.

The direction sensing is accomplished by logically using the cosine and the sine core outputs. Referring to Figure 8-1, let A and B represent the cosine and sine outputs, respectively. Let A', A', B', and B' represent the differentiated transition from logical 0 to the logical 1 state of the outputs A and B. Then during clockwise rotation of the disc the output of the clockwise "OR" gate will be represented by logical 1 ( $A' \cdot \bar{B} + \bar{A}' \cdot B + B' \cdot A + \bar{B}' \cdot \bar{A} = 1$ ), and the output of the counterclockwise OR gate will be represented by logical 0 ( $A' \cdot B + \bar{A}' \cdot \bar{B}' \cdot \bar{A} + \bar{B}' \cdot A = 0$ ). The reverse situation is applicable for counterclockwise rotation of the disc (Figure 8-1 originally appeared in Reference 8.1.)

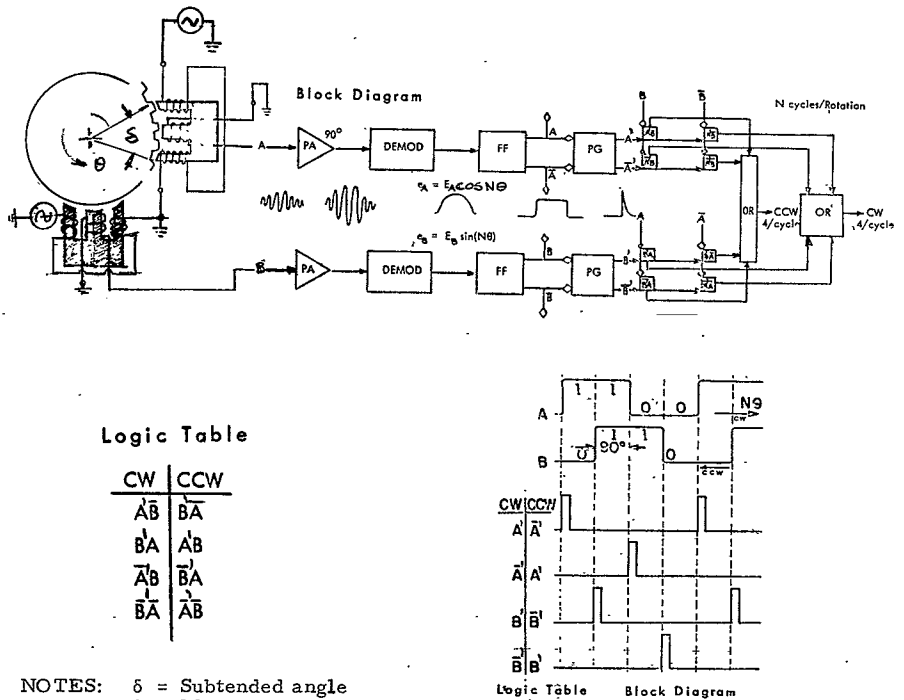


Figure 8-1. Incremental Reluctance Encoder Block Diagram (4N System)

### 8.1.3 Variable Capacitance Concept

As shown in Figure 8-2, the encoding transducer consists of a grounded metal rotor and two insulated metal stators. The periphery of the rotor has two rows of perfectly aligned teeth. Each stator also has a similar array of teeth on its inner surface, surrounding a corresponding row of rotor teeth. (Figure 8-2 originally appeared in Reference 8.2.)

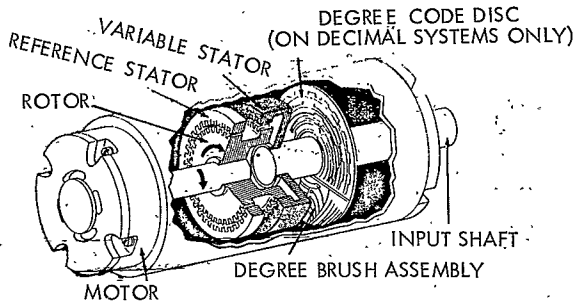


Figure 8-2. Microgyn Configuration

A constant-speed motor spins the grounded metal rotor inside the pair of stators. The stators are separated radially by a narrow air gap. The reference stator is fixed to the case of the encoding transducer, while the variable stator is attached to the shaft whose angle is to be measured. As the rotor turns inside the stators, the teeth produce a high capacitance between rotor and stator when the teeth are aligned and a low capacitance when the teeth are misaligned.

A voltage applied across the rotor-stator air gap causes a charging current to flow in the variable capacitor formed by the rotor and stator, generating an ac signal with a frequency equal to the number/sec of rotor teeth that passes a given stator reference point. The reference and the variable signal will be in phase only when the two stators are exactly in line. As the variable stator shaft is turned through one tooth pitch, the variable stator output (variable phase signal) will shift progressively through  $2\pi$  electrical radians with respect to the reference stator output

(reference phase signal). While the variable stator is turning, the instantaneous frequency of its output will differ from the reference signal by the product of the number of teeth and the velocity of the variable stator. The change in the phase angle between these outputs is thus independent of the variations in the rotor speed.

Implementation circuitry essentially identical to that described for the inductosyn (Subsection 8.2) may be utilized with this transducer.

#### 8.1.4 Magnetic Concept

Magnetic encoders are available in two forms, incremental and coded. The incremental encoder uses inductive coupling between two sets of printed electrical conductors to generate a sinusoidal output signal. Relatively complex accessory electronics are required to obtain digital position information from the analog output.

The coded magnetic transducer, Figure 8-3, is similar in configuration to the coded optical disc. Binary information is stored on the disc in the form of magnetized areas arranged in circular tracks, one track per bit. When they are interrogated, readout heads adjacent to the disc indicate the presence of a local field. A binary output is obtained only when the interrogation pulse is supplied.

#### 8.1.5 Induction Concept

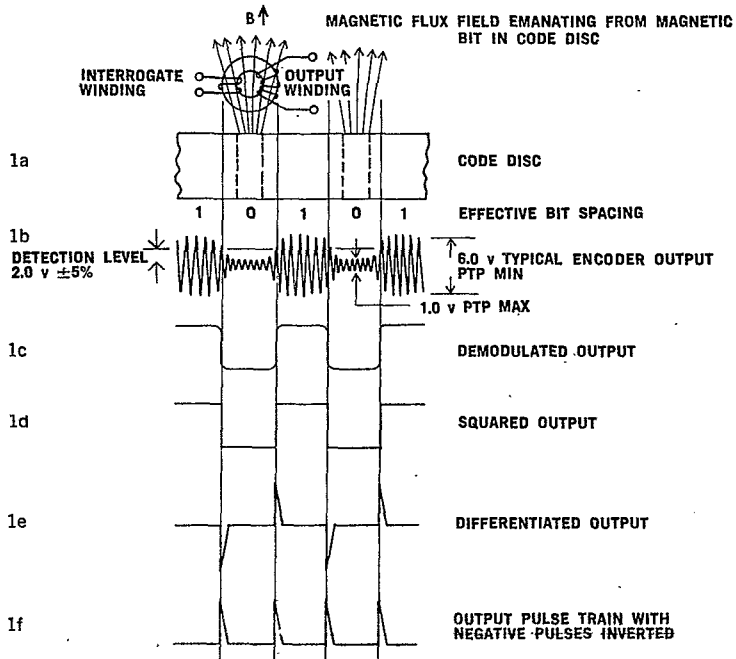
The simple two-pole resolver as well as the multipole resolver commercially known as inductosyn typify the electrical induction concept in encoding transducers.

The inductosyn is a multipole, air-core resolver with windings consisting of printed precision patterns on glass or metal support plates. A 720-pole inductosyn exhibits 360 cycles of accurate, sinusoidal, electromagnetic coupling between stator and rotor in one revolution. Output accuracy is not affected by minor plate mounting errors.

For special applications, the support plates may be mounted directly to the structure of a rotating mechanism. Weights quoted include only a pair of aluminum support plates.

For a digital system, a digitizing electronics package is required. Further discussion on the subject is given in Subsection 8.2.

(This figure originally appeared in Reference 8.3)



(Relationship between code disc pattern and output signal at successive stages of signal processing)

Figure 8-3. Magnetic Transducer

### 8.1.6 Mechanical Concept

The mechanical shaft angle encoder consists of a coded conducting plate and pickup brushes. A parallel binary output is readily obtained since the brushes are in constant contact with either the insulating or conducting portions of the code plate.

## 8.2 INDUCTOSYN SYSTEM

### 8.2.1 Principle of Operation

The inductosyn transducer can be considered a multipole resolver which depends on the inductive coupling between the stators and the rotor to generate an output signal. The rotor and the stator windings are flat metallic deposits bonded to flat annular rings. A typical inductosyn stator and rotor are shown in Figure 8-4. The particular configuration chosen initially for detail study was a 7 in. diameter unit with 720 poles, however, a 3 in. diameter unit would more than satisfy the accuracy and resolution requirements.

(This figure originally appeared in Reference 8.4.)

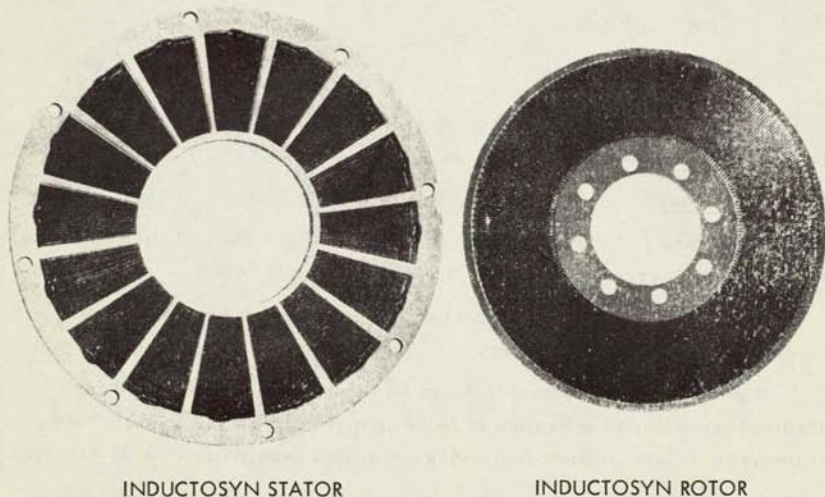


Figure 8-4. Inductosyn Transducer Discs

The voltages induced in the stators are proportional to the sine and cosine of the mechanical angle of the transmitter-rotor. The rotor output signal is transmitted via a rotary transformer used as a substitute for a slip ring assembly. The output signal derived from the inductosyn is the result of the averaging of the errors over the total number of poles; thus, the effect of small errors in individual windings is minimized. For this particular application, it was assumed that a 10 kc\* fixed carrier signal would be fed to one stator while an accurate quadrature signal of identical amplitude and frequency would be fed to the other stator winding. The resulting signal output from the rotary transformer may be described as

$$ER = EK \sin\left(\omega t - \frac{N\theta}{2}\right) = 30 \times 10^{-3} \sin\left(\omega t - \frac{N\theta}{2}\right), \text{ in v}$$

where

$$E = 2.1 \text{ v (peak)}$$

$$K = 1/70 \text{ at } 10 \text{ kc}$$

$$\omega = (2\pi)(10^4) \text{ rad/sec}$$

$$N = 720 \text{ poles}$$

$$\theta = \text{rotor angle}$$

A carrier frequency of 10 kc would take advantage of the optimum voltage transformation ratio, K. As a matter of interest, K at 1 kc = 1/120.

### 8.2.2 Accuracy

According to Ferrand (Reference 8.4), the accuracy of the unit being discussed is  $\pm 3$  arc sec. The error tolerance is not known.

The precision to which a mechanical position can be repeated on successive trials is 0.6 arc sec.

The smallest movement that can be reproduced or measured for normal bandwidths of operation (2 to 10 cps) is 0.15 arc sec. As a note of interest, a 3-in. inductosyn having a nominal sensitivity of 0.25 arc sec,

---

\* Subsequent studies have indicated that 10 kc is not required; that 5 kc would, in fact, be adequate.

when measured at a reduced bandwidth (1-sec time constant, single lag), indicated a noise level equivalent to a rotation of 0.001 arc sec. This manufacturer's data seems to be substantiated by TRW's inductosyn experience, which indicates that electrical noise is not a major problem. In fact, it was experimentally proved for a 3-in. inductosyn that the 1 $\sigma$  error for the instrument directly mounted onto a shaft was less than 3 arc sec.

In general, the errors introduced into the inductosyn system by the associated circuitry, wiring, and undesired mechanical motions such as shaft eccentricity and rotor coning, may be categorized as

- Once-per-revolution
- Fundamental
- Second harmonic, in phase
- Second harmonic, quadrature
- Fourth harmonic

The last four terms above are associated with the cycling frequency of the particular inductosyn being used. Hence, for a 720-pole inductosyn, the fundamental occurs once each mechanical degree.

#### 8.2.2.1 Once-Per-Revolution Errors

Once-per-revolution errors are caused by mechanical misalignment, specifically by mechanical misalignment in terms of eccentricity. For instance, for a 720-pole, 7 in. in diameter inductosyn, an assumed eccentricity of  $5 \times 10^{-4}$  in. will cause approximately 2 arc sec error.

#### 8.2.2.2 Fundamental Errors

Fundamental errors may be related to extraneous coupling of particular interconnecting cables. For instance, coupling either from stator line to a rotor line or from the reference excitation to either stator line can cause these errors.

### 8. 2. 2. 3 Second Harmonic Errors

Second harmonic errors of either type (in phase or quadrature) may be introduced by either mechanical or electrical means. The mechanical agency introducing the second harmonic errors is the coning of the rotor due to bearing and housing tolerances. However, these errors are small even for a relatively large coning angle and thus may be neglected.

Unequal electrical gain of the stator circuit will introduce the second harmonic error. A balance of 0.1 percent between the stator circuits will introduce an in-phase error of approximately 1/2 arc sec. The quadrature type second harmonic error is usually introduced by the cross-coupling of the stator circuits due to inadequate shielding.

### 8. 2. 2. 4 Fourth Harmonic Errors

Fourth harmonic errors are normally traced to the nonlinear components of the stator circuits, such as amplifiers or transformers not capable of linearly transmitting the full range of stator signal amplitudes. The manufacturer recommends a linearity of 1 part/1000.

### 8. 2. 3 Inductosyn Readout

The following paragraphs give a method for implementing a precise incremental angular encoder having a resolution of 3.5 arc sec. This system utilizes a precision multipole inductosyn depending upon the inductive coupling between the stator and the rotor to generate an output signal. The rotor output signal is transmitted through a rotary transformer to the electronics.

Table 8-I presents a preliminary size, weight, power, and parts count estimate of the proposed system. Table 8-II presents a preliminary reliability estimate of the incremental angle encoder system.

The proposed encoder is a binary incremented system capable of an angular resolution of 3.5 arc sec and of storing the angular information up to 360 deg. The readout of the shaft position takes place within 1 cycle of the excitation frequency. A readout rate up to 10,000 readings/sec is available. The proposed system exploits the fact that the rotor signal phase angle is directly related to the mechanical angular displacement. The design is adequate provided the velocity of the rotor is less than 150 rad/sec. For this case, under no condition will the angular readout change by more than 1 digital count during 1 carrier cycle period.

Table 8-I. Estimated Inductosyn System Characteristics

Circuits	Components										Physical Features		
	Crystal	Transistor	Integrated Circuit	Diode	Inductor	Resistor	Capacitor	Resolver	Delay Line	Transformer	Weight (lb)	Size (in. <sup>3</sup> )	Power Consumption (w)
Inductosyn Drive Circuit	1	10	13	4	2	20	20	1	-	1	1.8	40	5.5
Logic Circuits	-	4	4	-	-	10	2	-	1	-	0.7	35	
Zero-Crossing Detector	-	-	4	-	-	-	-	-	-	-			
Incremental Angle Sign Detector	-	4	20	8	-	18	2	-	-	-			
Totals	1	18	41	12	2	48	24	1	1	1	2.5	75	5.5

Table 8-II. Inductosyn Preliminary MTBF Calculations \*

Item	Crystal	Transistor	Integrated Circuit	Diode	Inductor	Resistor	Capacitor	Resolver	Delay Line	Transformer
Individual Failure Rate (bits/10 <sup>9</sup> hr)	76	20	150	20	30	5	5	?	30	30
Quantity	1	18	41	12	2	48	24	1	1	1
Total Failure Rate (Bits/10 <sup>9</sup> hr)	76	360	6150	240	60	240	120	?	30	30

Notes: MTBF = 10<sup>9</sup>/7306 = 137,000 hr

\* Using HI-REL failure rates (does not include system power supply).

\*\* Does not include inductosyn.

The incremental angular encoder consists of a 720-pole inductosyn, power drive circuitry, and logic control circuitry to obtain angular information. The information is in the form of a logical 1 or 0, indicating a change of angular position of 3.5 arc sec. The block diagram of a proposed system is presented in Figure 8-5.

A two-phase inductosyn is used to obtain the proper angle outputs, which are fed to peripheral equipment. The two-phase power is obtained in the following manner: A 10.24-mc oscillator is used as the system clock. The output of the oscillator is buffered and fed into a seven-stage counter that decreases the oscillation frequency by 128 or  $2^7$ . The output of this counter is fed into a seven-stage AND gate, the output of which is a 40 kc pulse train. This pulse train is fed into a four-stage ring counter and logic such that two square waves, precisely 90 deg out of phase, are obtained. These two square waves are filtered to produce sine waves. (The filters consist of precision components mounted in close proximity with each other to minimize the thermal effects on the precise 90 deg phase relation of the two sine waves.) These two sine waves are power amplified by 1-w amplifiers and applied to the two windings of the inductosyn. Figure 8-6 shows the wave shapes at various points on Figure 8-5.

For precise distinguishing of the difference between the inductosyn stator and rotor positions with respect to each other, a reference pulse synchronized to the stator drive voltage is used to set a control flip-flop, FF-1. The voltage induced in the rotor winding is amplified and level-detected to produce a discrete signal during a rotor voltage null crossing. This discrete signal resets the control flip-flop. The output of this flip-flop is a pulse whose width is proportional to the difference in mechanical phase between the stator and the rotor of the precision inductosyn. Since the function of the equipment is to detect relative change in the angular position between the stator and the rotor, the output,  $Q_1$ , of flip-flop 1, is used to control the input gates to up-down counters. The relative difference is obtained by first enabling the up gate of reversible Counter No. 1 (U/D-1) and allowing 10.24-mc pulses to be accumulated in the register. The number of pulses contained in this register is proportional to the width of control pulse  $Q_1$  and is therefore proportional to the phase difference between the stator and the rotor. During the next sampling period

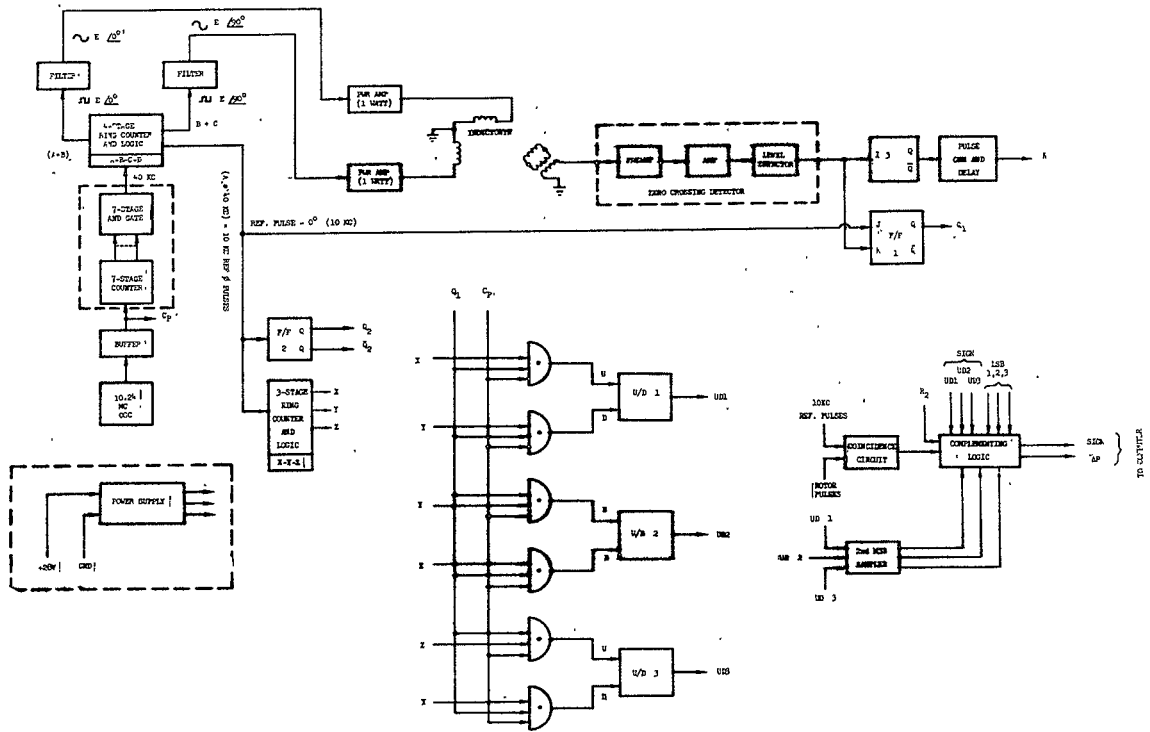


Figure 8-5. Incremental Angle Encoder Block Diagram

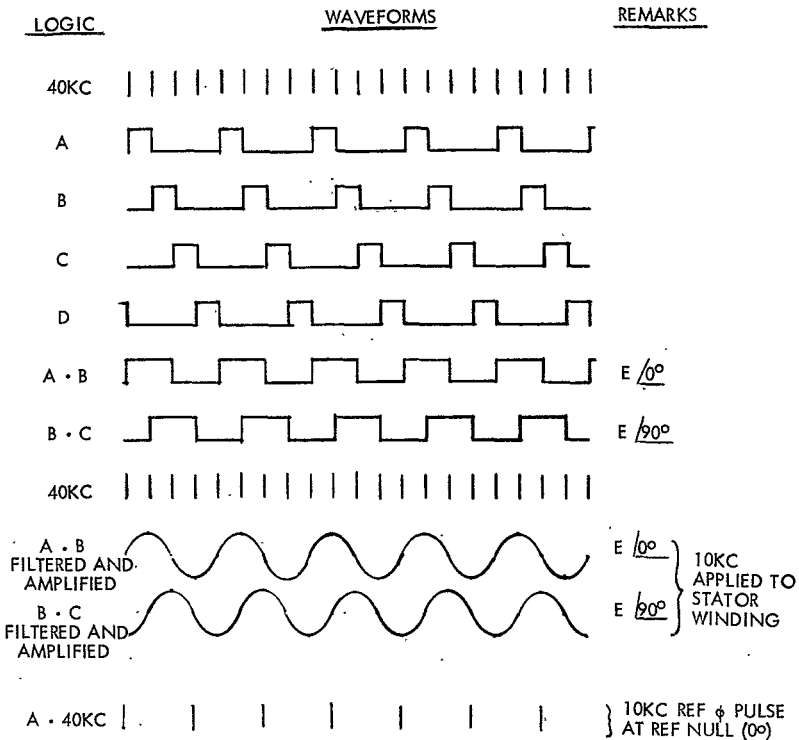


Figure 8-6. Waveforms — Incremental Angle Encoder

( $Q_1 = 1$ ) the high-frequency clock pulses are gated into the counted down input of UD-1. The contents of this register then represent the change in angular position which has occurred during the sampling interval (0.1 msec).

If a continuous difference between successive samplings is to be supplied, three reversible counters (UD-1, UD-2, and UD-3) and the steering logic from a three-stage ring counter must be used. The description thus far is valid for a positive difference. If, however, the difference is negative, the most significant bit (MSB) of the reversible counter will

be a logical 1. This information is used to complement the least significant bit of the reversible counters. It should be noted at this point that because of the selection of the sampling rates, the differences that will occur between any two sampling intervals will be  $\pm 1$  pulse or 0. Therefore, it is necessary that only the least significant bit of the reversible counters be sampled to determine whether there has been a relative change in the angular position of the rotor and the stator from the last sampling period. In the event that the rotor and the stator pulses occur at the same time (at the input to flip-flop 1) and also at the input of the coincidence circuit, logic is required to disable the reversible counters since coincidence is equivalent to a full register condition.

Even though the maximum number of pulses obtained during one sampling interval may be 1024, no more than three stages are needed in the reversible counters, because the reversible counters contain a difference of only two sampling periods, and the difference will never be greater than 1. The other two stages in the counter are used for obtaining the sign and for use in the control of the complementing logic. The output of complementing logic consists of sign information and the incremental change in the angular position between the rotor and the stator of the inductosyn.

### 8.3 THEODOSYN SYSTEM

#### 8.3.1 Description

The heart of the theodosyn system is a 1/4 in. thick, 3 in. diameter glass disc with an optical flat surface divided into  $2^{15}$  equally spaced clear and opaque radial sectors. The light source, a low-power subminiature lamp, is located under one side of the disc; the photocells are located 180 deg from the lamp. (See Figure 8-7.) The illuminated segment comprises several hundred sectors of the disc pattern. This segment is projected by the optical system to the cell side of the disc. When the disc is rotating, the instantaneous translation of the pattern is in one direction on the lamp side of the disc and in the opposite direction on the cell side. Hence, the light is alternately transmitted and blocked

in the area where the image is superimposed on the actual pattern and the relative displacement of the disc. Hence, the number of the lines on the disc is effectively doubled. The two 45 x 45 x 90 deg prisms and the roof prism accomplish the folding of the optical path. The two identical lenses between the roof prism and the 45 deg prisms facilitate the alignment of the optical components. (Figure 8-7 originally appeared in Reference 8.5.)

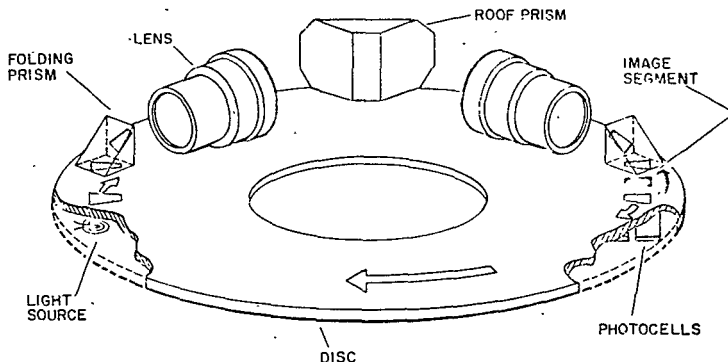


Figure 8-7. Theodosyn Configuration

The object plane corresponds to the front focal plane of the first lens; the image plane corresponds to the back focal plane of the second lens. The interference pattern by the counterrotation of the image and the object segments of the disc pattern is detected by photocells that convert the transmitted light intensities to voltages. The output of each photocell is a dc signal whose amplitude fluctuates at twice the rate of the disc pattern passing across the principal diameter. The theodosyn channel comprises two back-to-back connected photocells offset by  $1/2$  interference-pattern cycle, or 180 electrical deg. The output of the photocells varies sinusoidally.

Two such channels, in quadrature with respect to the shaft angle increment corresponding to one electrical cycle, provide direction sensing and the sine-cosine relationship required for phase-shift interpolation. The relative pattern position completes two cycles, or 39.6 sec of shaft rotation. Since these signals are 90 deg out of phase, their zero crossings are equally spaced and can be processed to provide directional information while their sine-cosine relationship is used to generate the additional phase-shifted waveforms required for increased resolution.

The output signal from theodosyn photocells are two quadrature-phased,  $2^{16}$  cycle revolution approximately sinusoidal waveforms whose amplitude is  $2 \times 10^{-6}$  amp p-p when terminated with a short circuit. These signals are amplified within the transducer to provide minimum ac signal of 100 mv. Discrimination of the two null crossings/cycle of the signals from each of the two quadrature channels provides angular resolution of  $2^{18}$  increments per shaft revolution at a minimum accuracy of  $\pm 1$  count at all shaft positions.

### 8.3.2 Theodosyn Errors

#### 8.3.2.1 Radial Runout

Because the theodosyn's output is effectively the result of two readings taken at both ends of the optical disc, the errors due to runout may be disregarded. It appears that for such gross misalignment as 0.01 in. only a 0.04 arc sec error would result.

#### 8.3.2.2 Axial Runout

Axial runout causes the object lens system to shift along the lens axis. Hence, for unity magnification, the separation of the image and the object surface is twice the magnitude of the axial motion of the disc. The defocussing effect of this separation, however, is not significant, unless it exceeds the depth of field of the lens.

#### 8.3.2.3 Disc Ruling Accuracy

Errors associated with disc ruling are limited by specification to  $\pm 2$  arc sec for 18-bit encoders.

## REFERENCES

- 8.1 Data Tech. Bulletin -- (eem-2000 and 2200); INCROSYN, Incremental Encoder.
- 8.2 Norden Bulletin, High Accuracy Angle Encoding System Microgyn.
- 8.3 Norden Data Sheet E 103, Norden Incremental Magnetic Encoders.
- 8.4 Farrand Control, Inc., Inductosyn Principles and Application.
- 8.5 Dynamic Research Theodosyn Encoders, Report E-523.

## 9. ELECTRICALLY REBALANCED OUTPUT AXIS SYSTEM

The study described earlier was oriented primarily toward the use of a SAP technique to provide the basic angular reference data. This section provides a discussion of certain aspects of an alternate technique of electrically rebalancing the output axis of a single-degree-of-freedom (SDF) rate integrating gyro. The first subsection is a tutorial discussion of the principle underlying this technique. This discussion is followed by an outline of pulse rebalancing techniques and a discussion of a typical electronic hardware mechanization.

### 9.1 PULSE TORQUING, SDF, RATE INTEGRATING GYROS

Precision pulse torquing of inertial instruments offers certain advantages that have led to their rather wide application to current guidance system design. While the design details of the various systems are widely different, there is much that all of these systems have in common. This presentation will develop a general description of the pulse torquing concept and will then discuss the electrical error sources for two generic categories.

The SDF rate integrating gyro is the only class of hardware involved in this study, thereby eliminating needless abstraction as the general analysis is pursued. However, from the electrical design point of view, the analysis is applicable to other instruments that lend themselves to precision pulse torquing.

A torque rebalanced, SDF gyro can be represented as a torque summing member having a moment of inertia,  $J$ , and a damping coefficient,  $D$ , about its output axis. Rotation about this axis,  $\theta$ , is caused by gyroscopic and electrical rebalance torques applied about the axis. The generalized output axis differential equation may be written

$$J_s \ddot{\theta} + D_s \dot{\theta} = \text{applied torque} \quad (1)$$

If the applied torque consists of a pulse of amplitude  $\alpha$  and duration  $\tau$ ,

$$Js^2\theta + Ds\theta = \alpha \left[ \frac{1 - e^{-s\tau}}{s} \right] \quad \theta = \frac{\alpha}{J} \left[ \frac{1 - e^{-s\tau}}{s^2 + \frac{D}{J}s} \right]$$

The rotation of the output axis gimbal due to this pulse can be determined with the final value theorem:

$$\begin{aligned} \lim_{t \rightarrow \infty} \theta &= \frac{\alpha}{J} \lim_{s \rightarrow 0} s \left[ \frac{1 - e^{-s\tau}}{s^2 + \frac{D}{J}s} \right] \\ &= \frac{\alpha}{J} \lim_{s \rightarrow 0} \left[ \frac{1 - e^{-s\tau}}{s + \frac{D}{J}} \right] \end{aligned}$$

Using L' Hospital's rule to circumvent the indeterminacy,

$$\lim_{t \rightarrow \infty} \theta = \frac{\alpha}{J} \lim_{s \rightarrow 0} \left[ \frac{\tau e^{-s\tau}}{2s + \frac{D}{J}} \right] = \frac{\alpha\tau}{D} \quad (2)$$

That is, the final value gimbal displacement is equal to the product of torque amplitude and the time of application, divided by the damping coefficient. Response time may be gauged by the fact that the mechanical time constant of a typical gyro is less than 0.5 msec.

The inertial angular rate input generates a torque about the output axis by acting through the angular momentum of the gyro wheel:

$$\text{inertial input torque} = \omega(t)H$$

where

$$\omega(t) = \text{angular rate input as a function of time, and}$$

$$H = \text{angular momentum of the wheel}$$

Applying superposition to the linear system,  $\omega(t)H$  may be approximated by the finite summation of a number of pulses of amplitude  $\omega_i H$  of width  $\tau$  so that, using Eq (2),

$$\theta_I(t) = \sum_{i=1}^n \frac{\omega_i H \tau}{D}$$

Allowing  $n \rightarrow \infty$  while  $\tau \rightarrow 0$  simultaneously,

$$\theta_I(T) = \frac{H}{D} \int_0^T \omega(t) dt \quad (3)$$

Eq (2) is now used to explain the generalized electrical pulse rebalance system. A number  $N$  of torque pulses, each of which will produce an angular displacement of  $\frac{\alpha \tau}{D}$ , are used to hold the output gimbal near null ( $\theta = 0$ , within the quantization limits) in opposition to the motion of Eq (3) that is,

$$\theta_I - \theta_E = \frac{H}{D} \int_0^T \omega dt - N \frac{\alpha \tau}{D} = 0$$

with  $\theta_E$  being the gimbal displacement due to the electrical rebalance pulses.

$$H \int_0^T \omega dt = N \alpha \tau \quad (4)$$

The pulse torque level  $\alpha$  is related to the electrical current in the torque generator by the relationship

$$\alpha = KBI \quad (5)$$

where  $K$  involves the structure of the torque generator,  $B$  is the magnetic flux density in the air gap, and  $I$  is the current through the torquer winding.

These factors are functionally related and will be discussed later.

Now,

$$H \int_0^T \omega dt = NKBI\tau, \text{ using Eqs (4) and (5)}$$

or

$$H \int_0^T \omega dt = NA, \text{ for brevity, with } A = KBI\tau \quad (6)$$

and

$$\frac{H}{A} \int_0^T \omega dt = N \quad (7)$$

Thus,  $N$  is a measure of the time integral of angular rate input, which is simply the net input angle turned from an initial reference position.

A generic pulse rebalance loop is depicted in Figure 9-1.

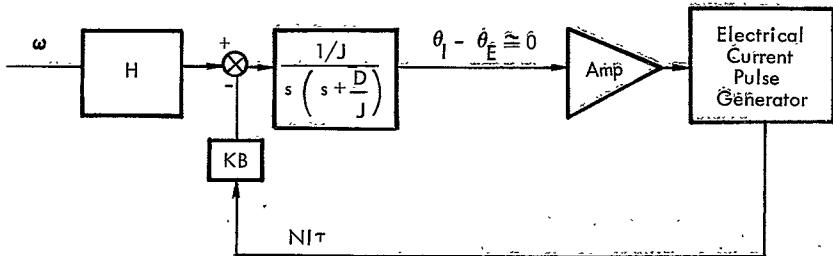


Figure 9-1. The Generic Pulse Rebalance Loop

In actuality the electrical current pulse generator will generate negative and positive pulses to balance positive and negative input angular rates. Thus

$$N = N^+ - N^-$$

Typically the positive and negative pulses will have different areas because of imperfectly controlled electrical current amplitudes and/or pulse widths. Eq (6) is rewritten to include these irregularities:

$$N^+(A + \Delta_1) - N^-(A + \Delta_2) = H \int_0^T \omega dt$$

$$N = N^+ - N^- ; - N^- = N - N^+$$

$$N^+(A + \Delta_1) + NA - N^+A - N^-\Delta_2 = H \int_0^T \omega dt \quad (8)$$

$$N^+\Delta_1 + NA - N^-\Delta_2 = H \int_0^T \omega dt$$

$$N = \frac{H}{A} \int_0^T \omega dt - \frac{N^+\Delta_1 - N^-\Delta_2}{A}$$

The first term is the ideal or desired measurement quantity of Eq (7). The second term is an error term related to pulse area errors and the specific pulse logic mechanization.

A number of pulse torqued mechanizations have been produced and used (see Subsection 9.2). A symbolic representation of the essential elements of the mechanization is presented in Figure 9-2. While other techniques have been used for current reversal, the bridge switch is typical and is usually constructed around switching transistors. Center-tapped torque generator windings and reverse polarity current sources have been used in this application also. In any event the problem is the same: The inherent difficulty in maintaining the current pulses constant and balanced plus to minus. The effects of these imperfections are pointed up in Eq (8). If these effects are to be separated into pure scale factor and bias terms, the equation must be modified to describe more specifically the mechanization.

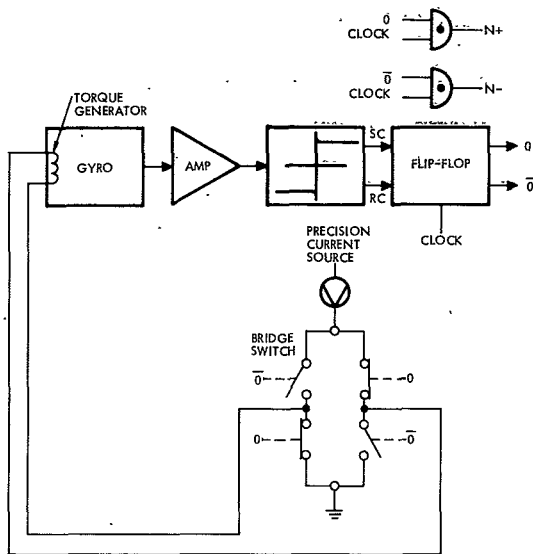


Figure 9-2. Constant Power Pulse Torque Representation

Recall Eq (7),

$$N^+ - N^- = \frac{H}{A} \int_0^T \omega dt$$

and bear in mind that for a constant power system

$$N^+ + N^- = CT$$

where  $C$  is the clock repetition rate and the reciprocal of  $\tau$ , the pulse width. The error term in Eq (8) will now be computed in terms of the nominal scale factor of Eq (7). The computational errors introduced as a result of using the nominal scale factor will be of the second order.

Solving the above two equations for  $N^+$  and  $N^-$ ,

$$N^+ = \frac{1}{2} \left( CT + \frac{H}{A} \int_0^T \omega dt \right)$$

$$N^- = \frac{1}{2} \left( CT - \frac{H}{A} \int_0^T \omega dt \right)$$

Substituting into Eq (8)

$$N = \frac{H}{A} \int_0^T \omega dt - \frac{\frac{1}{2} \left( CT + \frac{H}{A} \int_0^T \omega dt \right) \Delta_1 - \frac{1}{2} \left( CT - \frac{H}{A} \int_0^T \omega dt \right) \Delta_2}{A}$$

$$= \left[ 1 - \frac{\Delta_1 + \Delta_2}{2A} \right] \frac{H}{A} \int_0^T \omega dt - CT \frac{\Delta_1 - \Delta_2}{2A} \quad (9)$$

Comparison with the ideal relationship from Eq (8)

$$N = \frac{H}{A} \int_0^T \omega dt$$

shows that for a continuously rebalanced mechanization, a change in pulse area (the amplitude-time integral) results in clearly separable scale factor and bias errors (see Subsection 9.2). This derived relationship agrees with intuition. If the positive and negative pulse areas increase the same amount ( $\Delta_1 = \Delta_2$ ), a scale factor change will result, but the bias term will be zero. On the other hand, if the positive and negative pulses change so that  $\Delta_1 = -\Delta_2$  the error will appear as a pure bias term.

An alternate type of logic involves torquing only when the gimbal exceeds a certain deadband. This is often termed a "pulse-on-demand,"

(positive or negative) levels of the continuously rebalanced approach. A nominal zero rebalance torque level is added so that the system can call up a positive, a negative, or no-rebalance pulse depending upon the state of the gyro output axis. A small deadband is established around the gyro output axis null so that no pulse is called for when the output state is within this deadband. The continuous limit cycling of the binary system is eliminated. An extremely simplified symbolic representation of the pulse on demand prototype is shown in Figure 9-3. Again, techniques other than the bridge switch and the precision current source have been used to generate the reversible polarity pulses. Magnetic core and capacitor storage discharge have been used, but the problem of maintaining the constant and balanced current pulses remains. An additional problem occurs in maintaining the nominal zero rebalance torquing level sufficiently close to zero.

Systems having transistor switches in the configuration shown are most typical. Unbalanced transistor leakage current in the three-way switch mechanization is the primary source of unwanted gyro torques during the nominally zero torquing level periods. (A generalized equation describing the pulse-on-demand mechanization will be derived.)

Note that in this mechanization, once the gyro gimbal is within its null deadband and there are no input rates to the gyro, no pulses will be called up or applied to the gyro except as required to rebalance extraneous gimbal torques. (An ideal drift-free gyro is considered in this electrical analysis, so that the extraneous torques to be considered are due only to electrical leakage currents.) In the derivation of Eq (4) only two terms were considered, displacements due to inertial rate inputs and rebalance pulses. A third term is required for the pulse-on-demand mechanization to represent the gyro gimbal displacement due to the unbalanced leakage currents during the nominal zero pulse level.

The new equation is written:

$$\theta_I - \theta_E - \theta_L = \frac{H}{A} \int_0^T \omega dt - N \frac{\alpha_T}{D} - \left[ CT - (N^+ + N^-) \right] \frac{\beta_T}{D} = 0$$

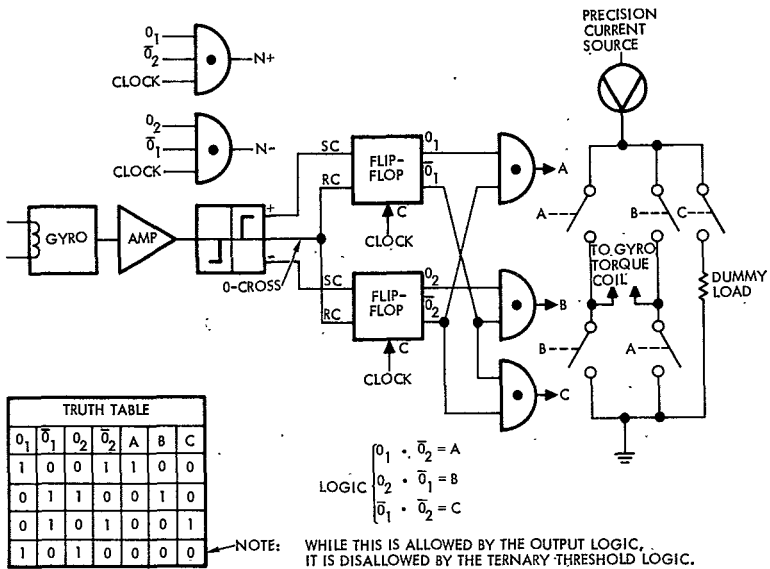


Figure 9-3. Pulse-on-Demand Pulse Torque Representation

where  $[CT - (N^+ + N^-)]$  is the number of pulse periods, in time (T) and with clock rate (C), where neither a positive pulse nor a negative pulse is called up.  $\frac{\beta\tau}{D}$  is the final value displacement for one period,  $\tau$ , with an unbalanced current torque,  $\beta$ , applied. The total final value of the displacement occurring because of the leakage current through the torquer, when it should be flowing into the dummy load is represented by

$$[CT - (N^+ + N^-)] \frac{\beta\tau}{D} = \theta_L$$

Canceling the D's, introducing pulse amplitude variations as in the derivation of Eq (8), substituting  $\alpha\tau = A$  and  $\beta\tau = \Delta_3$ , and solving for N, the pulse-on-demand equation may be written

$$N = \frac{H}{A} \int_0^T \omega dt - \frac{N^+ \Delta_1 - N^- \Delta_2}{A} - \frac{CT - N^+ - N^-}{A} \Delta_3$$

By substituting the nominal scale factors for  $N^+$  and  $N^-$ , that is

$$N^+ = \frac{H}{A} \int_0^T \omega^+ dt; \quad N^- = -\frac{H}{A} \int_0^T \omega^- dt$$

into the equation, the following equation is obtained:

$$\begin{aligned} N &= \frac{H}{A} \int_0^T \omega^+ dt + \frac{H}{A} \int_0^T \omega^- dt - \frac{\frac{H}{A} \int_0^T \omega^+ dt + \frac{\Delta_2 H}{A} \int_0^T \omega^- dt}{A} \\ &\quad + \frac{\frac{\Delta_3 H}{A} \int_0^T \omega^+ dt - \frac{\Delta_3 H}{A} \int_0^T \omega^- dt}{A} - \frac{CT\Delta_3}{A} \quad (10) \\ &= \left[ 1 - \frac{\Delta_1 - \Delta_3}{A} \right] \frac{H}{A} \int_0^T \omega^+ dt + \left[ 1 - \frac{\Delta_2 + \Delta_3}{A} \right] \frac{H}{A} \int_0^T \omega^- dt - \frac{CT\Delta_3}{A} \end{aligned}$$

Put in other terms, the output count  $N$  will be equal to the algebraic sum of the integral of positive input rate times its scale factor, the integral of negative input rate times its scale factor, and a bias term. The scale factor nonlinearity (discontinuity at zero) is caused by positive and negative pulse unbalance; the bias term is caused by unbalanced leakage currents occurring during the nominal zero pulse state; and deviations of the scale factor slope from its nominal value,  $H/A$ , are influenced both by pulse amplitude variations and the off-state leakage currents.

It is instructive to write Eq (10) in another form. Since

$$N^+ + N^- = \frac{H}{A} \int_0^T \omega^+ dt - \frac{H}{A} \int_0^T \omega^- dt = \frac{H}{A} \int_0^T |\omega| dt$$

Eq (10) may be rewritten as follows:

$$N = \frac{H}{A} \int_0^T \omega dt - \frac{H}{A} \left[ \frac{\Delta_1}{A} \int_0^T \omega dt + \frac{\Delta_2}{A} \int_0^T \omega dt \right] + \frac{\Delta_3}{A} \left[ \frac{H}{A} \int_0^T |\omega| dt - CT \right]$$

The first term is the ideal relationship. The other two terms represent errors that are dependent upon circuitry parameters and mission profile. It is significant that both error terms kinematically rectify alternating input angular rates so that drift rate will be a critical function of vehicle limit cycling. The second term, which results from pulse unbalance, will grow as the limit cycle  $\omega$ 's increase; the third term, which comes about due to the pulse off-state leakage, will decrease as  $\omega$  increases.

Before elaborating upon specific hardware errors, a few general comments must be made relative to the somewhat idealized mathematical models which have been generated. In Eq (6), which describes the generalized torque pulse, it is implicitly assumed that K (related to torque generator structure) and B (magnetic flux density) are constants. Actually, K, B, and I (torque generator current) are functionally related in a complicated manner and, in fact, the pulse torquing effort is primarily an attempt to tie down variations in these coefficients that limit analog torquing methods.

A magnetic torque generator is nonlinear with current for two reasons:

- (1) Purely magnetic effects.
- (2) Heating effects which change the flux density directly (magnetic material sensitivity) and indirectly through geometry changes primarily those which affect the air gap.

In the design of a high rate torque generator for a gyro, a tradeoff involving torque level, power, weight, and size is involved but goes beyond a simple electrical optimization. Numerous system requirements and gyro design features must be considered for a thorough understanding

of the situation. Among other things, a tradeoff between gyro mechanical drift performance and maximum torquing rate must be undertaken.

Given usual conditions, gyro mechanical drift rate is inversely proportional to the angular momentum of the gyro wheel. For high performance it is desirable to make H as high as possible, consistent with physical constraints. The general gyro torque rebalance equation

$$H \omega = \text{rebalance torque}$$

indicates that the torque level required to restrain the output axis gimbal near null is directly proportional to H and to the maximum input angular rate to be accommodated. Thus, if other system parameters are held constant, an increase in H to improve gyro drift rate performance requires a similar increase in torquing capability. Unfortunately, because of the increased mass of the gimbal about the output axis due to a larger wheel motor and a larger torque generator, the theoretical 1:1 drift performance improvement with increased H is not achieved in practice, so that gyro torque generator level requirements rise faster than any corresponding improvement in performance. Attempts at optimal high-level torquer design have led to awkward configurations and to large, heavy, high-power consuming devices, typically with torque-versus-current linearity no better than 0.05 percent. Unless an entirely new gyro and torquer design concept can be produced, significant linearity improvements are unlikely.

The purely magnetic part of the nonlinearity is reduced by operating the torquer at only two points on its torque-versus-current curve. This is, in fact, the essence of pulse torquing. However, due to magnetic material saturation characteristics and fringing effects, the torque-versus-current curve is a function of the applied frequency. Similarly, the frequency components in a pulse pattern will be a function of input rate, so that in spite of constant current pulses, the torque levels will change somewhat as a function of input rate. Odd-order terms in the nonlinearity will be reflected as small scale factor nonlinearities. Even-order nonlinearities will cause a more serious problem of torque rectification, with resultant gyro drift. These effects put constraints upon the torquer to be used for pulse torquing.

The binary or constant power mechanization offers an orderly solution to the heating problem. The torquing power is constant so that after warm-up the thermal conditions in the gyro will be constant. The constant power pulse-torqued system thus stabilizes the gyro parameter variations with input rate. While the discussion here has been centered about torque generator parameter variations, it should be noted that the constant gyro temperature also minimizes variations in the temperature and temperature gradient sensitive drift coefficients in the gyro.

The constant power system yields another advantage, of secondary importance this time. The torquer winding is typically wound with copper wire which has a resistance temperature coefficient of 0.4 percent/deg C. Where the indicated precision current sources deviate from the ideal, resistance changes in the torquer with temperature will be reflected as scale factor changes. A constant power torquing system will eliminate this effect on scale factor change with input rate. A variable power system retains the pulse torquing advantage of reducing the torque versus current nonlinearity due to direct magnetic effects, but it may suffer from the effects of continual, self-generating temperature variations which are a function of the angular rate input. These include magnetic material, geometric, and torquer wire resistance effects which influence the gyro scale factor and drift rate terms.

A conventional permanent magnet torquer typically will have a temperature sensitivity of no better than 100 ppm/deg F; however, magnetic shunting techniques may be applied to reduce this coefficient significantly. This compensation is most desirable in any case, even in a constant power system, to compensate for environmentally induced temperature changes. While this technique works well in the steady state, some difficulty is experienced in making the compensation track during input rate changes accompanying thermal lags.

A method has been proposed to obtain the advantages of the constant power mechanization (constant heat generation in the gyro) while the pulse-on-demand mechanization is used. It has been suggested that the dummy load required in the ternary system (see Figure 9-3) be placed in the gyro, but that it be interwound noninductively with the torquer winding. This design

can be justified only if it can be shown that the pulse-on-demand mechanization will provide superior performance for the specified mission and that constant power dissipation is required.

In summary, it can be said that

- (1) Pulse torquing will reduce scale factor nonlinearities caused by direct magnetic effects.
- (2) A constant power torquing system inherently provides an improved thermal environment for the gyro, leading to maximum stability of the gyro drift and scale factor error terms.
- (3) A basic variable power system will excite various gyro error terms either more or less, depending upon the design and input rates.

The system errors described up to this point are a function of the mechanization scheme, the instrument and circuit design, and the mission input rates. Empirical evaluation of the resultant system is generally required.

In the preceding discussion, it is assumed that the current pulses to the gyro are rectangular. But because of the inductive nature of the torque generator, this assumption is not strictly correct. At switching time, the current source cannot reverse the current instantaneously in the torque generator. Switching circuitry must consider transistor breakdown problems related to the inductive flyback voltage generated. For a feedback-regulated current source, the primary difficulty is that the attempted current reversal will throw the regulator into saturation for the major portion of the switching transient so that the transient time constant is determined by the static circuit parameters, i.e., the torquer inductance, resistance, and circuit series elements. With the regulator in saturation, the circuit is typically driven by the power supply as a voltage source. These factors argue strongly for a constant temperature torquer and a highly regulated voltage source if the transient occupies a significant portion of the pulse period. In any case, the transient in any pulse must be terminated essentially before the next switching time unless large-scale factor errors can be tolerated.

If the pulse rise time constants differs from the fall time constant, a scale-factor nonlinearity can arise. Under these conditions an isolated pulse will have a different weight than one pulse butted against another pulse. To prevent this condition, care must be taken to provide the same charge and discharge time constants for the torquer. The continuously rebalanced system comes closer to accomplishing this through inherent characteristics, but the pulse-on-demand system demands that special provisions be made for these constants.

Torquer tuning is sometimes used to shorten the transient, thereby reducing the regulator recovery time and the junction energy dissipated during transistor breakdown. This is accomplished to a first approximation by a series RC network across the torquer (Figure 9-4). The torquer may be approximated by a series inductor, L, and resistor, R. If the torquer time constant, L/R, is made equal to the tuning time constant, RC, and if the two resistors are made equal, the network will appear purely resistive at the torquer terminals.

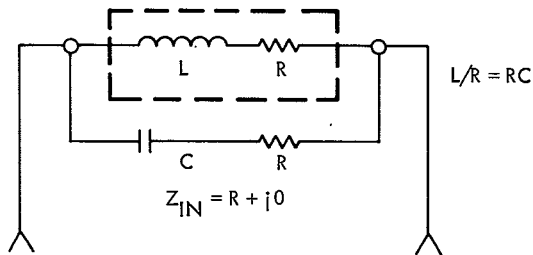


Figure 9-4. Torque Generator Tuning

$$Z_{in} = \frac{(R + j\omega L)(R + \frac{1}{j\omega C})}{(R + j\omega L) + (R + \frac{1}{j\omega C})} = R \frac{j\omega RC - \omega^2 LC + 1 + j\omega \frac{L}{R}}{j\omega RC - \omega^2 LC + 1 + j\omega RC}$$

= R + j 0, since the numerator and denominator are equal when

$$\frac{L}{R} = RC$$

Since the torque generator is not truly a lumped parameter system and is not completely described by  $R + j\omega L$ , the compensation is not perfect, although typically this simple compensation will markedly improve the torquer transient response. Refined compensation networks yield further improvement.

The idealized switches depicted in Figures 9-2 and 9-3 are only approximated in practice, usually by transistors with their troublesome shortcomings of junction offset voltages, series resistance, absence of current isolation between current drive and switch, parallel leakage currents, and their reacting to temperature and age. As in the case of the gyro, the temperature changes are both environmentally and self-induced, but an additional complication arises in the bridge circuit. In the constant torquing power system, the total electronics power is inherently constant, but the duty cycle for the diagonal switches in the bridge will change as a function of input rate. This unbalanced duty cycle will act to unbalance the temperature-sensitive parameters in the bridge as a function of input rate. In the variable power system, heating of the switching transistors will also be a function of input rate.

Because of the balanced bridge configuration, symmetrical changes are reproduced as pure scale factor changes. That is, both positive and negative pulses are affected similarly, while changes which unbalance the bridge potentially introduce both scale factor and drift error terms, depending upon the mechanization, the particular error source, and the mission rate inputs. Eqs (8), (9), and (10) reflect these errors in the  $\Delta$  quantities.

Typically, a gyro designed for high level (25 deg/sec) pulse torquing will have a sensitivity of about  $10^6$  deg/hr/amp. With the continuously rebalanced system and an electronic drift rate uncertainty of 0.1 deg/hr, it is necessary to keep the unbalance current below 0.1  $\mu$ a. On the other hand it is usually desired to maintain the scale factor uncertainty under 0.01 percent or 100 ppm, which implies a current stability of better than 10  $\mu$ a for a typical torquing current of 100 ma. Nominally then the current unbalance requirements are about 100 times more stringent than the requirements for current source stability.

## 9.2 CATEGORIES OF PULSE TORQUING LOGIC

Figure 9-5 presents a method of categorizing pulse torquing techniques.

### 9.2.1 Synchronized Pulse Rate (Period $T_s$ ): Fixed Pulse

#### 9.2.1.1 Two Charge State

The two charge state system is defined by the following equations:

$$\text{Pulse off time}/T_s = C$$

$$\text{Pulse on time}/T_s = 1 - C$$

where  $C$  is a constant,  $0 < C < 1$ . When  $C = \text{zero}$  the system has two current levels with the pulse time equal to  $T_s$ . When  $\text{zero} < C < 1$ , the system has three current levels. However, the charge or torque impulse produced during each clock period is one of two states. These states are positive maximum or negative maximum.

This system dissipates a constant energy per pulse in the sensor torquer by applying torquing pulses to the torquer at a fixed rate, regardless of the sensor pickoff position. Three types of two charge state systems are discussed below. Their characteristics vary depending on the relative frequency of the clock,  $f_c$ , and the dynamics of the sensor. The dynamics of the sensor can be discussed in terms of  $f_m$ , the maximum limit cycle frequency, which is defined as follows: Given a fixed energy torquing pulse,  $f_m$  is the maximum clock frequency for which a 1-1 moding of the system is possible, if closed loop operation for zero input consists of alternating positive and negative pulses.

If  $f_c$  is substantially less than  $f_m$ , the polarity of the amplified pickoff signal from the inertial sensor controls the torque polarity of the next pulse; however, the switching time is constrained to occur only at the time of a clock pulse. Typically, in this case the clock period and torque pulse width are identical. Since  $f_c$  is much less than  $f_m$ , it is possible with no input to force the gyro gimbal to move synchronously with  $1/2 f_c$ . Under these conditions, the sensor would be operating in a mode. Typical operating curves at zero input are shown in Figure 9-6.

REBALANCE TECHNIQUES

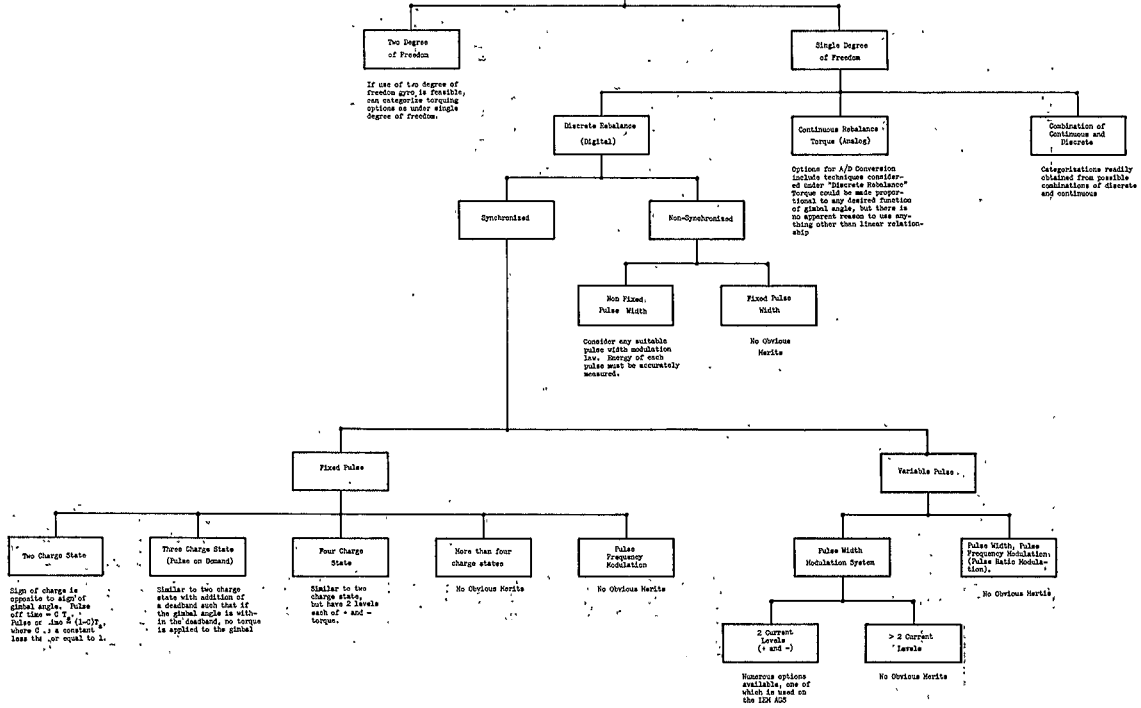
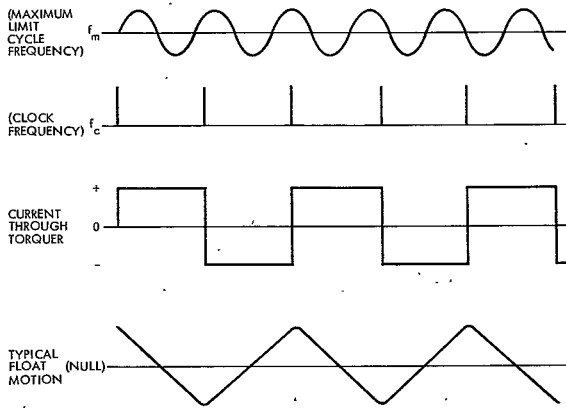


Figure 9-5. Classification of Output Axis Rebalance Techniques

9-18



NOTE: SYSTEM IS SHOWN WITH ZERO INPUT

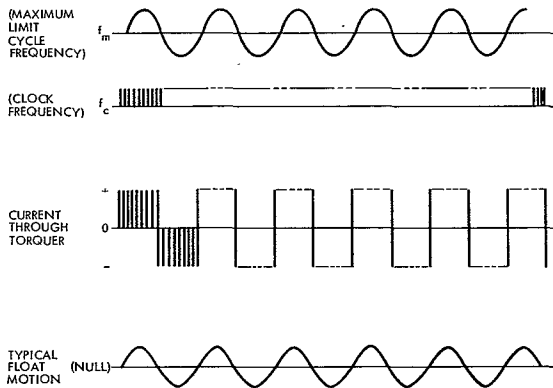
Figure 9-6. Synchronized Pulse Rate, Fixed Pulse Width, Two Charge State System ( $f_m > f_c$ )

If the sensor experienced an input, the mode would change accordingly. For example, the mode may be 1-1 for a while then change to 1-2, and so on. In other words, the mode will vary as a function of inputs. In this system, instantaneous inputs are not obtainable, and only integrated results are of any value. This is the case for practically all pulse torquing systems due to their fundamental characteristic of storing information in the float angle.

Now if  $f_c$  is much greater than  $f_m$ , a torque pulse (the width of one torque pulse is usually adjusted to be equal to the period of  $f_c$ ) is not sufficient to produce a phase reversal of the sensor pickoff signal prior to the arrival of the next clock pulse. The result is that the float motion no longer moves at the same  $f_c$  but at some other frequency dictated by  $f_m$  and the inertial sensor's input. In this case, stable limit cycles other than 1-1 can be achieved and in fact will be achieved. For example the

limit cycle may be 10-10 in which 10 clock pulses occur each one-half cycle of the float oscillating period, provided zero input is applied. (For  $f_c > f_m$ , see Figure 9-7.)

When the value of  $f_c$  is close to that of  $f_m$ , the limit cycle cannot be predicted unless some form of compensation is applied to stabilize the limit cycle (e.g., to a 1-1 system).



NOTE: SYSTEM IS SHOWN WITH ZERO INPUT

Figure 9-7. Synchronized Pulse Rate, Fixed Pulse Width, Two Charge State System ( $f_c > f_m$ )

#### 9.2.1.2 Three Charge State or Pulse-on-Demand

The three charge state or pulse-on-demand system uses three torquer current states and has a deadband associated with the sensor pickoff signal. The three charge states are

- (1) Full scale positive
- (2) Zero
- (3) Full scale negative.

When the pickoff signal is outside the deadband, a pulse of the appropriate polarity is applied to the torquer coil.

Typically, the pulse energy is selected in design to be equivalent to the information stored in the sensor (a  $\Delta$  velocity or a  $\Delta$  angle) when the sensor pickoff is at the edge of the deadband. When the pickoff is within the deadband, no current is applied to the torquer.\* The algebraic sum of the pulses through the torquer as a function of time corresponds to the change in angle rotation or velocity experienced by the inertial sensor during that time period.

### 9.2.1.3 Four Charge States

The charge as a function of gimbal angle is illustrated by Figure 9-8. The values of the torquing rates

$$\left( \frac{Q_1}{T_s} \text{ and } \frac{Q_2}{T_s} \right)$$

depend on the system requirements.

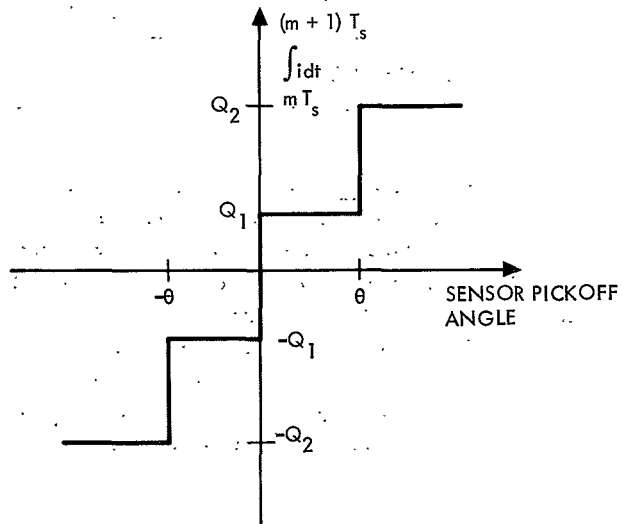


Figure 9-8. Four Charge State System

\* If it is desired to have constant power dissipated in the sensor torquer, the torquing pulses might be switched through a noninductively wound resistor in the torquer when the sensor pickoff is within the deadband.

This system's advantage is that throughout the major portion of the mission the torquing requirement will be less than the level corresponding to  $Q_1$ ; therefore, the torquer will be receiving a continuous power input. However, a large level pulse is available for the maximum vehicle rate to be considered during the mission.

#### 9.2.1.4 Five Charge States

After cursory examinations, systems of five charge states or more have no obvious merits. These systems would be extremely difficult to mechanize.

#### 9.2.1.5 Pulse Frequency Modulation

In pulse frequency modulation systems, the pulse width is fixed and the pulse frequency is made proportional to some function of sensor pick-off angle.

### 9.2.2 Synchronized Pulse Rate (Period $T_s$ ): Variable Pulse

#### 9.2.2.1 Pulse Width Modulated Systems

Pulse width is modulated to within  $T_s/N$ , where  $N$  is an integer.

9.2.2.1.1 Two Current Levels. Many techniques are available, only one of which will be discussed here. This system employs two clock signals,  $f_{c1}$ , and  $f_{c2}$ , which are derived from the same source. A low frequency clock,  $f_{c2}$ , is used to switch the logic circuits so that a particular polarity of torque is applied regardless of the sensor float position. A signal derived from the float position in conjunction with a high frequency clock signal,  $f_{c1}$ , is used to determine the precise time of the torque reversal, which always occurs in synchronism with the  $f_{c1}$  pulse train. By this means a pulse modulation system is achieved (see Figure 9-9).

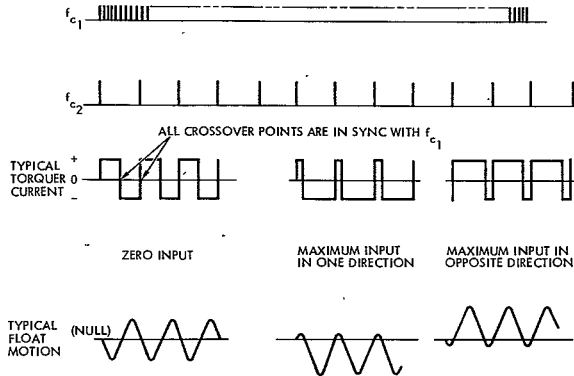


Figure 9-9. Pulse Width Modulated, Two Current Level System

The relative widths of the torquing pulses may be measured by using the logic circuits to gate the high frequency clock pulse,  $f_{c1}$ , to a counter.

9.2.2.1.2 Three Current Levels. There is no obvious merit to systems of two current levels or more.

#### 9.2.2.2 Pulse Width Pulse Frequency Modulation

There are no obvious merits to pulse width pulse frequency modulation systems.

#### 9.2.3 Nonsynchronous Pulses

There appears to be little advantage to fixed pulse width, nonsynchronous systems. The most desirable of the nonsynchronous approach appears to be a nonfixed pulse width system wherein the total energy of each pulse is accurately measured. (Of course, the concept of measuring the pulse energy to improve accuracy is applicable to all the systems discussed so far and, in fact, is often implicitly used.) Nonsynchronous systems, if desired, could be subdivided into systems similar to synchronous systems.

As an example, consider a two charge state, bang-bang, nonsynchronous system. The torquing signal would have two states, full positive or full negative. A negative signal from the sensor pickoff would turn on the full positive torquing current (this current would continue until the sensor pickoff was generating a positive signal. Then the torquing current would be switched to negative until the sensor pickoff signal changed state. Finally, a measurement of the applied pulse width and pulse area would have to be made.

### 9.3 PULSE TORQUING ELECTRONIC CIRCUITRY

In pulse torquing, an unbalance between the positive and negative pulses delivered to the sensor torquer can cause an apparent sensor drift. The magnitude of the drift depends upon the type of logic used and may also be a function of the rate input. And since low drift rates are desired, it may be necessary to take elaborate precautions in the design of the logic and power switching circuitry and the constant current generator to minimize asymmetry in the torquing pulses due to variation of circuit parameters. Also, any drift in this circuitry can cause the energy contained in the torquing pulse to change, thereby introducing an error in the scale factor (torquing weight per pulse).

The following discussion of a specific logic and power switching circuit and constant current generator for a fixed pulse width, two charge state, three current level system typifies the operation of such circuitry.

#### 9.3.1 Logic and Power Switching Circuitry

The logic and power switches are shown in Figure 9-10. Transistors Q1 through Q6 are the power switches. Q1 through Q4 determine the direction of the current through the torquer coil, and Q5 and Q6 switch the current through either the torquer coil or the dummy load in that order. The remainder of the circuit consists of flip-flops and transistor drivers and of pulse circuits for triggering the flip-flops.

The timing pulses are derived from the main counter chain to synchronize the operation of the various switching transistors. As indicated, the current through the torquer coil is turned off for an interval after each pulse and is directed into the dummy load instead. Thus, the same set of

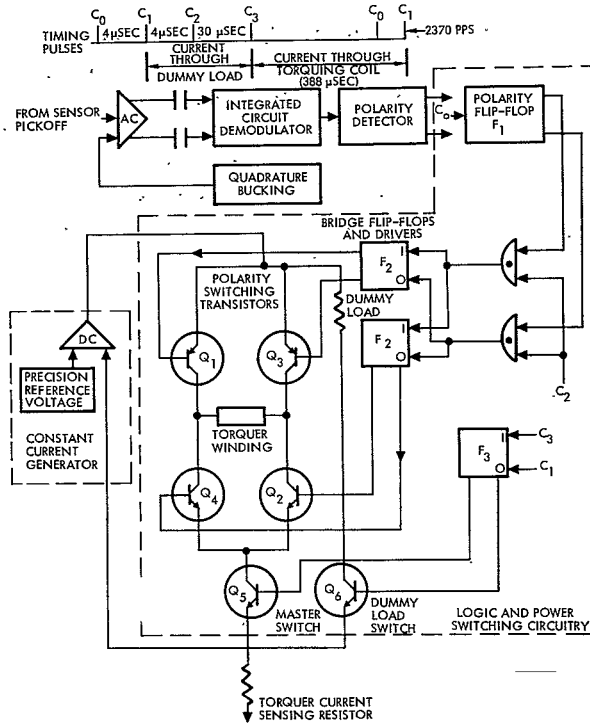


Figure 9-10. Pulse Torquing Channel

flip-flops, driver transistors and switching transistors are used for both the positive and negative torque pulses, thereby equalizing the effects of turn on and turn off delay and other anomalies.

Consequently, as explained below, the turn on and turn off rise times of the torquer pulses depend primarily on the turn on and turn off parameters of Q5, which is not polarity sensitive.

The sequence of operation with respect to the timing pulses is as follows: Between times C3 and C0, the applied torque pulse tends to move the gimbal (or pendulum in the case of the accelerometer) so that the demodulated signal out of the signal processing circuit changes polarity before C0. At the time of C0, whatever polarity is registered in the polarity

detector sets the state of the polarity flip-flop, F1, which stores this polarity (regardless of the polarity after C0) for determining the polarity of the next torquer pulse. It is essential that the polarity flip-flop be set before rather than after the end of the torque pulse in order to prevent the torque pulse turn off transient feeding into the signal lines from interfering with proper setting of the polarity flip-flop. Approximately 4  $\mu$ sec after the polarity flip-flop is triggered, C1 triggers the master switch flip-flop, F3 which turns off Q5 but does not turn off any of the bridge transistors (Q1 through Q4), thus making the turn off time of either positive or negative torque pulses dependent only on the turn off time of Q5. Approximately 4  $\mu$ sec after C1 turns off the torque pulse, C2 triggers the bridge flip-flops to change their states if there has been a polarity reversal or to remain unchanged if there has not been a polarity reversal. Thus, the bridge flip-flops are in their proper state and are driving base current into the selected pair of polarity switching transistors before the torquer current is switched on. This does not make the turn on time of the torque pulses completely independent of the turn on time of the bridge transistors, but it does make it independent of base current turn on time. Approximately 30  $\mu$ sec after C2, C3 triggers F3, which turns on the next torque pulse, thus completing a cycle.

Obviously, the parameters which contribute to a difference between the current time product of positive and negative pulses is the variation in the turn on voltages to the bases of Q1 through Q4 and the difference between the "turned on" collector current rise times of the positive and negative polarity switching transistors. This rise time is considerably shorter than the normal transistor turn on time, since the emitter base diode has been preset to the ON condition. Another accuracy consideration for the switching bridge is the saturation resistance of the various transistors.

Therefore, it can be said that errors contributing to apparent gyro drift (unequal positive and negative pulses) are attributable to differences in the collector turn on and turn off time of the polarity switching transistors, to bridge unbalance, and to variations in turn on voltage to the polarity switching transistors. Likewise, nonideal conditions which contribute to scale factor errors are those associated with the maintenance of a precise

value of current in the polarity switches, master switch, and torquer plus those associated with variations in the turn on and turn off times of the master switching transistor. Errors due to the inconstancy of the current source are discussed below.

### 9.3.2 Constant Current Generator

A block diagram of the constant current generator also is included in the functional diagram of Figure 9-10. As shown, the circuit consists of a precision reference voltage and a differential dc amplifier (current supply amplifier). The precision reference circuit supplies a reference signal to the differential amplifier, which compares the voltage developed across the torquer current sensing resistor with the reference voltage and corrects the output voltage to make the voltage across the sensing resistor approach the reference voltage. A detailed explanation is as follows:

The current supply amplifier is a solid-state chopper stabilized amplifier. The circuit consists of integrated circuit ac and dc amplifiers arranged with a semiconductor chopper in the standard chopper stabilized amplifier configuration. The inputs to the amplifier are the voltage reference and the voltage across the torquer current sensing resistor.

The precision reference circuit shown in Figure 9-10 and in more detail in Figure 9-11 consists of one circuit for maintaining a constant current through a zener reference, diode, and another circuit for supplying the precision reference voltage from a low output impedance source. The constant current is maintained through the zener diode as follows: if  $e_1$  is initially negative, the zener diode is of such low resistance that  $e_2$  will be more negative than  $e_3$ , and will produce a positive voltage at the amplifier output; as the output goes positive the static resistance of the zener diode is greater than  $R_1$  until the voltage across the zener diode has reached its low dynamic resistance region, so that the voltage across  $R_2$  will be less than that across the zener until the above zener voltage is reached. The zener voltage at which the static zener resistance is equal to  $R_2$  can be made to be very stable by making it a voltage at which the zener dynamic resistance is much smaller than  $R_2$ . At this point, variations in  $e_1$  will cause much greater variation in  $e_2$  than in the voltage across the zener.

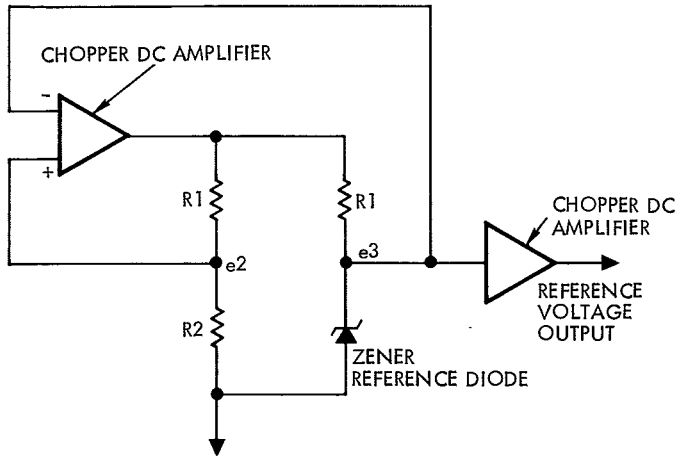


Figure 9-11. Precision Reference Voltage Generator

The zener diode voltage feeds the voltage isolation amplifier, which is a chopper dc amplifier having an emitter follower output with voltage feedback. The circuits in the voltage reference are integrated circuits and microminiature transistor circuits.

## 10. NEW CONCEPTS

During the period covered by the subject contract, no new concepts were conceived or first reduced to practice.

24 OCT 66 73768

1cy